Combined Diesel Particulate Filter/Heat Exchanger for Engine Exhaust Waste Heat Recovery with Organic Rankine Cycle

BY

©2016
Charles E. Sprouse III

Submitted to the graduate degree program in Mechanical Engineering and the Graduate Faculty of the University of Kansas School of Engineering in partial fulfillment of the requirements for the degree of Doctor of Philosophy

_____
Chairperson, Dr. Christopher Depcik

_____
Dr. Theodore Bergman

_____
Dr. Peter TenPas

_____
Dr. Edward Peltier

_____
Dr. Xinmai Yang

Date defended:_____

ACCEPTANCE PAGE

The Dissertation Committee for Charles E. Sprouse III
certifies that this is the approved version of the following dissertation:

Combined Diesel Particulate Filter/Heat Exchanger for Engine Exhaust Waste Heat Recovery with Organic Rankine Cycle

_____

Chairperson, Dr. Christopher Depcik

Date Defended:_____

ABSTRACT

Diesel Particulate Filters (DPFs) are currently being used to remove Particulate Matter (PM) from compression ignition engine exhaust streams with collection efficiencies approaching 100%. These devices capture soot by forcing the exhaust gases through porous walls, where entrapment of the particulates initially occurs. Eventually, a cake layer begins forming on the inlet channel walls, causing an increased pressure drop through the device and necessitating a soot combustion event to unload the filter. The exothermic nature of these regeneration events serve to enhance the thermal energy content of the exhaust, which already contains approximately one-third of the fuel energy being consumed by the engine. Typically, the energy from both sources is expelled to the atmosphere, destroying the ability to produce useful work from the exhaust heat. However, a novel device described here as a Diesel Particulate Filter/Heat Exchanger (DPFHX) may be coupled to an Organic Rankine Cycle (ORC) to simultaneously provide particulate matter filtration and waste heat recovery.

The DPFHX concept is based on the shell-and-tube heat exchanger geometry and features enlarged tubes to contain DPF cores, allowing energy capture from the engine exhaust while preserving the standard technique of PM abatement. Since the working fluid circulating on the shell side collects heat from the exhaust, the DPFHX serves as the organic Rankine cycle's evaporator. Along with the cycle's pump, expander, and condenser, the DPFHX forms an ORC capable of transforming exhaust waste heat into supplementary power for the engine. Reducing exergy destruction in this manner meets the two main objectives of engine research; the reduction of fuel consumption and emissions. The degree to which the proposed DPFHX-ORC

system achieves these goals is a focus of this dissertation, where the advancement of this technology occurs primarily through theoretical efforts.

As precursors to the eventual DPFHX-ORC computer model, individual ORC and DPF models are created. With respect to simulating an ORC, a historical study of the ORC WHR literature informs the design choices associated with building an ORC model. Authors in this research area note that the two dominant factors influencing cycle performance are the working fluid and expander selections. Based on these findings, eight dry fluids (butane, pentane, hexane, cyclopentane, benzene, toluene, R245fa, and R123) compatible with reciprocating expanders are identified for use in an ORC model. By simulating WHR from a Yanmar L100V diesel engine, the component-based ORC constructed illustrates an approximate 10% improvement to the engine's efficiency across all operating conditions and favors the use of pentane or cyclopentane as the cycle's working fluid. These results are consistent with reported ORC outputs in the literature and demonstrate the ORC model's value as a component of the DPFHX-ORC model.

The second foundational component is a DPF model, which is developed using the DPF governing equations in area-conserved format. A series of model validation efforts show that the DPF model is capable of generating accurate thermodynamic parameter profiles in the inlet and outlet channels, along with tracking the monolith temperatures and soot combustion. However, extension of the model to include external heat transfer to the ORC working fluid requires the creation of a novel multi-dimensional DPFHX computer model due to the small DPF core size and enhanced heat transfer in a DPFHX. This model does not follow traditional multi-dimensional modeling schemes by allowing heat transfer with and without the DPF cores as intermediaries. Also, the model does not couple inlet and outlet channels, or force all walls bordering an individual channel to have uniform conditions. The DPFHX model provides heat

recovery predictions for coupling with the ORC model, allowing power output predictions from the entire system based on the single cylinder Yanmar test cell at the University of Kansas as the waste heat source.

By matching the energy leaving the engine exhaust to the heat entering the ORCs working fluid, a DPFHX-ORC model is constructed in MATLAB. At very low engine load (227.3 W), the ORC system generates 156.8 W of power, corresponding to a 69.0% efficiency improvement over the engine alone. At typical engine loads (1726.7 W to 6205.5 W), the DPFHX-ORC system provides an efficiency increase between 9.5-13.7%. Along with the illustrated fuel consumption reduction is a reduction of all emissions by the same amount, following a short warm up period. The reduction of hydrocarbons and carbon monoxide are unaffected by installation of the DPFHX, and conversion efficiencies of nitrogen oxides are maintained by placing the selective catalytic reduction hardware before the DPFHX, alleviating concerns of low-temperature conversion. Due to the energy removal taking place in the DPFHX, PM collection occurs at reduced temperature levels; however, the efficiency of this process remains high due to the mechanical nature of filtration.

ACKNOWLEDGEMENTS

I have special gratitude to my wife, Tricia, for her unconditional love and unwavering support. Along with my son John-Paul and daughter Maria, my family has given me the strength and perseverance to complete this work. I am also grateful to my extended family, including my parents, sister, grandparents, and in-laws, for their encouragement and their confidence in me. Most of all, I thank God for providing me with more blessings in every area of my life than I will ever deserve.

TABLE OF CONTENTS

Chapter 1

Background, Waste Heat Recovery Methods, and Scope of Work

1.1 Background

Over the past century, the Internal Combustion Engine (ICE) has been a primary power source for automobiles, long-haul trucks, locomotives, and ships [1]. During this period, fluctuating fuel prices and concerns over foreign oil dependence combine with increasing anxiety over atmospheric pollution to spawn engine redesigns and emissions legislation. In an effort to improve the thermal efficiency of ICEs, engine manufacturers use enhanced fuel-air mixing, turbocharging, and variable valve timing. These techniques require increasingly complex engine designs where further decreases in fuel consumption are burdened by significant hardware costs. Moreover, incremental lowering of emission levels are causing engine manufacturers to limit combustion pressures and temperatures, lowering potential efficiency gains.

Among the exhaust species subject to Environmental Protection Agency (EPA) regulations under the Clean Air Act are particulate matter (PM), hydrocarbons (HC), carbon monoxide (CO), and nitrogen oxides (NO_x) [2], with future legislation targeting carbon dioxide (CO_2) on the horizon. To meet these standards, engine manufacturers are utilizing significant levels of cooled Exhaust Gas Recirculation (EGR) along with multiple in-cylinder fuel injection events in order to decrease combustion temperatures since NO_x increases exponentially with temperature through the thermal NO mechanism. This method subsequently diminishes the

efficiency of Compression Ignition (CI) engines because of the reduced work available due to the lower combustion pressures that result.

Since in-cylinder techniques and EGR are not capable of meeting EPA standards without aftertreatment devices, manufacturers of Spark Ignition (SI) engines are using the Three Way Catalyst (TWC), while CI engines have been fitted with a four-way aftertreatment system [3]. In both cases, catalytic devices convert harmful emissions to nitrogen gas (N_2), carbon dioxide (CO_2), and water (H_2O). Through modification of injection timing and rate shaping, CI engines often operate with reduced combustion temperatures to prevent the formation of NO_x as its conversion in a four-way aftertreatment system is relatively difficult. SI engines often accomplish a similar tactic by retarding the spark timing; however, TWC devices have the inherent advantage of using CO and HC to reduce NO_x. Therefore, there is less of a need to adjust the combustion timing. As mentioned previously, these strategies reduce engine efficiency by achieving less combustion at prime crank angles.

Current diesel engine aftertreatment systems group a Diesel Oxidation Catalyst (DOC) with a Diesel Particulate Filter (DPF) and Selective Catalytic Reduction (SCR) system, as shown by Figure 1. These systems contrast with Spark-Ignition (SI) engine aftertreatment systems because the three-way catalyst following SI engines is not capable of reducing NO_x in the presence of excess oxygen.
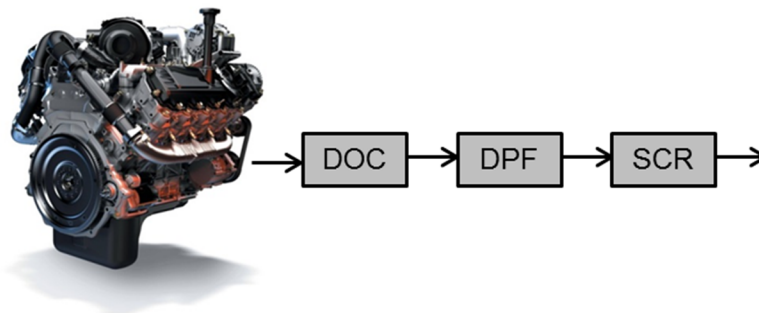
Figure 1: Diesel engine aftertreatment device schematic [4]

In the DOC, heterogeneous surface reactions reduce hydrocarbons and carbon monoxide to CO_2 and H_2O. To accommodate these species conversions, a DOC features a honeycomb of channels, which are coated in catalytic metals to lower the activation energy of the desired reactions. A different type of flow network is found in the DPF following, where a monolith of cordierite or silicon carbide porous walls provide a compact way to achieve filtration of PM. Since alternating channels of the DPF are blocked, all of the exhaust must pass through a porous wall before exiting the filter. For this reason, standard DPF terminology specifies that flow enters an inlet channel and passes through the porous wall into an outlet channel before finally exiting the DPF. As a result of this filtration eliminating nearly 100% of PM emissions, DPFs are currently the preferred industry method for carbon capture in diesel exhaust [5]. After removal of PM in the DPF, Diesel Exhaust Fluid (DEF) injection facilitates SCR of NO_x into H_2O and N_2 in a zeolite catalyst [6]. Reported conversion efficiencies around 90% establish SCR as the industry standard NO_x abatement technique [7].

Despite the progress in reducing fuel consumption and hazardous emissions, the ICE continues to be plagued by the same challenges; increasingly low emission limits, concerns over foreign oil, and high fuel prices. In addition, as shown by Figure 2 for California, gasoline and diesel consumption is expected to continually rise throughout the near future, creating further demand for new hardware capable of improving powertrain efficiency. While looking into the future, the potential for standards targeting CO_2 are also pressuring changes to the ICE. Unlike other harmful emissions, CO_2 is an inevitable result of combustion, requiring less fuel usage to reduce production. For this reason, legislated CO_2 limits are effectively mandates to improve engine thermal efficiency (when using carbon fuels). By recalling that recent technological

advancements are no longer returning adequate dividends, the need for a new approach to provide thermal efficiency improvements becomes apparent.
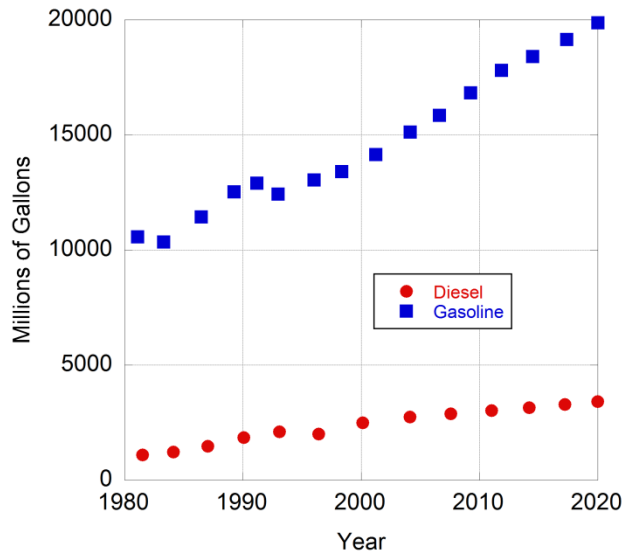
Figure 2: California fuel consumption projections [8]

One method for simultaneously reducing fuel consumption and emissions is highlighted by the one-third estimate of engines. This rule of thumb states that the 100% fuel energy input to the engine is transformed to approximately equal parts useful work, coolant waste heat, and exhaust waste heat (see Figure 3). Of course, the proportion of waste heat in each category changes significantly according to the engine operation, where city driving results in more coolant waste heat and highway speeds produce more exhaust waste heat. Along with the waste heat fractions, the amount of useful work relative to fuel input varies with engine speed and load. Still, the one-third rule is important for highlighting that around 60-70% of the fuel energy is lost as waste heat through the coolant or the exhaust [9].
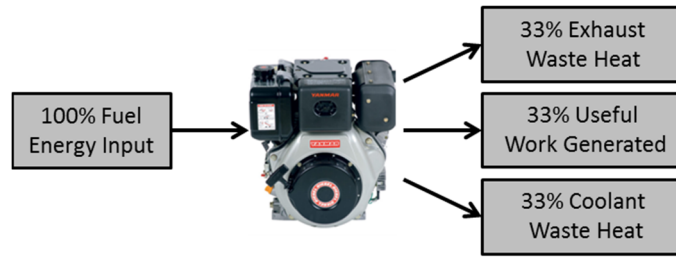
Figure 3: One-third estimate of engines [10]

With efforts targeting improvement of the useful work fraction encountering difficulties from expensive hardware and the efficiency-NO_x tradeoff, and with two-thirds of fuel energy being wasted as thermal energy, an opportunity exists to convert a portion of the waste heat to useful work through Waste Heat Recovery (WHR). By definition, WHR is the conversion of waste heat to a more useful form of energy, namely mechanical or electrical. As such, a variety of WHR methods are available. Among these are turbocharging, thermodynamic cycles, and thermoelectrics. Selection of a WHR approach requires consideration of the waste heat sources available and the system size. The two primary sources of waste heat from an ICE are the engine exhaust (medium-grade) and engine coolant (low-grade). Other options for heat recovery include the relatively smaller amounts available from an EGR cooler and Charge Air Cooler (CAC) [3]. Despite both primary sources having similar energy content, the higher temperature of the engine's exhaust makes it more thermodynamically attractive when viewed from the perspective of exergy. This results in a higher theoretical efficiency gain when coupled to a heat engine [9].

1.2 Waste Heat Recovery Methods

The most common WHR technique, particularly for diesel engines, is turbocharging. Here, a turbocharger utilizes the elevated pressure of the engine exhaust to boost the air into the engine. This approach enhances engine performance by improving volumetric efficiency; however, engine exhaust at the turbocharger exit still contains significant amounts of thermal

energy. For more complete WHR, the primary candidates for ICE WHR are ORCs, steam Rankine cycles, Brayton cycles, Stirling cycles, Kalina cycles, and carbon dioxide transcritical cycles. While publications are available on each concept, most small-scale WHR efforts prefer the Rankine cycle due to its simplicity, use of standard components, and ability to operate efficiently between small to moderate temperature differences [1].

1.2.1 Rankine Cycle

A Rankine cycle is a closed-loop system where a working fluid repeatedly circulates through four components to transform waste heat into mechanical or electrical power. If the selected working fluid is organic in nature, researchers often refer to this system as an Organic Rankine Cycle (ORC). As shown by Figure 4, the simple ORC operates by repeatedly circulating a working fluid through four components.
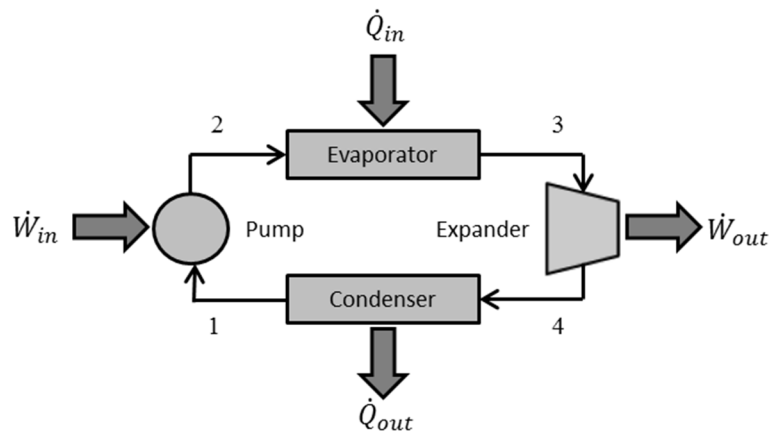
Figure 4: ORC components with inputs/outputs

To demonstrate the conversion of waste heat to useful work, the cycle description here begins with the evaporator (process 2-3 in Figure 4), where the working fluid captures available waste heat from the engine exhaust. The next step in the cycle is expansion of the working fluid, resulting in power generation (process 3-4 in Figure 4). A variety of expanders exist to generate mechanical or electrical power, including displacement and turbomachines. Following expansion

of the fluid, a condenser rejects low-grade thermal energy to the atmosphere (process 4-1 in

Figure 4). Completing the cycle, a pump compresses the working fluid back to its initial state

(process 1-2 in Figure 4). To note, there are two variations of the traditional Rankine cycle;

reheat and regenerative.

In the reheat version, the working fluid does not expand fully to the condenser pressure in

a single stage (process 3-4 in Figure 5b). Instead, the cycle sends the partially expanded working

fluid back to the evaporator for reheating (process 4-5 in Figure 5b) with a subsequent second

expansion resulting in the working fluid ending at the condenser pressure (process 5-6 in Figure

5b). The principle advantage of the reheat Rankine cycle is an increased quality at the expander

exit [11]. A higher working fluid quality indicates a reduction in moisture content, which

increases the lifetime of turbine expanders. In the regenerative variation, a portion of partially

expanded working fluid (process 5-6 in Figure 5c) preheats the condensed liquid before it enters

the boiler (process 2-3 in Figure 5c). Preheating in this manner decreases the amount of heat

added at low temperatures, increasing the mean effective temperature of heat addition while

enhancing cycle efficiency [12]. Of pertinence, these explanations only apply to traditional steam

Rankine cycles, not to ORCs; however, it is important to understand the fundamentals of these

cycles before expansion to ICE utilization. Figure 5 provides a comparison of the three Rankine

cycle variants for clarity of description.
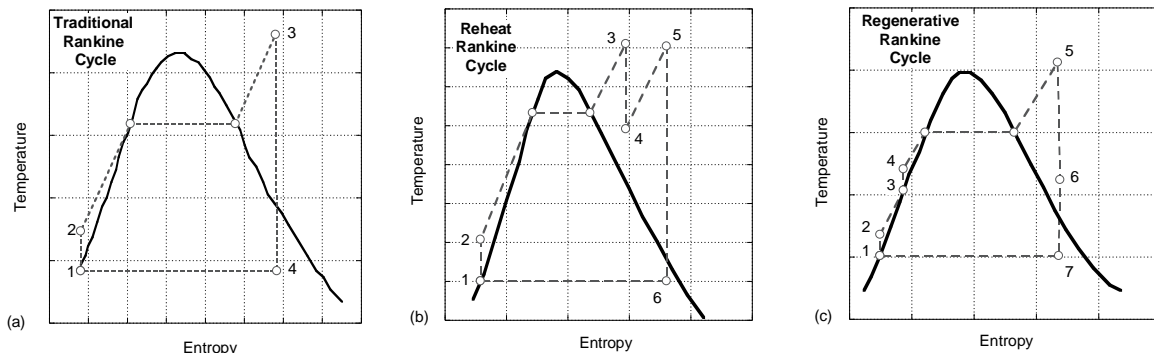
Figure 5: Variations of Rankine cycle: (a) Traditional, (b) Reheat, and (c) Regenerative [12]

A significant number of research efforts on ORC WHR are available in the published literature, including several works using engine exhaust as the waste heat source [1, 13]. In agreement with the historical works, a recent component-based simulation effort by the author shows cycle efficiencies around 15% with fuel economy improvements around 10% from a standard ORC across engine loads [14]. Further evidence of interest in Rankine cycle WHR is shown in recent efforts by Toyota, Wartsila, Honda, BMW, and Volvo [9, 15-18].

1.2.2 Alternative WHR Methods

It is also possible to achieve WHR using other unique thermodynamic cycles. One such method is the open Brayton cycle, which requires only three components. This cycle begins as a compressor draws atmospheric air into the system, pressurizing it above ambient conditions. A heat exchanger then adds heat to the air before the fluid passes through an expander, creating power and returning the air to the atmosphere [12]. Another common option is the Stirling cycle that includes a closed system comprised of a regenerator and a cylinder, which contains both a displacement and power piston [19]. The first process in this cycle involves an isothermal compression of the working fluid as the power piston moves from bottom dead center to top dead center. Heat is then added to the working fluid while the displacement piston moves downward, pushing the working fluid through the regenerator in a constant volume process. The next step is an isothermal expansion, where both pistons move downward to generate power. Finally, the displacement piston moves upward, pushing the working fluid through the regenerator rejecting heat in a constant volume manner [12].

More recently, increased focus has been placed on the development of Kalina cycle systems, which parallels an ORC in configuration with the addition of an absorber and flash tank [20]. This cycle uses a variable composition mixture of ammonia and water as the working fluid.

Similarly, supercritical carbon dioxide systems have drawn attention in various WHR applications. While most WHR research focuses on thermodynamic cycles, thermoelectric (TE) devices offer a unique alternative. Waste heat recovery is possible in this manner due to the combination of thermal, electrical, and semi-conducting properties in a TE [21]. This power generation capability comes from Seebeck's 1821 observation of the deflection of the needle of a magnet when exposing dissimilar metals to a temperature gradient. Nowadays, pairs of semi-conductors, usually bismuth telluride or silicon germanium, are arranged in order to create a TE system. One significant advantage of thermoelectric devices is their simplicity since they directly convert thermal energy into electrical energy.

1.2.3 Waste Heat Recovery Comparison

As previously elucidated, an ORC is the focus of most small-scale WHR efforts due to its simplicity and ability to operate efficiently between small to moderate temperature differences. Another primary advantage of the ORC is the use of widely available and affordable components because of the similarities between ORC and refrigeration systems. While no single WHR method is superior for every system size and waste heat source, the authors believe ORCs provide an attractive combination of efficiency and affordability for engine exhaust WHR. Some selected research efforts on alternative WHR methods are described in the following paragraphs simply to provide context and starting references for the reader, since an exhaustive comparison is outside the scope of this dissertation. Additional resources on Kalina cycles [22-25], thermoelectrics [26-28], and carbon dioxide transcritical cycles [29-31] are available.

By contrast, relevant studies have found that various Brayton cycles are marginally attractive as an alternative to turbo-compounding [32]; however, they require a longer payback time [33], and are less attractive for low to medium temperature WHR [34]. Similarly, Kubo

found that several Stirling cycle configurations to recover waste heat from an adiabatic diesel engine were not economically attractive [19], and fail to match previous performances of ORC [35] and steam Rankine cycle [36] systems. More recently, the ORC investigated by Bianchi and De Pascale was favored over the Stirling engine [34]. Kalina cycle research has focused primarily on large-scale facilities, demonstrating that these systems efficiently recover waste heat in the engine exhaust temperature range [20, 37-40]. Practical restrictions on maximum cycle pressure suggest that carbon dioxide transcritical cycles would not be feasible for exhaust WHR, despite the cycle's favorable performance shown by Chen at low temperatures [41].

A summary of the present and future applications of thermoelectric devices is provided by Riffat and Ma, defining their maximum temperature difference as 70°C and efficiency at around 5% [42]. Even with cascading devices, which will function for differentials of 130°C, the authors restrict the competitive regime of TEs to low temperature waste heat. If efficient WHR is not required to achieve the objective, such as meeting the electrical requirements of a family car, TEs could provide a viable alternative to ORC systems [43].

Of importance, in addition to ICE waste heat, Najjar recognizes the possibility of using ORCs for WHR from other power generating devices, such as gas turbines [44]. More recently, Quoilin and Lemort described the use of ORCs as part of several green energy systems [45]. Among these were biomass, solar, and geothermal stations. Both works include descriptions of previous publications in their respective research areas. However, the primary goal of the author is to increase the thermal efficiency of the ICE for lower greenhouse gas emissions without adversely influencing emissions. Of interest, there has been research on using recovered exhaust waste heat for automobile heating, offering a secondary avenue of usage [46].

1.3 Scope of Work

This effort describes the research of a novel combined Diesel Particulate Filter/Heat Exchanger (DPFHX) for simultaneous reduction of emissions and fuel consumption, by using the DPFHX as the evaporator in an ORC. In concept, the DPFHX (see Figure 6) functions identically to a standard DPF except that the device contains several small DPF cores (brown/black) instead of one large filter. To double as a heat exchanger, a working fluid circulates inside the DPFHX shell (blue) and over the tubes containing the DPF cores (dark gray), receiving energy from the engine exhaust. Through coupling the DPFHX to an ORC, installation of this device could result in a 10 to 15% savings in fuel consumption [1], with further energy capture possible from the regeneration event, where rapid combustion of the PM entrained releases large amounts of thermal energy.
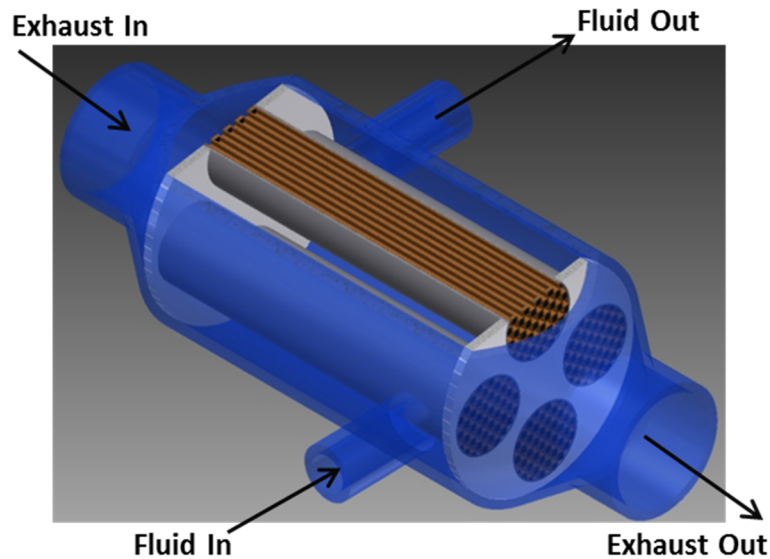
Figure 6: Section view of theorized DPFHX concept

In addition to the emissions and efficiency advantages of recovering heat during regeneration, the device also has the potential to limit DPF core temperatures during soot combustion, reducing the possibility of thermal cracking of the DPF. Thus, installation of a

DPFHX system will decrease premature failures of PM filtration devices, reducing maintenance costs and preventing damage to the engine from excessive backpressure. While the DPFHXs name suggests that applications are limited to diesel engines, recent design changes to SI engines must also be considered. Manufacturers are shifting from configurations where gasoline-air mixing occurs before entering the engine's cylinders in favor of Gasoline Direct Injection (GDI) engines. This allows SI engines to more easily draw air into the combustion chamber, at the cost of introducing heterogeneous combustion and increased soot formation. As a result, future gasoline engines will require filtration devices, vastly expanding the target applications of the DPFHX. Since the DPFHX concept is entirely original, researching the proposed DPF alternative requires the creation of computer models to evaluate its performance and laboratory experiments to examine the potential heat recovery.

Since the device exists within both engine and organic Rankine cycle systems, efforts to develop the DPFHX concept must be multifaceted. The first steps toward evaluating the viability of the concept involve the creation of a computer model of the DPFHX-ORC system while beginning to develop experimental capabilities to test waste heat recovery devices. Starting with the computer model, some important simplifications to the task are possible by examining each of the engine system's components. First is the engine itself, for which computer modeling is quite involved. Fortunately, a single-cylinder engine laboratory exists at KU and can provide the necessary exhaust parameters in deference to modeling. Future research includes computer models of the system that will couple an ORC and DPFHX model to a virtual engine.

Modeling of the ORC components is necessary to gauge the possible conversion of recovered waste heat to usable power. However, a variety of design choices are embedded within an ORC model, such as working fluid and expander selection. For this reason, it is important to

review the available literature on ORCs targeting waste heat sources with temperature levels and sizes comparable to ICE's. With an understanding of the applicable works, some of which were mentioned previously to motivate the selection of an ORC as the preferred WHR method for this enterprise, valuable insight can be used to inform the ORC design choices required by the application under study.

Following the chapter presenting previous works in the area of ORC WHR is a description of the virtual ORC developed, which simulates power generation from the ICE exhaust energy. To allow independent evaluation of the ORC and DPF models before creating one comprehensive model, a simple shell-and-tube evaporator stands in for the eventual DPFHX. After completing the virtual ORC, parametric studies of different working fluids and expander geometries allow design choices that are not possible in advance. By imposing practical constraints on various physical parameters, leading candidates for working fluids and the expander geometry are available for use in the subsequent DPFHX-ORC model.

Similar to the reasoning behind creating a stand-alone ORC model, development of a DPF model precludes the efforts to represent the entire DPFHX system. Consistent with classical works in the area, a 1+1D model of a single inlet channel-outlet channel pair represents an entire filter [47, 48]. Going further, the complexity of the DPF governing equations suggests a simplified representation of the flow (without heat transfer) as an initial study. By using this approach, results from the isothermal DPF model described in Chapter 4 can be compared to a previous publication for validation [49]. Once accurate thermodynamic property profiles are demonstrated within the channels and wall under isothermal conditions, inclusion of a monolith energy equation allows simulation of warm up conditions and a wall mass equation offers regeneration modeling capability. With a means of representing the DPF by numerical solution

of the associated governing equations, Chapter 6 focuses on foundational experimental efforts to test the heat recovery potential of a large tube heat exchanger.

Chapter 5 provides a thorough description of the DPFHX concept, along with the practical considerations of including the device within the exhaust stream of a diesel engine. Conversion of harmful species is discussed, along with basic design decisions such as tube size and DPF core material. Theoretical efforts then continue in Chapter 7, where the ORC and DPF models of previous chapters are adapted to model the DPFHX-ORC system.

Complete representation of the proposed system involves developing a new model structure and adding a multi-dimensional heat transfer terms to the DPF monolith energy equation to account for heat recovery and ensuring that the quantity of heat removed from the engine exhaust is added to the ORC working fluid. Using typical heat transfer parameters, the DPFHX-ORC model is capable of estimating the amount of waste heat the system can recover and subsequently convert to usable power across engine operating conditions. Therefore, the extent of possible fuel consumption and emissions reduction because of implementing the novel system can be elucidated.

In the final chapter, a concise summary of the previous sections and the implications of the results of the work are presented. Specifically, a large portion of the discussion surrounds the potential of the DPFHX-ORC system to advance diesel technology in the two main areas of concern, fuel economy and hazardous emissions. Although these metrics are crucial to the feasibility of the concept, practical concerns, such as the impact on engine and catalyst performance, also receive attention. Of particular importance is the ability to perform SCR at decreased exhaust temperature levels; hence, a number of applicable historical works are cited.

Finally, the next stages of research are listed, including preliminary efforts on creating a GT-Suite model of the single-cylinder diesel engine and evaluation of different DPFHX geometries.

Chapter 2

Organic Rankine Cycle Waste Heat Recovery Literature Review

2.1 Introduction

Since the 1970's, a large number of academic and industrial efforts seek to perform waste heat recovery using ORCs. For WHR based on using the DPFHX as an ORC evaporator, contributions surrounding waste heat sources at temperature levels comparable to engine exhaust are particularly relevant. This temperature range corresponds to a competitive regime between ORCs and steam Rankine cycles, which occurs around 650K [50]. For this reason, the literature works using organic fluids and water are considered to draw comparisons. Also, while the Rankine cycle is preferred over alternative WHR methods, a sampling of published works using other thermodynamic cycles is included to provide context to the current discussion. To assist the discussion regarding working fluid selection, authors use three main categories within organic fluids. The three classifications are dry, isentropic, and wet, referring to a fluid's saturated vapor curve slope (see Figure 7).
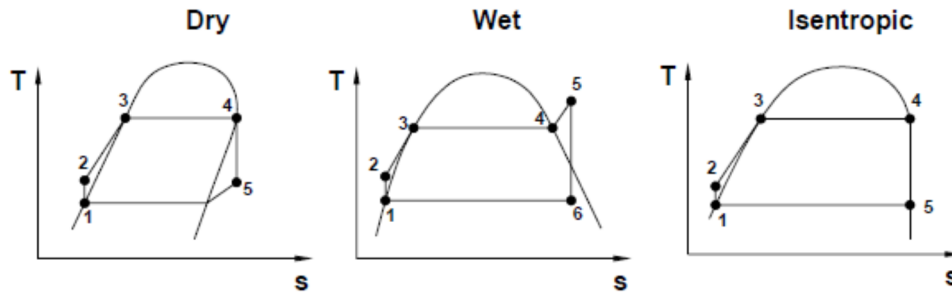
Figure 7: Classification of working fluids by saturated vapor curve slope [51] (Reprinted with Permission from SAE International)

A review of the ORC literature provides insight over a range of topics surrounding ORC implementation. Details of the available historical installations provide lessons regarding system design and control. One design choice concerns power transmission, where direct coupling between an expander and drivetrain must be weighed against using a generator to achieve electrical power. The reported ability to control the ORC system under fluctuating waste heat source conditions also applies to the DPFHX, where several potential applications recover heat from an ICE. Further practical considerations include packaging and payback time, where the viability of an ORC depends on whether the system can be housed onboard a vehicle and generate enough power to pay for itself through fuel savings within a few years. These determinations are possible through examining the impact of each constructed ORC, measured by the overall cycle performance and subsequent implementation.

Reviewing the WHR literature also begets creation of a realistic ORC model for eventual coupling to a virtual DPFHX by informing various design choices. Some modeling decisions surround component selection, while others assign reasonable values to parameters related to ORC performance. Therefore, the results of previous authors are valuable at all stages of ORC model creation, including selection of a modeling scheme, physical components, and individual device efficiencies.

2.2 Historical Review

In 1973, Morgan et al. were among the first to study the application of an external combustion Rankine engine in an automotive application [52]. Concerns about the ability of ICE's to meet the Clean Air Act mandated emission levels for 1976 motivated these researchers to investigate alternatives to traditional combustion engines. As a result, the group evaluated the potential of an ORC system as they recognized that separating the combustion process from the power cycle creates an inherent emissions advantage. Since an engine's emissions are contingent on the combustor geometry and its operation, optimization of the combustor design separately can minimize emissions, regardless of power extraction concerns. In order to determine whether sufficient power output was possible, the authors create computer models and a regenerative Rankine engine prototype.

The group used a 145.5 hp expander output for component sizing and determined the system would fit within a 1972 Ford Galaxie engine compartment with only minor modifications. They selected Fluorinol-85, 85% tetrafluoroethanol and 15% water by volume, as the working fluid because of a low freezing point (-82˚F), good thermal stability, nearly isentropic saturated vapor line, and acceptable cycle efficiencies for boiler temperatures of 500-625˚F. The prototype used a radial firing burner integrated with the vapor generator to evaporate the working fluid that generated power within the expander. Tests using a single and four-cylinder (V-4) expander found that the single cylinder expander exhibited superior efficiency. They observed good agreement between computer models and prototypes and concluded that an 11% fuel economy improvement was achievable based on 400 hours of testing utilizing a 5.5 hp system at Thermo Electron Corporation (TECO).

Three years later, Patel and Doyle documented the first application of using an ORC for engine WHR [53]. Their system used the exhaust waste heat of a Mack 676 diesel engine installed in a long haul truck by coupling the turbine pinion gear to the PTO with a speed reduction gearbox. While small vehicles with ICE's have potential for efficiency gains, the authors cite extended periods of near constant engine speed operation and high yearly mileage as reasons long haul trucks are more attractive for ORC applications. To minimize irreversibility, the group used Fluorinol-50 as the cycle working fluid in an attempt to minimize the temperature difference between the working fluid and engine exhaust. In specific, they operated between 650°F at turbine inlet and 158°F at condenser exit.

The constructed prototype used a vapor generator as part of the exhaust stack, a condenser combined with the existing truck's radiator, and a three-stage axial flow turbine expander. Figures within their report illustrate that the ORC components were readily configured within the truck's engine compartment. Subjecting the ORC equipped truck to a NAPCA control route demonstrated a 13% increase in maximum power output along with a 15% improvement in fuel economy. Moreover, this performance slightly exceeded model predictions at all power levels and speeds tested. They conclude that the $3000 ORC system could pay for itself with fuel savings in less than one year with 150,000 miles of travel at the current fuel cost of $0.45 per gallon.

Continuing the collaboration between TECO and Mack Trucks, Patel et al. describe plans for a yearlong single vehicle test of the ORC equipped model F7865T tractor in FY 1979 [54]. This paper also documents a planned expansion of the system for ten trucks in the FY 1981-1982; however, no further information exists on the planned expansion. Using the previously

determined 15% fuel consumption decrease, they mention saving 3120 gallons of fuel for every 100,000 miles traveled by the truck.

In 1981, Hall summarizes the increase in cogeneration, which he describes as the generation of energy from the excess energy supplied during another process [55]. This necessity stems from the 100% OPEC inspired price hike on oil, which made it less expensive to save a Btu than to generate an additional one. While concerns about the substantial capital investment still existed at the time of the paper, Hall contends that installation of cogeneration systems is not overly complex.

In the same year, Heywood provides a review of the status of conventional engines as compared to alternative versions [56]. During this time in the literature, the efficiency improvement potential of direct-injection and turbo-compounded diesels were being tested for future incorporation. The alternative systems identified by Heywood were gas turbine systems, Stirling engines, and Rankine cycle engines. This paper describes the advantages and disadvantages of each system; however, he did not intend the study to be definitive because of rapidly changing constraints. Of interest, Heywood acknowledges using an ORC for WHR as a possible method for further efficiency improvements over turbo-compounded diesels.

Also in 1981, Marciniak compares the suitability of seven different working fluids for Rankine cycle systems [57]. The fluids considered were water, methanol, 2-methyl pyridine/water, Fluorinol-85, toluene, Freon R-11, and Freon R-113. This working fluid evaluation occurred for 600-2400 kW industrial applications with waste heat temperatures between 500 and 1100 ˚F. Marciniak makes these working fluid recommendations after studying their thermo-physical properties, system performance and size, environmental impact and safety, various capital and operating costs, and potential return on investment. He does not exclude any

of the potential working fluids due to health or safety risks, believing these concerns were manageable through a careful system design. Under high temperature conditions, thermal stability concerns eliminated methanol and both Freon refrigerants from consideration. From an economic standpoint, this paper provides the estimated capital cost versus power output for the distinctive working fluids. As power output increases from 800 to 2400 kW, typical Rankine system costs are shown to exponentially decay from around $1000/kW to $600/kW, as shown by Figure 8. The least expensive system utilized water, followed by toluene, 2-methyl pyridine/water, and Fluorinol-85.
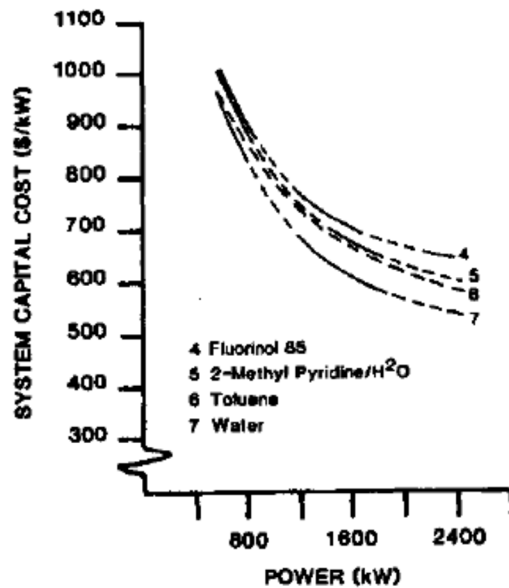
Figure 8: Capital costs based on 900 °F gaseous stream [57]

In 1983, Khalifa examined the technical and economic feasibility of operating a Brayton Bottoming Cycle (BBS) from the waste heat of adiabatic diesel engines [32]. This effort simulates several configurations over various driving cycles, with the results in Figure 9 showing that the pressurized BBS was capable of a 12% fuel economy improvement. Also, Figure 9 demonstrates that driving cycle selection has a significant influence on fuel savings predictions.

Despite the lower fuel consumption, discounted cash flow and payback calculations demonstrate that the BBS would be at best marginally attractive as a substitute for turbo-compounding.
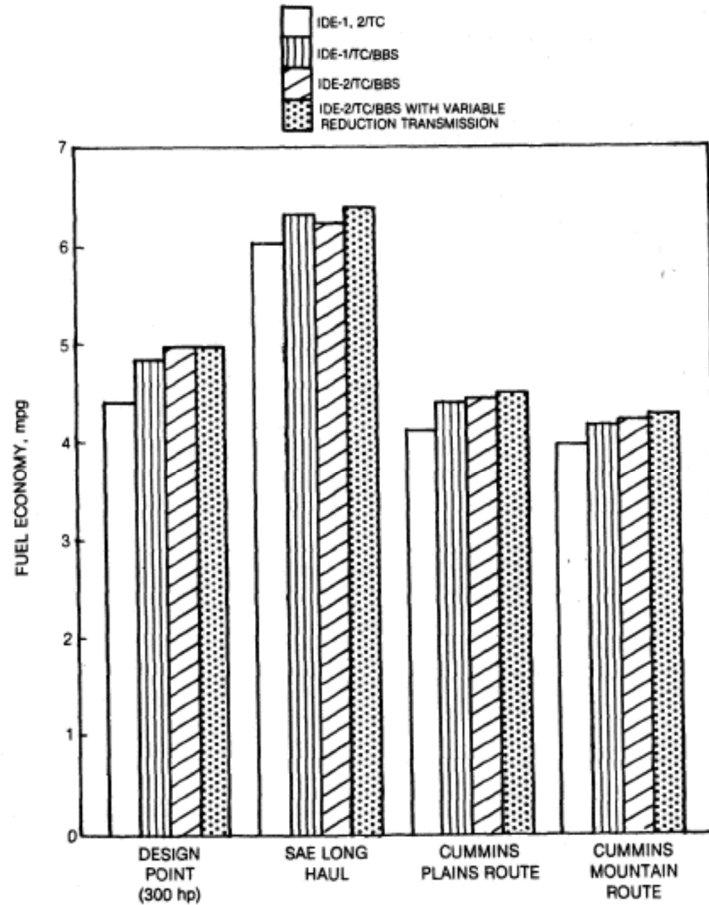
Figure 9: Simulated fuel economy for Brayton cycle equipped adiabatic diesel engines [32]

In the next year, Poulin et al. conduct a similar evaluation in running a steam Rankine cycle system off several adiabatic diesel configurations [36]. They simulate this system using turbocharged non-aftercooled (TC), turbocharged aftercooled (TC/A), turbocharged turbo-compound non-aftercooled (TCPD), and turbocharged turbo-compound aftercooled (TCPD/A) engines. They find a maximum brake specific fuel consumption (BSFC) improvement of 16.2% for the TC diesel with lesser improvements for the other configurations. The authors conclude that the payback time including maintenance would be 2.3 years, making the system economically attractive to the end user.

Also in 1984, Italian research in the field of ORCs was described by Angelino et al. [58]. This review of the authors' works includes 14 ORC engines with power outputs between 3 and 500kW, and maximum operating temperatures between 70 and 340°C. Of the studies featuring higher maximum cycle temperatures, high molecular weight wet (negative saturated vapor curve slope) fluids are used to generate power through multi-stage turbines. While relatively few cycle efficiency results are presented, the authors show a small increase in performance as the working fluid's molecular weight increases.

By 1985, increased interest in simulating ORCs led Badr to develop correlations for thermophysical properties of many of the period's refrigerants [59]. Badr bases these correlations off works by Martin [60] and Downing [61], while showing good agreement with the limited data available. This effort provides equations that can fit directly in a model for a working fluid's saturation pressure, specific volume, specific enthalpy, and specific entropy. Of importance, the correlations hold for each refrigerant as a saturated liquid, saturated vapor, and superheated vapor.

Badr publishes another paper in the same year describing the working fluid selection process for a low power output (<10kW) Rankine cycle engine operating between 40°C and 120°C [62]. This paper includes an evaluation of thermodynamic and physical selection criteria for 67 prospective working fluids, while identifying three superior candidates. While none completely satisfied all the criteria, the short listed fluids were the fluorinated hydrocarbons R-11, R-113, and R-114.

After considering a turbine or displacement-type machine for the Rankine engine expander, Badr chose to use a multi-vane type displacement machine. At this time, single-stage turbines were inefficient for this application due to impractical optimum blade velocity.

Moreover, the high cost of multi-stage turbines prohibited their inclusion. Computer modeling of the preferred fluids revealed R-11 exhibited the highest cycle efficiency (see Figure 10); however, since R-11 has a relatively low thermal stability limit of 120°C, this work concludes with R-113 as the best working fluid.
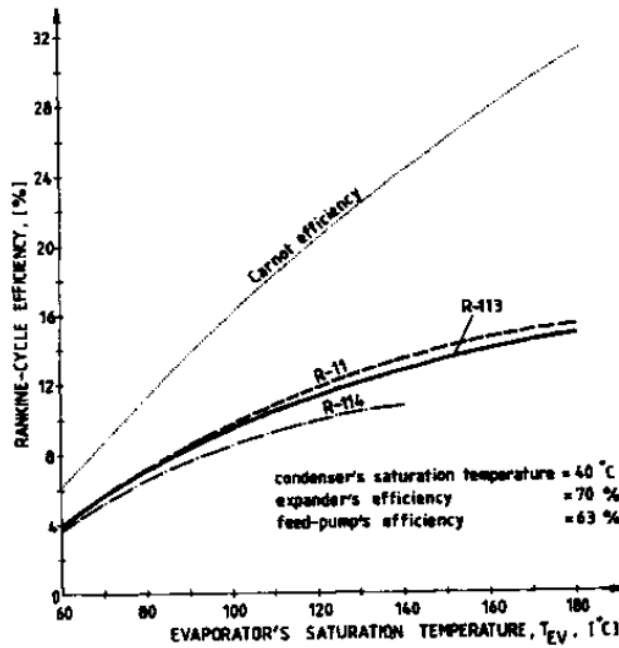
Figure 10: Cycle efficiency for prospective fluids across evaporator saturation temperatures [62]

Also in 1985, Bailey performs a technical and economic study of three alternative power cycles for WHR from an adiabatic diesel engine, and compares each system's performance with a baseline turbo-compounding diesel [33]. The power cycles examined were a steam Rankine, ORC with RC-1 working fluid, and various Brayton cycles (including air Brayton). Bailey documents engine specific fuel economy improvements via computer models, which are in direct proportion to improvements in vehicle fuel economy [63]. Simulations show the largest fuel savings were possible with the RC-1 ORC, followed by the steam Rankine, with smaller improvements from Brayton cycle systems. The calculations were based on 100,000 miles of annual travel, with the RC-1 ORC providing a fuel savings of approximately 1400 gallons, the largest among the different options. At 1985 fuel price levels, the steam Rankine cycle has the

shortest payback time at 3.2 years, followed by the RC-1 ORC and intercooled Brayton at around

4.1 and 4.7 years respectively (see Figure 11).
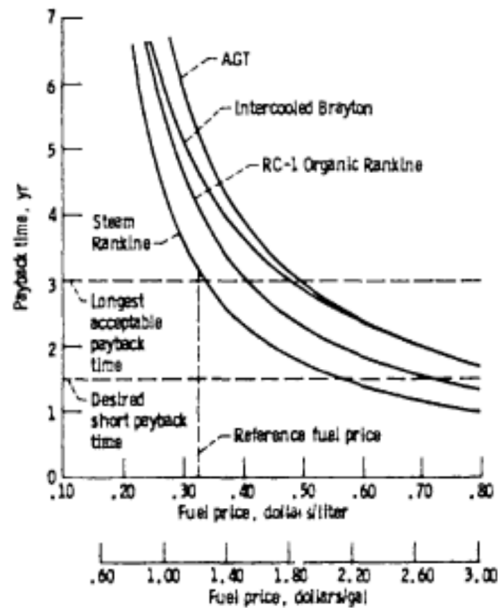
Figure 11: Power cycle payback time versus fuel price [33]

Six years later, Badr elaborates on his 1985 paper by ranking types of low power output

(5-20kW) expansion machines for use in a steam Rankine engine configuration [64]. A Rankine

cycle fits this application because it is able to achieve 60-70% of the Carnot limit for small

temperature differences; whereas, it can only achieve up to 50-60% for large differentials in

temperatures. He evaluates these devices for a combined heat-and-power (CHP) system, which

involves the simultaneous production of electrical power and useful heat from a single

generating power plant. A survey of previous research led the author to conclude that turbines

and reciprocating expanders were not particularly suitable for a low power, low speed

application. Badr concludes that a Wankel expander was best for the CHP system, slightly above

a helical-screw expander.

Jumping ahead to 1993, Oomori and Ogino develop a Rankine cycle system that uses the

waste heat from the engine coolant in a passenger car [15]. The authors chose not to recover the

25

higher-grade waste heat found in the engine's exhaust because engine speed fluctuations complicate the control process. They select HCFC123 (hydrochlorofluorocarbon) as the working fluid for this application in order to allow liquid-vapor phase change within the authors' low temperature evaporator. Moreover, they replace the engine water pump with an ORC pump, while using the engine coolant passages as the evaporator, and the existing radiator as the condenser. They measure output from the scroll expander in order to determine the fuel economy improvement during bench testing and find only a 3% gain for an ambient temperature of 25˚C.

Two years later, Larjola evaluates prototype high-speed oil free turbogenerator-feed pumps in an ORC for WHR from a 425°C source [65]. Instead of using the conventional separated configuration, the novel device directly couples the pump, turbine, and generator. Upon examination of several working fluids, toluene is chosen as the most suitable. The author notes the fluid's lower specific heat of vaporization and the possibility of using a single-stage turbine as advantages toluene has over water. This is further indicated in the results as a toluene-based ORC achieves 26% efficiency while a steam Rankine cycle manages only 11-19%.

In 1997, Hung compares the performance of six working fluids against water for use in a Rankine cycle for WHR of low-grade waste heat [50]. The candidate fluids were benzene, ammonia, R-11, R-12, R-134a, and R-113. Hung chooses water as the baseline fluid since it provides low Rankine cycle efficiency for waste heat sources below 370°C; thus, a direct comparison of organic fluids to water justifies the use of organic fluids in low temperature applications. Determination of working fluid suitability is a function of the examination of molecular weight, saturated vapor line slope, turbine enthalpy drop, maximum stability temperature, and critical point as indicated in Table 1. This paper involves a modeling study in order to determine the maximum Rankine cycle efficiency for each fluid at different turbine inlet

temperatures. As shown in Figure 2, benzene has the highest efficiency of the investigated fluids in spite of having a relatively high latent heat at low pressure. In general, the larger latent heat working fluids result in inefficient operation since the condenser rejects much of the fluid energy. In addition, for given evaporator and condenser temperatures, higher critical temperature working fluids exhibit superior first-law efficiencies in an ORC.

Table 1: Thermophysical working fluid properties [50]

Parameter	H_2O	NH_3	Benzene	R134a	R12	R11	R113
Molecular Weight	18	17	78	102	121	137	187
Saturated Vapor Curve Slope	Negative	Negative	Positive	Isentropic	Isentropic	Isentropic	Positive
Critical Point	647.0K 22.06MPa	405.3K 11.33MPa	562.2K 4.90MPa	374.2K 4.06MPa	385.0K 4.13MPa	471.0K 4.41MPa	487.3K 3.41MPa
Latent Heat at 1atm (kJ/kg)	2256.6	1347.0	438.6	215.5	166.1	178.8	143.9
Max. Stability Temperature (K)	None	750	600	450	450	420-450	450-500
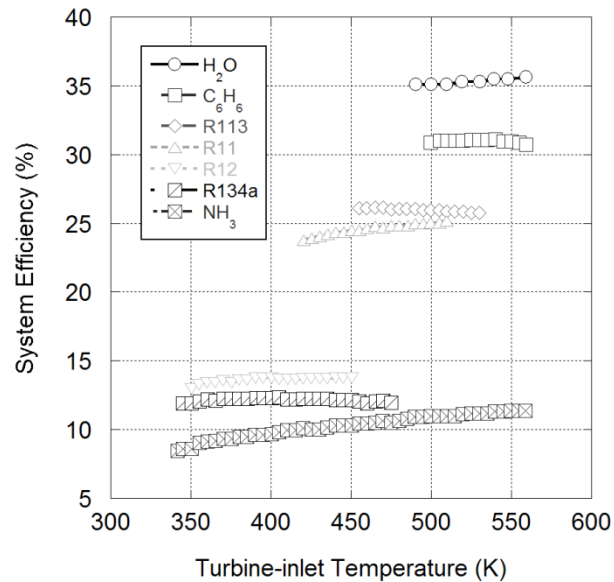
Figure 12: Variation in system efficiency with turbine-inlet temperature for various working fluids [50]

Hung follows up this earlier work four years later by examining the potential of five different dry fluids (fluids with a positive slope on their *T-s* diagram saturated vapor curve) to perform WHR in an ORC [66]. This investigation includes three hydrocarbons and two refrigerants as follows: benzene (C_6H_6), toluene (C_7H_8), p-xylene (C_8H_{10}), R113 and R123.

Using a 10MW waste heat source at 600K, Hung finds that p-xylene exhibits the lowest

irreversibility of the prospective fluids. Another study, using a constant 15°C temperature

difference between the turbine inlet and waste heat source, shows that p-xylene provides the

highest cycle efficiency (see Figure 13). The refrigerants perform relatively better with

decreasing source temperature; however, using these relatively expensive fluids in a large system

would add significant cost.
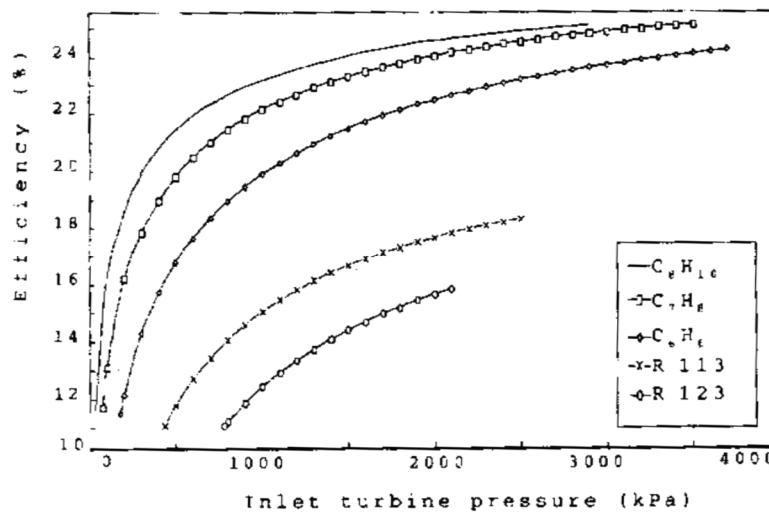
Figure 13: System efficiency at different turbine inlet pressures [66]

Also in 2001, Jonsson and Yan study ammonia-water bottoming cycles as an alternative

to steam Rankine cycles [38]. They state that previous studies demonstrate ammonia-water

cycles produce more power with sensible heat sources between 400-600 °C and large

temperature drops due to ammonia-water mixtures being non-azeotropic. This phenomenon is a

function of the composition change of the ammonia-water mixture during constant pressure

boiling. The waste energy source of this study involved using the process simulation program

IPSEpro to model spark-ignition natural gas and compression-ignition natural gas diesel engines

manufactured by Wartsila. In these simulations, the exhaust gas temperatures of the spark-

ignition gas engines were around 100 °C higher leading to a greater efficiency. The ammonia-

water bottoming cycle outperformed the steam Rankine in each of the five configurations analyzed, with arrangements ranging from the simplest possible ammonia-water cycle to significantly more complex configurations involving additional components. In all designs, the ammonia-water cycle system is more complex than a simple Rankine cycle system adding cost during manufacturing.

In 2003, Kane et al. propose creating a small hybrid power generator utilizing WHR for remote locations [67]. This station would recover thermal energy from solar collectors and a diesel engine while creating electricity through two superimposed ORCs. This design allows power generation during cloudy periods and at night via WHR from the engine block coolant and exhaust gas. The ORCs involve a topping cycle with HCFC-123 and a bottoming cycle using HFC-134a with power generation through a separate scroll expander unit. While a single definition of topping and bottoming will not apply to all the papers reviewed here, in general, a topping cycle will convert waste heat to mechanical or electrical energy; whereas, a bottoming cycle redirects the waste heat to a useful heating process. Earlier in this chapter, Khalifa indicates the nomenclature of a bottoming cycle in reference to a Brayton cycle generating power from engine exhaust waste heat. For Kane et al.'s paper, the authors associate the topping cycle with the higher exergy source (exhaust heat) and the bottoming cycle with the lower exergy sources (engine coolant and heat rejected from topping cycle condenser). To test efficiency, they ran three series of tests using the station including limited testing made in situ with the fully integrated system. Results show an overall cycle efficiency of $14.1 \pm 0.2\%$ with the performance deemed satisfactory for relatively low temperatures (up to 165˚C) and low power ranges (up to 10kW).

In the next year, Liu et al. conduct an analysis of working fluid selection on the performance of an ORC for WHR [68]. They model a simple ideal Rankine cycle in order to study the thermal efficiency of the system and total heat-recovery efficiency for various working fluids utilizing low-grade energy sources. For completeness, the authors choose to evaluate wet, dry, and isentropic fluids in the study (see Table 2). The authors determine that hydrogen bonding in water, ammonia, and ethanol results in wet fluids that are inappropriate for a low temperature ORC process. Simulation results predict that thermal efficiency is a weak function of the critical temperature of the fluid and lower critical temperature fluids provide less efficient heat recovery.

Table 2: Working fluids and classification [68]

Working fluids	Calculated by Eq. (5) (J/kg K^2)	Type[b]
Water	−13.1818	Wet
Ethanol	−5.4299	Wet
R11	−0.3903	Isentropic
R123	0.1202	Isentropic
HFE7100	1.8252	Dry
n-Pentane	1.2835	Dry
Iso-pentane	1.1801	Dry
Benzene	0.3316	Isentropic
Toluene	1.0600	Dry
p-Xylene	1.539	Dry

[a] The results are analyzed at the saturated vapor curve for the case T_H = normal boiling point.
[b] Analyzed results from thermodynamic data [12,13].

In the same year, Schmid examines potential CO_2 emissions reductions by utilizing WHR on marine engines [16]. Since these engines achieve around 50% thermal efficiency along with the typical tradeoff between efficiency and NO_x emissions, the author cites WHR as a more promising avenue for CO_2 emission reductions than engine redesign. Schmid proposes a heat recovery plant that generates electricity using a steam turbine and power turbine in order to drive a turbo-generator. Their calculations indicate that the operation of the heat recovery plant by means of a 68,640kW Sulzer 12RTA96C engine results in a 12% gain in overall efficiency.

Because the estimated payback time was only four years, the manufacturer went ahead and installed the complete heat recovery plant on some ships in the manufacturer's fleet [69].

In 2005, El Chammas and Clodic propose an ORC for WHR from the cooling circuit and exhaust of a 1.4-liter spark ignition engine within a hybrid vehicle [51]. With this configuration, conversion of mechanical turbine rotation to electrical energy with a generator allows subsequent storage in a battery pack for later use by an electric motor. The authors examine eight working fluids (water, isopentane, R-123, R-245ca, R-245fa, butane, isobutane, R-152a) for use in a Rankine bottoming cycle. The simulation results in Figure 14 utilize a condensing temperature of 55°C while indicating that water provides the highest cycle efficiency, followed by R-123, isopentane, and R-245ca. In spite of R-123 resulting in efficient operation, the authors note the fluid is an HCFC and thus unsustainable for environmental reasons.
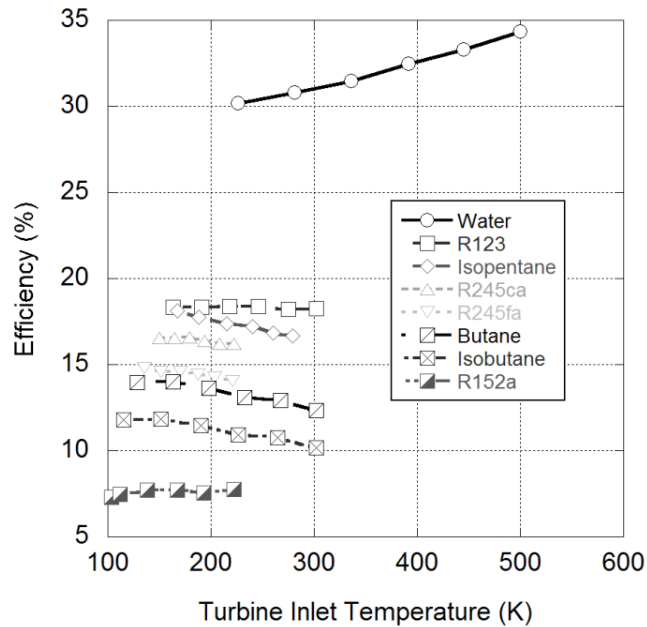
Figure 14: Rankine cycle efficiency for various working fluids [51] (Reprinted with Permission from SAE International)

Their efforts find that dry or isentropic fluids achieve similar or lower efficiencies with increasing superheat at the turbine inlet, while the cycle efficiency increases for wet fluids such

as water. Rankine cycle efficiency does increase for higher operating pressures; however, they mention that manufacturers must weight these benefits against the associated cost increase. A comparison of possible Rankine cycles, including a high-pressure steam Rankine cycle (HPSRC) and low-pressure steam Rankine cycle (LPSRC) show that the HPSRC had the highest actual efficiency as indicated in Table 3. In particular, HPSRC offers a 12-27% fuel economy improvement depending on engine speed and load, while the two favored organic fluids (isopentane, R-245ca) present a 17-32% improvement when used in an ORC. Additional exhaust backpressure introduced by the boiler dampens this performance increase, resulting in a horsepower loss of 1.5-2.5% at high loads and 0.2-0.5% at low loads.

Table 3: Comparison of Rankine cycle performances [51]

Parameter	HPSRC	LPSRC	ORC-R245ca	ORC-Isopentane
Net Electrical Output (kW)	5	5	5	5
Ideal Efficiency (%)	22.7	15.3	15.8	16.3
Actual Efficiency (%)	13.3	8.9	8.7	9.0
Max Pressure (bar)	25.0	8.0	22.5	19.0
Max Temp. (°C)	260	220	143	151
Mass Flow Rate (g/s)	15.2	22.7	241.0	121.0

In 2006, Stobart and Weerasinghe review and compare six previous WHR efforts for SI and CI engines with a summary of the considered studies [70]. Four of the six works recover heat from exhaust gas, with operating efficiencies between 9 and 25%. They construct two QSS-Toolbox computer simulation models for analysis of a steam hybrid system based off a 1.6 liter VW Golf car while simulating the performance of the WHR system over several drive cycles. They find fuel consumption decreases of 9.6%, 8.9%, and 26.2% respectively for the European, FTP 75, and US06 drive cycles. The lower fuel consumption of the US06 drive cycle can be attributed to the greater loads placed upon the engine during higher speed (highway) driving resulting in more exhaust energy potential. In addition to the simulation results, the authors

identify high efficiency as the main attribute of turbine expanders, while reciprocating expanders offer superior response to fluctuating exhaust conditions.

In the same year, Arias et al. consider three Rankine cycles for WHR from a spark-ignition engine in a hybrid vehicle [71]. The configurations include heat recovery from exhaust gas only, engine coolant + exhaust gas, and engine block + exhaust gas. The authors use an energy balance to quantify the amount of waste heat available in each configuration and couple this with experimental data from a 2004 Toyota Prius in order to form the basis of their computer simulations. These models show that using the engine block to preheat the working fluid before superheating the steam from exhaust energy was the most efficient configuration, converting 7.5% of the total waste heat to electrical power.

Also in 2006, Leibowitz et al. highlight the advantages of using screw expanders over turbines in small (20-50 kW) ORCs by considering both cost and performance [72]. At these sizes, the authors note the high rotational speeds of turbines require high ratio gearboxes and expensive lubrication systems. Of the different types of expanders, twin-screw type machines are identified as the most promising, citing their ability to operate at higher rotational speeds than vane, scroll, or reciprocating expanders. Consisting of a pair of meshing helical rotors, recent development of the "N" profile has improved the screw expander's performance by up to 10%. Furthermore, the twin-screw expander provides efficiencies around 70% during low speed operation (1500-1800 RPM), resulting in acceptable performance during periods of decreased waste heat supply. Cycle simulations showed an 8.5% increase in total power output by recovering exhaust heat from a gasoline engine generator at a cost of $1500-1800/kW.

Colonna and van Putten publish a two-part effort in 2007, describing a dynamic power cycle simulation software package called SimECS [73, 74]. This software uses conservation

(mass, momentum, energy) and constitutive (heat transfer coefficients, fluid properties, fluid dynamic correlations, rate of reaction) equations in order to describe the complete system. The use of bilateral coupling and the causality principle leads to a solvable system of low index algebraic and differential equations (DAE's). Validation of the software occurs through steady state and dynamic simulation of a 0.6MW steam Rankine system in the second part of the work. Results indicate a maximum discrepancy of 6% between Cycle-Tempo and SimECS computer simulation models. These works present a highly accurate method of modeling WHR systems during normal and off-design condition operation, representing one of the first detailed treatments of transient cycle simulation.

In the same year, Wei et al. investigate the performance of an ORC system during steady operation and under disturbances [75]. Exhaust from a gas turbine (610-650 K) acts as the waste heat source driving the cycle, which uses R-245fa as the working fluid and a separate turbine to generate power. This work validates cycle simulations on a 100 kW system through obtained experimental data, ensuring accurate model predictions. Optimization of the ORC performance suggested small sub-cooling (0.5-0.6 K) at the condenser outlet leads to the maximum WHR system output.

In this study, the authors quantify the effect on cycle performance of variations in exhaust mass flow rate, exhaust inlet temperature, air mass flow rate, and ambient temperatures. These simulations show linear increases in output power and efficiency for increasing exhaust mass flow rate, increasing exhaust inlet temperature, and decreasing ambient temperature. They observe a 30% decrease in output power from typical winter temperatures as compared to those of summer because of the higher cold sink temperature. Finally, the exergy destruction rate of the evaporator is the largest of all the ORC components in the cycle.

Also published in 2007 is a two-part effort by Teng et al. regarding WHR from heavy-duty diesel engines using an ORC [3, 76]. The authors propose a hybrid energy system for 2010 versions of these engines in the first paper, consisting of a diesel cycle hybridized with ORC for WHR. Transient operating conditions commonly lead to selecting reciprocating expanders above turbines, since variable heat addition leads to wetness late in the expansion process and potential damage to turbine blades. The working fluid selected for the cycle is a dry fluid having a critical pressure under 70 bars. Both first and second law analysis reveal that WHR from engine coolant was unattractive due its respective low energy level; however, their investigation indicates that energy from engine exhaust, EGR, and the CAC is suitable. The authors provide a schematic of the proposed system, where they place an exhaust cooler downstream of a Diesel Particulate Filter (DPF). Their simulations indicate that the supercritical ORC system can potentially recover 55 kW from the waste heat (169 kW) via the three devices, increasing the output of the engine by 20% without additional fuel. A further benefit in their proposed cycle is achievable by decreasing the condenser size through utilizing heat from engine coolant.

Their second paper discusses the merits of various working fluids for their ORC-WHR system based on thermodynamic properties. This paper documents inorganic and organic fluids as both pure fluids and binary-mixture fluids. In specific, characterizations of these fluids happen as wet (water), isentropic (R134a), or dry (R245fa). Of these, the authors determine isentropic, slightly wet, or slightly dry fluids are generally most suitable for ORC-WHR systems. However, selection of the proper working fluid depends on the temperature range of the system; hence, no single fluid will be best for all applications. The authors also conclude a properly selected binary-mixture working fluid is capable of improving the thermal efficiency of the ORC by up to 15%.

In the same year, Mago et al. investigate the performance of low temperature ORCs with seven working fluids [77]. The fluids considered were R134a, R113, R245ca, R245fa, R123, isobutane, and propane. They compare the performance of each fluid against water in waste heat temperature ranges such as less than 380 K, 380 to 430 K, and greater than 430 K. As mentioned in a previous paragraph, water is not economical for waste heat levels below a temperature of 643 K. Figure 15 presents the results of their efforts as a function of computer simulated ORC thermal efficiency with each fluid. This allows the researchers to make recommendations for each temperature range. In specific, the working fluid with the highest boiling point (R113) provides the highest efficiency, while they observe that the worst efficiency results from the fluid with the lowest boiling point (propane). This suggests that higher boiling point fluids work comparatively better in ORCs.
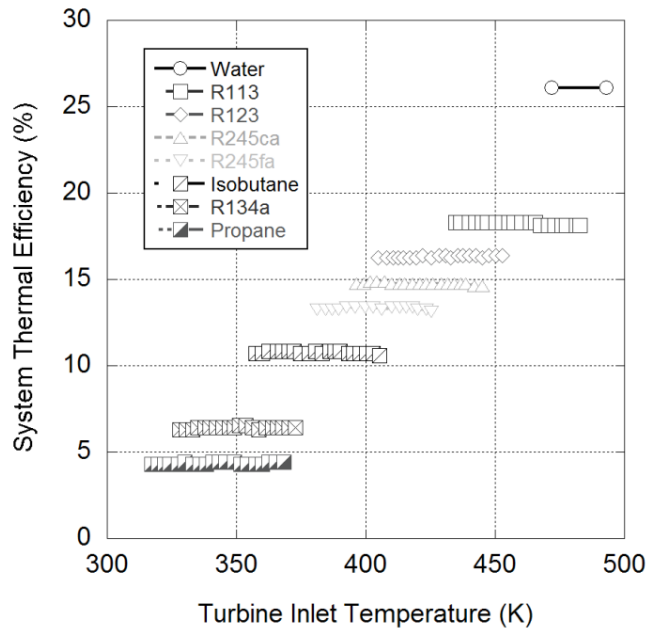
Figure 15: Thermal efficiency of Rankine cycle with turbine inlet temperature for various working fluids [77]

This year additionally provides the efforts of Endo et al. with respect to their experimental results involving a steam Rankine system installed on a Honda Stream hybrid vehicle [9]. The WHR power cycle utilizes the waste heat from engine cooling and engine

exhaust using an innovative catalyzed evaporation device that replaces the exhaust port of the engine. The system generates power from a swash plate axial piston type expander coupled to a generator. Electronic control of the generator load provides steam pressure regulation by imposing the rotational speed of the expander. The authors use feed-forward control of the steam flow rate in order to maintain the expander inlet temperature between 400 and 500 °C.

For proof of concept, they drive the vehicle in the EPA highway fuel economy test mode, Japanese 10-15 mode, and at constant driving speed of 100 km/hr. They observe successful control of the system during broad and dramatic engine load changes, the first reported instance of such transient control capabilities. Experimental data shows the novel evaporator recovers 95% of the exhaust energy as steam and heat from the catalytic purification reaction, while the expander achieves a maximum of 13% thermal efficiency. In addition, results show a 13.2% increase in thermal efficiency relative to the base vehicle, leading the authors to conclude that the Rankine system is an effective means for improving vehicle fuel economy.

Stobart et al. continue advancing the control literature with their effort on regulating thermal recovery systems in 2007 [78]. The lower manufacturing costs and high exhaust temperatures lead the authors to prefer spark ignition engines to compression ignition engines for vehicle implementation. Separation of thermal recovery from work production with a pressurized accumulator and hybrid architecture combat the unsteady waste heat conditions, improving controllability. Heating times for the 50kW engine example, achieving heat recovery with a steam Rankine cycle featuring an accumulator, ranges from about three to four minutes. Reduced heating times are achieved with smaller water volumes and after short stops. Of the expander options, reciprocating expanders are relatively efficient and simple to control.

In what continues as a busy year, Quoilin describes experimental results and optimization of a small scale ORC through simulations of a validated computer model [79]. After considering numerous prospective working fluids, selection of an isentropic fluid (R-123) happens because of its efficient operation with source temperatures between 100 and 200 ˚C. The authors present a schematic of their ORC test bench, which utilizes a scroll expander modified from a scroll compressor. Achieving maximum WHR potential of the system occurs by varying certain parameters such as the hot air source temperature, expander rotational speed, and refrigerant charge. Results demonstrate maximum cycle efficiency of 7.4%, while simulations accounting for recommended modifications predict a further efficiency gain up to 11.58%.

This same year, Kadota and Yamamoto develop a transient bench for simulation of Honda vehicles with various power-train configurations [80]. Among the simulated power plants were conventional IC engines, hybrid electric (HE), and HE with a steam ORC for WHR. Schematics in the paper present the components utilized in each model, which the researchers validated experimentally in an individual manner before evaluating system performance over a full driving cycle. The HE system with WHR demonstrates a 6.1% thermal efficiency improvement in the Japanese 10-15 mode. Fuel economy predictions were within ±1 percent of measured values.

In 2009, Ringler et al. investigate the use of an ORC on a four-cylinder engine for WHR [17]. They examine system performance as a function of heat recovery from exhaust only (system A) and exhaust + engine coolant (system B). Results from this effort determine that water was the most appropriate fluid for system A while an alcohol (e.g. ethanol) was best for system B due to a lower temperature heat addition. To predict additional performance, simulations using a Dymola modeling tool examine the different systems with A having better

performance when vehicle speeds exceed approximately 65 mph, as shown by Figure 16. Alternatively, system B demonstrates a higher potential for typical driving between 45 and 70 miles per hour, resulting in an engine performance increase in the range of 10%.
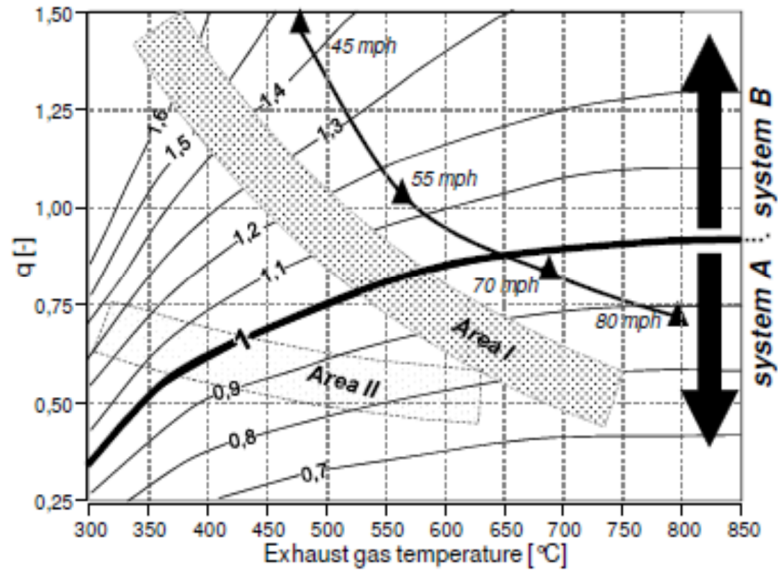
Figure 16: Comparison of system performance with vehicle speed [17] (Reprinted with Permission from SAE International)

Use of an ORC to recover waste heat from a high pressure ratio gas turbine studied by Chacartegui et al. is also accomplished in 2009 [81]. While the heat recovery is not achieved using an ICE as the power plant, the gas turbine exhaust temperature is comparable, making the results applicable to the current effort. Furthermore, this work is included because it compares the six potential working fluids of R113, R245, isobutene, toluene, cyclohexane, and isopentane. Parametric optimization of the ORC, along with several commercial gas turbines, is used to predict the overall system performance. Of the fluids, cyclohexane and toluene provide the highest global efficiencies, with comparable system costs.

That same year, a comparative study of four potential methods for waste heat recovery in cement plants is done by Wang et al. [40]. Two sources are used to power the thermodynamic cycles, the preheater (340 °C) and clinker cooler (320 °C), both resembling the low end of ICE

exhaust temperatures. The systems evaluated are single flash steam cycle, dual pressure steam cycle, ORC, and Kalina cycle. An exergy analysis is examined with genetic algorithm parameter optimization for each candidate, resulting in the conclusion that the Kalina cycle would achieve the best performance. For comparison, the ORC achieved 20.9% efficiency while the more complex Kalina cycle provided 24.1%.

In 2010, Srinivasan et al. examine the waste heat recovery potential of an ORC for improving the efficiency of a high-efficiency, low-emissions dual fuel Low Temperature Combustion (LTC) engine [82]. The authors' single-cylinder test engine uses Advanced Low Pilot Ignited Natural Gas (ALPING) LTC, where pilot diesel sprays mix with surrounding natural gas prior to combustion. Simulations using exergy and pinch-point analysis, along with measured engine exhaust parameters, predict Fuel Conversion Efficiency (FCE) and emissions improvements. Different injection timing, engine load, and EGR percentages are used to find results for a range of engine operation. On average, an R113 working fluid based ORC improved FCE by 7% while reducing NO_x and CO_2 emissions by 18%. Since R113 is a dry fluid, the authors achieve the optimum efficiency by evaporating to the saturated vapor curve, avoiding superheat.

Concurrently, Mohd et al. describe their low power output (<1 kW) ORC for energy generation from low temperature waste heat [83]. This work experimentally evaluates heat sources ranging from 60 to 100 ˚C and cold source temperatures between 10 and 30 ˚C. The authors choose HFC-245a as the working fluid for the cycle, while selecting a rotary-vane type expander in order to minimize system costs. Laboratory test results reveal a maximum thermal efficiency of 3.82% for an 80˚C temperature difference and an expander efficiency of 40%.

Additionally in this year, Espinosa et al. discuss the optimal ORC configuration for WHR on commercial trucks [18]. This work considers heat sources from the CAC, engine coolant, EGR, and exhaust gases. They mention that exhaust gases are the most practical waste heat source since simultaneous WHR from both EGR and the exhaust line adds complexity and increases cost. Moreover, the energy available in engine coolant is of low quality. The authors prefer using the ram air speed from vehicle motion in order to cool the ORC condenser since the power consumption of a fan would increase with the square of the required airflow rate. This work uses computer models to evaluate water, ethanol, and HFC-R245fa with the latter chosen as the most appropriate working fluid. The high global warming potential of HFC-245fa suggests an HFO fluid with higher critical temperature than HFO-1234yf could be promising in future Rankine cycles. Finally, they simulate the different ORC configurations using zero-dimensional and one-dimensional simulation models. The zero-dimensional model uses isentropic efficiencies and three-zone heat exchangers; whereas, the one-dimensional model comes from the commercial engine simulation program GT-POWER.

Meanwhile, three possible ORC configurations are considered by Vaja and Gambaratta in 2010 in order to recover waste heat from a 12 cylinder supercharged natural gas engine [84]. These candidates are a simple ORC using exhaust gas, a simple cycle using exhaust and coolant, and a regenerated cycle. Each of the three typical classes of working fluids are represented by benzene (dry), R11 (isentropic), and R134 (wet). Environmental and safety concerns are recognized in the paper; however, the authors conclude their results only based on thermodynamic attributes. The regenerative cycle, as well as the simple cycle using both exhaust and coolant waste heat along with benzene as the working fluid, provided the highest efficiency improvements over the engine rated value at around 12.5%. However, the simple cycle using just

exhaust energy and benzene has a comparable efficiency of 11.4%. As a result, the designer must weigh a slight drop in efficiency against a reduction in initial cost and complexity. R11 was noted as the next most attractive fluid, with efficiency increases around 10% for both simple cycles.

A further effort by Yamada et al. in 2010 describes a unique Rankine cycle configuration for WHR from a hydrogen ICE [85]. The authors propose an open Rankine cycle that discharges the working fluid to the atmosphere after expansion. In this system, a water separator recovers water from the exhaust pipe that passes through a filter and subsequently through the pump, indicating the start of the cycle. A modified exhaust manifold acts as the cycle evaporator, followed by an expander. The cycle was simulated with and without a condenser, leading to the conclusion that the condenser was not cost-effective. Inclusion of the open Rankine cycle without a condenser provides thermal efficiency improvements over the hydrogen ICE of 2.9-3.7% at various engine speeds.

A clear example of the progress toward efficient and economical small ORCs is presented by Quoilin et al. in the same year [86]. This work describes a semi-empirical model of an ORC using the refrigerant HCFC-123 along with a previously validated scroll expander model. By modifying a mass produced, oil-free open-drive scroll compressor to operate as an expander, the authors limit system cost while achieving heat recovery efficiency equal to 9.9%. This was accomplished after optimizing cycle parameters while generating power from two low temperature sources.

In what continues to mark a busy year, Weerasinghe et al. compare Rankine cycle WHR with turbo-compounding as methods to boost the thermal efficiency of diesel engines [87]. In effect, turbo-compounding directly expands exhaust gases in a turbine for power generation,

representing part of a Brayton cycle. An interesting aspect of the Rankine cycle is the steam storage reservoir between the evaporator and expander, which provides an energy buffer through periods of high-load or low-load engine operation. While water is chosen as the cycle working fluid, the authors note that further advancements in steam expanders are underway at the University of Sussex. A MATLAB based model using the QSS Toolbox simulates both systems over the US Federal Heavy Duty Transient Test Cycle, resulting in a fuel economy improvement of 20% or more with the Rankine cycle and only around a 2.5% savings from turbo-compounding.

One year later, the performance of an ORC using R-12, R-123, R-134a, and R-717 is parametrically optimized by Roy et al. [88]. Both a constant heat source temperature of 550 K and a variable heat source are considered in the study. In each case, R-123 produces the maximum efficiency (~19%) and lowest irreversibility of the candidate fluids. Along with the thermodynamic analysis of each fluid using MATLAB, environmental concerns are presented with respect to the Ozone Depletion Potential (ODP) and Global Warming Potential (GWP) of the refrigerants. They indicate that ammonia (R-717) has zero ODP and GWP, while R-12 (a chlorofluorocarbon: CFC) contributes to global warming and continually destroys ozone for up to two years. Furthermore, the HCFC studied (R-123) has both a low ODP and GWP; whereas, R-134a (a hydrofluorocarbon: HFC) does not have any ODP but has a high GWP.

While most authors are designing for maximum ORC efficiency, Quoilin et al. also consider the system size and cost in a paper published in the same year [89]. These criteria are used in a thermo-economic optimization using six working fluids: R245fa, R123, n-butane, n-pentane, R1234yf, and Solkatherm. Economic considerations find a different optimal design than a purely thermodynamic analysis. This is due in part to the high efficiencies that result from the

use of high critical temperature working fluids, which improve performance at the cost of increased component sizes required for low specific vapor densities. The economic optimum working fluid in their study is n-butane at the specific cost of 2136€/kW that results in an efficiency of 4.47%, below the thermodynamic maximum of 5.22%.

A valuable review of Rankine cycle thermal Exhaust Heat Recovery (EHR) is authored by Wang et al. in 2011 [13]. EHR is a sub-category of WHR limited to recovering heat at temperature levels provided by ICE exhaust, similar to the range of interest in this review. This work illustrates the diversity of research efforts in this area, along with the potential of EHR systems to improve overall powertrain efficiency. In comparison to Wang et al.'s effort, this paper provides historical context, practical cycle design considerations along with system and modeling descriptions while highlighting additional literature in this area. As a result, the combination of this chapter with Wang et al.'s review provides a nearly complete summary of research in this important area.

While the authors provide insight on working fluid and expander selection considerations, the length of the work prevents a detailed description of each study. Moreover, their efforts do not draw any definitive conclusions, as this manuscript will accomplish in the following section. However, briefly summarized here, their paper states that reciprocating expanders are preferred for locomotives, ships, and stationary engines, despite having a lower level of technical maturity. Working fluid selection is crucial for efficient EHR and achievement of high cycle efficiencies. Water's high stability temperature and evaporation enthalpy provide the maximum power but requires high boiler pressures, low condensing pressures, and a high degree of superheating. They find that implementing a Rankine cycle on heavy-duty applications can increase the total powertrain efficiency by up to 30% based on the NEDC driving cycle.

Also, they state that while developments in EHR have rapidly progressed over the past decade, attempts to apply EHR to production vehicles must continue moving forward in order to ensure meeting future fuel economy and emission standards. This requires demonstration of efficient thermal EHR and precise control with small hardware.

Just recently, Bianchi and De Pascale evaluated three thermodynamic cycles in order to recover low and medium grade waste heat [34]. These cycles are the ORC, Stirling, and the inverted Brayton of which they resolve that ORC is the most attractive of the candidates. Four organic fluids (R133a, R245fa, iso-butane, and benzene) were considered for the ORC, with benzene achieving the highest efficiency at around 20%.

2.3 Review Summary

Growing concerns over air pollution and escalating fuel prices through the 1970's resulted in attempts to find viable alternatives to the IC engine. However, the low power density, high cost, and low efficiency of other power cycles prevented a substantial change in vehicle propulsion. Instead, the focus narrowed to WHR systems in order to increase efficiency through cogeneration by supplementing the engine's power by means of converting thermal energy into a more useful form; either mechanical or electrical. Several efforts resulted in systems that increase the IC engine's efficiency; however, decreasing fuel prices in the 1980's and improved engine designs stalled implementation of the WHR architecture.

Recent published works sponsored by Honda, Toyota, Wartsila, BMW, and Volvo show a renewed interest in WHR in order to increase the thermal efficiency of ICE's [9, 15-18]. Motivating this resurgence is escalating fuel prices and future CO_2 emission regulations. In addition, these systems are becoming more viable due to recent technological advancements that have increased the efficiencies of individual components within WHR systems. Among these

improvements are smaller expander internal leakage areas [79] and improved rotor profiles [72], along with more efficient heat exchangers [9].

The historical review of the last section indicates that the majority of WHR researchers prefer steam Rankine systems or ORCs instead of Brayton, Stirling, Kalina, and supercritical CO_2 thermodynamic cycles along with being favored over thermoelectric devices. This is because Rankine cycle systems offer the most attractive combination of simplicity, component cost, and efficiency. For each intended application, the additional expenditure and complexity associated with incorporation of preheating with engine coolant waste heat or a recuperator (e.g. additional hardware) above the traditional Rankine cycle should be weighed against the resulting efficiency gains. No configuration is optimal for every waste heat source; hence, a thermodynamic analysis targeting the specific source must be conducted first.

A review of the literature demonstrates that selection of the working fluid and expander has a significant influence on the efficiency of the WHR system. Most applications achieve the highest ORC efficiencies using nearly isentropic and high critical temperature working fluids. However, these criteria fail to address numerous practical design conditions, such as operating pressures, component sizes, expander rotational speeds, expansion ratios, and environmental concerns. Thus, the space available onboard mobile waste heat sources should be determined prior to cycle design. In addition, further costs incurred from utilizing exceedingly high or low pressures at specific states of the cycle to promote efficiency must be justified. For instance, greater thermal efficiencies are achievable through higher evaporation pressures; however, this adds expense to the system in order to handle these high pressures [90].

Environmental concerns negate the use of many of the fluids discussed in early works. As a result, ORC systems should only utilize working fluids with low Global Warming Potential

(GWP) and Ozone Depletion Potential (OWP) [88]. Natural refrigerants or hydrocarbons are preferred, while HCFC's and HFC's provide fewer negative effects than CFC's [88]. Organic fluids and water lead to similar efficiencies in the range of normal engine exhaust temperature levels; however, organic fluids are favored at low temperatures and water is preferred as the source temperature increases. While water often yields a more efficient WHR process at these higher temperatures, condensing pressures below atmospheric pressure and wet expander exit conditions are common deterrents to their usage. In addition, water requires high expansion ratios that may not be met with reciprocating expanders or single-stage turbines and freezing occurs with low ambient temperatures.

Previous works have shown that turbines are superior for high temperature and high output WHR systems, while reciprocating expanders are preferred for small applications. Turbines generally provide higher efficiencies than reciprocating devices, but the aforementioned technological advancements have narrowed this disparity. In addition, turbines do have a higher initial cost, which is offset slightly by additional fuel savings through this increased efficiency. Of interest, practical advantages of reciprocating expanders such as lower rotational speeds, potential hermetic power generation, and decreased sensitivity to wet expander outlet conditions should be considered when choosing an option for the expansion process. Reciprocating expanders are also more controllable with respect to fluctuating waste heat conditions. Early efforts couple system expanders to output shafts with speed reduction gearboxes, while later work targets hybrid vehicles as to decouple energy recovery from usage. Belt systems link some reciprocating expanders to output shafts; however, turbine rotational speeds discourage this configuration.

A large portion of potential engine WHR applications are mobile vehicles, such as passenger cars and long-haul trucks. Since the space available for the ORC system is limited, high-density fluids and compact heat exchangers are desirable. It is possible to adjust for small heat exchanger size using forced convection, which can be achieved by exposing the condenser to ram-air or using a fan-equipped condenser. However, component size may be limited by selecting a working fluid with desirable heat transfer characteristics, as described by Lee [91]. With respect to pumping the working fluid throughout the cycle, the high fluid temperatures achieved tend to favor the use of diaphragm-type pumps. This is because they are designed to operate at high pressures and low flow rates, typically encountered for high ORC efficiency designs in small applications such as ICE WHR.

The largest portions of waste heat from internal combustion engines are lost through the high- and medium-temperature engine exhaust and coolant, respectively. Studies show that the higher exergy level of engine exhaust allows more efficient heat recovery; however, preheating a WHR system's working fluid using engine coolant energy can also be desirable [67, 71]. Selection of the optimal working fluid for a specific application requires WHR system models that are capable of comparing cycle performance using different fluids. The fluids with the highest critical temperature often appear the most desirable from a first law point of view, but practical and economic considerations should also receive attention.

Since these models often neglect heat transfer to the environment along with mechanical losses, actual WHR systems rarely achieve the performance suggested by idealized computer models. As a result, physical experiments often produce roughly half the power of the idealized WHR. On average, simulations forecast ORC efficiencies between 15-20%, while realistic

expectations lie in the range of 7-10%. Thus, since engine efficiencies are similar to exhaust waste heat fractions, fuel economy improvements around 10% are a feasible outcome.

Direct predictions of fuel economy improvements must account for a slightly reduced engine performance caused by the additional exhaust backpressure imposed. In particular, horsepower losses of 1.5-2.5% at high loads and 0.2-0.5% at low loads have been found [51]. Additionally, the powertrain efficiency gain only begins after sufficient heat is transferred to the working fluid, which requires approximately three to four minutes in the presence of an accumulator [78]. Systems without accumulators achieve reduced heating times, providing a larger reduction of emissions and fuel consumption under cold start driving cycle assessments. Most efforts locate waste heat recovery equipment downstream of catalytic devices. In this configuration, carbon dioxide emissions drop in proportion to fuel consumption, with marginal effects on emissions during engine warm up. Alternatively, combined evaporator/catalyst devices and upstream evaporators suffer from prolonged startup emissions, lessening the emissions advantage of ORC WHR systems.

Research suggests a properly designed ORC for WHR of engine exhaust can reduce emissions and pay for itself through fuel savings within a relatively short amount of time (approximately 2-5 years), primarily depending on annual travel. Hence, the system can help achieve future emission standards while reducing operating costs. Construction of a model that couples a virtual engine to a WHR system allows quantification of these advantages, while simultaneously meeting any packaging constraints or initial investment restrictions. To achieve the maximum ORC performance, parametric studies of operating variables (pump speed, expander load, etc.) should be conducted to yield the highest power. At the same time, second law analysis reveals where the largest amounts of exergy destruction are occurring. Going

further, the ORC can be optimized from an economic perspective, determining the configuration

that gives the highest fuel savings over a specified period of time [89].

Chapter 3

Organic Rankine Cycle Modeling

3.1 Introduction

In the previous chapter, the ORC-WHR literature provides a foundation for creating an ORC model for use with the DPFHX concept. These previous efforts inform the design choices associated with making an ORC model, which must occur in the context of the waste heat source(s) utilized. For the DPFHX-ORC system, small CI engines for mobile applications such as vehicles are the target WHR sources. On these engines, the preferred heat source is the exhaust, due to a higher exergy content leading to more efficient ORC operation [9].

After selection of the WHR source, an appropriate working fluid must be identified. To reiterate a previous statement, the ideal working fluid candidate is commonly selected through simulations from a group of prescreened fluids. This screening considers the temperature levels of the source, where typical exhaust ranges from 500-800 K. By performing the cycle with a high critical temperature fluid with chemical stability across cycle operating conditions, better ORC performance is possible while preventing fluid degradation. Attention is also due to safety and environmental concerns, requiring low ODP and GWP values [88]. One group of fluids that satisfy these criteria are hydrocarbons, which are an environmentally-friendly alternative to common refrigerants [14]. Also, the relatively simple molecular structure of water allows heating

to virtually any temperature without thermal degradation, and water does not pose a threat to the environment.

The decision between water and alternative working fluids reverts back to system size due to the thermophysical characteristics of water. Specifically, even though engine exhaust temperature levels are relatively high, water lends itself to use in larger applications. This is due to several properties of water that cause practical concerns; low condensing pressures, high expansion ratios, high freezing temperatures, and wet expander exit conditions. Condensing pressures well below ambient lead to air infiltration concerns, requiring advanced methods of sealing. Expansion ratios around 50 and above are only achievable with turbomachine expanders, and sometimes require multiple stages, leading to high initial costs. The expansion occurring during the transition from water to ice must also be mitigated to prevent the bursting of pipes and damage to Rankine cycle components. Due to water being a wet fluid, a large degree of superheat is necessary to prevent the formation of water droplets at the turbine exit, which decrease the lifespan of turbine expanders [3]. Consistently achieving this amount of superheat under fluctuating exhaust conditions using heat exchangers with packaging limitations is prohibitively difficult. This effect can be dampened by incorporating accumulators; however, further advancements in steam expanders are necessary and ongoing [78].

Alternatively, many hydrocarbons are dry fluids that require much lower expansion ratios. These characteristics permit the use of reciprocating expanders and lessen the possibility of internal damage from droplet formation, due to pure vapor expander-exit conditions and lower rotational speeds. Therefore, a moderate Rankine cycle efficiency reduction from hydrocarbon use is justified by a number of practical advantages over steam Rankine cycles.

Along with the working fluid, expander selection has a large influence on cycle performance [13]. Since the current study considers a variety of hydrocarbons, the choice of an expander can occur after simulation of a range of expansion ratios. A wide range of expander technologies are examined in the literature [64, 72], with reciprocating expanders being capable of expansion ratios between 3-30. The range of lower expansion ratios are commonly filled by scroll machines, while larger expansion ratios are possible with screw expanders.

The simplest ORC modeling approach uses steady-state reversible processes, resulting in the idealized T-s diagram of Figure 5a. However, performance predictions are improved by permitting entropy generation, which includes isentropic and actual thermodynamic states (see Figure 17). Figure 17 uses a wet fluid for consistency with Figure 5a, whereas the dry fluids of this chapter will have a positive saturated vapor curve slope and the dry fluid cycles will not utilize superheat at state 3. Also in Figure 17, isentropic processes result in states designated by "s" and actual processes are identified with "a". This approach is less complex than completing a detailed analysis of each component, such as the scroll machine modeling by Lemort [92]; however, the current type of model predicts reasonably accurate performance at significantly reduced computational cost and does not require detailed experimental knowledge of each component.
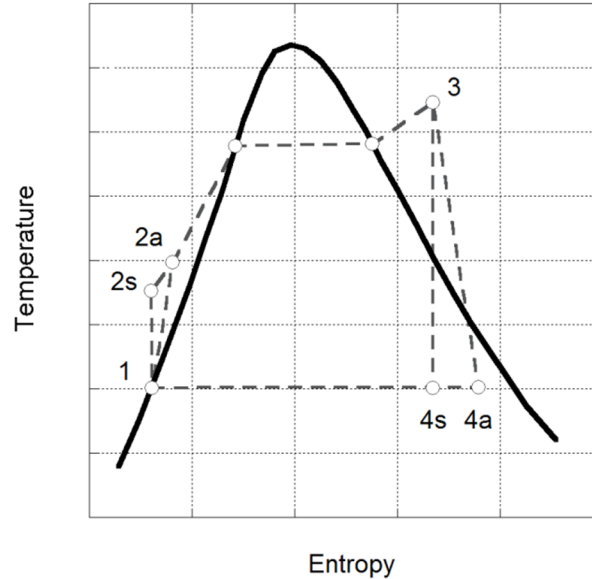
Figure 17: Actual Rankine cycle including both isentropic "s" and actual "a" thermodynamic states [14]

For the current study, a zero-dimensional steady-state ORC model with entropy

generation is simulated within MATLAB. This framework can later be expanded to associate

certain masses with each component, which would allow transient events to be estimated.

Certain transient ORC models exist [80]; however, the goal of this work is establishing ORC

performance at specific operating points and, therefore, does not require time-dependence.

Steady-state ORC models have proven valuable in cycle simulation, with some authors using a

quasi-steady-state assumption to model transient driving cycles. Also, the model uses the

common assumptions of perfect component insulation and no pipe losses between components,

which are effects that can be included following a final ORC design. Both of these effects lower

the cycle's power generation, which must be considered when analyzing results.

Since the evaporator and condenser parallel each other as heat exchangers, a similar

approach is often implemented in modeling the two devices. Of the various schemes available to

represent the evaporator and condenser, the two basic categories are the overall heat transfer

coefficient and effectiveness-NTU (Number of Transfer Units) methods. Some authors choose to

specify an effectiveness for each heat exchanger without using an overall heat transfer coefficient, which is a performance based technique used in conjunction with the inlet conditions to obtain values at the heat exchanger exit. This approach does not require a constant heat transfer area; however, calculation of the NTU based on an overall heat transfer coefficient and heat transfer area is possible to achieve component based modeling.

The additional complexity involved with calculating the NTU in order to obtain the effectiveness can be circumvented by using the overall heat transfer coefficient and heat transfer area directly as in:

$$\dot{Q} = UA\Delta T_{MEAN} \tag{3.1}$$

where $\dot{Q}$ is the heat transfer rate, U is the overall heat transfer coefficient, A is the heat transfer area, and ΔT_{MEAN} is the average temperature difference. The form of ΔT_{MEAN} varies between heat exchanger geometries, with the log mean temperature difference (ΔT_{LMTD}) being equal to the average temperature difference for parallel or counterflow heat exchangers. For other geometries, such as shell and tube heat exchangers, the heat equation takes the form:

$$\dot{Q} = UAF\Delta T_{LMTD} \tag{3.2}$$

where F is a temperature difference correction factor. The correction factor depends on the heat exchanger geometry, the ratio of the products of the mass flow rate times the heat capacity of the two fluids, and the heating or cooling effectiveness. In cases of phase change, heat capacities are effectively infinite, allowing the uncorrected use of the log mean temperature difference. Since much of the heat transfer occurring in the present model happens during phase change, and with the exact heat exchanger geometry undefined, the temperature difference correction factor will be assumed to be approximately equal to one. Upon refinement of the heat exchanger design, correction factors for complicated flow conditions come from Bowman et al. [93].

Without a correction factor, using an overall heat transfer coefficient and a log mean temperature difference is preferable over the effectiveness-NTU method since the current model avoids calculating the NTU as an intermediate.

$$NTU = \frac{UA}{(\dot{m}c)_{min}} \tag{3.3}$$

In Eq. (3.3), the denominator is the lower mass flow rate times specific heat (of the two fluids).

The overall heat transfer coefficient approach is well suited for modeling phase change, where multiple zones can be constructed based on the phase change of the working fluid. Since heat transfer occurs more rapidly during phase change [94], use of a single zone in this situation would introduce significant error. Also, when using a fixed heat transfer area, the overall heat transfer coefficient scheme easily allows variation of the area within each respective zone. It is possible to model multiple zones using the effectiveness-NTU method, as shown in Example 11.6 of [95].

Similar to the heat exchangers, the pump and expander are similar, particularly since the previous discussion led to selection of a reciprocating expander over a turbomachine. These devices have intrinsic geometric relationships, such as a compression or expansion ratio. Aside from complex models involving leakage areas and experimentally determined constants, authors use two basic approaches to represent these components. The first is specification of a maximum cycle pressure, which states that the pump will achieve a certain outlet pressure regardless of the inlet conditions. Alternatively, the approach here assigns a pressure ratio to the pump and expander, allowing the pump outlet pressure to vary. Maintaining a specific pressure ratio for reciprocating expanders will be discussed further in the results; however, system control methods such as adjusting valves and power input to the pump can be used to achieve specific ratios.

3.2 Model Construction

After selecting a modeling strategy, construction of a model begins with the waste heat source. In the current work, a single-cylinder Yanmar L100V diesel engine-generator is under evaluation, for which the laboratory measurements in Table 4 are known. These values designate the engine operating conditions for which the waste heat recovery will occur. The authors realize that WHR from a single-cylinder engine is not comparable to production engines; however, current laboratory limitations preclude subsequent validation of the model using a multi-cylinder engine. This is planned as future efforts utilizing a new engine test cell under construction.

Table 4: Engine data from a Yanmar single-cylinder engine running at 3600 rpm

Operating Point	Power (kW)	T_{ex} (K)	P_{ex} (kPa)	A/F (-)	$\dot{m}_{ex}$ (g/s)
1	0.23	491.92	100.66	57.04	11.13
2	1.73	547.46	100.63	43.25	11.08
3	3.41	619.35	100.67	33.26	11.39
4	5.00	701.63	100.90	25.49	11.28
5	6.21	785.29	101.56	20.55	11.20

From this data, the exhaust species are determined using typical diesel fuel atomic parameters of x=14.2 and y=25.54:

$$C_xH_y + a(O_2 + 3.76N_2) \Rightarrow bCO_2 + dH_2O + eN_2 + fO_2 \tag{3.4}$$
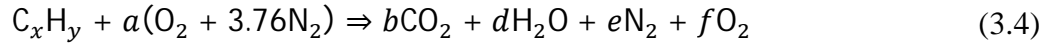
Subsequent mole fraction calculations then allow accurate determination of the exhaust enthalpy entering the evaporator, beginning with calculation of the fuel mass:

$$m_{fuel} = 12x + 1y \tag{3.5}$$

Next, the air-fuel ratio (A/F) can be used to calculate the mass of the air:

$$m_{air} = A/F * m_{fuel} \tag{3.6}$$

The constants a, b, d, e, and f are calculated using CHON atom balances:

$$a = \frac{m_{air}}{2*16 + 3.76*2*14} \tag{3.7}$$

$$b = x \tag{3.8}$$

$$d = \frac{y}{2} \tag{3.9}$$

$$e = 3.76 * a \tag{3.10}$$

$$f = \frac{2a - 2b - d}{2} \tag{3.11}$$

Mole fractions (X) are then found using the following equations:

$$X_{CO_2} = \frac{b}{b + d + e + f} \tag{3.12}$$

$$X_{H_2O} = \frac{d}{b + d + e + f} \tag{3.13}$$

$$X_{N_2} = \frac{e}{b + d + e + f} \tag{3.14}$$

$$X_{O_2} = 1 - X_{CO_2} - X_{H_2O} - X_{N_2} = \frac{f}{b + d + e + f} \tag{3.15}$$

Using the molecular weight (W) of each constituent, the mass fractions (Y) are calculated:

$$W_{CO_2} = 12 \frac{kg}{kmol} + 32 \frac{kg}{kmol} \tag{3.16}$$

$$W_{H_2O} = 2 \frac{kg}{kmol} + 16 \frac{kg}{kmol} \tag{3.17}$$

$$W_{N_2} = 2 * 14 \frac{kg}{kmol} \tag{3.18}$$

$$W_{O_2} = 2 * 16 \frac{kg}{kmol} \tag{3.19}$$

$$Y_{CO_2} = \frac{X_{CO_2} W_{CO_2}}{X_{CO_2} W_{CO_2} + X_{H_2O} W_{H_2O} + X_{N_2} W_{N_2} + X_{O_2} W_{O_2}} \tag{3.20}$$

$$Y_{H_2O} = \frac{X_{H_2O} W_{H_2O}}{X_{CO_2} W_{CO_2} + X_{H_2O} W_{H_2O} + X_{N_2} W_{N_2} + X_{O_2} W_{O_2}} \tag{3.21}$$

$$Y_{N_2} = \frac{X_{N_2} W_{N_2}}{X_{CO_2} W_{CO_2} + X_{H_2O} W_{H_2O} + X_{N_2} W_{N_2} + X_{O_2} W_{O_2}} \tag{3.22}$$

$$Y_{O_2} = 1 - Y_{CO_2} - Y_{H_2O} - Y_{N_2} \tag{3.23}$$

$$= \frac{X_{O_2} W_{O_2}}{X_{CO_2} W_{CO_2} + X_{H_2O} W_{H_2O} + X_{N_2} W_{N_2} + X_{O_2} W_{O_2}}$$

This analysis allows precise calculation of the exhaust enthalpy entering the evaporator.

Using REFPROP to retrieve the enthalpy of each component at the known temperature and

pressure, the mass fractions are used to accurately find the specific enthalpy of the exhaust:

$$h_{ex,in} = Y_{CO_2} h_{ex,in,CO_2} + Y_{H_2O} h_{ex,in,H_2O} + Y_{N_2} h_{ex,in,N_2} + Y_{O_2} h_{ex,in,O_2} \tag{3.24}$$

Here, the use of mass fractions instead of mole fractions occurs because the specific enthalpies

on a mass basis are provided by REFPROP. This distinction is important because mass fraction

is not unitless, with the numerator unit being the mass of an individual component while the

denominator is the mixture mass. A similar calculation exists for the exhaust leaving the

evaporator, as well as any internal points required by the multi-zone modeling scheme. Another

common approach uses a constant pressure specific heat; however, variable properties provide

enhanced accuracy with the degree of temperature change in the evaporator. Furthermore,

replacing the ideal combustion equation with experimentally determined exhaust fractions does

not significantly improve the specific enthalpy calculation.

Several other cycle design parameters are required before determining a modeling

scheme for each thermodynamic process. Among these is the mass flow rate over the condenser

($\dot{m}_{air}$), this value can be specified since the fan speed can be adjusted relatively easily. Due to

condenser size limitations, forced convection using an electric fan is a realistic feature, allowing

for smaller condenser heat transfer areas and providing an additional means of cycle control.

Finally, the working fluid quality is provided for states 1 and 3, requiring state 1 to lie on

the saturated-liquid line (Q_1=0) and state 3 on the saturated-vapor line (Q_3=1). While the state 1

specification is standard, choosing state 3 along the saturated-vapor line provides the highest

cycle efficiencies for dry fluids [88]. To be clear, ORC models using wet or isentropic fluids may

achieve more efficient WHR with various degrees of superheat.

3.2.1 Pump Processes (1-2s and 1-2)

Since an ideal pump compresses the working fluid isentropically, Eqn. (3.25) defines the

specific entropy (s) at state 2s.

$$s_{2s} = s_1 \tag{3.25}$$

This is not sufficient to fix state 2s, so a pressure ratio (PR) is chosen. Of note, some

authors simply choose p_{2s}, however using a pressure ratio is preferable because the parameter

can be controlled by adjusting valves. Also, specification of a pressure ratio is more likely to be

realized across engine operating conditions than an imposed maximum pressure.

$$PR = \frac{p_{2s}}{p_1} \tag{3.26}$$

Once the thermodynamic state is fixed in this manner, REFPROP can be used to look up the

remaining properties (T_{2s}, v_{2s}, and h_{2s}). This procedure has been described once here and is

implied for each of the cycle's other thermodynamic states. Modeling an isentropic compression

in the liquid regime using an incompressible flow equation results in no temperature or specific

volume change, while the variable property formulation excludes this assumption.

In order to implement an efficiency limitation on the pump, the actual pressure achieved

is set equal to the pressure achieved by an ideal pump:

$$p_2 = p_{2s} \tag{3.27}$$

While the discharge side of the pump features the same pressure for the actual pump and the

ideal pump, the work input required to achieve the outlet pressure is larger for the actual pump,

due to entropy production. The pump efficiency definition of Eqn. (3.28) facilitates this

comparison, allowing the actual state 2 enthalpy to be calculated after defining a pump isentropic efficiency (η_p).

$$\eta_p = \frac{-\left(\dot{W}_p/\dot{m}\right)_s}{-\left(\dot{W}_p/\dot{m}\right)} = \frac{h_{2s} - h_1}{h_2 - h_1} \qquad (3.28)$$

where ṁ is the working fluid mass flow rate and h is specific enthalpy. Thus, thermodynamic state 2 is fixed by the pressure and specific enthalpy.

3.2.2 Evaporator Process (2-3)

The first task in using a multi-zone heat exchanger approach is determining the appropriate number of zones. In the current model, the qualities at states 1 and 3 guarantee a two-zone scheme will be required, since the fluid will start out as a liquid and end the process on the saturated-vapor line. As described previously, the two-zone scheme discretizes the evaporator into zones according to the phase changes of the working fluid via Figure 18. The exhaust arrows in this figure indicate a counter-flow arrangement is being modeled, while parallel flow would be governed by the same schematic after reversing these arrows.
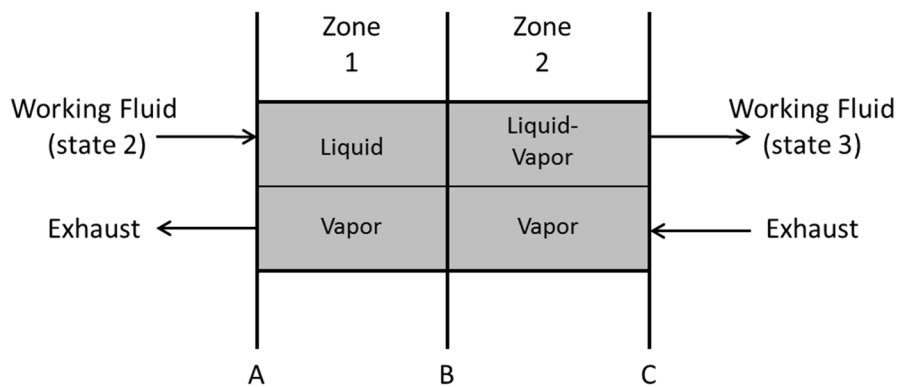
Figure 18: Evaporator schematic illustrating two-zone formulation

Application of the first law to these zones results in the following equations describing the heat transfer in Zone 1 and Zone 2, respectively:

$$\dot{Q}_{\text{AB}} = \dot{m}_{ex}\left(h_{ex,B} - h_{ex,\text{out}}\right) = \dot{m}(h_{\text{B}} - h_2) \qquad (3.29)$$

$$= U_{\text{AB}}A_{\text{AB}}F_{AB}\left[\frac{(T_{ex,\text{out}} - T_2) - (T_{ex,B} - T_{\text{B}})}{ln\left(\dfrac{T_{ex,\text{out}} - T_2}{T_{ex,B} - T_{\text{B}}}\right)}\right]$$

$$\dot{Q}_{\text{BC}} = \dot{m}_{ex}\left(h_{ex,\text{in}} - h_{ex,B}\right) = \dot{m}(h_3 - h_{\text{B}}) \qquad (3.30)$$

$$= U_{\text{BC}}A_{\text{BC}}F_{BC}\left[\frac{(T_{ex,\text{B}} - T_{\text{B}}) - (T_{ex,\text{in}} - T_3)}{ln\left(\dfrac{T_{ex,\text{B}} - T_{\text{B}}}{T_{ex,\text{in}} - T_3}\right)}\right]$$

where h_{ex} and T_{ex} are the specific enthalpy and temperature of the engine exhaust respectively

and subscripts (A, B, and C) indicate location within the two-zone schematic. To clarify the

physical meaning of this scheme, each of the three expressions in Eqn. (3.29) can be

investigated. In the absence of external heat loss, the heat transfer occurring between points A

and B (Zone 1) is equal to three expressions (listed from left to right); the heat leaving the

exhaust, the heat entering the working fluid, and the heat transferred from the exhaust to the

working fluid. Any external heat transfer will increase the energy leaving the exhaust above the

other two terms.

The properties at point A are equal to the properties at state 2 ($T_A = T_2$, $h_A = h_2$). The

temperature and enthalpy of the working fluid can be calculated at point B (T_B, h_B) because of

the known pressure and quality at that point ($P_B = P_2$ and $Q_B = 0$). Furthermore, temperature and

enthalpy of the working fluid can be calculated at point C (state 3: $T_C = T_3$, $h_C = h_3$) from the

known pressure and quality at that point ($P_C = P_3 = P_2$ and $Q_C = Q_3 = 1$). However, neither of the

individual areas (A_{AB} and A_{BC}) in the two zones are known.

In addition, the algebraic sum of equations (3.29) and (3.30) may also be used, as long as both are not used independently. Thus, one could use the overall first law expression covering both zones:

$$\dot{Q}_{\text{AC}} = \dot{m}_{ex}\left(h_{ex,in} - h_{ex,out}\right) = \dot{m}(h_3 - h_2) \tag{3.31}$$

Equations (3.29) and (3.30) further demonstrate the choice of using overall heat transfer coefficients instead of the effectiveness-NTU method. First, the use of individual temperature differences and overall heat transfer coefficients more effectively models constant temperature boiling and accounts for large coefficients during phase change. Since the performance of a specific heat exchanger is demanded from the model, the total heat exchanger area (A_{evap}) is known. As a result, the sum of the areas in the respective zones is equal to the total evaporator heat exchange area:

$$A_{\text{AB}} + A_{\text{BC}} = A_{evap} \tag{3.32}$$

In order to simplify the analysis of the evaporator, the pressure drop can be estimated to be zero:

$$p_3 = p_2 \tag{3.33}$$

Therefore, pressure and quality fix thermodynamic state 3. Future improvements to the evaporator model could impose experimentally determined pressure drops to achieve more accurate thermodynamic property values, although the relatively slow working fluid flows in common ORCs suggest this error is small in the present model. Also, representative constant overall heat transfer coefficients are used, while future experimental efforts will develop a more detailed calculation of the overall heat transfer coefficients. In particular, these heat transfer coefficients are dependent on the specific heat exchanger geometry, and proper correlations are based on dimensionless flow parameters such as the Reynolds number through the device.

3.2.3 Expander Processes (3-4s and 3-4)

Similar to the ideal pump analysis, the entropy will be constant for an ideal expander:

$$s_{4s} = s_3 \tag{3.34}$$

To find another thermodynamic variable at this state, the same pressure ratio used across the pump can be prescribed:

$$PR = \frac{p_3}{p_{4s}} \tag{3.35}$$

Justification of this approach comes from examination of the pressure changes occurring across the other three components, where previous sections describe a pressure increase according to the pressure ratio over the pump and isobaric modeling of the evaporator. Furthermore, since the condenser will also be represented as a constant pressure process, the cycle requires a pressure drop in the expander paralleling the pressure increase through the pump. In displacement expanders, the internal structure imposes a geometric constraint on the degree of expansion, which can be represented by a pressure ratio or expansion ratio.

For modeling of a non-ideal expansion process, an expander isentropic efficiency (η_e) is imposed:

$$\eta_e = \frac{\left(\dot{W}_e / \dot{m} \right)}{\left(\dot{W}_e / \dot{m} \right)_s} = \frac{h_3 - h_4}{h_3 - h_{4s}} \tag{3.36}$$

Use of this parameter allows entropy generation during fluid expansion, providing a measure of the actual power generation from the expander as a fraction of the power created by an ideal machine. The definition of an isentropic efficiency requires the outlet pressure from the ideal and actual processes to be the same:

$$p_4 = p_{4s} \tag{3.37}$$

Since the fluids considered are dry with state 3 on the saturated-vapor line, expansion must end in the superheated vapor region.

3.2.4 Condenser Process (4-1)

Modeling of the condenser is performed using the two-zone scheme previously illustrated in Figure 18, according to the phase change of the fluid (see Figure 19). In order for this methodology to be correct, one must assume that the working fluid enters as a vapor and exits as either a liquid-vapor mix or saturated liquid. The inlet superheated vapor component is guaranteed by setting $Q_3=1$ and using a dry fluid resulting in state 4 being a superheated vapor. The exit phase is guaranteed by requiring $Q_1=0$.
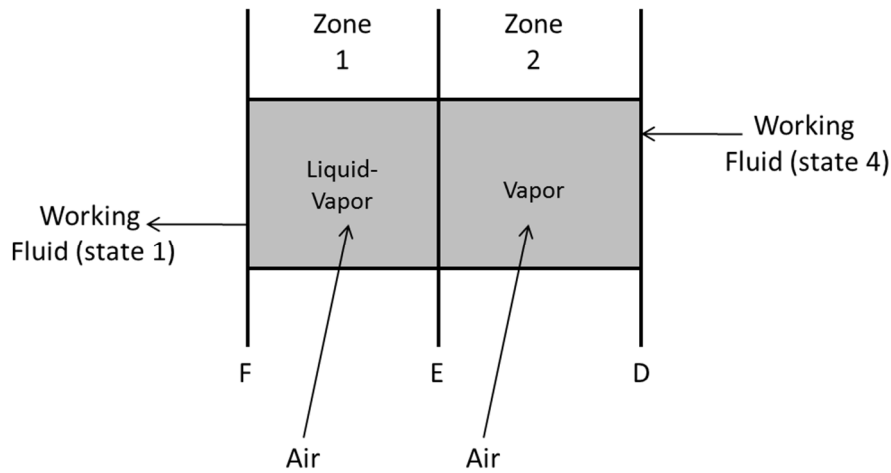
Figure 19: Condenser schematic illustrating two-zone formulation

Performing a first law energy balance on the condenser results in two equations (analogous to the evaporator), one for each zone:

$$\dot{Q}_{\mathrm{DE}} = \dot{m}_{air,\mathrm{DE}}\left(h_{air,in} - h_{air,out,\mathrm{DE}}\right) = \dot{m}(h_{\mathrm{E}} - h_4) \tag{3.38}$$

$$= U_{\mathrm{DE}}A_{\mathrm{DE}}\left(\frac{T_{air,in} + T_{air,out,\mathrm{DE}}}{2} - \frac{T_4 + T_{\mathrm{E}}}{2}\right)$$

$$\dot{Q}_{\text{EF}} = \dot{m}_{air,\text{EF}}\left(h_{air,in} - h_{air,out,\text{EF}}\right) = \dot{m}(h_1 - h_{\text{E}}) \tag{3.39}$$

$$= U_{\text{EF}}A_{\text{EF}}\left(\frac{T_{air,in} + T_{air,out,\text{EF}}}{2} - \frac{T_1 + T_{\text{E}}}{2}\right)$$

where h_{air} is the specific enthalpy of ambient air flowing over the condenser.

In this case, arithmetical average temperatures are utilized for the condenser, as opposed to the log mean temperature difference scheme of the evaporator. This discrepancy can be understood by remembering that air is flowing externally over the condenser, altering the temperature difference profile. Specification of the exact condenser geometry is left as a later design refinement, perhaps being a type of finned compact heat exchanger. Two further restrictions are derived from mass and area conservation, respectively:

$$\dot{m}_{air} = \dot{m}_{air,\text{DE}} + \dot{m}_{air,\text{EF}} \tag{3.40}$$

$$A_{cond} = A_{\text{DE}} + A_{\text{EF}} \tag{3.41}$$

Finally, the small condenser pressure drop is ignored through use of the following equalization:

$$p_1 = p_4 \tag{3.42}$$

3.2.5 Performance Parameters

To determine the net power output ($\dot{W}_{net}$) and system thermal efficiency (η_{th}), the individual component energy flows must be considered. The expander power ($\dot{W}_e$), pump power ($\dot{W}_p$), and heat recovery from the exhaust ($\dot{Q}_{in}$) are found as:

$$\dot{W}_e = \dot{m}(h_3 - h_4) \tag{3.43}$$

$$\dot{W}_p = \dot{m}(h_1 - h_2) \tag{3.44}$$

$$\dot{Q}_{in} = \dot{m}(h_3 - h_2) \tag{3.45}$$

In this effort, a fan power consumption term ($\dot{W}_{fan}$) is included, as calculated from basic

fan laws. While fan and pump power consumption decreases performance, their negative values

(power output is positive) explains the '+' signs in the following calculations for thermal

efficiency and net power, respectively:

$$\eta_{th} = \frac{\dot{W}_e + \dot{W}_p + \dot{W}_{fan}}{\dot{Q}_{in}} \tag{3.46}$$

$$\dot{W}_{net} = \dot{W}_e + \dot{W}_p + \dot{W}_{fan} \tag{3.47}$$

A commonly reported metric is thermal efficiency; however, the present discussion will focus on

power output since power generation is the goal of WHR.

3.2.6 Model Constants

A number of constant parameters must be chosen before running simulations, these

variables and associated values are included in Table 5.

Table 5: Constant model parameters

Variable	Constant Value
η_p	0.7
η_e	0.8
A_{evap}	0.2 m^2
A_{cond}	1.5 m^2
U_{AB}	100 W/(m^{2}K)
U_{BC}	150 W/(m^{2}K)
U_{DE}	75 W/(m^{2}K)
U_{EF}	150 W/(m^{2}K)

The overall heat transfer coefficients in Table 5 are optimistic values from [94], which

are preliminary estimates for design work instead of precise values that accompany specific heat

exchanger geometries and fluid conditions. Achievement of values on the upper end of

applicable ranges may require heat transfer enhancement techniques in a final design. To provide

perspective on the impact of the overall heat transfer coefficient on working fluid selection,

simulations will also occur for lower heat transfer coefficients in Section 3.3.

Selection of the isentropic efficiencies in Table 5 agrees with previous publications in the

area [66]. Here the pump has been assigned a lower efficiency due to the combination of high

pressure differences and low flow rates. With attention given to packaging restrictions,

limitations on heat transfer areas (by virtue of volumetric limits) are considered. Thus, heat

transfer areas of a miniature shell-and-tube evaporator and small automotive radiator-type

condenser are under study (corresponding to the single-cylinder application). Another

component of WHR performance is in regards to the overall heat transfer coefficients. Using

estimates for rapidly moving exhaust gas and nearly stagnant working fluid flow, estimates for

U_{AB} and U_{DE} are possible [94]. The remaining two coefficients are slightly larger, due to the

reduced thermal resistance present during phase change.

3.2.7 Solver Operation

In the main code, the solution procedure begins by making initial guesses for the 12

function variables (h_1, h_2, $h_{ex,out}$, $h_{ex,B}$, A_{AB}, A_{BC}, h_4, $h_{air,out,DE}$, $\dot{m}$, A_{DE}, A_{EF}, and $h_{air,out,EF}$), which is

accomplished through use of reasonable T_1, $T_{ex,out}$, and zone area (A_{AB}, A_{BC}, A_{DE}, A_{EF}) estimates.

The *fsolve* feature of MATLAB is then employed in order to find the actual values of the

function variables. This is done by repeatedly evaluating the 12 function variables within a trust-

region-dogleg method, followed by updating the 37 dependent variables outside the function. A

function tolerance of 1E-5 is allotted and convergence requires variable values below 0.01 for

successive iterations. Also, the accuracy of the converged parameters is given a final check

through placement of these results in governing equations.

3.3 Model Results

A number of valuable insights result from simulating the eight working fluids through a

pressure ratio sweep at each engine operating point. One such revelation is a linear relation

between pressure ratio and the expansion ratio (v_4/v_3), as shown by Figure 20 for the third engine operating point and an air flow rate of 0.5kg/s (discussion of the choice of air flow rate will follow later in this section). Since the expansion ratio is determined by geometry for reciprocating expanders, this illustrates that a reciprocating expander will provide consistent pressure ratios across cycle operating conditions. Hence, a pressure ratio sweep will be sufficient for analysis of the different phenomenon.
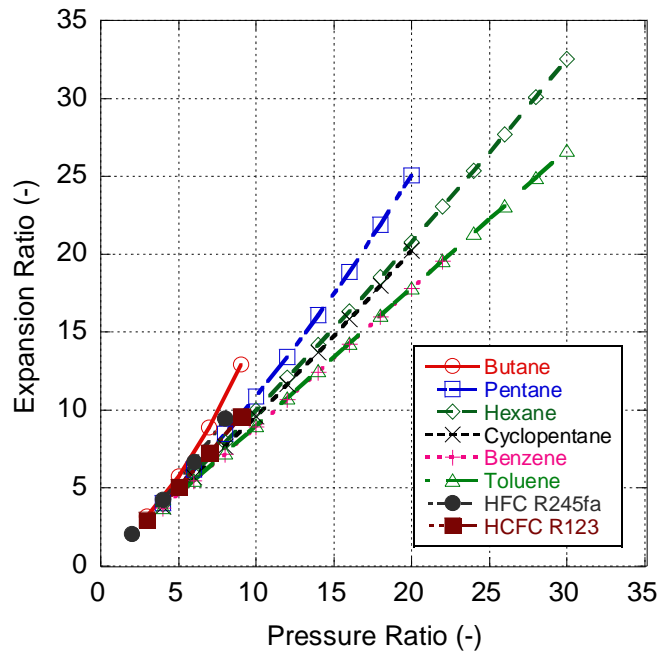
Figure 20: Fluid expansion ratio versus pressure ratio as a function of the eight working fluids

For applications using a reciprocating expander, determination of which type of expander to use depends on the desired expansion ratio. For the HFC R245fa and HCFC R123 working fluids, lower expansion ratios are required, suggesting a scroll expander [96]. However, long chain hydrocarbon species require higher expansion ratios, lending to screw expanders [72].
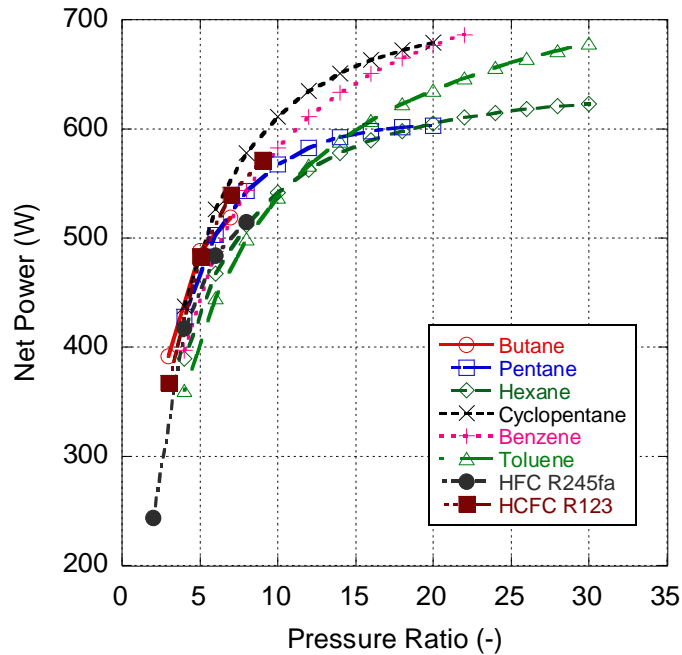
Figure 21: ORC power generation illustrating enhanced WHR with increased pressure ratios

Figure 21 illustrates enhanced WHR with increasing pressure ratio for the fifth engine operating point utilizing an air flow rate of 0.5kg/s. This figure illustrates that the model predicts large gains in net power at smaller pressure ratios. However, a minimal return on investment occurs towards the high end. This effect is clearly present in simulations for part-load engine operation, where results show the net power output eventually begins to decrease at the largest pressure ratios.

For context, the engine output associated with Figure 21 is 6.21kW. As a result, around a 10% engine efficiency improvement is achievable with several of the working fluids. Similar fuel consumption reductions are present across the other engine loads simulated. While benzene, toluene, and cyclopentane provide the highest ORC work output, an examination of condensing pressures for the second engine operating point raises air infiltration concerns (see Figure 22).
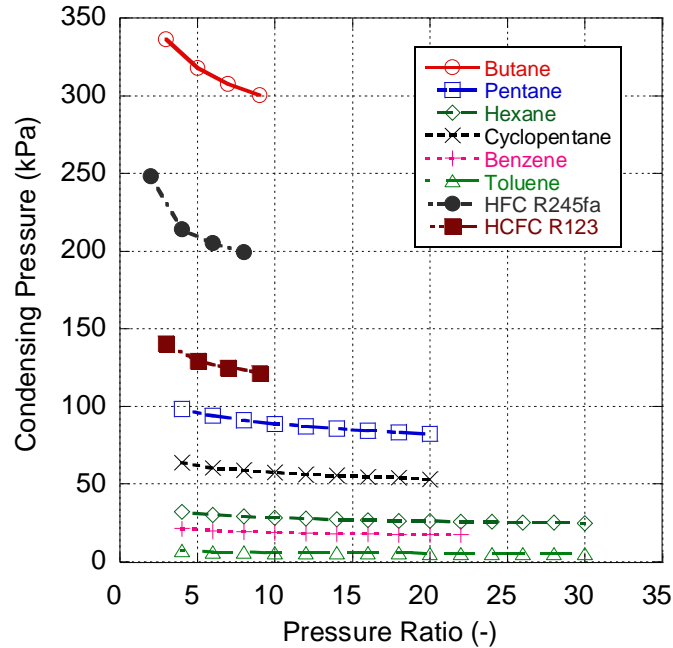
Figure 22: Condensing pressures demonstrating that a few of the working fluids are prohibitively low

In particular, excessively low condensing pressures of a few fluids (benzene, toluene, and hexane) result in eliminating them from consideration. Furthermore, butane operates at the highest evaporating pressures, in excess of 3 MPa at high pressure ratios. For an ORC recovering heat from a single-cylinder engine, this pressure requires exceedingly robust components.

The choice of 0.5 kg/s for the air flow rate in the previous parametric studies is supported by the comparative study in Figure 23, using hexane as the working fluid and the third engine operating point. A small increase in ORC output is observed as the air flow rate increases from 0.2 kg/s, followed by increasing WHR efficiency losses above 0.4 kg/s. This trend occurs because temperature differences are larger with high volumes of air flow; however, the fan power consumption eventually outweighs this advantage. The optimal air flow rate varies slightly between working fluids and engine loads and 0.5 kg/s is found to perform well under the various conditions simulated.
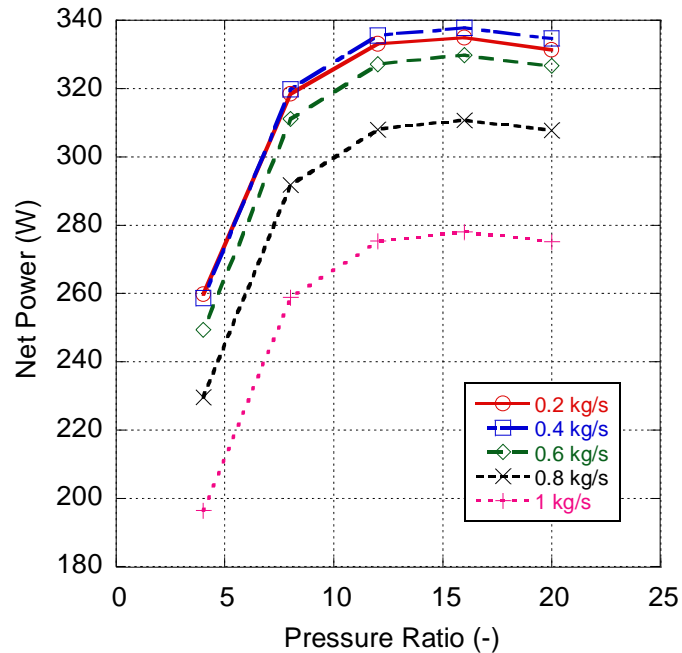
Figure 23: Simulation of varying air flow rates results in the choice of 0.5 kg/s as an optimal value

Another study considers the counter-flow and parallel-flow evaporator configurations. Typically, the counter-flow arrangement is assumed to provide the highest heat transfer, since larger log mean temperature differences are achieved. However, a competing phenomenon exists in heat exchangers with multiple zones, where some zones feature a phase change and some do not. In this instance, it is advantageous to provide larger temperature differences in areas of lower heat transfer coefficients promoting overall greater heat transfer. To explore this effect, a variety of overall heat transfer coefficients in region BC are modeled in a comparison of counter-flow and parallel-flow configurations (see Figure 24).
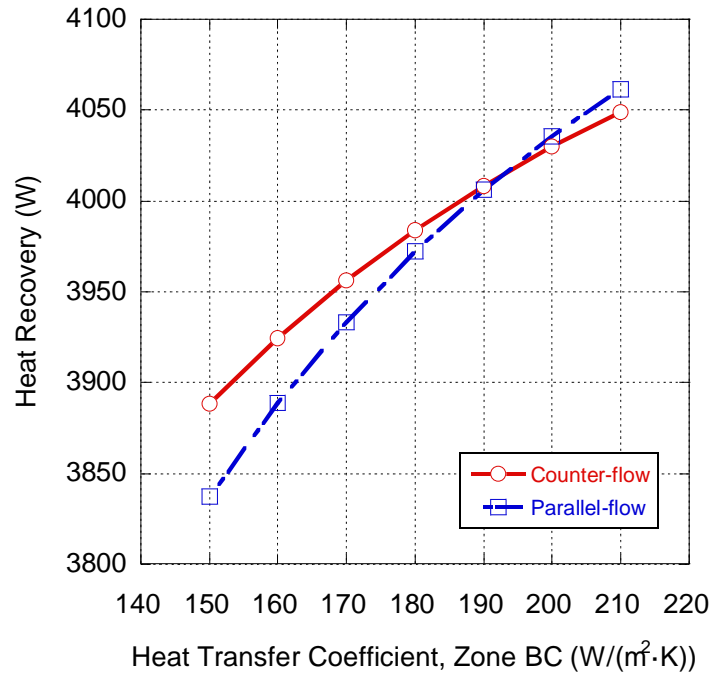
Figure 24: Comparison of counter-flow and parallel-flow configurations

This study uses the fourth engine operating point and hexane as the working fluid, showing a small benefit to using the counter-flow configuration for the overall heat transfer coefficients used here. However, increasingly large heat transfer coefficients, due to phase change, eventually support the use of parallel-flow. This result illustrates that choosing the most efficient flow configuration requires a complete thermodynamic analysis.

To investigate the influence of overall heat transfer coefficient on working fluid selection, the simulation parameters of Figure 21 are replicated with the exception of the lesser overall heat transfer coefficients shown in Table 6.

Table 6: Decreased Overall Heat Transfer Coefficients

Variable	Constant Value
U_{AB}	50 W/(m^{2}K)
U_{BC}	55 W/(m^{2}K)
U_{DE}	30 W/(m^{2}K)
U_{EF}	35 W/(m^{2}K)

These retained values include the 0.5 kg/s air flow rate, the fifth engine operating point, and the component efficiencies and heat transfer areas of Table 5.

With a component-based model, the fixed heat transfer area tends to cause condensing temperatures to rise, as larger temperature differences are required to reject heat. Higher condensing temperatures require lower pressure ratios for subcritical cycles and produce higher condensing pressures, which may be beneficial for those fluids with air infiltration concerns. Net Work values across pressure ratios for the lower overall heat transfer coefficients are shown in Figure 25.
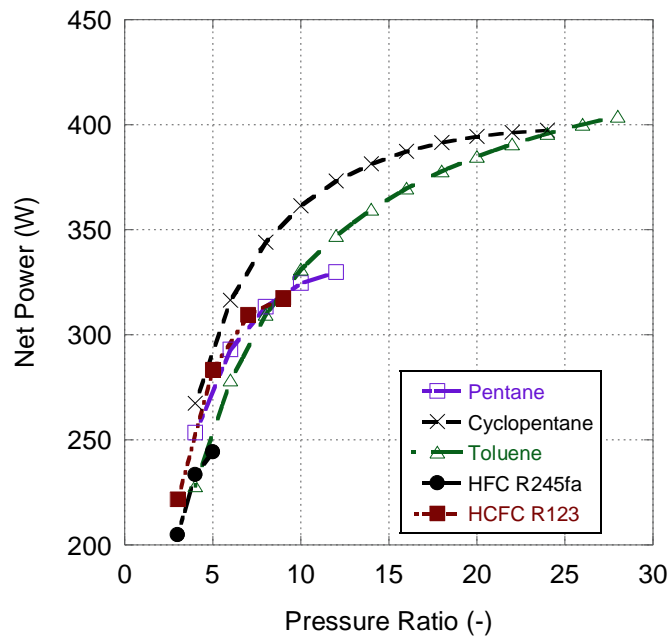
Figure 25: ORC performance with reduced overall heat transfer coefficients

With the pressure ratio specified, the evaporating temperature varies with the condensing temperature to obtain the appropriate temperature differences in the evaporator and condenser. Thus, although the temperature difference in the evaporator is slightly diminished and that in the condenser is slightly increased, the lower power values of Figure 25 result primarily from reduced working fluid flow rates. However, the primary result of the study is the similar shapes

of the performance curves and the similar hierarchy of performance among fluids (when compared to Figure 21).

3.3.1 Summary of ORC Modeling

A computer simulation of an ORC using dry fluids has been developed in MATLAB and modeled using experimental conditions from a single-cylinder diesel engine. Function evaluations are performed on 12 variables, which are followed by updates of 37 other variables, primarily performed by REFPROP. In contrast with the popular effectiveness-NTU method, the model considers physical heat exchangers with fixed heat transfer areas and uses multiple zones in order to incorporate the heat transfer enhancing effects of phase change, along with assigning more accurate temperature differences.

Eight dry working fluids are included in pressure ratio sweeps at five engine operating points. The first results support a linear relationship between pressure ratio and expansion ratio, showing that pressure ratio sweeps provide a comparable substitute for expansion ratio sweeps. This correlation is valuable in determining the most applicable type of expansion device for each working fluid. A majority of the fluids considered will function well with screw expanders, while scroll expanders are preferable for HFC R245fa and HCFC R123.

Benzene, toluene, and hexane are shown to suffer from low condensing pressures, creating the possibility of air infiltration. Alternatively, butane requires evaporative pressures in excess of practical limitations for a small-scale ORC unit. One fluid that proves viable and achieves efficient WHR is pentane. Thermal efficiencies around 15% are achieved and an ORC using pentane as the working fluid can provide a 10% increase in efficiency above the standalone engine-generator. These percentages are relatively constant across engine operating conditions, demonstrating the ORCs applicability in a variety of applications. Another attractive working

fluid candidate is cyclopentane, which offers slightly more ORC power generation at the cost of featuring condensing pressures around 60-70 kPa.

A detailed study of the air flow rates over the condenser suggests an optimal value exists between the 0.2 kg/s and 1 kg/s limits examined. While the optimal value varies between engine loads and working fluid selections, the 0.5 kg/s flow rate used in the majority of simulations is validated. Final installation of the ORC can adjust the air flow rate with fluctuating operating conditions in order to maximize power generation. However, ORC performance is relatively insensitive to condenser air flow rate unless the rate deviates significantly from the optimal value. Finally, the unique heat transfer situation found in the ORC evaporator is shown to require thermodynamic analysis before selecting a flow configuration. For the overall heat transfer coefficients used in this study, the counter-flow and parallel-flow arrangements recover a similar amount of heat. Although the counter-flow arrangement is widely-used, the parallel-flow configuration demonstrates an advantage if slightly larger differences in heat transfer coefficients exist between zones.

In relation to the overall objective of creating a DPFHX-ORC system model, this exercise serves the primary purpose of developing an ORC computer model. This model provides a mechanism for translating the WHR of the DPFHX to the power generation potential of the DPFHX-ORC system. As a result, engine efficiency improvements of approximately 10% across engine loads demonstrate the viability of the system, particularly when considering the additional energy from regeneration in a DPFHX device not included in the current evaporator model. Another improvement over the current power production estimate could result from more efficient heat transfer in a DPFHX device over a conventional shell and tube heat exchanger.

Additionally, the effort provides a screening process for the best working fluid based on practical considerations and performance, narrowing the eight working fluid candidates to pentane and cyclopentane. Among these candidates, cyclopentane should be utilized in any system where condensing pressures slightly below atmospheric are sustainable due to superior power generation. Examination of the optimal expansion ratios for both fluids favors the use of a screw-type expansion device for maximum efficiency. Furthermore, an important need for examining both parallel and counter-flow evaporator configurations is highlighted, while the most effective arrangement often remains as counter-flow.

Chapter 4

Diesel Particulate Filter Modeling

4.1 Background

The EPA is enacting increasingly stringent regulations on engine exhaust emission levels. These levels are currently low enough that improvements to the engine's combustion and fuel delivery technology can no longer meet these standards without the aid of aftertreatment devices. In particular, diesel engine aftertreatment systems must specifically target PM emission levels. For this purpose, Diesel Particulate Filters (DPF's) have been utilized for nearly three decades, beginning with direct-flow fibrous bed DPF's [97]. These devices captured PM according to three classical aerosol filtration mechanisms as shown by Figure 26. Interception occurs when a particle follows a streamline near the filter and touches a fiber, while larger particles diverge from the gas streamline due to their inertia, leading to inertial impaction [98]. The final mechanism, diffusion, results from collisions between small particles that cause random motion.
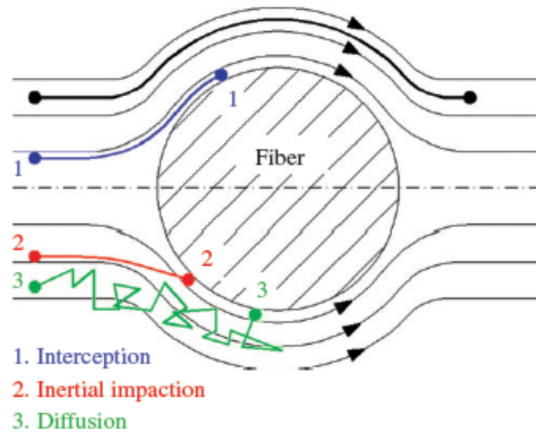
Figure 26: Methods of particle collection by a single fiber [97] (Reprinted with Permission from SAE International)

Although the collection efficiency of direct-flow fibrous bed DPF's is initially high, inherent limitations on flow area during filtration prevents simultaneously achieving low pressure drop and efficient PM collection, while another challenge is satisfying packaging restrictions. In addition, the tendency of the soot particles to adhere to the fibers decreases over time [99]. Modern wall-flow DPF's overcome these shortcomings and capture PM with near 100% effectiveness [5].

The structure of a modern DPF is similar to modern catalytic converters in that DPF's have a grid of channels through which the exhaust gas must flow. However, DPF's are manufactured with alternating channels blocked so that the flow is forced through a porous wall structure as seen in Figure 27.
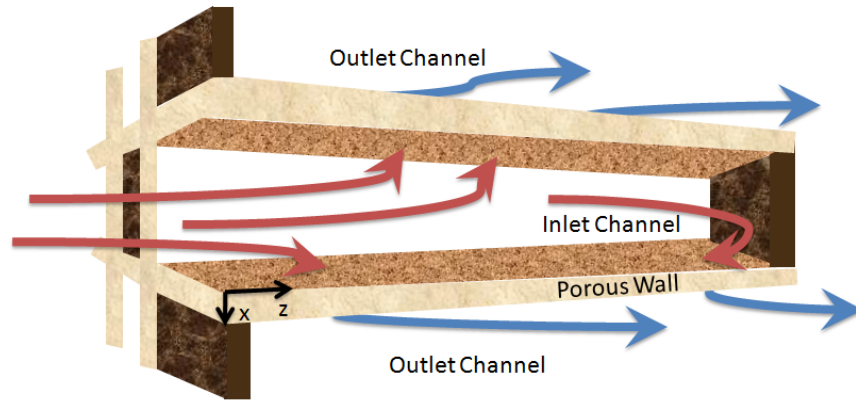
Figure 27: Inlet channel and outlet channel pair showing flow being forced through porous wall

By forcing the flow through the porous walls, the small pores of the wall capture PM in the exhaust, leaving relatively clean exhaust in the outlet channel of the DPF. Initially, the flow restriction of the DPF is small, but collection of additional PM in and on the filter walls causes the DPF to become more restrictive of flow. Once the filter wall fills with soot, a PM layer begins to grow on the inlet channel wall surfaces, as depicted in Figure 28 [100].
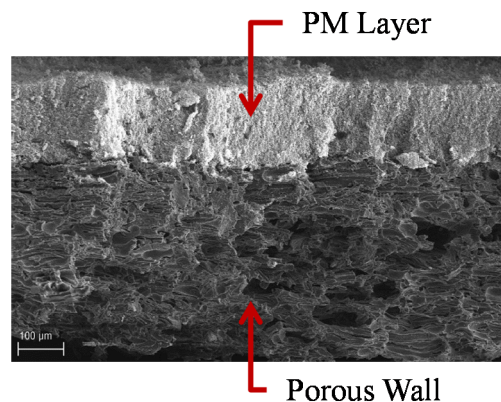
Figure 28: Enlarged image of soot layer on porous wall to show PM accumulation [100]

The loading of PM on the porous wall adversely impacts engine efficiency and fuel economy by causing an increased pressure drop in the exhaust; thus, decreasing the pressure difference and subsequent exhaust flow from the cylinder to the exhaust manifold [101]. Because of these negative effects, DPF's must intermittently undergo regeneration to oxidize the PM that collects in and on the filter walls [5]. As a result, the 'soot cake' coating the inlet channel and PM

stored within the wall convert to gaseous CO_2 and exit the DPF, decreasing the pressure drop across the filter wall. This combustion of the stored PM is possible due to the excess oxygen present in diesel engine exhaust.

DPF models have been widely utilized in order to better understand the effects of soot loading and regeneration on engine performance through the simulation of the pressure drop across the device. Moreover, filter models are useful tools for comparative evaluation of different DPF designs. As such, the influence of using different porous wall materials, wall thicknesses, channel, and overall dimensions are quantifiable through simulations. More generally, such representations of a DPF provide the thermodynamic properties within the channels and porous wall for the purpose of studying individual physical phenomena within any theorized DPF.

Building on past efforts, such as Bissett's 1984 pioneering work on wall-flow DPF modeling [47], the goal is to represent steady-state and transient operation of a DPF. Since the DPF is an inherently three-dimensional device, variations in soot loading and temperature levels exist among the channels. However, previous modeling efforts demonstrate that simplification of the 3-D geometry to a 1-D representation of a single inlet channel-outlet channel pair can provide suitable results [47, 48, 102, 103]. Such models offer significantly faster simulation times, allowing large numbers of DPF designs and aftertreatment system configurations to be studied. Furthermore, several authors propose adaptations to simplified 1-D models for inclusion of multi-dimensional effects [104, 105].

The simplification procedure that reduces the 3-D channel flow to 1-D involves a number of reasonable assumptions as illustrated by Figure 29 [106]. Reduction in this manner begins by changing 3-D Cartesian coordinates (x, y, z) to 2-D cylindrical coordinates through defining an

axial and radial direction (z, r), effectively neglecting angular variations within the channel. By also assuming that the flow at all radial locations has similar properties, the model becomes 1-D.
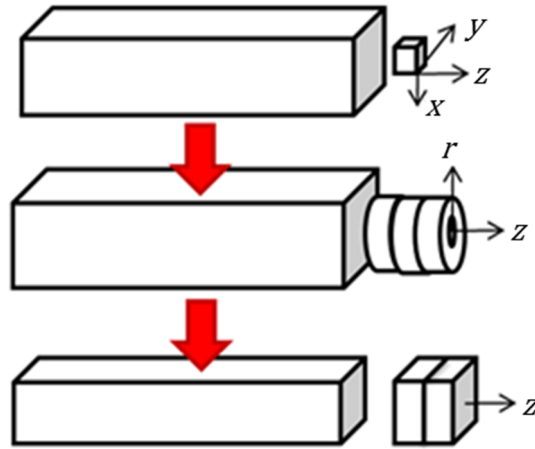
Figure 29: Simplification of 3-D channel flow to 1-D

Following the progression depicted in Figure 29 allows a 3-D channel to be modeled as flow solely dependent on the axial direction (z). However, a further assumption removes the necessity to solve each channel within the DPF, with channel numbers in the thousands. By assuming each channel pair is identical, a single inlet channel-outlet channel pair can represent an entire DPF. Single inlet channel-outlet channel 1-D models consist of a single inlet channel, porous wall and outlet channel. As previously elucidated, multi-dimensional effects such as wall-flow and convective heat transfer are included through adaptation of a 1-D model.

As shown in Figure 27, the distance along the channel is given the dimension 'z' while the porous wall dimension is referred to as 'x'. Since the flow in the channel varies only in the z-direction and the exhaust at each wall location varies with respect to x only, the single inlet channel-outlet channel technique is known as a 1+1D model [49, 107]. That is, a 1+1D model means that the channel properties vary with z (1 dimensional) and the wall properties vary with x (1 dimensional), forming a 1+1D model. This creates four flow regions (inlet channel, soot layer,

porous wall, and outlet channel) with different 1-D governing equations. In the governing equations, the following designations correspond to different parts of the flow regime: inlet channel $'I'$, outlet channel $'II'$, exhaust gas in soot layer $'s'$, exhaust gas in wall $'w'$, physical soot layer $'d'$, and physical filter wall $'f'$.

4.2 DPF Governing Equations

As a result of the modeling choice to implement a 1+1D model, the general differential equations for one-dimensional Eulerian fluid flow provide the starting point for representing the flow within each channel. More specifically, the channel formulations must allow for changing geometry by using area-conserved format (sometimes termed quasi-one-dimensional) and account for multi-dimensional effects through the use of source terms. By using this format, derivation of the appropriate conservation of mass, momentum, and energy equations for the inlet and outlet channels becomes possible. Furthermore, the large temperature and pressure changes occurring within the DPF requires consideration of compressibility, an effect that can be quantified through inclusion of the ideal gas law [108].

In order to model the exhaust flow through the soot and wall layers, a design choice exists between using one wall density and velocity [47, 103, 109] or two densities and velocities corresponding to independent values within the soot and wall layers, respectively [49]. The work described here utilizes both approaches, requiring presentation of both methods. Use of the one component model only occurs to validate the channel and porous wall solutions (no soot isothermal case), while the two component model is featured in the warm up and cool down oxidation simulations.

To account for the pressure drop across the soot and wall layers, researchers widely use Darcy's law for porous media [110, 111] as a simplification of the soot and wall conservation of

momentum equations. With respect to conservation of mass, an algebraic relationship exists between the soot and wall flow in conjunction with the soot combustion equation. Despite the possibility of exhaust temperatures exceeding 1000K for short periods during the regeneration event, the ideal gas law can also be imposed on the soot and wall gases.

In addition to the channel and wall equations pertaining to the exhaust gas, the final expressions in the DPF model presented here are a monolith temperature equation and soot combustion equation for the purpose of tracking the physical soot and wall temperatures. With an introduction to the overall set of equations included in the current DPF model now complete, the following series of derivations highlight the underlying assumptions and governing equations in final form. These simplifications include many of the original assumptions of Bissett [47] as listed by Koltsakis et al. [5]:

1) The properties of the gas entering the front face of the monolith are spatially uniform; however, they can be time dependent.

2) The model assumes perfect insulation for the circumferential walls of the monolith.

3) A single inlet and outlet channel represents the behavior of all inlet and outlet channels.

4) Radiative heat transport in the channels is negligible because the long thin channel walls have similar view factors and should have similar temperatures.

5) The thickness of the PM layer is so thin compared with the channel thickness during the initial period of operation; the change in the channel geometry due to the presence of the PM layer can be neglected. Symbolically this means the soot layer thickness (t_d) is much less than the channel diameter (d_m), or $t_d << d_m$.

6) The emitted particles do not interfere with the flow due to their low mass fraction within the bulk gas.

7) Although not explicitly stated in his article, Bissett omits the time derivatives of the gaseous state variables, effectively stating that there is not any storage in the gas according to a quasi-steady-state approximation.

4.2.1 Conservation of Mass

As previously mentioned, the channel geometry allows for the use of the 1-D area-conserved differential mass conservation expression. Following assumption 7 of Bissett, the time derivative can be neglected, leaving only a mass flow term on the left hand side. This term is identical for the inlet and outlet channels and equates to the source term, which differs between the inlet and outlet channels as a result of the fluid dynamics within the porous wall. These source terms account for the 2-D effect of wall flow, where u represents the x-direction speed and S is the surface area per unit length (or perimeter) of the respective channels.

$$\frac{\partial(\rho_I A_I w_I)}{\partial z} = -S_I \rho_s u_s \tag{4.1}$$

$$\frac{\partial(\rho_{II} A_{II} w_{II})}{\partial z} = S_{II} \rho_w u_w \tag{4.2}$$

In the above expressions, ρ is the density, A is the cross-sectional area of the channel, and w is the speed in the z-direction. Since square DPF channels are the predominant geometry, the cross-sectional area and surface area per unit length are given by:

$$A_I = (d_m - 2t_d)^2 \qquad A_{II} = d_m^2 \tag{4.3}$$

$$S_I = 4(d_m - 2t_d) \qquad S_{II} = 4d_m \tag{4.4}$$

In the two component model, the integration occurs with respect to the mass flow rate $\dot{m}$, while the one component formulation uses a dummy variable G.

$$\dot{m} = \rho A w \tag{4.5}$$

$$G = \rho w \tag{4.6}$$

In both instances, the boundary values on the right hand side of Eq.'s (4.1)-(4.2) are local average velocities and densities. Thus, the final forms of the channel conservation of mass equation for the two component model take the form:

$$\frac{\partial \dot{m}_I}{\partial z} = -S_I \rho_s u_s \tag{4.7}$$

$$\frac{\partial \dot{m}_{II}}{\partial z} = S_{II} \rho_w u_w \tag{4.8}$$

In the two component formulation, mass conservation is insured by equating the magnitude of the channel mass equation source terms (right hand side of Eq.'s (4.7)-(4.8)). By doing so, the mass flow exiting the inlet channel and entering the outlet channel must be identical, effectively ignoring the contribution of soot collection and regeneration on mass flow through the wall. Using this methodology, the two component continuity equation becomes:

$$\rho_s u_s S_I = \rho_w u_w S_{II} \tag{4.9}$$

This description assumes representative densities and velocities within the soot and wall layers, instead of integrating the governing equations in the x-direction while accounting for the surface area per unit length change from S_I to S_{II} through the soot layer. Of interest, the thermodynamic properties vary throughout the wall layer as well; however, the surface area per unit length is constant.

Alternatively, the one component model expands the left hand side of Eq.'s (4.1)-(4.2) using the product rule and assumes constant channel cross-sectional area to obtain the denominator of Eq.'s (4.10)-(4.11).

$$\frac{\partial G_I}{\partial z} = -\frac{4d_m}{\left(d_m - 2t_{d,avg}\right)^2} \rho_w u_w \tag{4.10}$$

$$\frac{\partial G_{II}}{\partial z} = \frac{S_{II}}{A_{II}} \rho_w u_w \tag{4.11}$$

This additional assumption requires constant soot thickness over the discretization solved. To prevent mass accumulation, the surface area per unit length of the inlet channel (S_l) must neglect the soot layer, effectively equating the source terms of the respective channels in the absence of PM collection and regeneration events.

4.2.2 Conservation of Momentum

According to a traditional derivation of the differential conservation of momentum equations, or equations of motion, the material time derivative of a fluid element's momentum equates to the resultant force acting on the fluid element [112]. The material derivative initially generates four terms; however, most authors neglect the local acceleration and retain only the axial convective acceleration term. To be clear, all DPF models require wall-flow through the wall in the *x*-direction only, explaining the absence of wall-flow source terms apart from the axial convective acceleration and resultant force.

Presuming the *z*-direction has no gravitational acceleration, the surface forces associated with the fluid element become sufficient to obtain the resultant force. Following the common assumption of inviscid flow associated with exhaust gas, shearing stresses on the fluid element become negligible and pressure replaces the normal stress. As a result of expecting fluid pressure to act in compression of the fluid element, the pressure derivative features a negative sign. By incorporating an additional term in the form of an area derivative to balance the force associated with changing channel geometry, the resultant force comes from two terms.

The last term of the channel momentum equations accounts for friction at the interface between the channels and porous wall, following the form of Bissett [47]. This friction component results from a reduction of *w* to zero at the walls according to the no-slip condition, and represents a correlation for fully-developed laminar flow in a square channel. By

incorporating this correlation for solid walls, the drag effect calculated neglects turbulence and the small fraction of flow passing through the wall at each axial location.

Following this methodology, Eq.'s (4.12)-(4.13) show the inlet and outlet channel momentum equations, exactly recovering the area-conserved momentum equations first shown by Depcik and Assanis in 2008 [49]. The left hand side of these equations account for the advection of momentum through the channels, while the first two right hand side terms are the resultant force, followed by the friction term at the channel boundary. These equations are similar to traditional, area-conservation works of Liu et al. [113], Onorati et al. [114], and Depcik et al. [106].

$$\frac{\partial(\rho_I w_I^2 A_I)}{\partial z} = -\frac{\partial(p_I A_I)}{\partial z} + p_I \frac{\partial A_I}{\partial z} - \frac{F\mu w_I S_I}{d_m - 2t_d} \tag{4.12}$$

$$\frac{\partial(\rho_{II} w_{II}^2 A_{II})}{\partial z} = -\frac{\partial(p_{II} A_{II})}{\partial z} + p_{II} \frac{\partial A_{II}}{\partial z} - \frac{F\mu w_{II} S_{II}}{d_m} \tag{4.13}$$

In the preceding equations, F is one-fourth of Bissett's friction factor and μ is the dynamic viscosity of the exhaust gas.

Due to the obvious similarity between the inlet and outlet channel momentum equations, the inlet channel presentation here is sufficient to reconstruct the outlet channel derivation. For the current two component model, expansion of the left hand side derivatives via the product rule using the mass flow rates and z-velocities as variables results in the left hand side of Eq. (4.14). Following a similar process on the pressure force term allows cancellation of the area derivative, leaving the desired pressure derivative.

$$\dot{m}_I \frac{\partial w_I}{\partial z} + w_I \frac{\partial \dot{m}_I}{\partial z} = -A_I \frac{\partial p_I}{\partial z} - \frac{F\mu w_I S_I}{d_m - 2t_d} \tag{4.14}$$

The only remaining manipulation involves removing all direct dependence on w_I. As described in a later section, this step is necessary since the mass flow rate and density are the preferred

state variables. Therefore, using Eq. (4.14) and rearranging to isolate the pressure derivative results in:

$$\frac{\partial p_I}{\partial z} = \frac{1}{A_I}\left[-\frac{F\mu S_I}{d_m - 2t_d}\frac{\dot{m}_I}{\rho_I A_I} - \dot{m}_I \frac{\partial\left(\frac{\dot{m}_I}{\rho_I A_I}\right)}{\partial z} - \frac{\dot{m}_I}{\rho_I A_I}\frac{\partial \dot{m}_I}{\partial z} \right]$$

(4.15)

As a result of the substitution, the quotient rule must be applied before achieving a momentum equation compatible with the aforementioned state variable form. Furthermore, another application of the product rule to the denominator of the previous step and distribution of the cross-sectional area provides:

$$\frac{\partial p_I}{\partial z} = -\frac{F\mu \dot{m}_I S_I}{(d_m - 2t_d)\rho_I A_I^2} - \frac{\dot{m}_I}{A_I}\left(\frac{1}{\rho_I A_I}\frac{\partial \dot{m}_I}{\partial z} - \frac{\dot{m}_I}{\rho_I A_I^2}\frac{\partial A_I}{\partial z} - \frac{\dot{m}_I}{\rho_I^2 A_I}\frac{\partial \rho_I}{\partial z} \right)$$
$$- \frac{\dot{m}_I}{\rho_I A_I^2}\frac{\partial \dot{m}_I}{\partial z}$$

(4.16)

Finally, an algebraic simplification results in the final two component inlet channel momentum equation, and by extension provides the accompanying outlet channel expression (where no soot layer nullifies the area derivative).

$$\frac{\partial p_I}{\partial z} = -\frac{F\mu \dot{m}_I S_I}{(d_m - 2t_d)\rho_I A_I^2} - \frac{2\dot{m}_I}{\rho_I A_I^2}\frac{\partial \dot{m}_I}{\partial z} + \frac{\dot{m}_I^2}{\rho_I^2 A_I^2}\frac{\partial \rho_I}{\partial z}$$

(4.17)

$$\frac{\partial p_{II}}{\partial z} = -\frac{F\mu \dot{m}_{II} S_{II}}{d_m \rho_{II} A_{II}^2} - \frac{2\dot{m}_{II}}{\rho_{II} A_{II}^2}\frac{\partial \dot{m}_{II}}{\partial z} + \frac{\dot{m}_{II}^2}{\rho_{II}^2 A_{II}^2}\frac{\partial \rho_{II}}{\partial z}$$

(4.18)

The one component momentum equations result from a similar tactic, with the exception of using the state variable G of Eq. (4.6) instead of the mass flow rate. Following the work of Haralampous and Koltsakis [115], the area derivative can be neglected while still accounting for the difference in geometry between the channels.

$$\frac{\partial p_I}{\partial z} = -\frac{F\mu G_I S_I}{(d_m - 2t_d)\rho_I A_I} - \frac{2G_I}{\rho_I}\frac{\partial G_I}{\partial z} + \frac{G_I^2}{\rho_I^2}\frac{\partial \rho_I}{\partial z} \tag{4.19}$$

$$\frac{\partial p_{II}}{\partial z} = -\frac{F\mu G_{II} S_{II}}{d_m \rho_{II} A_{II}} - \frac{2G_{II}}{\rho_{II}}\frac{\partial G_{II}}{\partial z} + \frac{G_{II}^2}{\rho_{II}^2}\frac{\partial \rho_{II}}{\partial z} \tag{4.20}$$

There is some variation among the available literature regarding momentum conservation in porous media. Several early authors use an effective viscosity to account for the diffusion of velocity in the soot and filter wall [116-118]; however, Nield and Bejan suggest this effect can be ignored without introducing any significant error [110]. Furthermore, it is appropriate to use Darcy's law to model porous wall flow [110, 111]. This principle applies for low Reynolds number flows through porous media where inertial effects can be ignored [119], and removes the necessity of including a convective term in the momentum equations [120]. In area-conserved format, the soot and wall equations are:

$$\frac{\partial (p_s A_s)}{\partial x} = p_s\frac{\partial A_s}{\partial x} - \frac{\mu_s u_s A_s}{K_d} - \beta_d \rho_s A_s u_s^2 \tag{4.21}$$

$$\frac{\partial (p_w A_w)}{\partial x} = p_w\frac{\partial A_w}{\partial x} - \frac{\mu_w u_w A_w}{K_f} - \beta_f \rho_w A_w u_w^2 \tag{4.22}$$

where K is permeability and β is the Forschheimer inertial coefficient. For square channels, the cross-sectional area per unit axial length in the soot layer varies in the x-direction while the wall layer cross-sectional area is constant.

$$A_s = 4\left[d_m - 2\left(t_d - \frac{y}{\tan(\theta)}\right)\right] \; where \; \tan(\theta) = 1 \tag{4.23}$$

$$A_w = 4d_m \tag{4.24}$$

Further simplification of Eq.'s (4.21)-(4.22) is possible by recognizing that most DPF modeling efforts neglect the Forschheimer effect [49]. Thus, expanding the pressure derivative

and using a single discretization across the soot and wall layers respectively results in the traditional Darcy's law expressions:

$$u_s = \frac{p_x - p_I}{-\mu_s t_d / K_d} \tag{4.25}$$

$$u_w = \frac{p_{II} - p_x}{-\mu_w t_{fw} / K_f} \tag{4.26}$$

This nomenclature utilizes a new state 'x' located at the boundary between the soot and wall layers as shown by Figure 30.

Soot Layer

p_I
p_s
p_x
t_d
t_{fw}
p_w
p_{II}
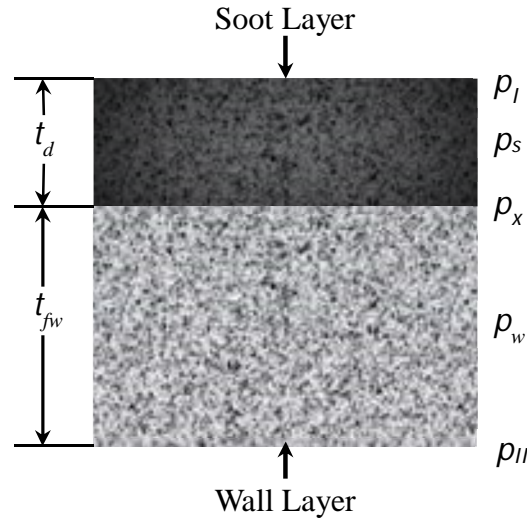
Wall Layer

Figure 30: Schematic of two wall velocity pressures through soot and wall layers

Due to the placement of pressure states within the adopted scheme, an algebraic pressure relationship is assumed to exist within each layer [5]:

$$p_s = \frac{p_I + p_x}{2} \tag{4.27}$$

$$p_w = \frac{p_{II} + p_x}{2} \tag{4.28}$$

The relatively simpler one component scheme uses an algebraic constraint equation to determine the wall pressure (Eq. (4.29)) [103] and results in a single Darcy's law expression incorporating the pressure drops for the soot and wall layers.

$$p_w = \frac{p_I + p_{II}}{2} \tag{4.29}$$

$$u_w = \frac{p_I - p_{II}}{-\dfrac{\mu_w t_{fw}}{K_f} - \dfrac{\mu_s t_d}{K_d}} \tag{4.30}$$

4.2.3 Conservation of Energy

Similar to the wall-flow terms accounting for mass defection to (from) the porous wall in the inlet (outlet) channel continuity equations, the energy associated with these flows contribute to the channel first law expressions. For conservation of mass, the inlet channel sink term and the outlet channel source term equate to prevent mass accumulation, ignoring collection and regeneration effects. However, heat transfer occurs as the flow passes through the porous wall and soot layers, allowing a change in energy between flow entering and exiting the soot and wall layers respectively. Instead of modeling the heat transfer process in the soot and wall layers, some authors assume the wall flow immediately reaches the filter temperature (T_f), resulting in the relationship:

$$T_s = T_w = T_d = T_f \tag{4.31}$$

which removes the temperature dependence in the x-direction while still permitting temperature variations in the axial direction along the wall. Through extensive modeling, Depcik validates this assumption [49]. Physically, this expression equates the gas temperature in the soot and wall layer to the solid soot and filter temperatures.

To obtain the appropriate first law expressions for the inlet and outlet channels, a number of physical phenomena must be considered. Among these is the time-varying energy storage within the exhaust, an effect that is excluded from the governing equations by assumption 7 of Bissett. With respect to work, the absence of mechanical devices within the channels leaves only the flow work, which transforms from an expression containing shear stresses to a pressure

derivative by the hydrostatic pressure condition. Following the standard progression, a comparison of magnitudes within the energy advection term reveals that the kinetic and potential energy is small in relation to the thermal energy present. Therefore, the thermal energy and flow work combine to create a specific enthalpy (h) advection term.

The two physical effects not yet described are heat transfer and wall flow, where heat transfer must consider conduction, convection, and radiation. As previously mentioned in assumption 4 of Bissett, the similar view factors for long thin channel walls allows for removal of all dependence on radiation. Going further, the contribution of axial conduction is commonly presumed to be much less than convection, allowing for representation of heat transfer in the form of a single term based on the temperature difference between the channel gas and porous wall. To account for the multi-dimensional effect of wall-flow, Kostoglou et al. [121] and Konstandopoulos et al. [122] approximate the gas temperature entering (exiting) the porous wall as T_I (T_w), instead of using the more physically accurate boundary value calculation in the work of Depcik [49]. As with the wall-flow terms in the conservation of mass equations, a difference in sign occurs because of energy loss to the wall from the inlet channel and flow into the outlet channel. The resulting differential equations are:

$$\frac{\partial(\rho_I w_I h_I A_I)}{\partial z} = -S_I\left[h_{g,I}(T_I - T_d) + \rho_s u_s h_I\right] \tag{4.32}$$

$$\frac{\partial(\rho_{II} w_{II} h_{II} A_{II})}{\partial z} = -S_{II}\left[h_{g,II}(T_{II} - T_f) - \rho_w u_w h_w\right] \tag{4.33}$$

where h_g is the convective heat transfer coefficient between the channel gas and wall surface, with the inlet channel transferring heat to the soot while the outlet channel borders are the porous wall.

A heat transfer correlation from [49], created using experimental data of [123-131] is adopted, which quantifies the effects of suction and injection on heat transfer. The resulting expression calculates the fully-developed Nusselt number (Nu) of the flow using the Peclet number (Pe) according to:

$$Nu_s = \frac{h_{g,I}(d_m - 2t_d)}{k_{g,s}}$$

(4.34)

$$= 2.71 - 0.504Pe_s + 0.0381Pe_s^2 - 0.00102Pe_s^3$$

$$Nu_w = \frac{h_{g,II}d_m}{k_{g,w}} = 2.71 - 0.504Pe_w + 0.0381Pe_w^2 - 0.00102Pe_w^3$$

(4.35)

where k_g is the thermal conductivity of the gas. Depcik notes the above correlation is only valid for square channel flows with exhaust gas Prandtl numbers near that of air (approximately 0.72). In order to account for the influence of suction and injection on convection, the Peclet number expressions differ by sign as shown by:

$$Pe_s = -\frac{u_s(d_m - 2t_d)}{\alpha_s}$$

(4.36)

$$Pe_w = \frac{u_w d_m}{\alpha_w}$$

(4.37)

where α is the thermal diffusivity of the exhaust gas.

The state variable form of the two wall velocity model again requires manipulation to achieve dependence on the chosen state variables; for the energy equations, most authors integrate with respect to temperature. Expanding the inlet channel expression using the product rule on the mass flow rate and specific enthalpy with subsequent isolation of the eventual temperature derivative results in:

$$\dot{m}_I \frac{\partial h_I}{\partial z} = -S_I\left[h_{g,I}(T_I - T_d) + \rho_s u_s h_I\right] - h_I \frac{\partial \dot{m}_I}{\partial z}$$

(4.38)

The second and third right hand side terms can then be cancelled through substitution of Eq. (4.7), the inlet channel continuity equation. Then, by using the constant pressure specific heat (c_p) of the inlet channel gas, the two wall velocity first law becomes:

$$\frac{\partial T_I}{\partial z} = -\frac{S_I}{c_{p,I}\dot{m}_I} h_{g,I}(T_I - T_d) \tag{4.39}$$

In a similar manner for the outlet channel, expansion of Eq. (4.33) and substitution of Eq. (4.8) allows for isolation of the temperature gradient, resulting in:

$$\frac{\partial T_{II}}{\partial z} = -\frac{S_{II}}{c_{p,II}\dot{m}_{II}}\left[h_{g,II}(T_{II} - T_f) - \rho_w u_w(c_{p,w}T_w - c_{p,II}T_{II})\right] \tag{4.40}$$

The procedure for the one wall velocity derivation proceeds the same way from Eq.'s (4.32)-(4.33), except using the state variable G instead of the mass flow rate. Through substitution of the appropriate mass conservation equations (Eq.'s (4.10)-(4.11)) while neglecting soot thickness variations, the channel conservation of energy equations are:

$$\frac{\partial T_I}{\partial z} = -\frac{S_I}{G_I c_{p,I} A_I} h_{g,I}(T_I - T_d) \tag{4.41}$$

$$\frac{\partial T_{II}}{\partial z} = -\frac{S_{II}}{G_{II} c_{p,II} A_{II}}\left[h_{g,II}(T_{II} - T_f) - \rho_w u_w(c_{p,w}T_w - c_{p,II}T_{II})\right] \tag{4.42}$$

4.2.4 Ideal Gas Law

The algebraic form of the ideal gas law is the final form utilized in the majority of DPF modeling efforts:

$$\rho = \frac{p}{R_{ex}T} \tag{4.43}$$

which is valid in both channels and wall layers. In some instances, it is necessary to obtain the derivative of the ideal gas law using the quotient rule to assist in integrating the channel equations. The result of this procedure and subsequent algebraic simplification equals [132]:

$$\frac{\partial \rho_{I,II}}{\partial z} = \frac{1}{R_{ex}T_{I,II}^2}\left(T_{I,II}\frac{\partial p_{I,II}}{\partial z} - p_{I,II}\frac{\partial T_{I,II}}{\partial z}\right) \tag{4.44}$$

4.2.5 Filter Energy Equation

In the current discussion, only the one and two component formulations are being considered. Therefore, the alternative option of allowing solid phase temperature dependence in the axial and wall directions will not be discussed as most authors use a single filter temperature at each axial location. In addition, the close proximity of the physical soot and filter wall suggests that a single solid phase temperature will sufficiently approximate each axial location. As such, the energy storage within the physical soot and porous wall are combined into a single equation. Using the volume per unit length terms of Depcik and Assanis [49] instead of soot and wall layer thicknesses, the modern filter energy equation is:

$$
\begin{aligned}
\left(\rho_f c_f V_f + \rho_d c_d V_d\right)\frac{\partial T_f}{\partial t} \\
= \dot{Q}_{cond} + \dot{Q}_{multi} + \dot{Q}_{conv} + \dot{Q}_{wall} + \dot{Q}_{supply} + \dot{Q}_{rad} \\
+ \dot{Q}_{reac} + \dot{Q}_{cat} + \dot{Q}_{inner} + \dot{Q}_{DPFHX}
\end{aligned}
\tag{4.45}
$$

where the left hand side includes the specific heat (c) and volume per unit axial length (V) of the filter and wall. To be clear, these quantities are based on the totality of the DPF, a distinction that becomes important when developing the heat transfer terms on the right hand side. Adapting the approach used in 1-D catalyst modeling [106] to the relevant DPF geometry, the following procedure obtains the volume per unit axial length terms present in the filter energy equation. Introduction of this scheme is first published by Depcik and Assanis [49].

The empty channel volume per unit axial length of the entire DPF (V_e) is the cross-sectional area of each channel in the absence of soot times the number of channels.

$$V_e = d_m^2 N_c \tag{4.46}$$

After calculating the total volume of the DPF per unit axial length (V_{DPF}) using the diameter of the DPF core (d_{DPF}), the empty void fraction without soot (ε) can be determined.

$$V_{DPF} = \frac{\pi d_{DPF}^2}{4} \tag{4.47}$$

$$\varepsilon = \frac{V_e}{V_{DPF}} \tag{4.48}$$

Physically, the empty void fraction without soot is the portion of the filter that is not porous wall. Therefore, the total volume of solid filter per unit length (V_f) is:

$$V_f = (1 - \varepsilon)V_{DPF} \tag{4.49}$$

In certain loading situations, the soot layer reduces the empty channel volume appreciably, reducing the flow area available in each inlet channel. Accounting for this change in geometry by using reduced inlet channel dimensions, the channel volume per unit axial length (V_{de}) results from:

$$V_{de} = \frac{N_c}{2}[(d_m - 2t_d)^2 + d_m^2] \tag{4.50}$$

Calculation of the void fraction in the presence of soot (ε_d) uses this volume instead of the empty channel volume, according to:

$$\varepsilon_d = \frac{V_{de}}{V_{DPF}} \tag{4.51}$$

As a result, the total volume of soot on the surface per unit axial length is:

$$V_d = (\varepsilon - \varepsilon_d)V_{DPF} \tag{4.52}$$

Several of the heat flux terms in Eq. (4.45) are commonly omitted in the literature; however, the present discussion identifies the physical effects associated with each term and justifies their exclusion before presenting the final expression. The $\dot{Q}_{inner}$ term accounts for heat transfer to the wall from the gas and vice versa as flow passes in the x-direction, but is ignored

due to the assumption in Eq. (4.31) of rapid gas temperature change. Three effects can be grouped into the catalytic reaction term $\dot{Q}_{cat}$; conversion of PM by a catalytic porous wall surface [133], interaction of metal additives with surface and imbedded PM [134], and gaseous phase reactions taking place during wall-flow [135, 136]. All three contributions are neglected here as they have small impacts overall and are beyond the scope of the current study. The heat transfer from radiation, $\dot{Q}_{rad}$, is now commonly presumed to have a small influence on the filter temperature in regenerative applications [137], after being initially neglected by Bissett (Assumption 4). Recent efforts by Haralampous et al. [105, 138] acknowledge that high temperatures achieved during regeneration increase the influence of radiation; however, the current study retains the assumption that only a small error is introduced by ignoring radiative effects. Special cases of active heating for regeneration ($\dot{Q}_{supply}$) and heat transfer due to multiple dimensions ($\dot{Q}_{multi}$) are also not included in the current model. Included within the multi-dimensional heat transfer term is external heat transfer, making the current model adiabatic. For a discussion of the relevant equations to incorporate the effects neglected here, the interested reader is referred to [5].

Of importance for this effort, an additional term has been added to this equation ($\dot{Q}_{DPFHX}$) in order to account for the heat transfer to the ORC working fluid. It is neglected in this chapter when validating the DPF model; however, it will be reintroduced in Ch. 7 and its functional form explained. Due to the aforementioned simplifications, the resulting filter temperature equation is:

$$\left(\rho_f c_f V_f + \rho_d c_d V_d\right)\frac{\partial T_f}{\partial t} = \dot{Q}_{cond} + \dot{Q}_{conv} + \dot{Q}_{wall} + \dot{Q}_{reac} \tag{4.53}$$

where the heat transfer due to axial conduction, convection in the channels, internal heat transfer, and heat produced by regeneration are $\dot{Q}_{cond}$, $\dot{Q}_{conv}$, $\dot{Q}_{wall}$, and $\dot{Q}_{reac}$ respectively. Using

Fourier's law and neglecting small deviations in soot layer thickness in the axial direction produces the following conduction term:

$$\dot{Q}_{cond} = \left(k_f V_f + k_d V_d\right)\frac{\partial^2 T_f}{\partial z^2} \tag{4.54}$$

where k is thermal conductivity. Advanced models use a local volume per unit axial length, as presented by Koltsakis et al. [5].

Convection to the filter wall matches the corresponding channel energy equation terms, resulting in:

$$\dot{Q}_{conv} = \frac{N_c}{2}\left[h_{g,I}S_I(T_I - T_d) + h_{g,II}S_{II}(T_{II} - T_f)\right] \tag{4.55}$$

where N_c is the total number of channels, and half of the channels are subject to each convection term.

Heat transfer between the wall and exhaust gas is calculated as the difference in exhaust energy between entering and exiting the wall. In the absence of integrating the gas energy equation through the soot and wall layers to obtain values at the wall boundaries, a common approximation is:

$$\dot{Q}_{wall} = \frac{N_c}{2}\left[\rho_s u_s h_I S_I - \rho_w u_w h_w S_{II}\right] \tag{4.56}$$

The last contribution comes from soot oxidation, where the exothermic regeneration event serves to increase the filter temperature. While a variety of reactions oxidants are available in the exhaust stream, excess oxygen is the dominant species involved. Using a partial oxidation factor (α_{O_2}) to account for incomplete combustion resulting in carbon monoxide formation, the molar soot combustion reaction takes the form [139-141]:

$$C_{(s)} + \alpha_{O_2}O_2 \rightarrow 2\left(\alpha_{O_2} - 0.5\right)CO_2 + 2\left(1 - \alpha_{O_2}\right)CO \tag{4.57}$$
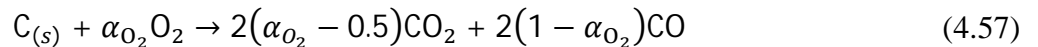
Furthermore, oxygen levels are tracked using the following combustion rate expression:

$$\dot{S}_{O_2} = S_p \rho_s Y_{s,O_2} k_{O_2} \tag{4.58}$$

where the specific surface area of soot, mass fraction of oxygen on the surface, and Arrhenius reaction rate constant are S_p, Y_{s,O_2}, and k_{O_2}, respectively. Use of the Arrhenius equation is widespread for representing chemical reactions, since the method accurately models both temperature dependence and activation energy (E). By including a combination of the filter temperature and a pre-exponential factor (A), the Arrhenious rate law for O_2 takes the form of:

$$k_{O_2} = A_{O_2} T_f exp\left(\frac{-E_{O_2}}{R_u T_f}\right) \tag{4.59}$$

The loss of soot corresponds to the oxygen combustion rate, with additional dependencies on the molecular weights and the partial oxidation factor. As shown by [49], the overall soot combustion rate is:

$$\dot{S}_{C_{(s)}} = \dot{S}_{O_2}\left(\frac{W_{C_{(s)}}}{\alpha_{O_2} W_{O_2}}\right) = \frac{S_p \rho_s Y_{s,O_2} k_{O_2} W_{C_{(s)}}}{\alpha_{O_2} W_{O_2}} \tag{4.60}$$

When using the soot combustion rate in calculation of the reaction heat, recall that regeneration only occurs in the inlet channels, due to the absence of soot loading on the outlet channel walls. Combustion in this manner results in additional mass within the wall and soot layers, which early formulations choose to neglect while writing oxidation as a function of soot thickness [47, 48, 121, 134, 136, 137, 142, 143]. An alternative approach uses a mass basis to account for the source component in the soot mass equation [105, 138, 144-146]. Using this technique, the reaction heat term becomes:

$$\dot{Q}_{reac} = -\left(\frac{N_c}{2}\right)\left(\frac{m_d \Delta H_{reac}}{\rho_d W_{C_{(s)}}}\right)\dot{S}_{C_{(s)}} \tag{4.61}$$

where the soot mass per unit length and heat of reaction are m_d and ΔH_{reac} respectively. The heat of reaction (or enthalpy or reaction) represents the change in enthalpy between the products

and reactants. For soot combustion, the reaction is exothermic and, therefore, the heat of reaction is negative.

4.2.6 Soot Particulate Mass Equation

Changes in soot layer thickness associated with combustion of particulate matter must consider two effects. The first is PM collection (ς), which increases the soot layer thickness as soot particles accumulate on the inlet channel surfaces. Acting opposed to PM collection is the aforementioned soot oxidation, where combustion of stored PM results in decreased soot thickness. To ensure dimensional agreement, the overall soot combustion rate can be divided by the soot density to provide the inverse soot combustion time scale (χ):

$$\chi = \frac{S_p \rho_s Y_{s,O_2} k_{O_2} W_{C_{(s)}}}{\alpha_{O_2} W_{O_2} \rho_d} \tag{4.62}$$

Both of these effects are considered in the soot mass on the surface per unit length differential equation:

$$\frac{\partial m_d}{\partial t} = \varsigma - \chi m_d \tag{4.63}$$

However, the current study neglects the soot collection term.

4.3 Solver Formulation

One strategy for developing a complete DPF model is formulating a series of progressively complex virtual experiments, where each result compares to those found in the historical literature. This model validation procedure is similar to Depcik and Assanis [49], differing only by the development of two separate solvers for solution of the governing equations within the channels. Section 4.4 details each of the validation efforts, while this section describes the solution techniques in the channels and wall, boundary conditions, and overall layout of the solvers.

4.3.1 Solution of Channel Equations

The traditional DPF system of equations for the inlet and outlet channels consists of both differential and algebraic equations; hence, known as Differential Algebraic Equations (DAE's). The method of solution for DAE's is strongly dependent on whether the set of equations is semi-explicit or fully-implicit [147]. An example of a semi-explicit system is the Robertson problem, given as a prolog to LSODI [148]. The Robertson problem can also be written in fully-implicit DAE form, and modeling of electrical circuits often leads to fully-implicit DAE systems. This distinction arises because the derivative (y') can be separated from the variable (y) terms in semi-explicit systems,

$$M(t)y' = f(t, y) \tag{4.64}$$

while that arrangement cannot be performed in fully-implicit systems:

$$0 = G(t, y, y') \tag{4.65}$$

The DAE set forms shown represent the independent variable as t and the dependent variable vector as y with both M and G involving square vectors with the dimensions of y [147].

Popular codes known as DASSL and LSODI do exist for solution of semi-explicit and fully-implicit DAE's; however, these methods are not implemented since they must be interfaced with MATLAB in this work. Performing this interface requires implementation of a SLICOT library to allow use of Fortran 77 algorithms. Since future adaptations of the model may take place in the Simulink environment with coupling to a virtual engine [149], this interfacing would add unwanted complexity.

Instead, two methods are developed to solve the inlet and outlet channel sets within MATLAB. The first method requires the use of Eq. (4.44) in order to create a system of Ordinary Differential Equations (ODE's) and uses the MATLAB ODE solver ode15s in order to integrate.

The method of transforming a DAE system to a system of ODEs by differentiating the algebraic equation is a common procedure for numerical integration of DAE sets [150]. The function ode15s is preferable over other available solvers, such as ode23 and ode45, since ode15s allows parameterization of the function,

$$f(t, y, \Pi) = 0 \tag{4.66}$$

while other solvers only allow

$$y' = f(t, y) \tag{4.67}$$

In the previous equations, Π is a vector of parameters while t is the independent variable and y the dependent variable [151]. By looking specifically at the channel momentum equations, Eq.'s (4.19)-(4.20), it becomes apparent that the form of Eq. (4.67) is not achievable for the equation sets and therefore the ODE model must use ode15s. Said another way, the derivatives (y') can not be separated from the variable (y) terms.

The second method took advantage of the ability of the MATLAB routine ode15i in order to solve index 1 DAEs (introduced in 1999). To be clear, the index is the number of differentiations required to create a non-singular derivative coefficient matrix and eliminate all algebraic constraints. In the DPF channel equation sets, the DAE's are index 1. Since the ode15i solver can directly evaluate a DAE system, the ideal gas law derivatives are not included. As its name indicates, this solver is capable of solving equations written in implicit form. However, the ode15i feature was not originally designed for solving fully-implicit DAE systems and failures have been documented [150]. Therefore, the ode15s solver corroborates the findings of the ode15i solver, in addition to providing researchers an alternative method for solving the channel DAE's not seen in DPF literature.

4.3.2 Solution of Wall Equations

An important qualitative difference exists between the one component and two component schemes for obtaining the properties within. In the first case, direct solution of the wall parameters is possible using Eq.'s (4.29)-(4.31), (4.43). Alternatively, the two component technique requires an iterative scheme to solve Eq.'s (4.25)-(4.28), (4.31), (4.43). This contrast leads to a design choice on the part of the researcher; using the one component method for decreased computational burden or opting for the two component version to achieve improved accuracy.

Since the wall pressure is immediately available in the one component scheme using Eq. (4.29) and the wall temperature equates to the filter temperature, the wall density can be determined using Eq. (4.43). These two calculations fix the thermodynamic state of the wall-flow and allows the wall velocity to be found using Eq. (4.30). Such an approach is not possible in the two wall velocity scheme since none of the applicable equations depend solely on known values. This requires generation of initial guesses for the soot and wall parameters to be refined by a rootfinding function. Furthermore, the use of REFPROP for property values in Eq.'s (4.25)-(4.26) introduces nonlinearity, preventing the use of matrix methods. Therefore, the MATLAB function 'fzero' for rootfinding of nonlinear systems of equations must be implemented. However, an alternative approach using the previous time step's soot and wall viscosities is chosen in the current model to directly solve the wall-flow equations.

4.3.3 Boundary Conditions

While the channel and wall solvers differ significantly between the validation efforts, the boundary conditions remain constant. Exhaust properties entering the inlet channels are specified, whether as experimental measurements or exit values from a computer model of an

upstream engine or aftertreatment device. Some efforts consider the flow expansion from the exhaust pipe to the inlet channels; however, that contribution is often ignored. At the opposite end of the inlet channel, the axial velocity reduces to zero as the flow encounters a wall:

$$w_I|_{z=L} = 0 \tag{4.68}$$

where L is the channel length. Depending on the state variables utilized, this imposes a null value on the dummy variable (G_I) or the mass flow rate ($\dot{m}_I$).

At the beginning of the exit channel, two values are immediately known. The first is physically obvious in a similar manner as the velocity at the end of the inlet channel; the outlet channel velocity begins as zero by the stagnation condition.

$$w_{II}|_{z=0} = 0 \tag{4.69}$$

This also produces the same effect on the state variables for flow. A second quantity is available as a result of a method of characteristics analysis at the outlet channel boundary, with contributions from the wall-flow and the neighboring axial location in the outlet channel. Derivation of this expression for temperature at $z=0$ in the outlet channel begins with a governing equation from [106, 152] and generates the relationship:

$$T_{II}|_{z=0} = T_w - \frac{\rho_w u_w}{h_g}(h_{II} - h_w) \tag{4.70}$$

At the end of the outlet channel, if the DPF is the last aftertreatment device present, the pressure should correspond to the ambient: however, many researchers instead assign this value from integrating the outlet channel momentum equation.

The filter wall temperature equation also requires boundary conditions when using the central difference scheme to approximate the second order derivative associated with axial conduction. In this context, DPF models often impose insulated boundaries at both axial extremes of the DPF.

$$\frac{\partial T_w}{\partial z}\Big|_{z=0} = \frac{\partial T_w}{\partial z}\Big|_{z=L} = 0 \qquad\qquad (4.71)$$

By extension, these filter wall boundary conditions are applied to the soot layer, since the current formulation calculates the temperature of both layers simultaneously.

4.3.4 Layout of Solvers

Within the validation experiments there are instances where a less elaborate code is sufficient; such as the steady-state isothermal case where time-stepping is unnecessary and heat accumulation in the wall is ignored. However, these scenarios can also be represented by zeroing certain values in a complete DPF model. For this reason, the arrangement of the final DPF model is described here and the alterations required for simpler studies are listed in the respective model validation sections.

As with any transient simulation, initial values are given to all the gaseous and solid phase variables. This includes assigning ambient temperatures to the wall and soot layers, while the exhaust gas in the channels and wall receive reasonable quantities. The adopted method of integrating the filter energy equation is the forward-time centered space method [153]. Since the temperature at each axial location becomes a function of thermodynamic properties at the previous time, direct calculation at each node is possible. As mentioned previously, the filter temperature can then be assigned to the physical soot layer as well as the exhaust gas within the soot and wall layers.

After loading all the inlet conditions, an iterative procedure must be incorporated due to the unknown outlet channel pressure at $z=0$. The first iteration requires a guess for this pressure, while subsequent calculations receive a revised guess from a Newton-Raphson scheme. In the two wall velocity version, a solution is reached when Eq. (4.68) is satisfied. Physically, this means a single outlet channel pressure value will result in stagnation at the inlet channel

106

boundary *z=L*. Once the initial guess is loaded into the solver, the outlet channel conditions at

z=0 can be calculated, allowing calculation of the soot and wall parameters at the same location.

Using these wall values, a channel solver integrates the governing equations in both channels

axially to the next node, beginning a repetitive process that concludes at *z=L*. At a significant

computational cost, the wall solver can also update during the channel solver integration, an

option that is recommended when accuracy is critical.

To be clear, the procedure thus far has calculated all the wall temperatures at the new

time and used these values to obtain thermodynamic properties throughout the DPF. However,

there is no guarantee of inlet channel stagnation since an outlet channel pressure at *z*=0 guess

preceded these calculations. Thus, the Newton-Raphson scheme examines the supplied pressure

and if necessary generates a revised guess. In doing so, the numerical procedure considers the

influence of changing the outlet channel pressure at *z*=0 on the mass flow rate at *z=L* of the inlet

channel using the equation:

$$p_{II,new}|_{z=0} = p_{II}|_{z=0} - \frac{\dot{m}_I|_{z=L}}{\frac{\partial \dot{m}_I|_{z=L}}{\partial p_{II}|_{z=0}}} \qquad (4.72)$$

It is clear from this expression that a correct outlet channel pressure guess is unchanged by the

Newton-Raphson scheme, allowing the simulation to proceed in another time step. For clarity, a

schematic of the DPF model layout is included in Figure 31.
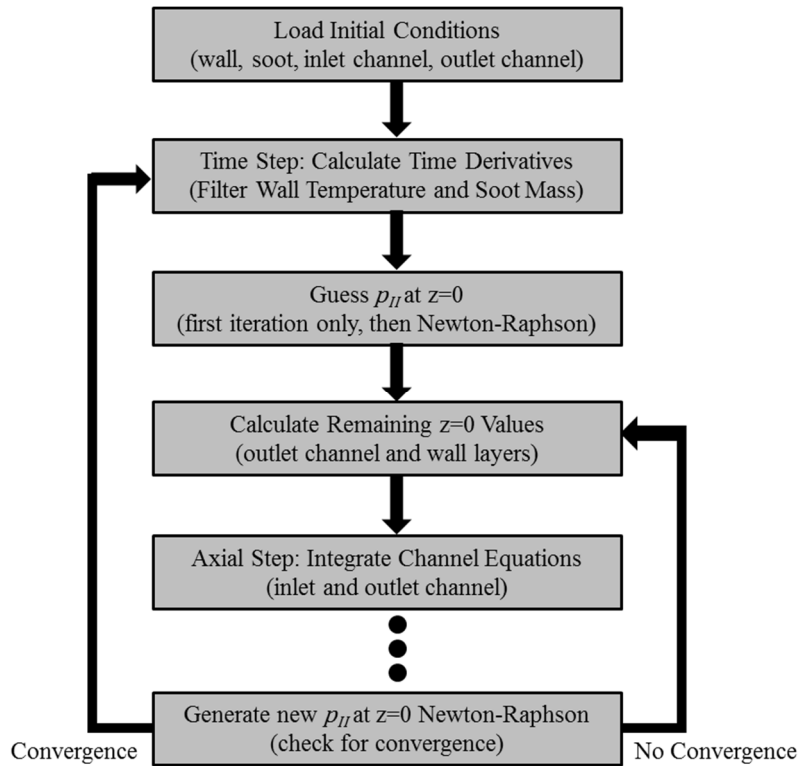
Figure 31: Schematic of solver layout

4.4 Model Validation

As mentioned previously, efforts to corroborate the current model begin by simulating simpler flow scenarios and later include more complex physical phenomena. The first step confirms that the two channel solvers, the version solving the traditional DAE's (ode15i) and the unique ODE system (ode15s), produce the same channel profiles. In doing so, a new modeling tool is available to DPF researchers. At the same time, comparison of the ode15i model to published results for a simple no soot and isothermal case validates both solvers.

Expanding on the isothermal simulation to incorporate the filter energy equation and transient inlet conditions provides a warm up simulation. By including a soot layer on the surface, the model considers three important physical phenomena not present in the no soot isothermal run. Following the warm up simulation is a cool down oxidation test, which simulates the thermal response of the monolith during regeneration of a portion of the soot stored on the

porous wall surface. Each of the three validation efforts described resemble the procedure adopted by Depcik and Assanis [49].

4.4.1 No Soot Isothermal Case

In order to validate the two channel equation solvers, each model uses a constant wall temperature (632.18 K), an artificially imposed inlet temperature (800 K), and simulates the exhaust as nitrogen gas. Constant parameters and boundary conditions found in Table 7 are used to facilitate comparisons to Depcik and Assanis [49].

Table 7: Isothermal no soot constants for solver comparison

Variable	Value	Variable	Value
Inlet Velocity	24.8 m s^{-1}	Inlet Pressure	1.0132 bars
EX-80 Permeability	2E-13 m^2	EX-80 Forscheimer	5E8 m^{-1}
Channel Diameter	2.11 mm	Channel Length	12 in.
Wall Thickness	0.432 mm	DPF diameter	5.66 in.
Cell Density	100 cells in^{-2}	Substrate Density	1300 kg m^{-3}
Pore Diameter	12 μm	Substrate Thermal Conductivity	0.5 W m^{-1} K^{-1}
Substrate Specific Heat	600 J kg^{-1} K^{-1}	Porosity	50%
Total Mass Flow Rate	0.075 kg s^{-1}	Inlet Temperature	800 K
Number of Cells	2516		

In addition to the constant values above, the model requires thermodynamic properties of the exhaust gas; such as thermal conductivity, dynamic viscosity, and specific heat at constant pressure. These property determinations result from external calls by MATLAB to REFPROP.

Due to the absence of soot, the isothermal model uses the one component model governing equations in the channels and wall. However, this technique still follows the steps of Figure 31 with the exceptions of using steady-state conditions and not calculating a wall temperature profile, which is held at 632.18 K for all axial locations.

To determine the relative agreement of the ode15i and ode15s formulations, the validation mechanism involves comparisons between the channel and wall variable profiles. In the original publication associated with these profiles, additional assumptions of identical mass

flow at each axial location, simplified thermodynamic property calculations, and a simplified

version of the heat transfer coefficient (using *Nu*=2.71) are imposed. Figure 32 through Figure

36 demonstrate that the models produce nearly identical results.
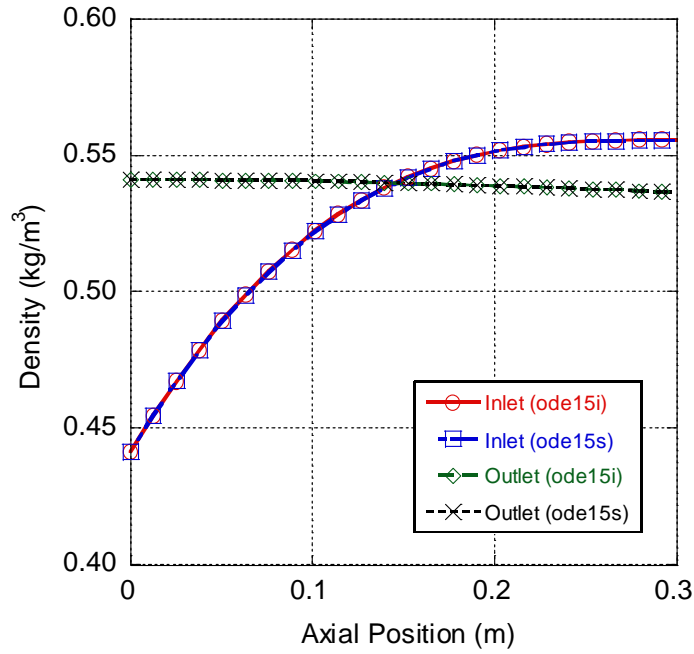
Figure 32: Axial profiles of channel densities for solver comparison
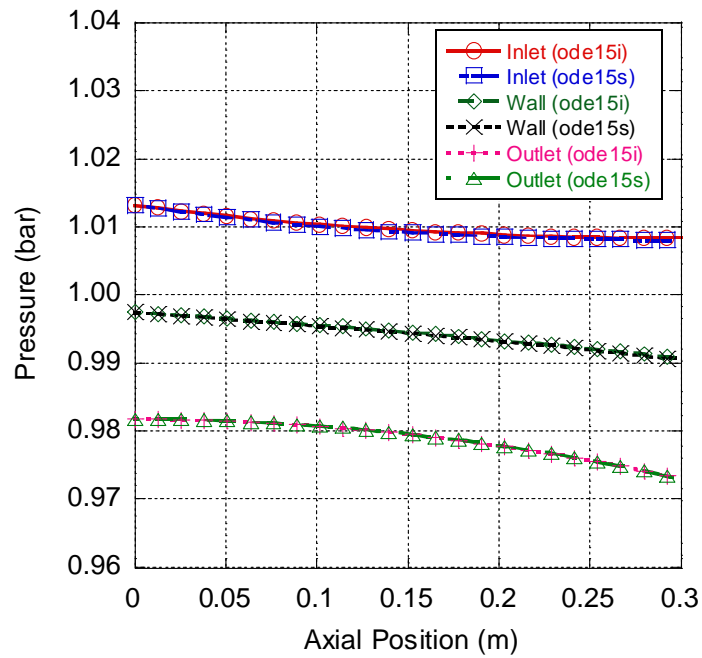
Figure 33: Axial profiles of pressures for channel comparison
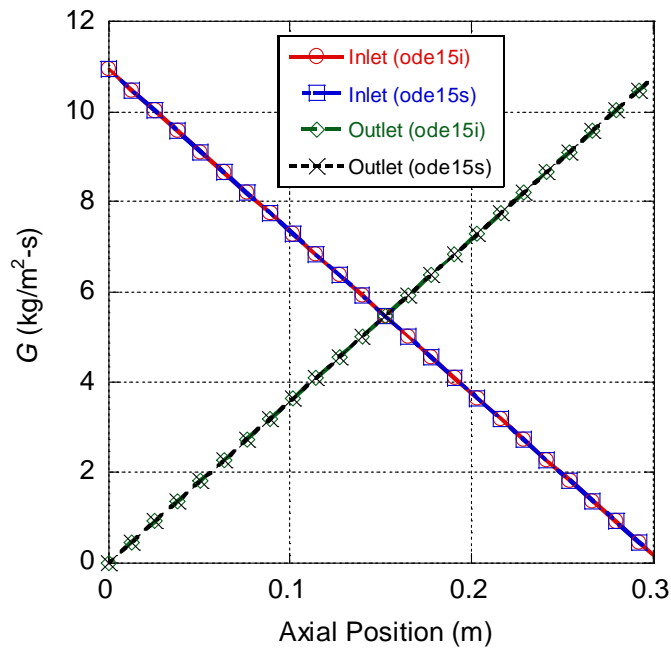
Figure 34: Axial profiles of channel density*velocity (*G*) for model comparison
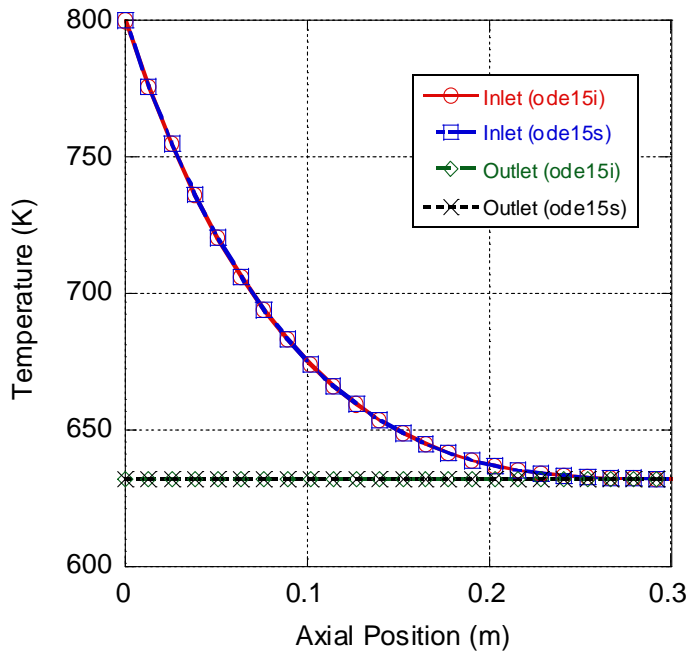
Figure 35: Axial profiles of channel temperatures for model comparison
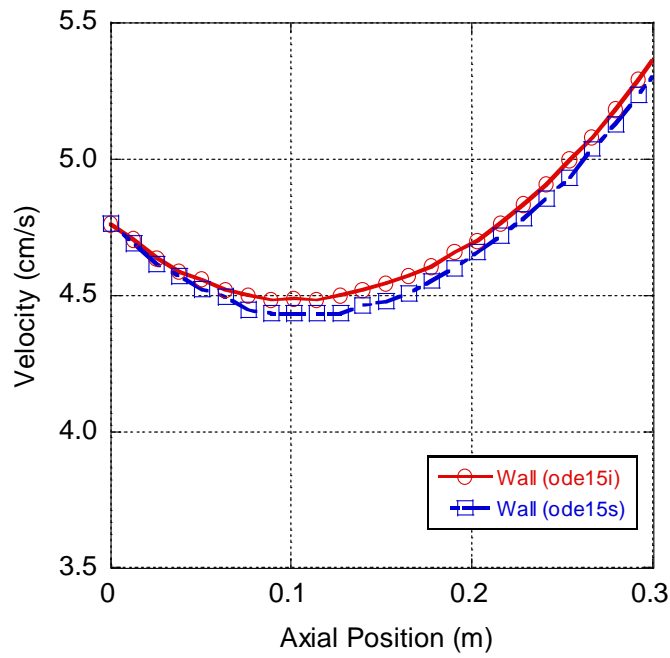
Figure 36: Wall velocity profiles for model comparison

While the agreement between the ode15i and ode15s models is evident in the figures above, further confirmation can be provided by checking the algebraic constraint equation. By plotting the left and right hand sides of Eq. (4.43), as shown by Figure 37, the accuracy of the ode15s model's ideal gas law integration becomes apparent.
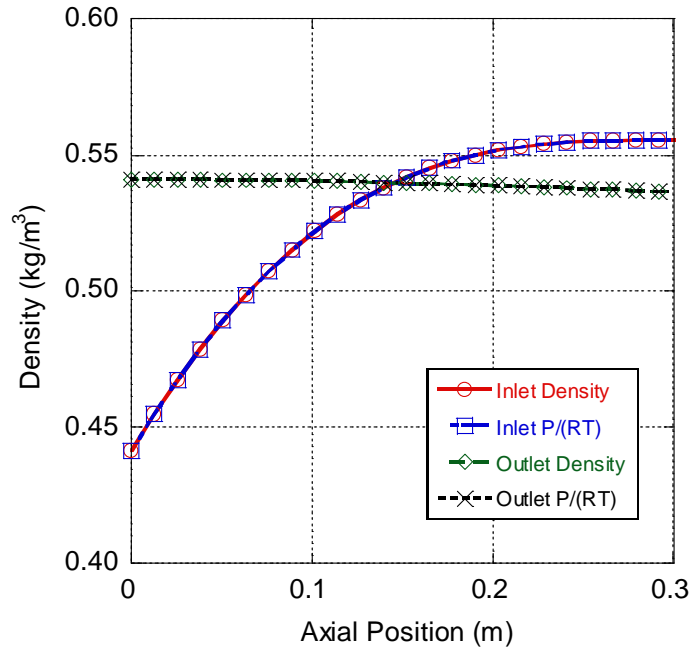
Figure 37: Validation of use of derivative of ideal gas law in ode15s model

The degree of agreement between the ode15i and ode15s models confirms that solution

via transformation of DAE's to ODE's is possible for the DPF governing equations, a procedure

not found in the historical DPF literature. By producing the same results for the two approaches,

future authors have a valuable tool that can be used to check for the potential failures in solving

fully-implicit DAE sets as noted by Shampine [150].

In order to compare the computational burden of the two solvers, the stopwatch feature of

MATLAB is available. Studies of the relative run times using the modeling scenario above

reveal the ode15s solver requires around 40% more time in order to solve the inlet and outlet

channel equations (see Table 8). The simulations presently described used an Altec desktop

computer, operating Windows Vista, with an Intel Xeon processor and 8GB of RAM.

Table 8: Computational comparison of solvers

Solver	Average (s)	Standard Deviation (s)
ode15i	0.164	0.004
ode15s	0.232	0.002

While it is clear the ode15s solver is less efficient for the present study, further investigation into the relative computational burden across different error tolerances and using the complete heat transfer correlation would provide additional insight. Before validating both models by comparison with published results, another preliminary result of the DPF publication [132] deserves attention.

An important factor in predicting the wall-flow of a DPF is the permeability, which is one of the parameters appearing in Darcy's law to relate the wall pressure drop to the average velocity. The model validation efforts described here use manufacturer provided permeabilities; however, several notable permeability models exist in different disciplines. For a comparison of the different physical effects included in each respective permeability models and presentation of each model's predicted pressure drop in the flow scenario above, the reader should consult [132].

Following establishment of the result similarity between the two models, comparison of a related modeling effort to literature values confirms the channel and wall solvers. As an isothermal no soot simulation, the channel inlet temperature and physical wall are held at 632.18K. With the exceptions of the inlet temperature and pressure, all the parameter values are consistent with Table 7. In order to facilitate comparison with [49], the inlet pressure imposed is 1.0119 bars, since Depcik accounts for property changes before the flow reaches the inlet channels. Of interest, the heat transfer correlation is irrelevant here due to the absence of temperature differences.

Again using the one component model since no soot layer is present within the inlet channel, the ode15i model produces the following results, presented alongside values supplied by Depcik and Assanis.
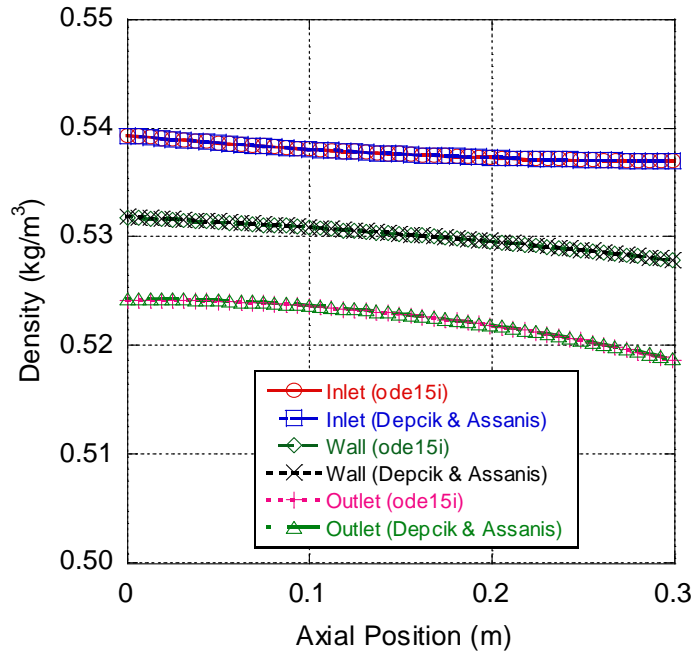
Figure 38: Density comparison with literature values
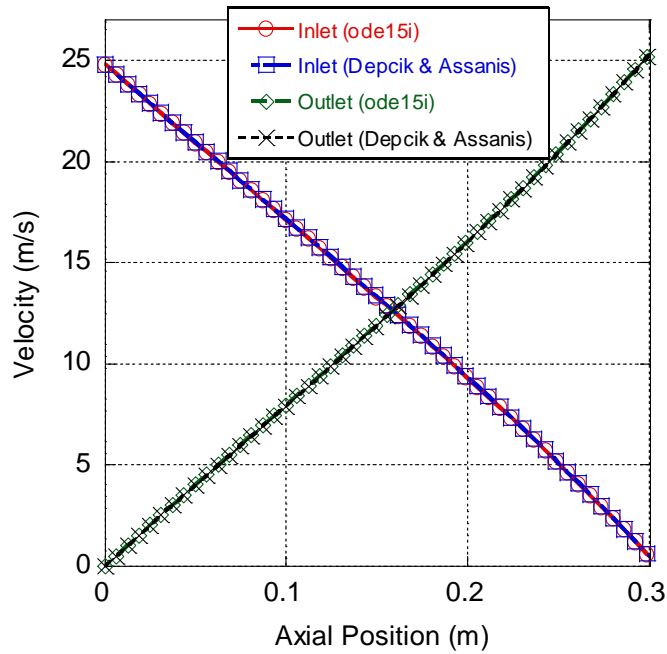

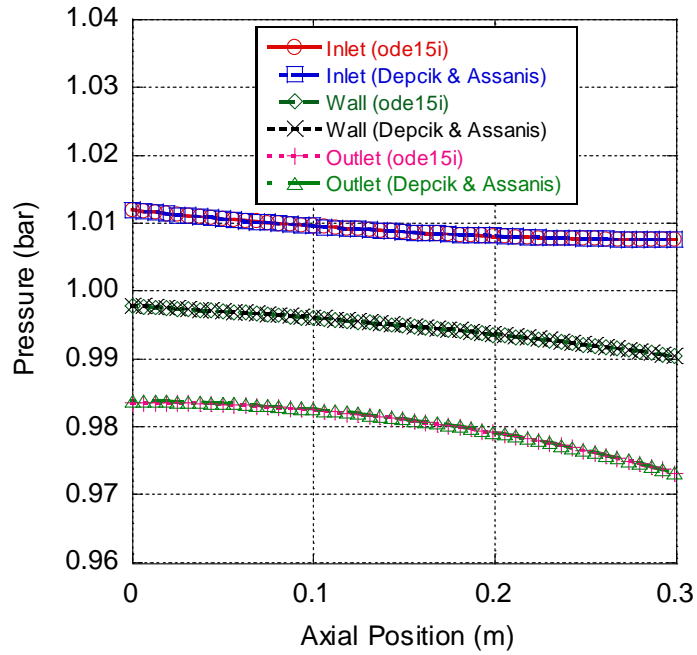**Figure 39: Velocity comparison with literature values**

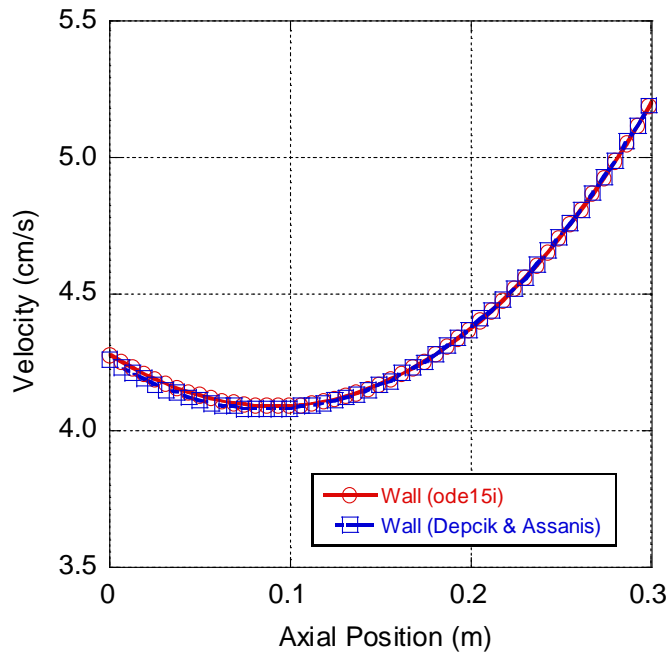**Figure 40: Pressure comparison with literature values**

Figure 41: Wall velocity comparison with literature values

4.4.2 Warm Up Case

Expanding on the no soot isothermal case, a simulation using the inlet conditions of

Young et al. [154] considers several previously ignored aspects of DPF modeling. First, Young

et al.'s inlet parameters are variable since the inlet temperature increases over time. This demands the implementation of the forward-time centered-space method described in Section 4.3.4. The warm up model must also consider a specified amount of soot present in the inlet channels, presumed to be uniformly loaded in the axial direction. For this reason, the warm up model uses the two component method and the set of channel equations featuring the mass flow rate as a state variable.

The filter temperature equation also contributes, considering each of the heat transfer mechanisms to determine the change in filter temperature over time. However, regeneration is intentionally prevented by specifying that the inlet flow contains only nitrogen gas (N_2). In the absence of oxygen, simulations using this inert species show the gas dynamics outside the regenerative event, allowing validation of the soot oxidation equation in a separate experiment. Besides the varying inlet conditions and soot loading, other parameters of the warm up model differ from the no soot isothermal case. Table 9 shows the relevant values for use in the warm up case study:

Table 9: Parameters for warm up, cool down, and oxidation simulations

Variable	Value	Variable	Value
Cell Density	28 cells cm^{-2}	Wall Thickness	0.43 mm
Wall Thermal Conductivity	15 W m^{-1} K^{-1}	Bulk Density	0.76 g cm^{-3}
DPF Diameter	144 mm	DPF length	150 mm
Particulate Thermal Conductivity	2 W m^{-1} K^{-1}	Particulate Specific Heat	889 J kg^{-1} K^{-1}
Pore Diameter	8 μm	Monolith Type	B-Silicon Carbide
Porosity	41%	Cell Diameter	1.46 mm
Number of Cells	4560	Substrate Specific Heat	1025 J kg^{-1} K^{-1}
Substrate Density	1885 kg m^{-3}	Particulate Density	75 kg m^{-3}
Particulate Permeability	5.10E-14 m^2	SiC Loaded Permeability	1.70E-13 m^2
SiC Empty Permeability	3.00E-13 m^2		
Young et al. Warm up			
Volumetric Flow Rate	1500 l min^{-1}	Mass Flow Rate	0.296 kg s^{-1}
Deposit Loading	37.11 g	Inlet Pressure	1.0132 bars
Young et al. Cool down and Oxidation			
Volumetric Flow Rate	700 l min^{-1}	Mass Flow Rate	0.0138 kg s^{-1}
Inlet O$_2$ After 40 s	18%	Inlet Pressure	1.0132 bars

Similar to the no soot isothermal case, all thermodynamic property calculations stem from REFPROP. Following the loading of Young et al.'s input data from an external file, the warm up simulation occurs over a period of 250 s following the solver layout of Figure 31. Results from the present simulation are compared with experimental data from Young et al. [154] and published results of Depcik and Assanis [49].
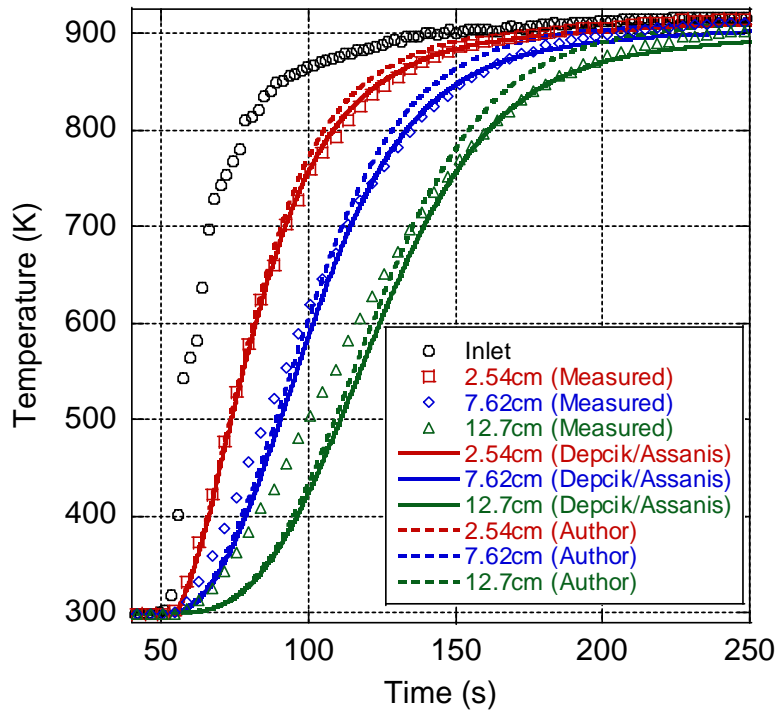
Figure 42: Warm up simulation result comparison with experimental and measured values

As shown by Figure 42, simulation results resemble both the experimental data of Young et al. and the simulation effort of Depcik and Assanis, with larger deviations present at downstream axial locations. The increased discrepancies away from the entrance of the DPF are explained by considering the integration along the channels beginning at z=0, where the upstream locations are in closer proximity to specified flow conditions.

Several sources may contribute to the differences between measured and simulated filter temperatures; including pulsating flow, variations in soot layer thickness, and multi-dimensional

effects. However, any increase in accuracy from extension to multi-dimensional and multi-channel modeling is burdened by significant computational expense. The relatively small differences between the current simulation and the published results of Depcik and Assanis are explained by variations in solvers, thermodynamic property calculations, and wall pressure drop expressions. Overall, the current warm up model predictions are relatively accurate with respect to experimental data and correlate well with other published models.

4.4.3 Cool Down Oxidation Case

The final DPF model validation exercise is the cool down oxidation test. As the title suggests, the simulation occurs over a period where the exhaust gas temperature undergoes a significant decrease while soot oxidation occurs. This approach examines the predicted regeneration of the filter, while accounting for the combustion heat generation and soot layer thickness changes. To create an opportunity for soot combustion, the exhaust gas considered contains 18% oxygen and 82% nitrogen, by mass fraction. By using these species instead of purely nitrogen gas, an appropriate amount of oxidant is available to facilitate the desired chemical reaction.

A number of parameters that are specific to the cool down oxidation test are shown in Table 9, while the Arrhenius and combustion rate expressions require additional specifications. These include an activation energy of 125 kJ/mol [155], a specific surface area of soot of 5.5E7 m^{-1}, and a partial oxidation factor of 0.72 that represents the middle of the range of values found in the literature (0.55-0.9) [49]. Due to variations in sensible enthalpy associated with temperature changes during the cool down oxidation simulation, the heat of reaction varies with time. However, this effect is small in comparison to the magnitude of the heat of reaction, which allows this parameter to be held constant at an average value (-237.5 kJ/mol) without introducing

significant error or computational expense. In an effort to match the stated 54.7% conversion rate of Young's cool down oxidation test, the simulation uses a pre-exponential constant of 0.00272 $m \cdot K^{-1} \cdot s^{-1}$.
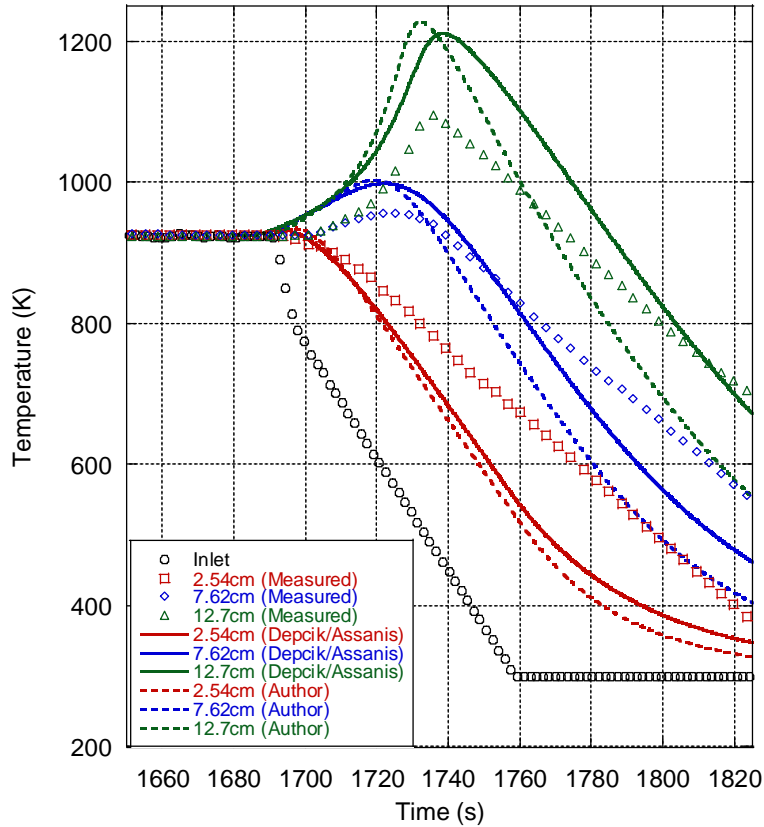
Figure 43: Result comparison for cool down oxidation simulation

Results of the cool down oxidation simulation are compared to both experimental and literature results [49] in Figure 43. Presently, the author's model predicts a regeneration of 54.94% of the filter cake layer's mass, which is comparable to the target of 55%. As discussed prior, the variations in solvers, thermodynamic property calculations, and wall pressure drop expressions between the author's model and Depcik's version largely account for the difference in the pre-exponential constant value (0.00272 $m \cdot K^{-1} \cdot s^{-1}$ instead of 0.0024 $m \cdot K^{-1} \cdot s^{-1}$). For the purposes of this effort, the results illustrate the successful incorporation of exothermic soot

combustion reactions into the model solver paving the way for subsequent efforts including simultaneous DPFHX regeneration and WHR.

Chapter 5

Diesel Particulate Filter Heat Exchanger Concept

5.1 Introduction

The original DPFHX concept is based on the shell-and-tube heat exchanger geometry, where enlarged tubes contain DPF cores, allowing waste heat recovery from engine exhaust and allowing further energy capture from the exothermic PM regeneration event. Subsequently, the heat transferred to the working fluid on the shell side of the DPFHX becomes available for use in a secondary power cycle, which is an increasingly attractive method of boosting powertrain efficiency due to fuel savings of around 10 to 15%. Since the shell side of the DPFHX represents a commonly studied portion of a shell-and-tube heat exchanger, heat transfer performance estimates are possible from previous efforts. However, the heat transfer rates occurring inside the tubes with the DPF cores installed is unknown, and valuable insights are possible through DPFHX modeling in Chapter 7.

This chapter describes the DPFHX concept, including the heat transfer mechanism, materials, design tradeoffs, and impact on emissions. To recall the initial DPFHX design and DPF core positioning, the reader may consult Figure 44. In this rendering, the DPF cores are brown and exist within the dark gray tubes (numbering four in Figure 44).
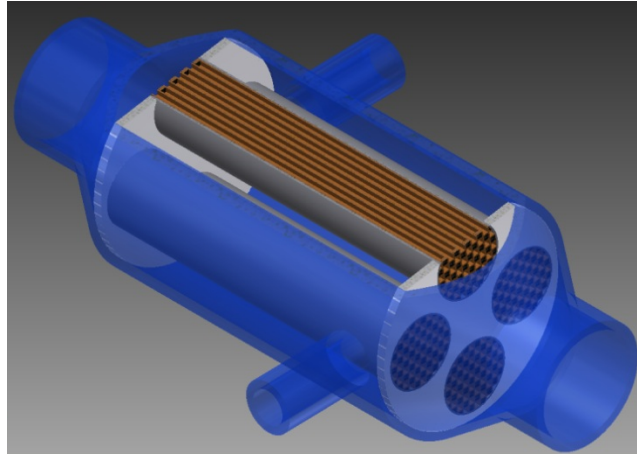
Figure 44: DPFHX concept based on shell and tube geometry

The envisioned design would be scalable to different engine sizes, with the shell size and number of tubes increasing proportionally with engine size. There are two primary materials for the DPF cores, cordierite and silicon carbide. Chapter 7 will explore the selection of a DPF core material in depth, as well as the choice of DPF core size. The shell itself, along with the tubes and plates, will be constructed from a non-corrosive metal, such as stainless steel, and be sized to tightly contain all the DPF cores. Final material selection and tube wall thickness specification should occur after designing the waste heat recovery cycle, as the materials should be compatible with the chosen working fluid and the structure (shell, tubes, and plates) must sustain the working pressure of the fluid. Since the DPFHX will serve as the secondary cycle's evaporator, the device falls on the high pressure side of the WHR system, emphasizing the need to consider operating pressures while designing the device.

5.2 DPFHX-WHR Concept Fundamentals and Heat Transfer

In order to properly discuss the DPFHX concept, a fundamental thermofluid analysis is necessary. This description of the DPFHX's operation, in combination with the previously discussed research on organic Rankine cycles (see Chapter 3 and [1, 14]), also provides context

to the DPFHX within a diesel engine aftertreatment system. To facilitate the explanation, Figure 6 is being repeated here as a reference for the reader.
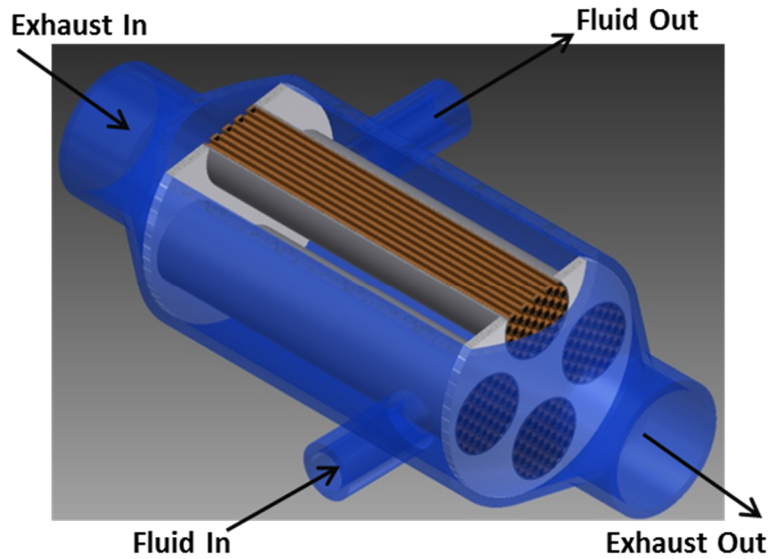
Figure 45: Section view of theorized DPFHX concept (repeated from Ch. 1)

Derivation of the first law energy balance for the DPFHX results from modification of the general expression below:

$$\dot{Q} - \dot{W} = \frac{dE_{cv}}{dt} + \sum \dot{m}_{out}\,(h + ke + pe)_{out} - \sum \dot{m}_{in}\,(h + ke + pe)_{in} \qquad (5.1)$$

where $\dot{Q}$ is the rate of heat transfer across control surfaces, $\dot{W}$ is power, $\frac{dE_{cv}}{dt}$ is the rate of change of energy in the control volume, $\dot{m}$ is mass flow rate, h is specific enthalpy, ke is specific kinetic energy, and pe is specific potential energy. Not surprisingly, the subscripts '*in*' and '*out*' refer to flows entering and exiting the control volume, respectively. In application, the obvious choice for the control volume is the shell (shown blue in Figure 45).

The next step is identification of negligible terms, beginning with power, since the DPFHX has neither work input nor output. Also on the left hand side, the heat transfer term becomes nullified by making the assumption of an insulated DPFHX for simplicity. In addition, all laboratory tests occur under steady-state conditions, allowing exclusion of the energy

derivative. Lastly, small changes in potential and kinetic energy relative to the changes in enthalpy allow these terms to be omitted, resulting in the following equation:

$$0 = \sum \dot{m}_{out}\, h_{out} - \sum \dot{m}_{in}\, h_{in} \tag{5.2}$$

Going further, the four instances of flow across control surfaces (see Figure 45) comprise the summation terms, where the subscripts '*ex*' and '*wf*' refer to engine exhaust and working fluid flows, respectively:

$$\dot{m}_{ex}\left(h_{ex,in} - h_{ex,out}\right) = \dot{m}_{wf}\left(h_{wf,out} - h_{wf,in}\right) \tag{5.3}$$

To achieve the expression above, the steady-state continuity equations must also be applied, which equate the inlet and outlet mass flow rates of the exhaust, as well as the working fluid. This control volume analysis represents a 'black box' approach to studying the DPFHX, so further insight results from a heat transfer model. Such an effort requires understanding the heat transfer mechanism through examination of the DPFHX geometry (see Figure 46).
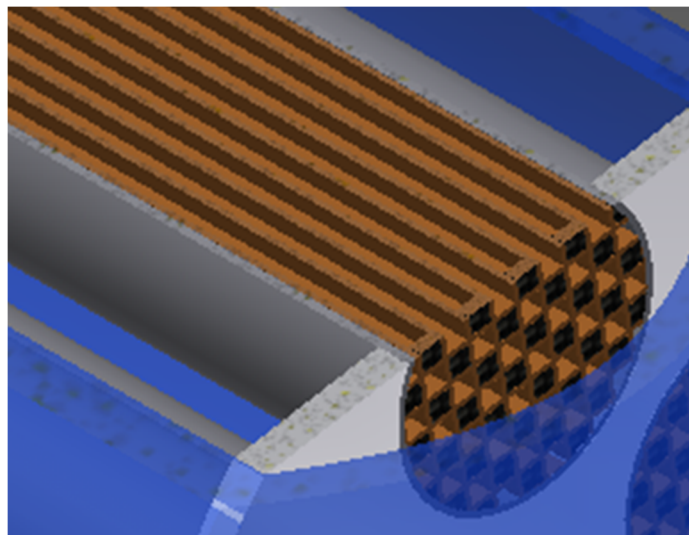
Figure 46: Detail view of the DPFHX highlighting stages of the heat transfer mechanism

Heat transfer from the exhaust gas to the interior of the tubes (dark gray) can occur following three pathways. The first method is direct convection between the flowing gas and the tube, which is present only in the outermost DPF channels (of note, these channels are on the

order of 1 mm in width and height). An alternative avenue for heating the tubes uses the intermediate of the DPF core (brown), where convection from the exhaust gas to the core occurs in the channels and porous wall, preceding conduction to the tube interior. Radial conduction from the tube interior to the tube exterior is the next heat transfer process, and presumably occurs rather efficiently for metal tubes. As heat reaches the extent of the DPF cores, a thermal joint with a thermal contact resistance is present between the DPF core and the tubes. Finally, the working fluid contained between the DPFHX outer wall (blue) and the DPFHX inner tubes (dark gray) convects heat from the exterior of the tubes.

This exterior convection causes significant thermal resistance in areas of the DPFHX where the ORC working fluid is in the liquid phase with much less resistance occurring if the working fluid is boiling (i.e., the convective heat transfer coefficient for a boiling working fluid is significantly higher) [95]. Thus, heat transfer from the exhaust to the tube interior should be the predominant thermal resistance when the ORC working fluid is boiling. Whereas, liquid convection may be comparable to recovery within the tubes elsewise, due to similar coefficients for heat transfer aided by the DPF cores and slow ORC fluid flow. In a final commercial design, heat transfer enhancing techniques, such as finned tubes, could be incorporated to increase the heat transfer coefficient. Also, complex flow structures may be present through the use of baffling. Further clarification of the specific heat transfer pathways within the DPFHX is possible by examining the heat transfer resistor network of Figure 47. Of interest, Figure 47 excludes radiative heat transfer by citing Bissett's observation that "long thin channel walls have similar view factors and should have similar temperatures" [5].
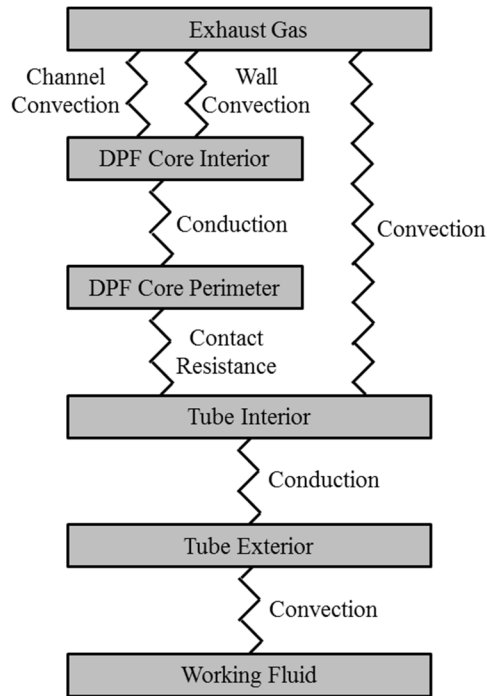
Figure 47: Resistor network illustrating the heat transfer mechanism of a DPFHX

With an understanding of the heat transfer mechanism, construction of a heat transfer model requires selection of an overall framework, which Chapter 3 describes as a decision between the Log-Mean Temperature Difference (LMTD) method and the effectiveness-NTU (Number of Transfer Units) method. For the DPFHX, a primary concern is accounting for working fluid phase changes, which can significantly influence the rate of heat transfer. While the effectiveness-NTU method can incorporate this effect, assignment of different heat transfer coefficients is easily accomplished through the use of a multiple zone LMTD scheme. Either method will also work in laboratory testing, since both inlet or outlet measurements are achievable.

To incorporate a LMTD heat transfer model into the first law analysis above, the standard form for the heat transfer rate below provides a starting point:

$$\dot{Q} = UA\Delta T_{MEAN} \tag{5.4}$$

where U represents the overall heat transfer coefficient, A is the heat transfer area, and ΔT_{MEAN} is the average temperature difference. Calculation of the overall heat transfer coefficient requires combination of each step in the aforementioned heat transfer mechanism, while the heat transfer area is solely dependent on geometry.

For simple counterflow and parallel flow heat exchangers, the average temperature difference is equal to the log mean temperature difference (LMTD). For shell and tube heat exchangers, the average temperature difference comes from a correction factor (F) times the LMTD. To find the average temperature difference, the LMTD comes from the inlet and outlet temperatures of both fluids, through the use of the expression below:

$$\Delta T_{MEAN} = F \Delta T_{LMTD} = F \frac{\Delta T_1 - \Delta T_2}{ln\left(\frac{\Delta T_1}{\Delta T_2}\right)} \tag{5.5}$$

where the subscripts '1' and '2' correspond to the different ends of the DPFHX (or different ends of an individual zone for multi-zone models). When no working fluid phase change occurs, Equations (5.4) and (5.5) comprise a complete heat transfer model. However, when boiling of the working fluid occurs, the model must feature additional heat transfer zones, similar to the ORC work discussed in Ch. 3 and a published effort of the author [14]. For example, Figure 48 shows a two-zone schematic for use with liquid-vapor mixture or saturated vapor working fluid exit conditions, while superheating of the working fluid requires a three-zone model (see Figure 49). Of importance, the bi-directional arrows for the exhaust do not represent reversing flow; rather, the arrow direction depends on whether the flows enter at the same or opposite ends of the device (parallel flow or counter flow, naming simply by flow entrance location instead of the traditional use of parallel and counter as a complete geometric description).
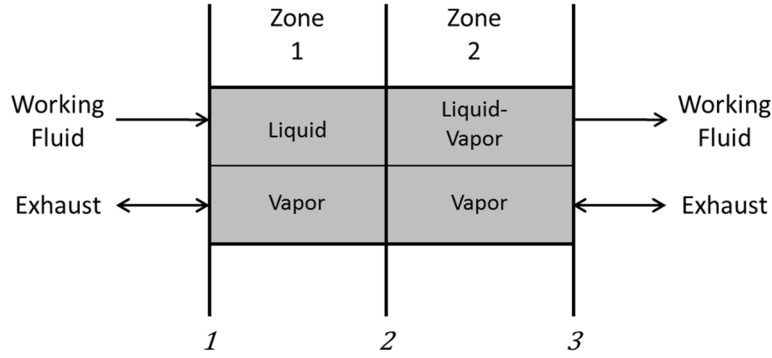
Figure 48: Example of two-zone modeling scheme when the ORC working fluid is leaving the system as a two-phase liquid and vapor or saturated vapor
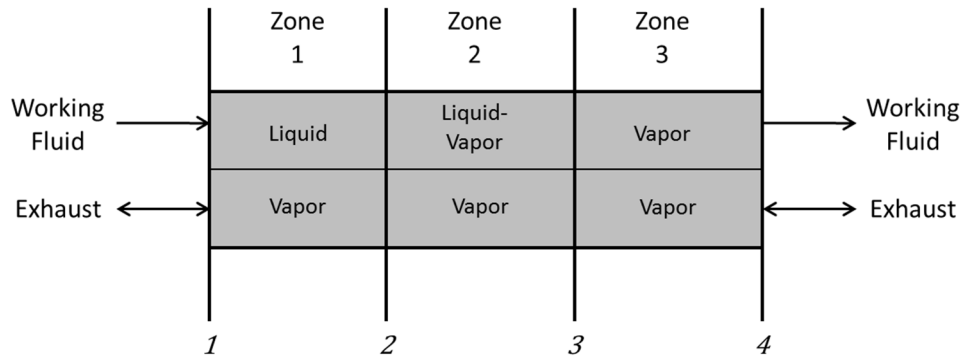
Figure 49: Example of three-zone modeling scheme when the ORC working fluid is leaving the system as a superheated vapor

Expansion of the single-zone LMTD scheme to include phase change effects is relatively straight-forward, requiring application of the single-zone scheme to each additional zone. For clarity, the three-zone LMTD scheme of Figure 49 results in the heat transfer model below:

$$\dot{Q} = U_{12}A_{12}F_{12}\frac{\Delta T_1 - \Delta T_2}{ln\left(\frac{\Delta T_1}{\Delta T_2}\right)} + U_{23}A_{23}F_{23}\frac{\Delta T_2 - \Delta T_3}{ln\left(\frac{\Delta T_2}{\Delta T_3}\right)}$$
$$+ U_{34}A_{34}F_{34}\frac{\Delta T_3 - \Delta T_4}{ln\left(\frac{\Delta T_3}{\Delta T_4}\right)}$$

(5.6)

In this equation, the individual heat transfer areas (A_{12}, A_{23}, and A_{34}) must sum to equal the total DPFHX heat transfer area (A_T), as shown by the following equation:

$$A_{12} + A_{23} + A_{34} = A_T$$

(5.7)

129

Before discussing the overall heat transfer coefficient, further explanation of using a consistent methodology with respect to the heat transfer areas is warranted. Since the overall heat transfer coefficient in each zone is calculated on the basis of a particular type of heat transfer area (e.g., tube exterior areas), both the individual zone areas and the total area are relative to this basis.

In the present case, the exterior tube area ($A_{T,TO}$) provides a viable selection as the heat transfer area basis, because of the complexity of the DPF heat transfer area when the DPF core is installed. Therefore, this choice is presently made as a matter of convenience. While some individual coefficient values vary depending on the working fluid phase, the form shown below applies to all zones of Figure 48 and Figure 49:

$$UA_{T,TO} = \frac{1}{\sum_1^n R_n} = \frac{1}{R_{ex,TI} + R_{TI,TO} + R_{TO,wf}} \tag{5.8}$$

where R stands for thermal resistance. The three resistances present are from the exhaust (*ex*) to the tube interior (*TI*), from the tube interior to tube exterior (*TO*), and the tube exterior to the working fluid (*wf*).

As previously described in Figure 47, the first resistance contains two pathways when the DPF cores are installed. The first is direct convection from perimeter channels to the tube interior, the second is convection to the solid filter followed by conduction to the limit of the DPF core and to the tube interior after overcoming the thermal contact resistance. This thermal resistance could be measured experimentally for a particular DPFHX tube geometry. For the second and third thermal resistances, representing conduction and convection respectively, the standard forms [94] are present:

130

$$UA_{T,TO} = \frac{1}{\sum_1^n R_n} = \frac{1}{\frac{1}{U_{ex,TI}A_{ID}} + \frac{ln(r_{TO}/r_{TI})}{2\pi kL} + \frac{1}{h_{TO,wf}A_{OD}}} \tag{5.9}$$

where h is the convective heat transfer, r is the tube radius, k is the thermal conductivity of the tubes, L is the total tube length, and A is the heat transfer area. The subscripts provide the basis for these areas, with 'ID' and 'OD' representing a basis of inner diameter and outer diameter respectively. As mentioned previously, the thermal resistance is negligible for conduction through the pipes, resulting in the omission of the middle term of Eqn. (5.9) in the final energy equation for a counterflow arrangement:

$$\dot{m}_{ex}(h_{ex,in} - h_{ex,out}) = \dot{m}_{wf}(h_{wf,out} - h_{wf,in})$$

$$= \frac{1}{\frac{1}{U_{ex,TI}A_{ID}} + \frac{1}{h_{TO,wf}A_{OD}}} F \frac{(T_{ex,in} - T_{wf,out}) - (T_{ex,out} - T_{wf,in})}{ln\left(\frac{T_{ex,in} - T_{wf,out}}{T_{ex,out} - T_{wf,in}}\right)} \tag{5.10}$$

In other words, the energy lost from the exhaust flow is equal to the energy gained from the ORC working fluid (when the device is assumed to be adiabatic), which can be measured using the LMTD method including the heat transfer resistance network employing appropriate coefficients. This final expression corresponds to a single-zone model due to the working fluid exiting before boiling occurs, while the multi-zone approaches presented previously are incorporated in the presence of phase change (i.e., right hand side of Eqn. (5.10) replaced by Eqn. (5.6)).

5.3 Impact of DPFHX on WHR, Power, and Emissions

Examining the fluid dynamics within the DPFHX tubes reveals several physical phenomena that enhance heat transfer. As highlighted by the resistor network of Figure 47, convection to the cores and subsequent conduction to the tube interior provides an additional heat transfer pathway. Also, interaction between the exhaust gas and tube wall increases by

forcing flow through the porous walls, augmenting the heat transfer component perpendicular to the tubes. Conversely, the central cells are more isolated from the tube interior and, therefore, depend on conduction by the DPF cores. However, relatively few of these central cells exist with circular DPFHX tubes.

In an earlier section of this paper, the current diesel engine aftertreatment device configuration is reported as DOC, DPF, and SCR. However, this arrangement is not necessarily optimal when using a DPFHX, due to the large amounts of energy being removed from the exhaust. Therefore, a thorough discussion of the influence of installing a DPFHX into a diesel engine's exhaust stream is warranted after finding its enhanced heat transfer characteristics.

When reporting the 10-15% fuel economy improvement resulting from ORC power generation, predictions should also account for the slightly reduced engine performance caused by the additional exhaust backpressure imposed. Under normal WHR circumstances, this factor results in horsepower losses of 1.5-2.5% at high loads and 0.2-0.5% at low loads [51]. However, the CI engine exhaust system already requires a DPF, which contributes a pressure drop. In other words, adding a heat exchanger to the exhaust produces an additional pressure drop; whereas, the DPFHX pressure drop should be relatively comparable to a DPF. In addition, powertrain efficiency gains only begin after sufficient heat is transferred to the working fluid, requiring three to four minutes in the presence of an accumulator [70]. Reduced heating times are present for systems without accumulators, decreasing the warm up period. Another consideration is the weight of the DPFHX-ORC system, which should be slightly less than a stand-alone ORC system due to the DPFHX being lighter than independent DPF and evaporator devices. This effect is not expected to significantly influence the WHR potential of mobile applications, since

Larjola predicts a weight/power ratio of 6 kg/kW for an ORC that generates 4 kW electric power [65].

Since the engine exhaust passes through the DOC before reaching the DPFHX, conversion efficiencies for HC and CO are unaffected during and after startup. Therefore, these emissions are reduced in proportion to the fuel consumption improvement with the DPFHX-ORC system. In the proposed concept, the DPF core is non-catalyzed; therefore, the only change in emissions through this device would be via the standard PM storage mechanisms. In this situation, the primary emissions concern becomes the reduction of NO_x in the presence of reduced exhaust temperatures coming from the DPFHX.

Qi et al. suggest that 90% conversion efficiencies are achieved by Fe-ZSM-5 from 350-500°C and similar performance is observed for Cu-ZSM-5 from 250-350°C, while a combined catalyst will provide NO reduction over a wide temperature range [7]. Confirmation of this suggestion is found in the work of Krocher and Elsener in the same year, where combinations including vanadia catalysts are also evaluated [156]. As an alternative, Pt-ZSM-5 catalysts using propylene injection have been shown to convert almost 80% of NO at 140°C [157]. Therefore, NO_x conversion may be possible at temperatures well below standard engine exhaust levels and this is a current avenue of research. Furthermore, adjustment of the ORC working fluid mass flow rate can occur in order to maintain a higher outlet gas temperature.

As a result, the final design of a diesel aftertreatment system featuring a DPFHX should also consider placing the SCR system upstream of a DPFHX. In this configuration, the NO_x reduction efficiency will be unaffected and the overall nitrogen oxide emissions will decrease in the same manner as HC and CO. However, initiation of the regeneration event for the DPFHX

will be affected and will need to be considered. As an alternative to late fuel injection events, actively heating the DPF cores could provide further control.

The final emissions species to examine are CO_2 and PM. As expected, the change in carbon dioxide emissions is proportional to the fuel consumption decrease, which starts out as zero and increases after the DPFHX reaches operational temperatures. Even after the DPFHX heats up, filtration of PM must occur at reduced temperature levels. However, these conditions will not harm the PM collection efficiency because the filtration mechanisms are primarily mechanical in nature. Modification of engine operation for higher loading events simply involves fewer periods of post combustion fuel injection events, allowing more of the fuel's chemical energy to go towards power generation, instead of being utilized to heat the filter.

With respect to cost, the DPFHX concept requires additional expense when compared to an aftertreatment system without WHR, due to the DPFHX being more complex than a standard DPF. However, when incorporating WHR the DPFHX would be more affordable than a separate DPF and heat exchanger. Some of this advantage results from the large tubes within the DPFHX generating fewer joints than standard heat exchangers. Also, the cost of large numbers of small tubes tends to exceed a small number of large tubes.

In addition to the DPFHX, the other three ORC components (expander, condenser, and pump) must be included for conversion of waste heat to usable power. With three of the four ORC components being unchanged and the DPFHX's cost advantage described previously, the cost-benefit analysis of the DPFHX-ORC system resembles that of an ORC. While the annual miles traveled and engine size influence the payback period, under normal circumstances the additional expense of an ORC (or DPFHX-ORC) may be offset in 2-3 years through fuel savings. After this period of recuperating the additional up-front cost, the consumer retains the

10-15% fuel savings. Future design changes to the DPFHX could also require additional

expense, such as featuring bellowed joints to reduce thermal stresses.

Chapter 6

Waste Heat Recovery Experiments and Analysis

6.1 Introduction

Although the modeling efforts of Chapter 7 are the means employed in evaluating the performance of the DPFHX-ORC concept, initial steps are being taken to allow the eventual testing of an ORC and a DPFHX in University of Kansas laboratories. This chapter describes the completion of the initial phase of developing experimental capabilities in waste heat recovery; i.e., the design and building of an apparatus to measure waste heat recovery from the Yanmar single-cylinder engine in the laboratory. Specifically, tests looked primarily at the degree to which experimental results agreed with the first law of thermodynamics. Completion of the first phase has opened the possibility of future ORC and DPFHX experiments.

Following the design and construction of the WHR device and DAQ system, operation of the Yanmar single-cylinder engine followed the previously reported protocol by Mangus and Depcik [158]. Similar to other single-cylinder engine test cell efforts [159], engine fuel economy was optimized in order to minimize brake specific fuel consumption at each load while utilizing a single-injection event at a pressure of 42.0 ± 0.03 MPa. At each loading, the WHR apparatus flowed water before initiating engine fuel injection and data collection occurred once the exhaust and water conditions reached steady-state as determined by the exhaust inlet temperature to the

DPFHX varying by less than one percent per minute. Under these conditions, measurements were taken over a 10 minute period in order to minimize random error.

Engine tests occurred at low engine speeds and loads to prevent boiling of the working fluid, which would complicate the measurement of the energy flow into the working fluid. The water flow rate during a trial came from a series of three weight scale measurements, occurring at 0, 5, and 10 minutes. Since the pump was designed to provide a constant flow rate, the water flow during the first half of the trial agreed in every case with the last five minute period. Exhaust flow rate measurements occurred every 0.1 s, while temperature and pressure values were obtained in 0.333 and 0.600 s increments. Processing the steady-state data consisted of synchronizing the timing of the engine and WHR apparatus measurements along with averaging all the steady-state data while calculating the standard deviations.

6.2 WHR Apparatus

Proper design of the laboratory system acknowledges that Eq. (5.3) holds for a simple heat exchanger (HX) without heat losses and potential and kinetic energy changes. Although this principle holds that the energy gained by the working fluid equals the energy lost by the exhaust, preservation of the ability to measure both quantities independently is desirable from a WHR testing system.

The first function of the WHR system is to circulate a working fluid through a heat exchanger. To accomplish this, a pump exists between working fluid reservoirs, as shown by Figure 50. In this system, the centrally located HX exchanges heat between the engine exhaust and working fluid, where measurements of the working fluid and exhaust allow analysis of the heat exchange.
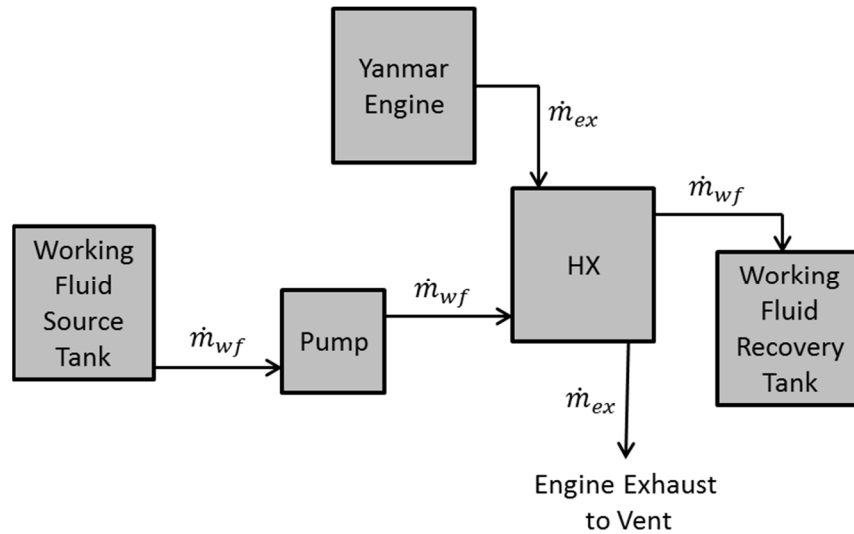
Figure 50: WHR system working fluid circulation schematic

Analysis of the HX requires fixing the thermodynamic state of the exhaust and working fluid entering and exiting the device. To fix each state, data acquisition (DAQ) equipment records the temperature and pressure of the fluids. This is accomplished by placing pressure transducers and thermocouples at each of the four flow ports on the HX, designated by 'P' and 'T' in Figure 51. However, these measurements are only sufficient for fixing the thermodynamic state when neither fluid exits as a liquid-vapor mixture. To ensure this, working fluid flow rates must be high enough to prevent phase change. Although the WHR system design features insulation on the HX to minimize heat losses, four thermocouples (designated by '4 T') on the outside of the HX monitor the temperature level inside the insulation. In the schematic, red circles and boxes designate DAQ system hardware. Furthermore, the mass flow rate of the working fluid comes from a flow sensor (shown with $\dot{m}_{wf}$) and existing engine hardware measures the mass flow rate and composition of the exhaust.
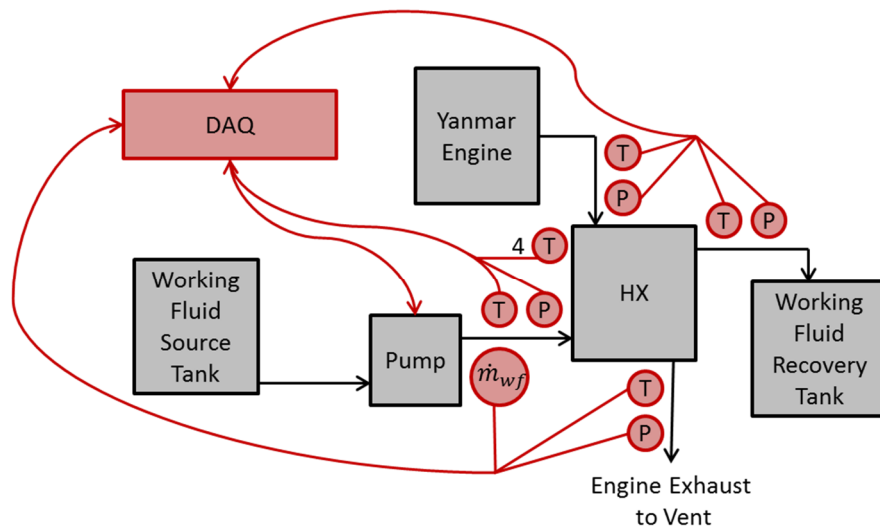
Figure 51: Schematic of DAQ system for measuring HX heat transfer performance

6.3 WHR Apparatus Construction

To create the system, it is necessary to select: a working fluid, pressure transducers, thermocouples, a flow meter, a DAQ platform, a pump, and working fluid tanks. The DAQ platform facilitates recording sensor measurements and uses an output signal to control the pump; thus, controlling the working fluid flow. A description of selecting the apparatus components is provided in the following section, and is followed by a description of the DAQ system's creation.

6.3.1 Component Selection

The first design choice is the working fluid, since many of the components contact the fluid during operation. A desirable working fluid is; compatible with standard sensors and construction materials, affordable, and non-toxic. To suit these defining characteristics, the laboratory WHR apparatus uses water as the working fluid. Of course, final working fluid selection must also consider ORC performance; however, the initial studies described here use a practical working fluid (water) for safety and to avoid calibrating sensors. The use of REFPROP

139

in the modeling efforts will allow for relatively easy expansion of this effort to other working fluids by simply replacing the specific properties of water.

A pump provides for the circulation of the ORC working fluid, which passes water through the HX at a specified rate. Originally, laboratory test plans included some testing with saturated liquid water; however, pump manufacturers could not provide a pump capable of withstanding 100^0C temperatures. For this reason, water inlet conditions are kept under 50^0C. Due to the low flow rates present, a suitable choice was a positive displacement diaphragm digital dosing pump from Grundfos (model number DDA 30-4 AR-PP/E/C-F-31U7U7BG). As the part number represents, this pump is capable of flowing 30 liters/hr at pressures up to 4 bar. Simple calculations using the waste heat available from the single-cylinder engine exhaust and the specific heat of water suggest this dosing pump is appropriately sized to achieve water exit conditions below boiling. As an example, the calculation that follows shows the parameters of the Yanmar engine exhaust corresponding to water exit conditions without boiling at a flow rate under the pump's 30 liters/hr maximum.

$$\dot{m}_{ex}\left(h_{ex,in} - h_{ex,out}\right) = \dot{m}_{wf}\left(h_{wf,out} - h_{wf,in}\right)$$

$$= 0.00128\frac{kg}{s} * 1000\frac{J}{kg*K}\left(701.63K - 400K\right)$$

$$= \dot{m}_{wf} * 4179\frac{J}{kg*K}\left(398K - 298K\right)$$

(6.1)

The result is a mass flow rate of 0.0081 kg/s, which translates to 29.31 liters/hr.

With this model, the rate of circulation is controlled via a 4-20 mA signal from the DAQ system, as described in following paragraphs. Figure 52 shows the pump selected, where a multi-function valve is connected to the flow exit atop the left hand side of the pump to provide the necessary pressure differential.

Figure 52: Stock photo resembling the Grundfos WHR apparatus pump

A few other basic hardware components are necessary to complete the water flow circuit; such as tubing, fittings, and buckets. Since the working fluid is water, chemical compatibility is less of a concern than the ability to handle the elevated temperatures. In order to handle temperatures exceeding 200°F, NSF-certified polyethylene buckets (McMaster part 4344T72) and high temperature silicone tubing (McMaster part 51135K77) are implemented. To prevent corrosion caused by water and air, stainless steel is the material choice for the required pipe fittings, hose barbs, clamps, and bungs.

With the goal of eventually creating a DPFHX, a first prototype was created by exploring standard shell-and-tube heat exchangers. This was accomplished in order to test the incorporation within the WHR apparatus and energy loss/recovery data, which can be used to prepare for the potential design and fabrication of a DPFHX prototype and modifications to the WHR apparatus. Therefore, the WHR apparatus required a heat exchanger with large tubes, shell-and-tube geometry, access to tubes, ability to withstand exhaust temperatures, and appropriate dimensions for the single-cylinder Yanmar L100V engine in the authors' test cell laboratory. With respect to size, a relatively simple MATLAB heat exchanger model suggested a reasonable heat transfer area for this application was around 0.2 m^2, providing substantial heat

recovery without ignoring packaging restrictions [14]. A single-cylinder engine platform was chosen based on its availability for testing and that only a relatively small heat exchanger was required, reducing time in the construction and instrumentation phase. Future work can scale the single-cylinder findings to the creation of larger WHR devices and apparatuses for use with a multi-cylinder engine test cell at the University of Kansas.

Initial heat exchanger product research included consideration of standard device offerings from Southwest Thermal Technology, SEC Heat Exchangers, Exergy, Polar Power, McMaster Carr, Bosal, Niagara Thermal Products, and Alfalaval. Unfortunately, the uniform use of small tubes by manufacturers for improved heat transfer complicated the search. In addition, spiral-flow and bellowed shell-and-tube heat exchangers are more common for high temperature applications due to thermal stresses. While no standard product offerings have sufficiently large tubes, a custom build, commissioned by another company from SEC Heat Exchangers and later declined, provided a starting point. This device (see Figure 53) featured active tube areas 18" in length with 0.75" ID and 0.875" OD tubes. By considering that the heat exchanger contained six equivalently sized tubes, the resulting heat transfer areas based on the inner and outer tube diameters were 0.1642 m^2 and 0.1915 m^2 respectively, an adequate match with the Yanmar engine's exhaust energy.
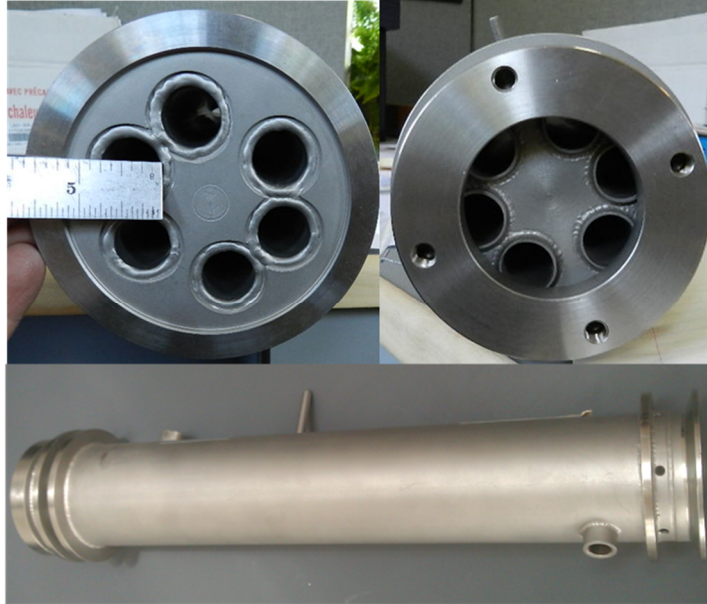
Figure 53: End and side views of heat exchanger for WHR experiments

The remaining components of the WHR laboratory apparatus are associated with data acquisition. Selecting a DAQ platform is the first step toward taking measurements, where the two primary options from National Instruments are the CompactRIO and CompactDAQ, with the former being faster and more costly. Since high speed data collection is not a requirement of the project, a 4-slot CompactDAQ is the DAQ platform chosen for processing sensor signals and pump control. A single module is required for each of the following functions; analog input for four exhaust/working fluid thermocouples (NI9211), analog input with excitation for four pressure transducers (NI9237), analog output for pump control (NI9265), and a second analog input for the four external thermocouples (NI9211). (The original mass flow meter operated with a digital input module (NI9411), prior to measuring the water flow rate with a scale). Since the standard CompactDAQ power supply is not capable of providing the required excitation, this supply is replaced with a LS75-12 unit from TDK-Lambda. This model is capable of providing 75W of 12VDC power.

In addition to the CompactDAQ and modules, obtaining the desired measurements requires several sensors. Rugged pipe plug thermocouples from Omega (product TC-J-NPT-G-72) provide the temperature measurements, while stainless steel pressure transducers from Omega (product PX309-030AV) give the pressures. Type K thermocouple wire serves to provide the external temperature measurements. The final physical quantity is the water flow rate, and although a flow rate measurement is available from the pump, this is an estimated value. For this reason, the original DAQ system design had the flow rate coming from an Omega FTB601 electro-optical sensor. In the experimental phase, this plan had to be modified due to the flow sensor's inaccuracy with the pulsating flow from the pump. Instead, an Adam CPWplus 35 bench scale (75 lbs max) with a digital display and RS-232 bidirectional interface provides measurements of flow by measuring the weight of water leaving the upstream bucket as a function of time.

After obtaining the sensors and pipe bungs for the exhaust and water systems, the HX was connected to the engine exhaust and outfitted with pipe bungs to hold the sensors. Stainless steel concentric reducers (3" to 1") provided the necessary size differential from the DPFHX ends to the engine exhaust. On one end, directly welding the reducer to the DPFHX established the connection, while a flange was manufactured for the other end, preserving access to the tubes for maintenance and eventual DPF core replacement. This custom flange, created by the KU Machine Shop, was welded to the reducer and subsequently bolted to the HX. Moving further away from the HX, short sections of straight pipe allowed for installation of the sensors (see Figure 54).

Figure 54: Connection between HX and engine exhaust showing sensor ports, concentric reducer, and flange

However, the high temperature of the incoming exhaust exceeded the specifications of the pressure sensor, requiring a pitot tube arrangement as shown by Figure 55. After the sensor containing pipes, standard stainless steel piping completed the exhaust system through connection to the existing Yanmar exhaust pipe and laboratory ventilation system. Finally, wrapping the HX and adjacent piping with Longacre fiberglass composite header insulation from Summit Racing (product LNG-64870) reduced the heat loss and allowed for (initially) the assumption of adiabaticity. Following initial tests, the header insulation was replaced with two layers of 1" very high-temperature fiberglass insulation sheeting (McMaster Carr product 9356K11), seams were sealed with high temperature tape.

Once all the components were available for assembly of the laboratory WHR apparatus, developing a modular architecture for easy installation in the available test cell pad space became essential. To accomplish this, 1" aluminum T-slotted extrusions and impact-resistant polycarbonate sheeting combined to provide a support structure for the components (see Figure 55).
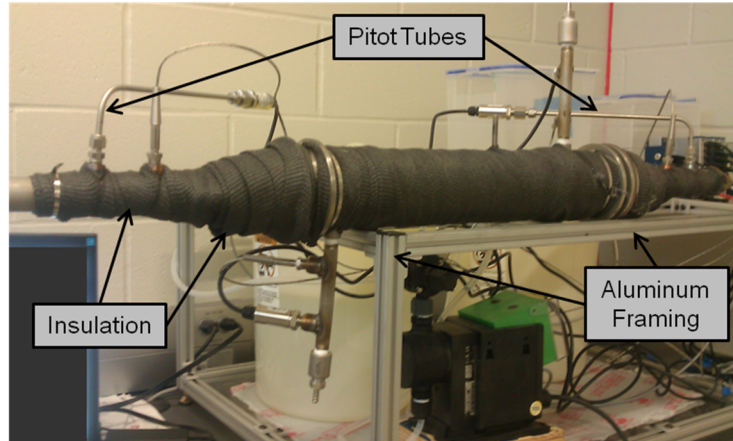
Figure 55: Partially constructed laboratory WHR apparatus showing pitot tubes, insulation, and aluminum framing

Underneath the insulation were four contact thermocouples, two on the shell of the HX and one on each concentric reducer. Figure 56 shows the placement of the external thermocouples.
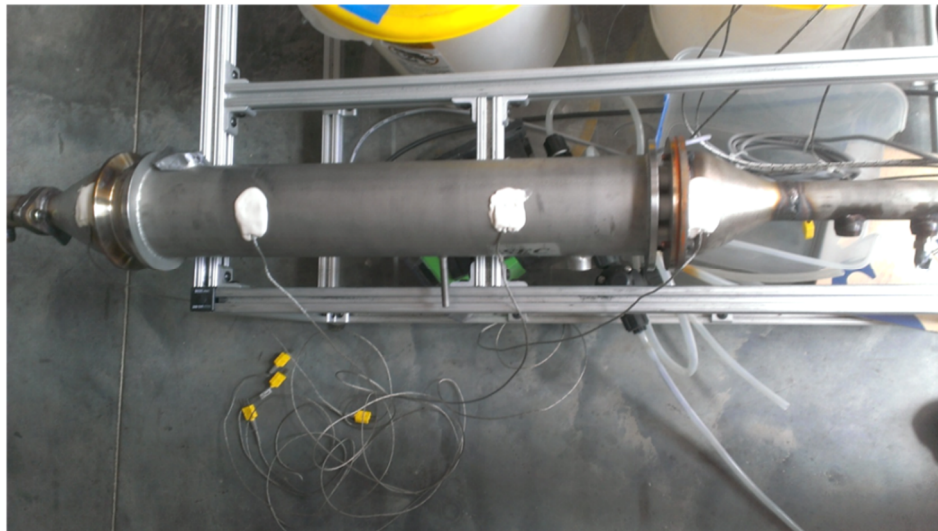
Figure 56: Heat exchanger with four external thermocouples

In order to monitor operation of the water and exhaust systems, the DAQ system obtained sensor signals and stored measurements. Using the aforementioned sensor ports, the pressure and temperature sensors were installed and the associated wiring was routed to the CompactDAQ. For the flow sensor, barbed fittings and tubing allowed placement within the water system after the pump. Signal wires from these sensors connected to the CompactDAQ, with the

146

thermocouple wires using direct screw terminal connections and the other three modules requiring adapters. Once all the components were assembled on the aluminum structure and the electrical wiring was completed, the WHR laboratory apparatus shown in Figure 57 was fully constructed. To prevent damage to the CompactDAQ in the event of water leakage, the DAQ system was enclosed in a waterproof container.
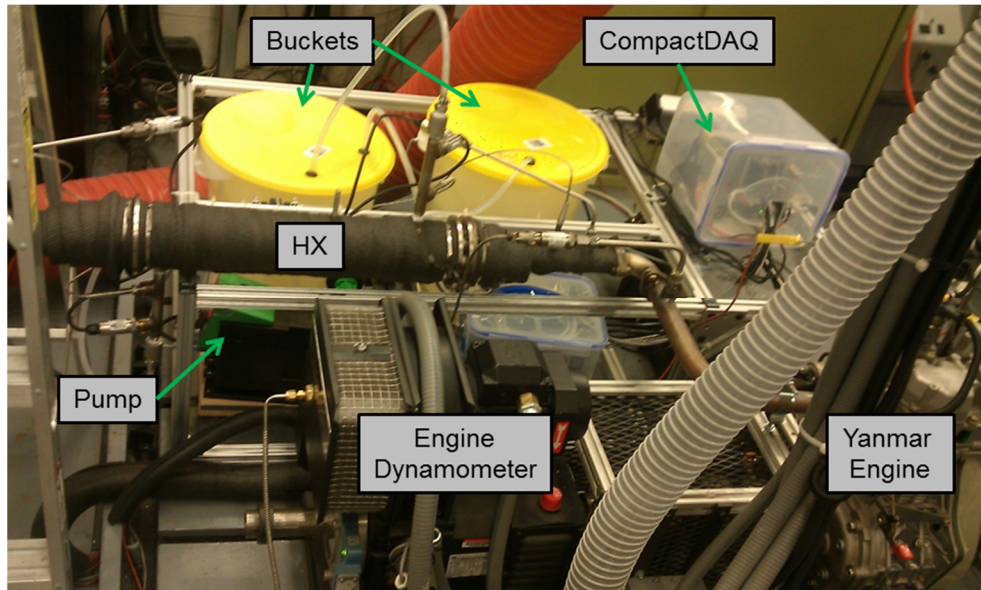
Figure 57: Completed WHR apparatus installed in engine test cell

6.4 WHR Apparatus LabVIEW Code

A LabVIEW code was created to operate the aforementioned 4-slot CompactDAQ with the following modules: NI 9211 (analog input, 4-Channel, 14 S/s, 24-Bit, ±80 mV thermocouple input module), NI 9237 (analog input with excitation, ±25 mV/V, 24-Bit simultaneous bridge module), NI 9265 (4-Channel, 100 kS/s, 16-Bit, 0-20 mA analog output module), and NI 9211 (analog input, 4-Channel, 14 S/s, 24-Bit, ±80 mV thermocouple input module) (originally a NI 9411 (6-Channel, 500 ns, ±5-24 V digital input module)). The CompactDAQ connects by USB and provides the functionality to use NI DAQmx drivers on the host machine to interface with the CompactDAQ. This system served the functions of recording temperature and pressure

measurements while also controlling the pump. To accomplish this, a single VI called 'readandrecordall' was created.

In this VI, exhaust/water temperatures and pressures were measured and stored in separate technical data management solution (TDMS) files, while a third TDMS file stored external temperatures and a fourth received the water flow rates. A total of two while loops were used, with the first recording temperature measurements and the second storing the pressures and flow rates. Due to steady-state conditions allowing low sample rates, temperatures were stored at 3 samples/sec and pressure and flow readings occurred every 0.6 sec. As expected, the sampling frequency similarity between the pressure and flow measurements is a result of these operations occurring in a single loop. In other words, pressure measurements are hardware timed and synchronized to the flow measurements.

With respect to the NI 9211 temperature measurements, the module provides 24 Bits of resolution and is hardwire timed, meaning that the sample rate is determined by the CompactDAQ. To ensure accuracy, the NI 9211 has cold-junction temperature compensation, which keeps one of the thermocouple junctions at a controlled reference temperature. Furthermore, no calibration of this module was necessary since the heat transfer experiments either occurred within one year of factory calibration or shortly thereafter. In fact, all the modules were of a similar age, so no calibration was necessary for any of the CompactDAQ modules.

For the 24-Bit NI 9237's pressure readings, the module's internal excitation of 3.3 VDC was used instead of employing the power supply. This decision leads to less heat generation at the cost of a slight decrease in sensitivity. The NI 9237 is also ratiometric, so any changes in the voltage to the strain gauge will not affect the output, ensuring that pressure fluctuations are the

only factor that can change the readings. This results from the module automatically adjusting an anti-aliasing filter to provide an alias free bandwidth to a frequency of 0.45 times the sampling frequency. Again, due to the steady-state nature of the experiments, the module's lowest allowable sampling frequency (1613 samples/sec) was used. Since this quantity of measurements was still excessive, the root mean square (RMS) value of every 1000 readings was sent to the 'prestestdata' TDMS file.

Also in the pressure measurement loop was the NI 9411's flow reading. Using external excitation from the power supply, the flow sensor produced an output signal of varying frequency proportional to the flow rate. When pulses from the flow sensor were present, pulses were counted for the duration of the loop (1000/1613 sec) and made available to the computer. In periods of no fluid flow, this module caused an error in the VI, since the module will not send a pulse rate of 0 Hz. To counteract this, a case structure was constructed to allow flow readings to be temporarily turned off, allowing the VI to run uninterrupted.

In addition to the flow sensor, the current output module (NI 9265) received excitation from the power supply. By using the mA specified via the program's Graphical User Interface (GUI), the NI 9265 provided the pump a 16-Bit current between the 0-20 mA module limits. As opposed to the pump mA coming from the GUI, the time of day and elapsed time are sent from the VI to the GUI. While this information is pertinent for synchronizing the WHR apparatus and engine DAQ system's measurements, the data is waveform and, therefore, automatically loads the sample rate and initial start time into the TDMS files.

For monitoring the experiments, a GUI was created for display on the computer running the 'readandrecordall' VI. As shown by Figure 58, the GUI features a slider bar for adjusting the current flowing to the pump. Also, all four temperatures and pressures are visible on the two

large graphs, which are useful in preventing unsafe operating conditions and determining when steady-state conditions are reached.
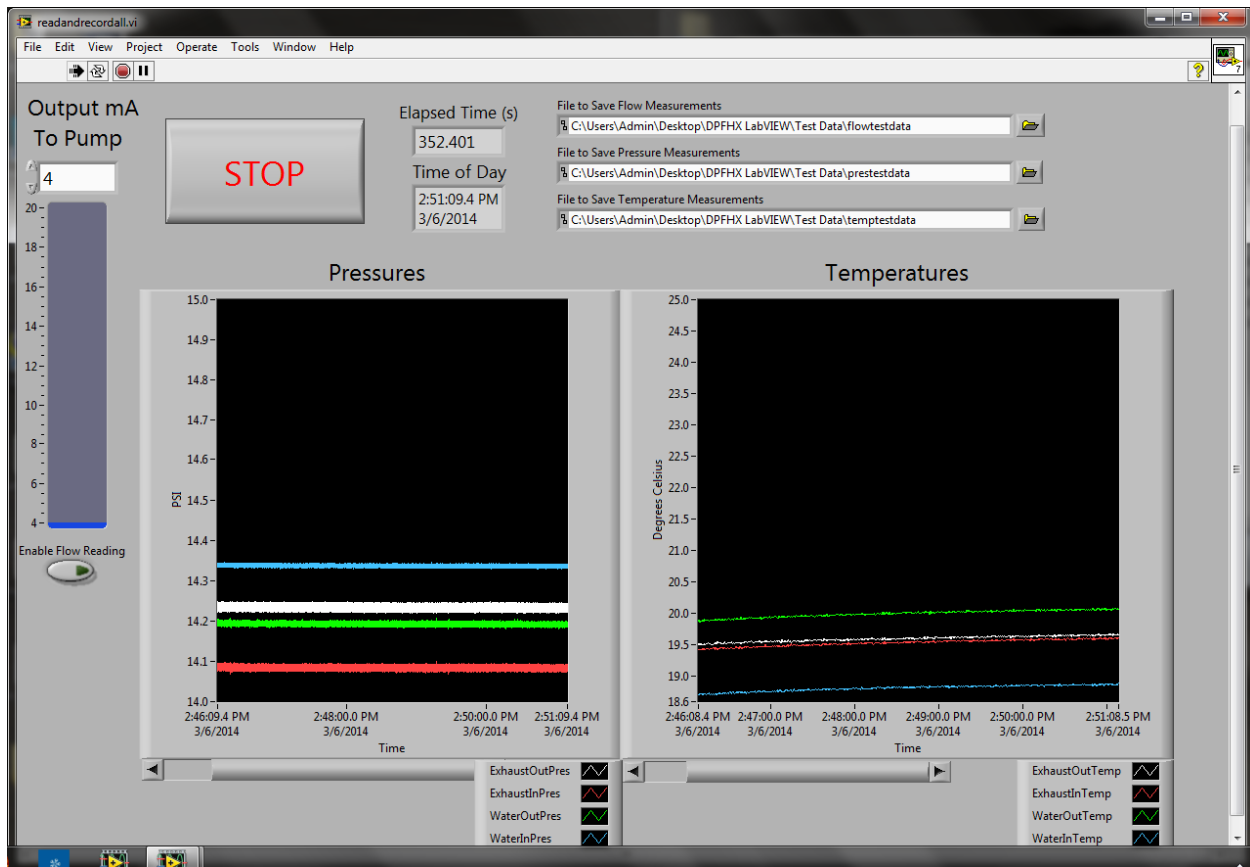
Figure 58: LabVIEW GUI for heat transfer experiments showing the information available to the operator

Underlying the graphical display of Figure 58 is a block diagram corresponding to the signal processing and storage. Figure 59 shows the storage of measurements, the output of signals to the GUI, and the two while loops controlling the reading of sensors. Numerical values of the external temperature measurements were displayed in the final code instead of using graphs, since monitoring changes in the water/exhaust pressures and temperatures was the primary concern during testing.
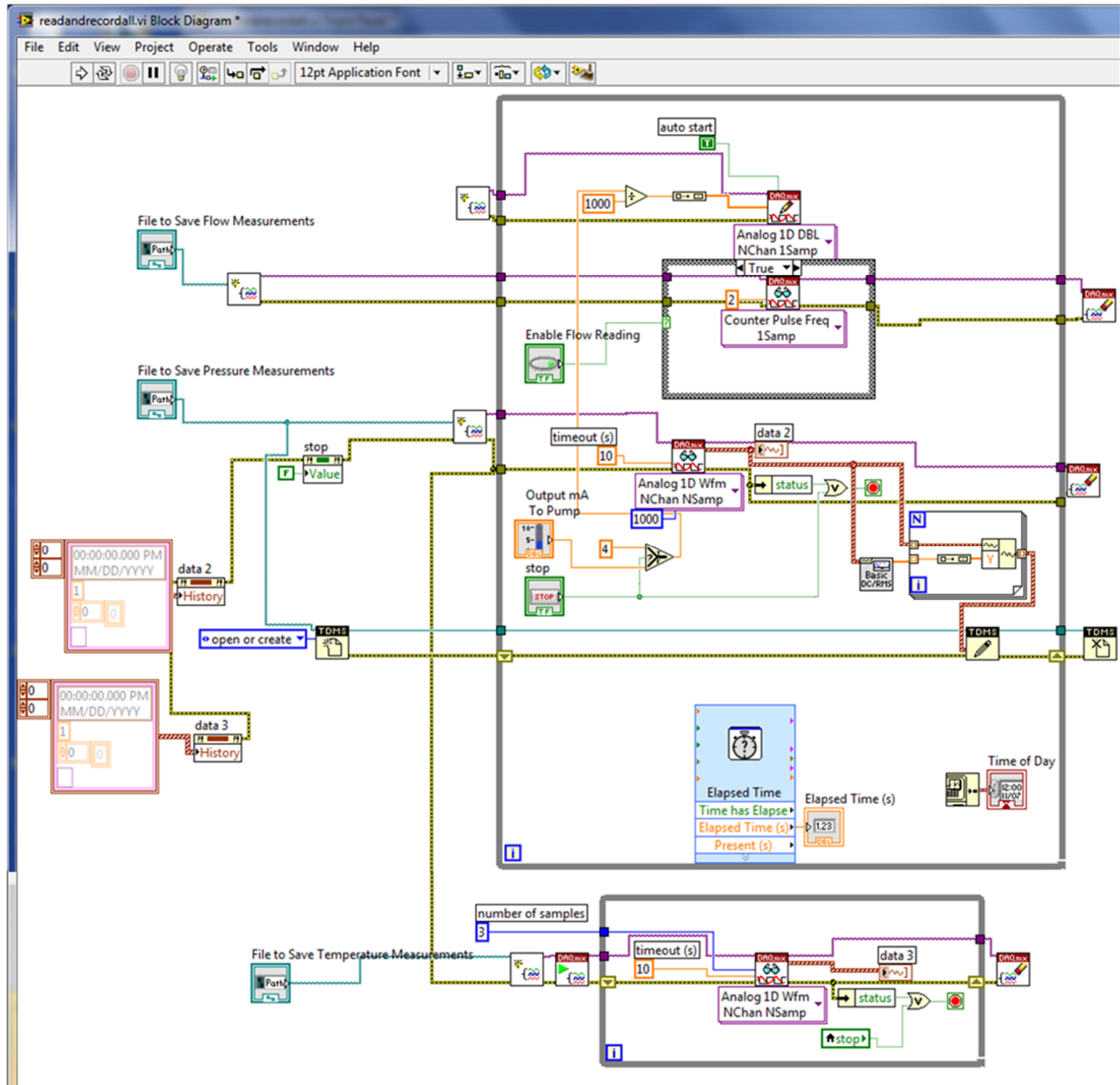
Figure 59: LabVIEW block diagram for data acquisition in WHR experiments

6.5 WHR Energy Balance Testing

All of the experimental trials using the waste heat recovery apparatus targeted achieving

an energy balance (heat transfer to water = heat transfer from exhaust). Of course, it is

impossible to eliminate heat losses to the ambient, so the work sought to minimize this source of

imbalance. In this section, the apparatus described in Sections 6.1-6.3 is employed in three

periods of testing.

The gathered data contains the necessary information for fixing all of the thermodynamic states present; however, some of the required properties are not directly measured and must be calculated from the data. For instance, the engine test cell measurements of the air and mass flow rates in conjunction with the combustion equations of Ch. 3 provide the exhaust species concentrations. The relative amounts of each exhaust constituent are then used in calculating exhaust enthalpies for use in Eqn. (5.10). This process has been explained in Ch. 3 and will not be repeated here. It is worth noting, however, that averaging of the data occurs in Excel, while subsequent calculations take place in MATLAB using thermodynamic properties from REFPROP.

6.5.1 Testing Results

The first period of testing occurred with the original header wrap insulation and occurred at a range of engine loads. Although care was taken to insulate the heat exchanger and keep the water exit temperature below boiling conditions, heat loss to the atmosphere and heat loss to latent heat of vaporization still contributed to an energy imbalance.

Table 10 shows the results from the first set of experiments, demonstrating a discrepancy between the heat leaving the exhaust and the heat entering the water. Considering that all four pressures were nearly atmospheric, vaporization of water will not occur at temperatures below 373 K.

Table 10: Results from first WHR apparatus experiments

Engine Speed (RPM)	Engine Load (N·m)	$\dot{m}_w$ (kg/s)	$\dot{m}_{ex}$ (kg/s)	$T_{ex,out}$ (K)	$T_{ex,in}$ (K)	$T_{w,out}$ (K)	$T_{w,in}$ (K)	$\dot{Q}_{ex}$ (W)	$\dot{Q}_w$ (W)
1800	4.5	5.000E-04	6.048E-03	336.03	413.15	363.96	302.91	481.46	57.27
1800	4.5	1.017E-03	6.056E-03	331.70	412.53	353.42	302.18	505.09	97.63
1800	4.5	1.483E-03	6.066E-03	329.06	412.89	346.72	301.82	524.62	124.77
1800	4.5	2.017E-03	6.057E-03	327.83	413.99	342.22	301.22	538.42	154.84
1800	9.5	2.017E-03	6.077E-03	337.95	471.07	363.50	302.59	845.15	230.46
1800	9.5	2.517E-03	6.368E-03	334.35	458.85	357.22	302.21	825.95	259.60

1800	9.5	3.033E-03	6.331E-03	334.75	470.15	352.22	301.84	894.36	286.37
1800	9.5	3.533E-03	6.391E-03	333.41	472.12	343.63	300.21	924.64	287.33
1800	9.5	4.167E-03	6.650E-03	331.65	469.73	338.32	299.43	956.83	303.29
1800	13.5	3.283E-03	5.941E-03	342.45	529.53	365.09	301.77	1176.70	390.09
1800	13.5	3.550E-03	5.962E-03	341.30	528.48	361.20	301.26	1181.07	399.10
1800	13.5	4.067E-03	6.026E-03	339.30	527.06	354.83	300.74	1196.72	412.29
1800	13.5	4.600E-03	5.929E-03	339.55	528.86	351.59	300.76	1187.81	438.13
1800	18	4.900E-03	5.924E-03	345.53	596.11	364.01	300.18	1597.63	586.69
1800	18	5.150E-03	6.003E-03	345.03	594.82	360.59	299.89	1612.39	586.15
1800	18	5.617E-03	5.911E-03	346.80	594.54	356.28	300.43	1575.93	588.04
1800	18	6.100E-03	5.883E-03	346.83	593.55	351.15	300.27	1561.65	581.55
1800	18	6.667E-03	5.874E-03	347.26	592.30	348.10	301.15	1548.35	586.38

Examining the WHR apparatus for sources of energy balance disagreement begins with an examination of the apparatus equipment, specifically the mass flow and temperature measurements. While errors in the pressure measurement contribute secondarily through slight alterations in the specific enthalpy REFPROP lookup, these magnitudes are negligible due to specific heat being a weak function of pressure. Using the stated linearity error of the Adam CPWplus35 scale (0.02 kg) in combination with the total water mass flow during each individual test, percentage error contributions to the overall heat transfer coefficient values are found. As expected, this percentage is larger for slower flow rates (around 5%) and decreases to below 0.5% with rapid water circulation. For the temperature measurements, the given tolerance of 0.75% for the Omega TC-J-NPT-G-72 thermocouples can be directly applied. These individual sensor contributions, although important, are not responsible for the error magnitudes shown in Table 10.

The remaining error sources are external heat loss and water boiling. In the worst case studied, a temperature difference of 65 K existed between the ambient (299 K) and the water (364 K). With approximately ¼" thick fiberglass insulation (k=0.05 W·m⁻¹·K⁻¹) around the 3.5" diameter HX, over the 19 inch main section of the HX, only around 143 W of external heat loss

would be present. This 143W figure is an estimate, since much of the shell will be cooler than the water exit temperature (364 K) and areas of imperfect wrapping cause heat to escape more readily. Hence, external heat loss is a small (yet significant) portion of the over 1000 W difference in the warmest 18 N·m trial.

After the first set of tests, it became clear that the precautions taken to address the potential error sources of external heat loss and water boiling were necessary. External heat loss was minimized by adding fiberglass header wrap insulation, but the error source could be further minimized by using higher thermal resistance insulation and specifically thoroughly covering heat leakage areas (insulation seams). Boiling was reduced by preventing water exit conditions above boiling temperatures, but exhaust conditions needed to be held below boiling to prevent pockets of vaporization for those water molecules contacting the HX tubes.

To modify the WHR apparatus's insulation, the HX and all the sensors were removed from the WHR apparatus. This intensive process was necessary to allow a single sheet of 1" high temperature fiberglass insulation to wrap completely around the HX, leaving a single large seam and small gaps around the water and exhaust holes. After completing the first layer of insulation, the HX received another insulation layer with the seam on the bottom of the device instead of the top. Thorough taping of all seams then marked the completion of the enhanced external heat loss abatement. All the sensors, pitot tubes, and water tubes were then reinstalled, including the four additional surface thermocouples on the outside of the device (see Figure 56).

Another round of testing then commenced, using only engine operating conditions that produce exhaust temperatures below water's boiling point. This restricted the testing to a narrow range of 1800 RPM conditions, since the injection of substantial amount of fuel would quickly increase exhaust temperatures significantly above 373 K. It should be noted that conditions

reaching a few degrees above this mark occurred, as shown in the results of Table 11, which could not produce any significant boiling before reducing in temperature below the soft limit indicated. These calculations utilized time averaged results from two separate tests, with post processing in MATLAB using REFPROP.

Table 11: Experimental results from WHR apparatus with improved heat transfer agreement.

Engine Speed (RPM)	Engine Load (N·m)	$\dot{m}_w$ (kg/s)	$\dot{m}_{ex}$ (kg/s)	$T_{ex,out}$ (K)	$T_{ex,in}$ (K)	$T_{w,out}$ (K)	$T_{w,in}$ (K)	$\dot{Q}_{ex}$ (W)	$\dot{Q}_w$ (W)	ε (-)
1800	0.53	5.667E-03	6.413E-03	320.58	375.57	309.83	296.36	361.34	318.98	0.571
1800	0.63	4.833E-03	6.360E-03	321.92	376.91	312.63	297.19	358.45	312.02	0.558

Table 11 shows a significant improvement in energy balance consistency between the exhaust and water, suggesting that the additional steps taken to limit external heat loss and water boiling were effective. As the steps towards having a complete WHR apparatus continue to advance, as described in the next section, further modifications will be made to the apparatus to allow broader test conditions.

As the results show energy balance consistency, Table 11 includes a representation of the the performance of the heat exchanger as a dimensionless quantity, effectiveness (ε). Effectiveness is calculated using:

$$\varepsilon = \frac{q}{q_{max}} = \frac{\dot{m}_c \cdot c_{p,c}(T_{c,out} - T_{c,in})}{(\dot{m} \cdot c_p)_{min}(T_{h,in} - T_{c,in})} = \frac{\dot{m}_h \cdot c_{p,h}(T_{h,in} - T_{h,out})}{(\dot{m} \cdot c_p)_{min}(T_{h,in} - T_{c,in})} \tag{6.2}$$

where the subscript *h* refers to the fluid entering at the hottest temperature and *c* refers to the fluid entering at the lowest temperature. In the equation, *q* is the rate of heat transfer, q_{max} is the maximum possible heat transfer, $\dot{m}$ is the mass flow rate, *c* is the specific heat capacity, and *T* is the temperature. Theoretically, the heat transfer leaving the hot fluid would exactly equal the heat transfer entering the cold fluid; however, heat losses inevitably occur so the heat gained by

the cold fluid is the most appropriate rate of heat transfer to include in the numerator. In both experiments, the water has the lower heat capacity rate ($\dot{m} \cdot c_p$).

6.5.2 Future Plans for WHR Apparatus

One improvement to the WHR apparatus's potential already occurred through robustly shielding and bleeding the fuel system in the laboratory test cell. Successful WHR apparatus tests require long windows of steady engine operation, which could not previously occur due to signal interference and air infiltration into the fuel system. With the excellent reliability of the current test cell, the third round of WHR apparatus testing in the future should be able to include a significant number of trials. Of course, the other factor allowing more testing is the modification to the WHR apparatus to allow for testing with exhaust conditions that may cause localized water boiling.

For the WHR apparatus to function properly with the engine operating at high load conditions, the apparatus must provide accurate measurements of water energy recovery during steam production. An active solution is to directly measure steam production, where saturated water vapor must be separated from liquid water exiting the HX and the saturated water vapor would then be condensed and measured (perhaps with another scale). Various types of steam traps separate condensate from steam and may be compatible with the WHR apparatus. A passive method would be to enhance the mixing of the steam and liquid water to ensure that all the water molecules leave the HX at a temperature below boiling. This could include a mixing vessel that promotes heat exchange between the two phases of water leaving the HX, where water flow conditions would still have to remain fast enough that the bulk exit temperature would fall below boiling temperatures.

All future tests should retain the best practices of the first rounds of testing, neatly wrapped insulation and high temperature tape must prevent airflow from coming into direct contact with the HX, a factor that is particularly relevant due to the high air replacement rate in the laboratory test cell. Both the water and exhaust connections must provide tight seals to prevent a loss in either fluid. The use of various water inlet temperatures offers an additional variable during testing, as long as the inlet temperatures fall within the specifications of the pump. Other materials must also be compatible with the water and exhaust temperatures, with the temperature limit of 1200 °F for the insulation, 390 °F for the silicon rubber tubing, and 170 °F for the insulation duct tape.

Chapter 7

Diesel Particulate Filter/Heat Exchanger Modeling

7.1 Introduction

The overall system under study is a compression ignition internal combustion engine outfitted with a diesel particulate filter/heat exchanger functioning as the evaporator for an organic Rankine cycle. This concept has the potential to reduce emissions through using exhaust waste heat recovery to decrease fuel consumption while maintaining PM conversion efficiencies. By conducting modeling studies, these benefits can be quantified to provide further support for implementation of the concept, while also laying the foundation for subsequent optimization of the DPFHX device geometry. One potential application of this concept at the University of Kansas is for the EcoHawks series hybrid beetle shown in Figure 60.
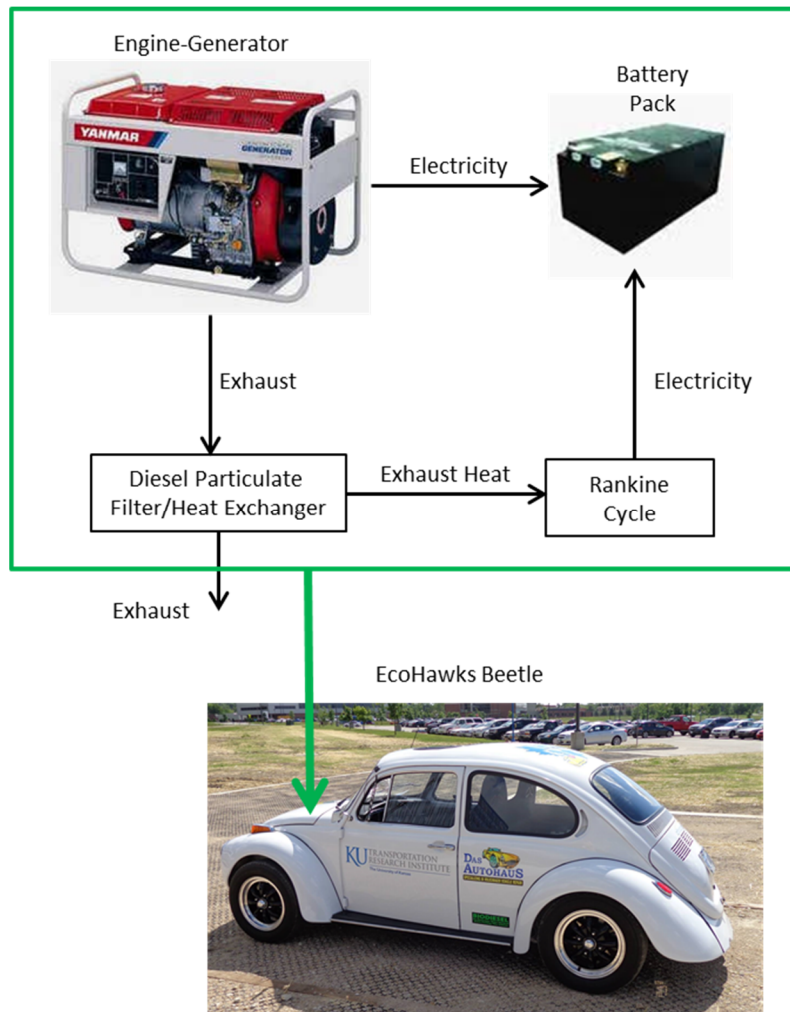
Figure 60: DPFHX-ORC system schematic for vehicle installation.

In this arrangement, the DPFHX follows the vehicle's Yanmar L100V engine within the exhaust system. The working fluid of the ORC passes through the DPFHX to recover waste heat from the engine exhaust and uses this thermal energy to generate electricity through an expander-generator couple. Electricity from the ORC serves to charge the on-board battery pack to supplement the current coming from the engine-generator itself, providing a secondary power source. Since the vehicle is powered through an electric motor, the ORCs output is available for vehicle propulsion without requiring a gearbox and the recovered power is preserved even when the vehicle is not in motion.

Packaging of the DPFHX-ORC system in the vehicle's trunk is possible due to the engine-generator's placement near the vehicle's firewall (see Figure 61), leaving space toward the front of the vehicle. To be clear, the electric motor is located at the rear of the vehicle, while the battery pack is housed in the back seat. Due to the absence of significant logistical hurdles, this concept provides a viable avenue for implementation of the DPFHX-ORC system at the University of Kansas. However, before initiating physical construction of the proposed alternative powertrain, predictions of the supplementary power from the DPFHX-ORC are needed.

Figure 61: View of EcoHawks beetle trunk showing space near firewall away from the engine-generator

To facilitate the construction of a computer model of the DPFHX-ORC architecture, previous chapters have described the individual efforts that enable the creation of this novel simulation tool. Beginning in Chapter 2, a historical perspective on previous engine exhaust WHR efforts using Rankine cycles suggests the use of a reciprocating expander and dry working fluids with high critical temperatures. Using these directives, Chapter 3 describes the creation of a component-based ORC model for simulating the power generation potential of a secondary cycle with reasonable component efficiencies and sizes. These efforts comprise the necessary background to represent the ORC portion of the DPFHX-ORC system.

The other foundational modeling area is diesel particulate filters, as discussed in Chapter 4. Through simulating a single inlet channel, outlet channel, porous wall, and soot layer, representative fluid property profiles are attained for an average DPF channel pair. The filter energy equation in the DPF model uses heat flow terms from the literature to represent all the physical phenomena except external heat transfer. Since standard DPF's are not commonly configured to promote waste heat recovery, many DPF models follow the 1+1D scheme described in Chapter 4. The background of DPF modeling with additional dimensions and the current DPFHX model will be described in sections 7.2 and 7.3-7.4 respectively.

7.2 Multi-Dimensional DPF Modeling Background

Traditional DPF models, beginning with Bissett and Shadman [47, 48], solve for the thermodynamic properties of the filter over time (t) in the axial direction of the filter (z) and the wall direction (x) independently. For reasons such as non-uniform inlet flow, external heat transfer, the presence of cement layers, and oval-shaped DPF's, moving beyond this framework is necessary.

The first work representing a significant shift from the 1+1D model structure is published by Konstandopoulos et al. in 2001 [104], containing a multichannel problem formulation using a two-dimensional indexing system (i, j) for the channels. To handle the different walls adjacent to the individual channels, the authors introduce a third index (k), which takes the values of N(orth), E(ast), S(outh), and W(est). Konstandopoulos et al. choose not to pursue a solution to the equations developed due to the computational power required to simulate each of the thousands of channels within a typical DPF [162]. Instead, the authors employ a homogenization approach to study the regeneration of the DPF.

The first step of the homogenization occurs by rendering the gas properties continuous across channels before eventually deriving continuum level equations following an approach outlined as an appendix to the paper. In brief, Konstandopoulos et al. use Taylor expansions to express the variables as continuous around the middle point of each channel. These expressions are then substituted into the multichannel problem formulation equations and simplified algebraically. Finally, an order of magnitude analysis allows certain terms to be neglected, resulting in a system of equations that the authors indicate as having errors of order $(a/D_{trap})^2$, where a seems to represent the filter cell size, although the variable is not defined as such, and D_{trap} is the diameter of the entire trap. Using the model, the authors study the impact of inlet, catalyst, and loading non-uniformities on regeneration.

In the same year, Miyairi et al. place individual sets (consisting of an inlet cell and an outlet cell) of quasi one-dimensional DPF models in a line with thermal conductance between them. Using the model the authors estimate the temperature distributions present for different materials, cell structures, and DPF sizes during regeneration.

Haralampous et al. continue a trend of using multi-dimensional models to study regeneration in 2003 by modeling the DPF in the axial and radial directions. The focus of their simulations is the need to consider the soot distribution pattern radially and axially instead of simply considering the maximum soot loading at the start of regeneration. By performing two-dimensional modeling of the filter, the authors capture radial variations in thermodynamic properties and inlet conditions while avoiding the time-consuming CFD approach.

An important work on 3-dimensional modeling of DPF's is published by Koltsakis et al. in 2005 to handle the effects of segmented filters and non-axisymmetric designs, again having a goal of predicting transient temperature fields during regeneration [163]. Of particular interest is

accounting for the lesser flow rates in the channels bordering the cement layers, since fewer of the adjacent walls allow flow. The model is an extension of the 2-dimensional model presented the previous year [144, 164], which primarily differs from the 2003 work of Haralampous et al. by modeling catalyzed filter walls. To discretize the solid filter model the authors use a finer grid near the cement layers. For the channels, sets of channels (one inlet channel and one outlet channel) are still utilized.

The next year Guo and Zhang compare the loading and regeneration results of a one-dimensional channel model to a three-dimensional channel model consisting of simplified Navier-Stokes equations, computing the flow and temperature fields within a box containing four one-quarter cells with porous walls in-between. Using an integral method to solve the simplified Navier-Stokes equations, the authors develop correlations for the flow and temperature fields.

Koltsakis et al. publish a study that explores the effects of different inlet pipe geometries in 2009 [165]. The study utilizes a coupled model consisting of the authors' 3-dimensional DPF model and a commercial CFD code to explore variations in soot distribution during loading and regeneration, showing a self-balancing effect that produces a nearly uniform distribution except under high flow rates.

To respond to the need for a multi-dimensional model capable of being run on an engine control unit, Depcik et al. create a lumped radial DPF model in 2014 [166]. Instead of using individual inlet channel-outlet channel pairs in each radial zone, the model eliminates the distinction between inlet channels and outlet channels. Also notable in the paper is the use of an average wall velocity. The overall calibrated model mimics the results of Young's individual experiments [154], providing a model with the ability to predict the behavior of a DPF via an on-board computer.

7.3 Slice Model

Since the multi-dimensional models described prior are not designed to evaluate the performance of a DPFHX with relatively few channels, partial channels, and promoted heat transfer, a different type of model has been developed. The slice model simulates the filter at a single axial location (the filter inlet), focusing on steady-state heat transfer as opposed to transient events, such as warmup and regeneration.

7.3.1 Trap Discretization

Without using the simplification of homogenizing the trap, which makes the filter uniform at each radial location as shown in Figure 62, a complete geometric calculation of the filter slice is necessary.
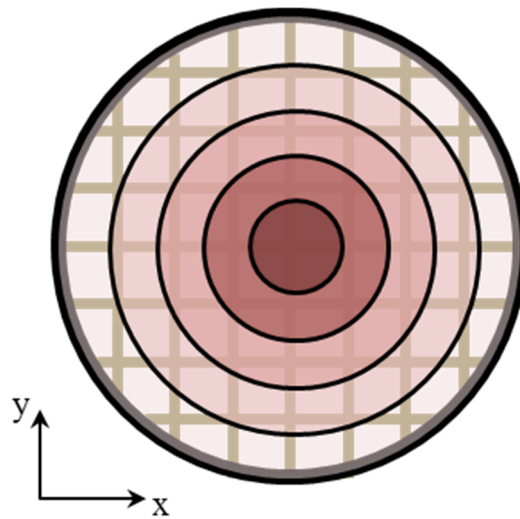
Figure 62: Illustration of homogenized radial model showing different radial zones.

Furthermore, many of the available literature models pair individual channels (see examples in upper right quadrant of Figure 63) instead of allowing multiple flows to enter a single outlet channel. As explained in section 7.3.2, the current model permits multiple flows to enter a single channel (see examples in lower left quadrant of Figure 63). In Figure 63, the cells designated with "I" are inlet channels and those labeled "II" are outlet channels.
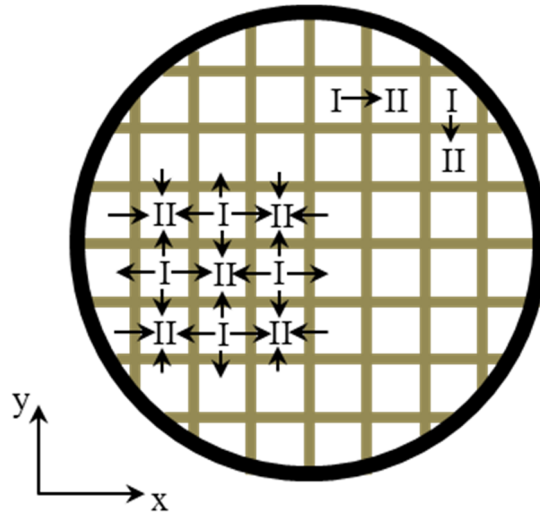
Figure 63: Schematic of modeling with paired channels (upper right) versus unpaired channels (lower left)

After requiring the center of a wall intersection to occur at the center of the filter, the model specifies characteristics of the filter cells and walls. Using the same nomenclature as Chapter 4, geometric quantities include the diameter of the DPF (D_{DPF}), the size of one side of an empty channel (d_m), and the thickness of filter walls (t_{fw}).

As the model is also capable of dividing a single filter wall into multiple segments, another feature not present in existing models, the number of wall discretizations is specified once the DPF's geometric characteristics are known. The square area where walls intersect is treated as a single cell, while the longer walls adjacent to channels can be further divided into multiple cells. This concept is shown in Figure 64, where the wall intersection is a single cell and the channel-bordering walls can be treated as a single cell (left) or multiple cells (e.g., two cells as shown at right).
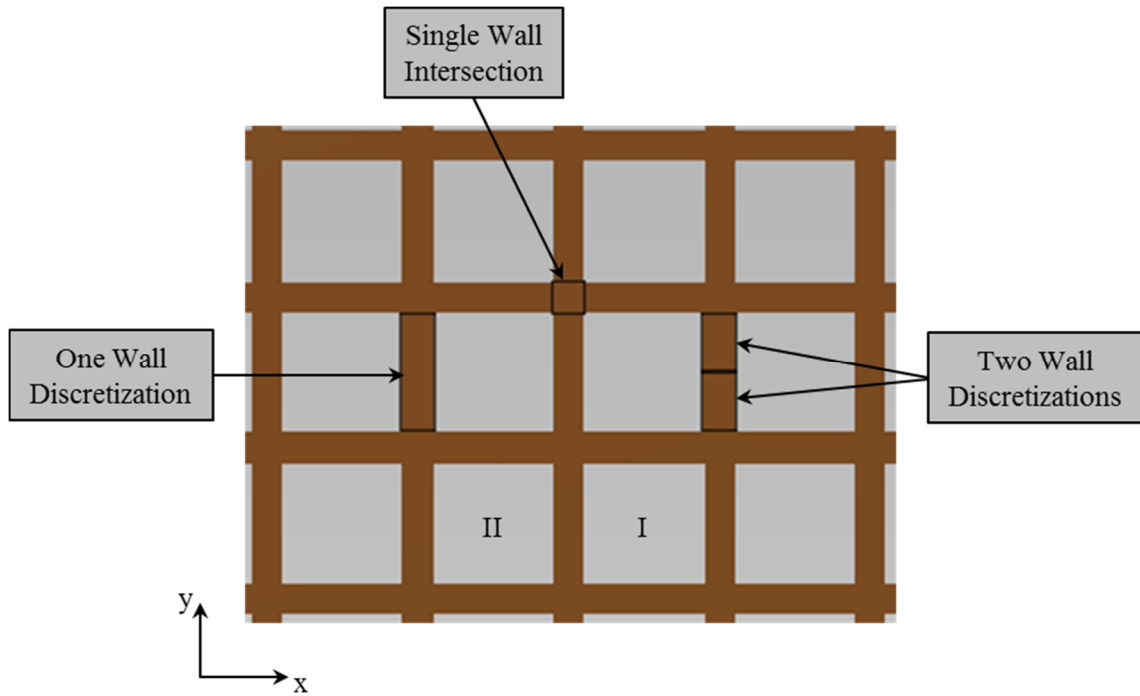
Figure 64: Discretization of the filter grid into cells, including different wall discretizations.

Also shown in Figure 64 are examples of flowable walls (those labeled one wall discretization and two wall discretizations) and non-flowable walls (labeled single wall intersection).

The following is a description of the wide range of geometric quantities that need to be calculated for each cell, along with the rationale behind each calculation. For the slice model, all of the modeling activities occur on the x-y plane, and each cell is assumed to be at a constant temperature. In order to allow distance calculations for phenomena such as conduction, the centroid of each cell is calculated, ignoring the presence of the DPF boundary. The effects of the DPF boundary on these calculations are accounted for later in the model. Finding the centroid occurs exactly as in calculating the center of mass:

$$C_x = \frac{\sum C_{ix} A_i}{\sum A_i} \tag{7.1}$$

$$C_y = \frac{\sum C_{iy} A_i}{\sum A_i} \tag{7.2}$$

166

where C_i and A_i are the central coordinate of a region of the shape and the area of a region of the

shape, respectively, which are summed to calculate the centroid (C). Individual area elements of

a shape may be broken up in any way; one such example using two area elements is given in

Figure 65.

Figure 65: Calculation of cell centroid using multiple elements.

Each cell is then assigned a code corresponding to whether the cell is solid or within a

channel, which becomes important when calculating all the energy terms in the governing

equations. Beyond simply categorizing each cell as solid or channel, the type of solid cell (wall

intersection with no flow or flowable wall) or the type of channel (inlet or outlet) is contained

within each cell's code. Once the cell code calculation is complete, the cross-sectional areas of

each cell are calculated, again deferring consideration of the DPF boundary. Cross-sectional

areas are important for properly accounting for the thermal capacity of the cells.

Another calculation occurring for each cell is the length of each side. Side lengths are

utilized to determine the surface area per unit length available for convection and wall flow.

Such values are calculated simply by the type and orientation of each cell. These lengths are final

for cells not touching the DPF boundary; whereas, border cells have certain lengths recalculated.

Accounting for the DPF boundary occurs next, which begins by calculating the x and y-coordinates of each corner of the cells ignoring the boundary, and then checking whether any of the corners are farther away from the origin than the DPF's radius. Those cells touching the boundary are assigned a code, and different codes are assigned to cells completely inside and outside the boundary.

After being classified as boundary cells, further classification occurs depending on the cell geometry (e.g., three, four, or five sides). For each type of boundary cell, relational statements execute a specific segment of code to update several geometric quantities. The appropriate cell side lengths are recalculated, along with a recalculation of the cell's x-y plane area. Also, cell centroids are recalculated.

In addition to the properties previously mentioned and motivated, the boundary surface area per unit length of the cell (S_o) is calculated; this quantity is utilized in calculating direct convection from the channel gas to the tube interior. Similarly, the center of the border arc is calculated for use in quantifying conduction. With these calculations completed the geometry in the x-y plane is completely known. A visual representation of the slice model's discretization is shown in Figure 66 for a wall discretization of 2, a filter diameter of 0.75 in., a channel size of 0.002 m, and a wall thickness of 0.0005 m. Also in Figure 66, cell boundaries are shown in black, inlet channel cells are shaded yellow, outlet channel cells are shaded magenta, and solid filter walls are shown in red.
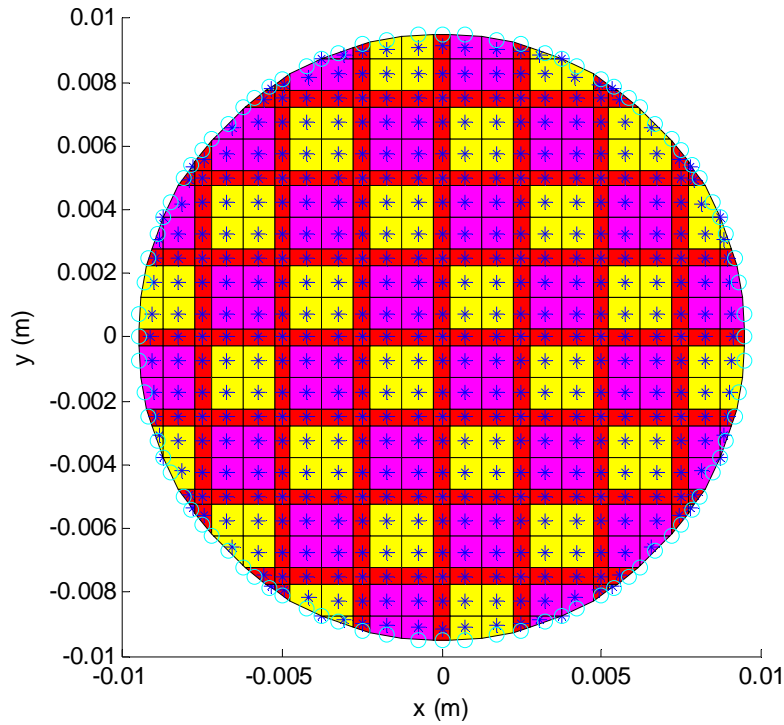
Figure 66: Schematic of slice model filter discretization

Three-dimensional matrices are then created to store the indexes of inlet and outlet channels as follows: the row and column of each cell in a channel is stored as an individual row, with the number of rows in the matrix equaling the number of cells in the channel, and the third dimension is for each different (inlet or outlet) channel. Storage of indexes in this way allows calculations to be completed that are specific to the type of cell (inlet channel, outlet channel, or solid wall) without logical statements, which is less computationally less expensive. The matrix of indices is also useful in keeping the physical properties within each channel (such as the temperature) uniform for each cell.

Traditional DPF models have the same filter wall length where flow enters the wall (inlet channel) as where flow exits the wall (outlet channel). This condition does not exist at certain locations along the boundary of the DPFHX core; hence, the average length between these two is used to represent the flowable area of the wall per unit axial length (S_{1s}). Such a technique

recognizes that flow will not exclusively pass in the direction perpendicular to channel flow in these rare unique areas.
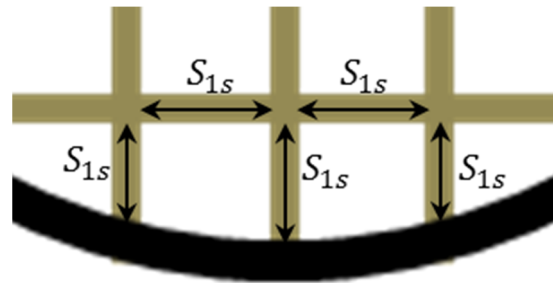
Figure 67: Examples of flowable area of individual walls per unit length

After loading measurements from the University of Kansas' Yanmar L100V engine test cell in Table 12, which is a duplication of Table 4 for the convenience of the reader, experimental data from the engine for a single operating point is incorporated. Exhaust species concentrations are then calculated based on the idealized lean combustion calculations of Chapter 3. A suitable time step for the simulation is then determined from the stability criterion (Forward-Time Centered-Space – FTCS) using a multiplier (less than one) to account for the limitations imposed by the convection and external heat transfer terms not present in the simplified time-step expression.

Table 12: Steady-state operating conditions of Yanmar L100V engine

Operating Point	Power (kW)	T_{ex} (K)	P_{ex} (kPa)	A/F (-)	$\dot{m}_{ex}$ (g/s)
1	0.23	491.92	100.66	57.04	11.13
2	1.73	547.46	100.63	43.25	11.08
3	3.41	619.35	100.67	33.26	11.39
4	5.00	701.63	100.90	25.49	11.28
5	6.21	785.29	101.56	20.55	11.20

Using the mole and mass fractions of the exhaust mixture, REFPROP is utilized to calculate representative thermodynamic properties of: specific gas constant (R_{ex}), specific heat at contant pressure (c_p), and absolute (dynamic) viscosity (μ). These properties are not calculated

repeatedly in the program to limit computational times; therefore, a representative temperature is chosen as the average temperature between the exhaust inlet temperature and the previously-chosen working fluid temperature. Selection of the working fluid temperature occurs through identifying a common boiling temperature (i.e., 380 K) for efficient dry working fluids operating at optimal expansion ratios (see Chapter 3). Also, constant convective coefficients on the exterior of the DPFHX and within the DPFHX channels are utilized. The slice model uses a moderate flowing gas convection coefficient of 50 W/(m^{2}K) for the channel flows and a relatively low liquid boiling convection coefficient of 750 W/(m^{2}K), with the latter being a conservative estimate that could also be achieved in the absence of phase change [94].

Specification of the solid filter properties occurs next, where several quantities must be known before initiating simulations. Such characteristics are: filter permeability (K_f), filter density (ρ_f), filter specific heat (c_f), and filter thermal conductivity (k_f). The primary determinant of these physical properties is the material from which the filter is constructed (Cordierite or Silicon Carbide); however, other influential factors exist such as soot loading and the manufacturing processes utilized. The simulations here simply use a single representative core made from each material, with the physical properties listed below:

Table 13: Physical properties of Cordierite and Silicon Carbide [167, 168]

DPF Material	Permeability (m^2)	Density (kg/m^3)	Specific Heat (J/(kg·K))	Thermal Conductivity (W/(m·K))
Cordierite	3E-13	2600	1465	3
Silicon Carbide	3.25E-13	3100	750	15

As a last step before performing calculations at the initial time, a module of code allows for preconditioning the thermal capacitance of each solid wall cell [152]. This is a common technique to reduce the instabilities associated with large cell size variations, as can be found on

the perimeter of a DPFHX core. By preconditioning small cells to have a higher specific heat, their energy capacity becomes comparable to larger cells and reduces temperature fluctuations between time steps. Since cells are not heating up or cooling down at steady-state, preconditioning does not contribute inaccuracies to steady solutions.

The initial filter solution calculates from the test cell conditions previously loaded, and separates the mass flow into each inlet channel based on the wall surface area of the channel over the length of the filter. In other words, the amount of mass flow coming into the channel is proportional to the area available for wall flow leaving the channel. Other inlet parameters, such as temperature, pressure, density, and velocity, are assumed uniform at the filter inlet.

Filter wall temperatures are set initially to the working fluid temperature, in order to reduce any large temperature swings creating instability in the early stages of simulation. Also, the filter outlet temperatures, where flow comes from the adjacent walls at the working fluid temperature, are set to the working fluid temperature. The remaining portion of the initial solution calculations pertain to the filter wall, where the outlet channel pressure results from an initial guess, producing the wall pressure as the average of the inlet and outlet channel pressures (each of which are uniform). Subsequently, the density and velocity of wall flow are calculated with the ideal gas law and wall mass flow, respectively.

While the wall flow calculations are relatively simple, they are only conducted correctly by assigning wall flow only to solid filter cells that have area and are bordered by both an inlet and outlet channel. As a last step before beginning the iterative portion of the code, the newly calculated wall flow is utilized to create a three-dimensional matrix of cells with wall flow, similar to that described for inlet and outlet channels above. Again, such a matrix streamlines the application of equations that are applicable only to certain types of cells (e.g., inlet channels).

7.3.2 Iterative Steady-State Solver

The governing equations must be resolved in a specific order to achieve physically-based solutions. In particular, the DPFHX theoretical expressions can be repeatedly solved until reaching steady-state conditions following the initial guess for the filter temperature. This leads into the solver formulation, which includes the order that the equations are solved and the handling of different types of cells, each of which have different governing equations. For the slice model, calculation of new non-boundary solid wall cell temperatures occurs first.

For non-boundary solid wall cells that do not contain flow (at the wall intersections), the energy equation is:

$$\left(\rho_{f|i,j}c_{f|i,j}A_{i,j}\right)\frac{\partial T_{f|i,j}}{\partial t} = \dot{Q}_{cond,x} + \dot{Q}_{cond,y} \tag{7.3}$$

where $\dot{Q}_{cond,x}$ and $\dot{Q}_{cond,y}$ consist of:

$$\dot{Q}_{cond,x} = \frac{2A_{i,j}}{(dx_+ + dx_-)}\left(\frac{dT_{x+}k_{f|x+}}{dx_+} - \frac{dT_{x-}k_{f|x-}}{dx_-}\right) \tag{7.4}$$

$$\dot{Q}_{cond,y} = \frac{2A_{i,j}}{(dy_+ + dy_-)}\left(\frac{dT_{y+}k_{f|y+}}{dy_+} - \frac{dT_{y-}k_{f|y-}}{dy_-}\right) \tag{7.5}$$

In Eq's (7.3)-(7.5), the subscripts i and j refer to the matrix entries in the x and y directions respectively. Of note, the wall intersections are the only locations with conduction in the x and y directions. Also, the + and - notation signifies the direction in which the property is evaluated. For example, dT_{x+} is evaluated as follows:

$$dT_{x+} = T_{i,j+1} - T_{i,j} \tag{7.6}$$

The form of Eq.'s (7.4)-(7.5) is valuable in allowing non-uniform spacing in the grid as found in the wall simulations of [49].

For non-boundary solid wall cells that do contain flow (not wall intersections), the energy equation is:

$$\left(\rho_{f|i,j}c_{f|i,j}A_{i,j}\right)\frac{\partial T_{f|i,j}}{\partial t} = \dot{Q}_{cond,x} + \dot{Q}_{cond,y} + \dot{Q}_{conv} + \dot{Q}_{wall} \tag{7.7}$$

where $\dot{Q}_{cond,x}$ and $\dot{Q}_{cond,y}$ remain as Eq.'s (7.4)-(7.5) and $\dot{Q}_{conv}$ and $\dot{Q}_{wall}$ will be described shortly. For flowable walls, one conduction term is non-zero. Example cells with conduction in both directions, as well as each direction individually, are shown in Figure 68.
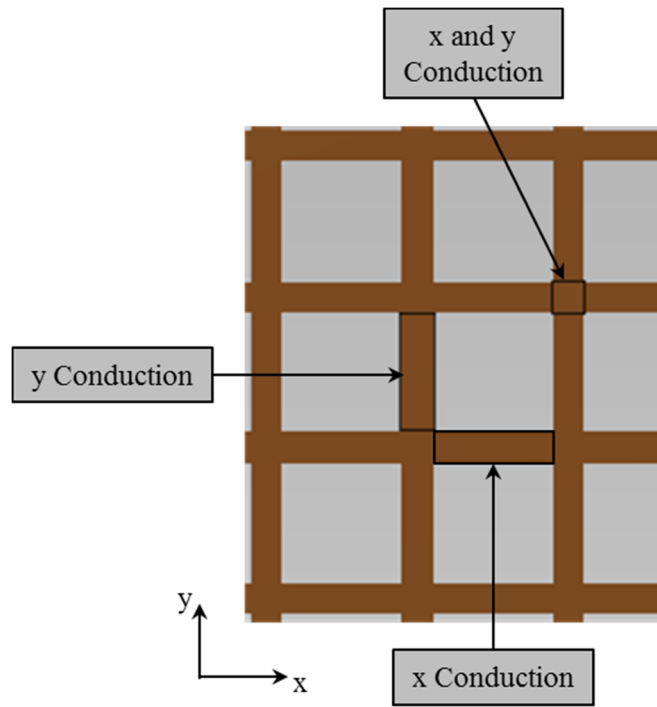
Figure 68: Example cells with *x* and *y* conduction, *x* conduction, and *y* conduction

Calculation of $\dot{Q}_{conv}$ follows from:

$$\dot{Q}_{conv} = h_g\big[S_{x-|i,j+1}\left(T_{i,j+1} - T_{i,j}\right) + S_{x+|i,j-1}\left(T_{i,j-1} - T_{i,j}\right)$$
$$+ S_{y-|i+1,j}\left(T_{i+1,j} - T_{i,j}\right) + S_{y+|i-1,j}\left(T_{i-1,j} - T_{i,j}\right)\big] \tag{7.8}$$

The convection terms on the right-hand-side of Eq. (7.8) represent the length of one side of the neighboring cell (the S terms) and the temperature difference between that cell and the solid wall cell where energy is being calculated (location i,j). These surface area per unit length

terms for neighboring cells are only non-zero when the neighboring cell is within an inlet or outlet channel. In other words, some of the neighboring cells will also be solid wall cells where there is no convection to the cell under evaluation.

In Eq. (7.7), $\dot{Q}_{wall}$ is the energy transferred as flow passes through the wall, and calculation of the term occurs from:

$$
\dot{Q}_{wall} = \rho_{w|i,j} u_{w|i,j} c_p \big[S_{1s|y+|i,j}(T_{i+1,j} - T_{i,j}) + S_{1s|y-|i,j}(T_{i-1,j} - T_{i,j}) \\
+ S_{1s|x-|i,j-1}(T_{i,j-1} - T_{i,j}) + S_{1s|x+|i,j+1}(T_{i,j+1} - T_{i,j}) \big]
\tag{7.9}
$$

For calculation of solid cells (with and without flow) that touch the filter boundary, application of a boundary condition occurs. In the case described here, the thermal resistance found at the joint between the filter core and DPFHX tube interior is accounted for, along with the thermal resistance of the radial conduction to the tube exterior and the working fluid convection on the tube exterior.

Inclusion of the thermal resistance surface boundary condition occurs with a balance of the heat conducting from the core to the heat passing from the core boundary to the working fluid. The condition specified is a boundary condition of the third kind, or a condition obtained from a surface energy balance. Since the form of the equation varies based on the boundary being in the *x* or *y* direction, an example for the *x*-direction is provided in Eq. (7.10) and that for the *y*-direction is given by Eq. (7.11).

$$
-k_f A_f \frac{\partial T_f}{\partial x}\bigg|_{\frac{D_{DPF}}{2}} = \frac{T_f\big|_{\frac{D_{DPF}}{2}} - T_{wf}}{R_t}
\tag{7.10}
$$

$$
-k_f A_f \frac{\partial T_f}{\partial y}\bigg|_{\frac{D_{DPF}}{2}} = \frac{T_f\big|_{\frac{D_{DPF}}{2}} - T_{wf}}{R_t}
\tag{7.11}
$$

The filter's temperature (T_f) and thermal conductivity (k_f) combine with the filter's local conductive area (A_f) to create the left hand side of Eq.'s (7.10)-(7.11), while the right hand side also involves the total thermal resistance from the filter boundary to the working fluid (R_t), along with the terminal temperature of the heat transfer (T_{wf}).

Thus, using a finite difference approximation of the temperature derivative, the resulting expression at a positive x-boundary is:

$$T_f\big|_{\frac{D_{DPF}}{2}} = \frac{1}{1 + \frac{R_t k_f A_f}{x_{\frac{D_{DPF}}{2}} - x_{i,j}}}\left(T_{wf} + \frac{R_t k_f A_f}{x_{\frac{D_{DPF}}{2}} - x_{i,j}}T_{i,j}\right) \tag{7.12}$$

Similarly, at a positive y-boundary:

$$T_f\big|_{\frac{D_{DPF}}{2}} = \frac{1}{1 + \frac{R_t k_f A_f}{y_{\frac{D_{DPF}}{2}} - y_{i,j}}}\left(T_{wf} + \frac{R_t k_f A_f}{y_{\frac{D_{DPF}}{2}} - y_{i,j}}T_{i,j}\right) \tag{7.13}$$

At negative x-boundaries:

$$T_f\big|_{\frac{D_{DPF}}{2}} = \frac{1}{1 + \frac{R_t k_f A_f}{x_{i,j} - x_{\frac{D_{DPF}}{2}}}}\left(T_{wf} + \frac{R_t k_f A_f}{x_{i,j} - x_{\frac{D_{DPF}}{2}}}T_{i,j}\right) \tag{7.14}$$

And at negative y-boundaries:

$$T_f\big|_{\frac{D_{DPF}}{2}} = \frac{1}{1 + \frac{R_t k_f A_f}{y_{i,j} - y_{\frac{D_{DPF}}{2}}}}\left(T_{wf} + \frac{R_t k_f A_f}{y_{i,j} - y_{\frac{D_{DPF}}{2}}}T_{i,j}\right) \tag{7.15}$$

As an extension of the DPFHX heat transfer mechanism discussion of Chapter 5, the total thermal resistance between the filter boundary and the working fluid consists of three parts. The interface between the filter and the tube interior is not a resistance-free joint; therefore, a thermal contact resistance is present over a short distance. Heat then proceeds via radial conduction to the

tube exterior, where convection transfers heat to the working fluid. Since these thermal resistances occur in series, the total thermal resistance is calculated as the sum of each individual stage, as found in Eq. (7.16).

$$R_t = \sum_{n=1}^{N} R = \frac{R_{tc}}{A_{tc}} + \frac{ln\left(D_{TO}/D_{TI}\right)}{2\pi k_T \Delta z} + \frac{1}{h_{TO,wf} A_{TO}} \tag{7.16}$$

In Eq. (7.16), R_{tc} and A_{tc} are the thermal contact resistance and the cross-sectional area of the contact resistance, while D_{TO} and D_{TI} are the outer and inner diameters of the tubes. Also, k_T is the thermal conductivity of the tubes and $h_{TO,wf}$ is the convective heat transfer coefficient between the tube exterior and the working fluid.

A simplification of Eq. (7.16) recognizes the coupling between the filter conduction area and the thermal resistance terms, which all involve a distance in the z-direction. Removing the z-direction dependency from Eq. (7.16) produces a slice thermal resistance:

$$R_{tz} = \sum_{n=1}^{N} R_z = \frac{R_{tc}}{S_o} + \frac{ln\left(D_{TO}/D_{TI}\right)}{2\pi k_T} + \frac{1}{h_{TO,wf} S_o \frac{D_{TO}}{D_{TI}}} \tag{7.17}$$

The updated boundary conditions using this form are:

$$T_f\big|_{\frac{D_{DPF}}{2}} = \frac{1}{1 + \frac{R_{tz} k_f \Delta y}{x_{\frac{D_{DPF}}{2}} - x_{i,j}}} \left(T_{wf} + \frac{R_{tz} k_f \Delta y}{x_{\frac{D_{DPF}}{2}} - x_{i,j}} T_{i,j} \right) \tag{7.18}$$

$$T_f\big|_{\frac{D_{DPF}}{2}} = \frac{1}{1 + \frac{R_{tz} k_f \Delta x}{y_{\frac{D_{DPF}}{2}} - y_{i,j}}} \left(T_{wf} + \frac{R_{tz} k_f \Delta x}{y_{\frac{D_{DPF}}{2}} - y_{i,j}} T_{i,j} \right) \tag{7.19}$$

$$T_f\big|_{\frac{D_{DPF}}{2}} = \cfrac{1}{1 + \cfrac{R_{tz}k_f\Delta y}{x_{i,j} - x_{\frac{D_{DPF}}{2}}}} \left(T_{wf} + \frac{R_{tz}k_f\Delta y}{x_{i,j} - x_{\frac{D_{DPF}}{2}}} T_{i,j} \right) \tag{7.20}$$

$$T_f\big|_{\frac{D_{DPF}}{2}} = \cfrac{1}{1 + \cfrac{R_{tz}k_f\Delta x}{y_{i,j} - y_{\frac{D_{DPF}}{2}}}} \left(T_{wf} + \frac{R_{tz}k_f\Delta x}{y_{i,j} - y_{\frac{D_{DPF}}{2}}} T_{i,j} \right) \tag{7.21}$$

Using a tube wall thickness of 1/16", a tube thermal conductivity similar to stainless steel (17 W/(m·K)), a convective heat transfer coefficient of 750 W/(m^2·K), simulations are possible including the surface energy balance. Specification of a representative thermal contact resistance without performing experiments on the actual physical setup involves uncertainties [95]; however, known results from a similar joint can provide a good estimate. Since the current configuration may involve an epoxy joint between a metal and a ceramic, the model utilizes a typical thermal resistance for an epoxy joint between a silicon chip and aluminum of 0.55E-4 m^{2}K/W.

The contributions of the different thermal resistances are often disproportionate, allowing one or more terms to be neglected. Simple calculations may provide context on the relative importance of including each thermal resistance term. Before beginning to discuss the elements of the surface energy balance from the boundary of the filter to the working fluid, the process of heat reaching the boundary is also relevant. Thermal conduction is the primary mechanism responsible for heat reaching the boundary of the DPFHX cores. Due to heat entering the filter core throughout the slice cross-section, the conduction distances are constantly changing, as are the temperature gradients. Thus, while recognizing the distances present and materials of limited thermal conductivity, conduction to the boundary must be included in the model.

As the first stage of heat transfer from the filter boundary to the working fluid, the thermal contact resistance will begin the analysis. With a thermal resistance of 0.55E-4 m²·K/W and recognizing that a typical border surface area per unit axial length of a cell is approximately the filter wall thickness (0.0005 m), the slice thermal resistance is 0.11 m·K/W. The radial conduction term is then 0.0011 m·K/W, and the exterior convection term is the dominant resistance at 3.55 m·K/W. Thus, at least the radial conduction term may be safely omitted from the computations.

Occasionally, a boundary cell may conduct to adjacent cells in the x and y directions, in which case the conduction terms would not include the influence of the boundary. For these rare cells, an additional energy term ($\dot{Q}_{DPFHX,bcond}$) allows heat transfer from the small portion of the cell touching the boundary:

$$\dot{Q}_{DPFHX,bcond} = -\frac{T_f\big|_{\frac{D_{DPF}}{2}} - T_{wf}}{R_{tz|i,j}} \qquad (7.22)$$

where $R_{tz|i,j}$ is the slice thermal resistance of Eq. (7.17). An example cell where this would occur is shown in Figure 69.
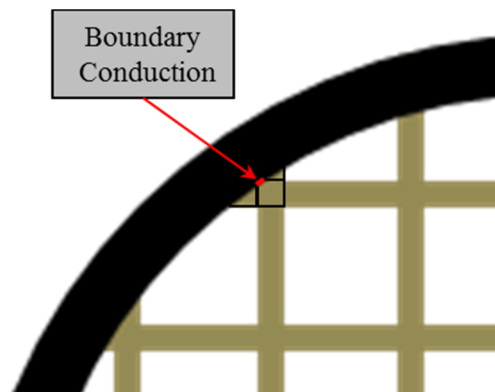

Figure 69: Solid filter conduction to boundary.

After calculation of the new filter temperatures, the gaseous properties following the time step are calculated. Much of the calculation process is designed to produce an average pressure

drop across the filter walls for use in calculating wall flow properties. The use of an average wall velocity has been used recently by Depcik [166]. In the current model, the wall flow speeds throughout the entire trap are weighted by the surface area per unit length the flow passes through in determining an overall average velocity. With the average wall velocity the outlet channel pressure can be determined using Darcy's law.

$$P_{II} = P_I - \left(\frac{u_{w|avg}\mu_w t_{fw}}{K_{fw}}\right)$$

(7.23)

As in Chapter 4, μ_w, t_{fw}, and K_{fw} stand for the wall flow's viscosity, the thickness of the filter walls, and the permeability of the filter walls, respectively. The viscosity of the wall flow is found using REFPROP, while the filter wall thickness and permeability are constants for the simulated filter.

The outlet channel pressure is then assigned to the cells that have an outlet channel code, and the inlet channel pressure remains a specified inlet condition. Using the inlet and outlet channel pressures, the wall pressure can be found as an average as done prior [103]:

$$P_w = \frac{P_I + P_{II}}{2}$$

(7.24)

Subsequently, the final properties of the exhaust within the wall can be calculated. The flow's temperature is identical to the solid filter that the flow is passing through (Eq. (4.31)). The ideal gas law can be utilized to determine the density (Eq. (4.43)), and speed of the wall flow comes from the known amount of flow moving through the cell and the flow's density (Eq. (4.6)).

Since all inlet channel temperatures are known due to being inlet conditions, the final temperature computation is the weighted average of the flows coming into each individual outlet

channel. Starting with an energy balance of the flows coming into an outlet channel (Eq. (7.25)), the constant specific heat assumption leads to the final form in Eq. (7.26):

$$\sum_{c=1}^{d} \rho_w u_w h_w S = h_{II|z=0} \sum_{c=1}^{d} \rho_w u_w S \tag{7.25}$$

$$T_{II|z=0} = \frac{\sum_{c=1}^{d} \rho_w u_w T_w S}{\sum_{c=1}^{d} \rho_w u_w S} \tag{7.26}$$

where the summation is over each of the flows coming into an outlet channel. The temperature then leads to the outlet channel density by using the ideal gas law with the known temperature and pressure. As the inlet channels' velocity is known as an inlet condition and the outlet channel velocity at $z=0$ is zero, the gaseous properties throughout the slice are known.

The final segments of code determine the change in temperature of each of the solid wall cells and set the newly calculated values as the old values for the next iteration. Included in the calculations is a measure of the energy loss from the boundary channels directly to the tube interior, applicable to both inlet and outlet channels:

$$\dot{Q}_{DPFHX,bconv} = -h_{g|ex,TI} S_o (T - T_{wf}) \tag{7.27}$$

where the resistance network has immediately been simplified to include only convection in the channels, since radial conduction through the tube and convection from the tube exterior present far less thermal resistance, with the latter being due to a higher surface area and convective coefficient.

Before the old values are erased, the change in temperature of each solid wall cell is calculated and compared to the established convergence requirements. To illustrate the structure of the entire slice model, and the looping structure in particular, Figure 70 is provided.

181
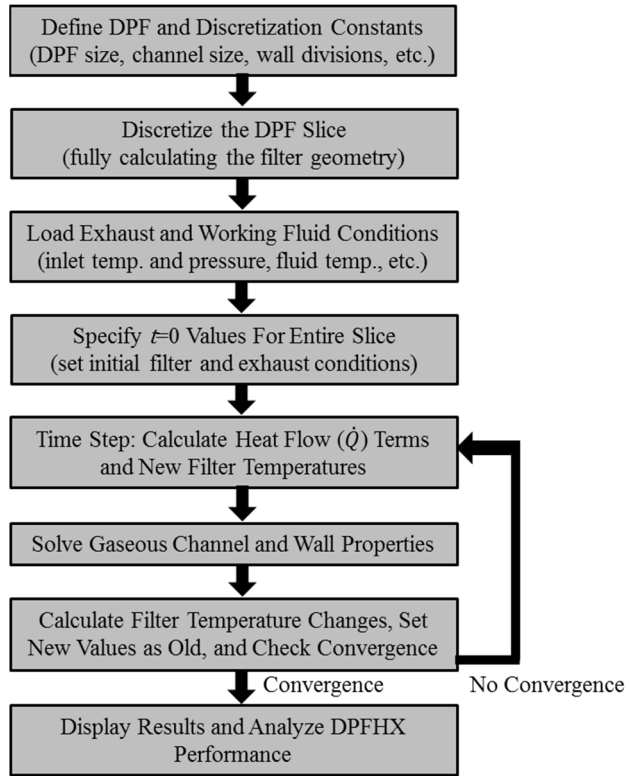
Figure 70: Slice model solver structure

Further illustration is provided by Figure 71, which shows the type of cells that significant equations apply.
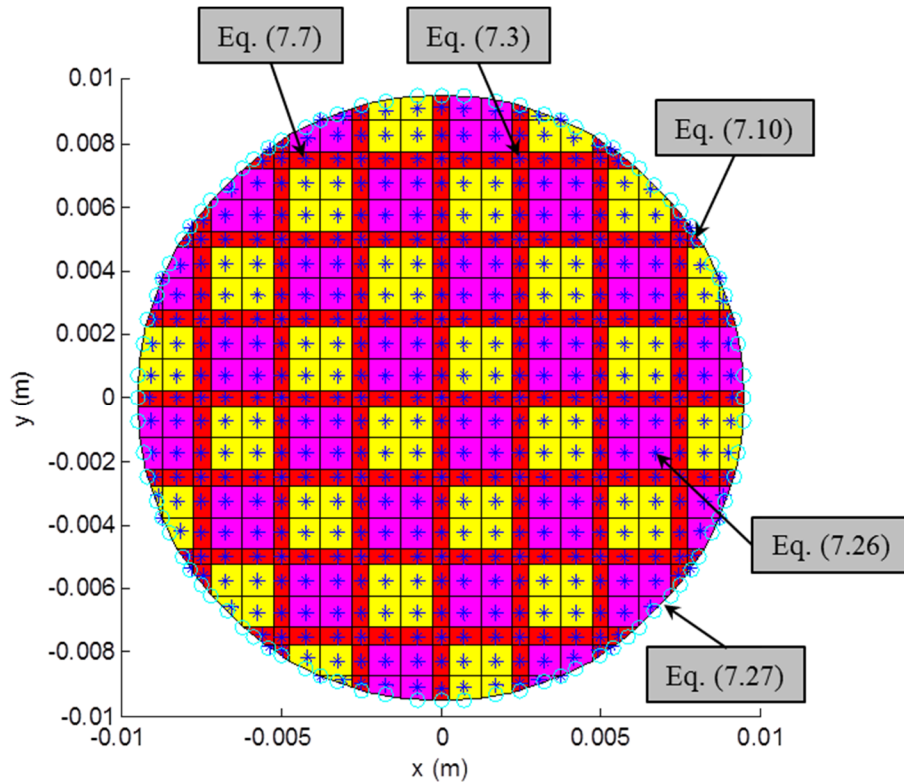
Figure 71: Connection between significant equations and applicable cells.

7.3.3 Slice Model Results

The slice model is particularly useful for drawing comparisons between different DPFHX designs. Relevant decisions include the diameter of the DPF cores, the size of the DPF channels (0.002 m), the thickness of the filter wall (0.0005 m), the length of the DPF cores (15"), the number of DPFHX tubes, and the filter material. Performance comparisons also require consideration of different engine operating points, which is another factor broadening the scope of the simulations.

Since the diameter of the DPF cores and the number of DPFHX tubes are related, pairs of these parameters will be included. Two smaller tube options with nine 0.75" and five 1" cores are investigated alongside two larger tube options with three 1.3" cores and two 1.6" cores, each providing a similar flow area. Flow areas of these options are 3.98 in^2, 3.93 in^2, 3.98 in^2, and

183

4.02 in^2, respectively. These sizes represent a practical range of sizes for a DPFHX design, due to limiting core numbers and preserving heat recovery performance. The two common filter materials previously mentioned, silicon carbide and cordierite, are the materials under consideration. With four geometric pairs and two materials, along with five engine operating points, a total of 40 simulations can be included. However, since the trends can be established with engine operating points 1, 3, and 5, conditions 2 and 4 can be excluded, leaving 24 simulations.

The importance of creating multiple wall divisions (i.e., Figure 64) must be investigated before extending the slice model in the axial direction. Taking the third engine operating point with both materials and 1" cores, the results of Table 14 are generated.

Table 14: Heat Recovery Simulations using Different Wall Discretizations

Number of Cores	Size of Cores	Filter Material	Wall Discretizations	Engine Operating Point 3 Heat Recovery (W/m)
5	1"	Cordierite	3	12268
5	1"	Cordierite	2	12406
5	1"	Cordierite	1	13896
5	1"	Silicon Carbide	3	16864
5	1"	Silicon Carbide	2	17023
5	1"	Silicon Carbide	1	18668

Due to the larger temperature gradients within the filter, cordierite filters benefit more from additional wall discretizations when compared to silicon carbide. Silicon carbide filters have more uniform wall temperatures, as the high thermal conductivity of the cells makes the profile more dependent on the boundary conditions than the interior cells. However, both types of filters can be simulated to ~90% accuracy with a single wall discretization. Furthermore, due to the DPFHX's goal of promoting heat transfer, silicon carbide filter cores are more suited for a final product because of its higher thermal conductivity, while also suffering less inaccuracy with the single wall division discretization.

In running the silicon carbide simulation with a single wall division, convergence occurs after 152 seconds, a substantial reduction in run time from the 560 seconds required with three wall divisions. Such a time reduction contributes to creating a multi-slice model with runtimes of hours instead of days, where roughly one hundred slices must be simulated. However, this metric is an understatement of the reduction in computational burden that occurs, since streamlined computational techniques are available. For example, without having multiple cells in a single channel, routines are not required to keep the thermodynamic properties of all the cells within an individual channel uniform.

Using a single wall discretization and the third operating point, profile comparisons between a material of higher thermal conductivity (silicon carbide) and lower thermal conductivity (cordierite) are straight-forward. As shown by Figure 72, the silicon carbide filter recovers significantly more energy than cordierite filters across the filter sizes. Moving downward, the figure shows 0.75", 1", 1.3", and 1.6" cores, respectively.
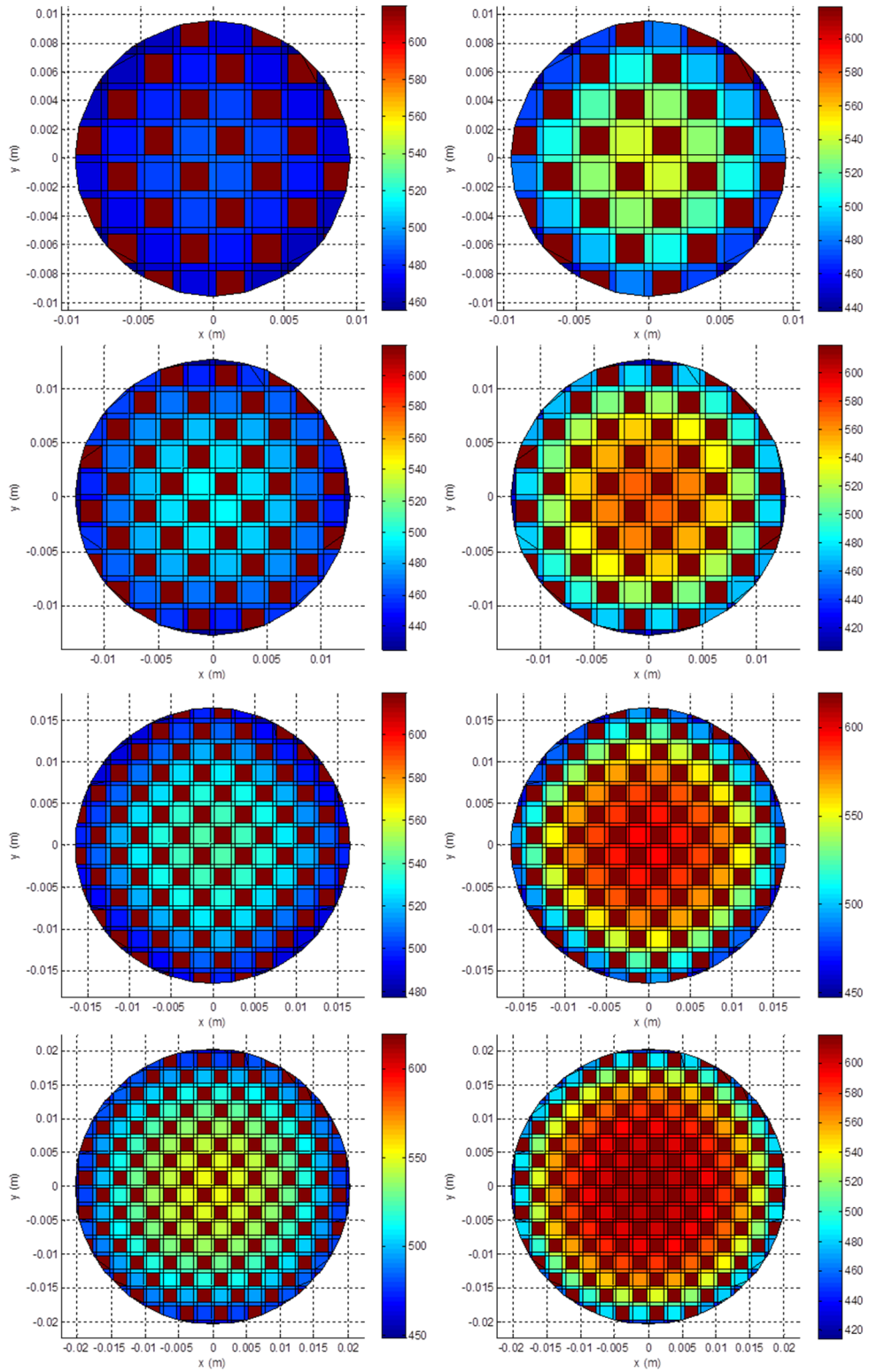
Figure 72: Slice temperature profiles for silicon carbide (left) and cordierite (right) with filter sizes ranging from 0.75'', 1'', 1.3'', and 1.6'' from top to bottom, respectively

Taking into account the direct loss of energy from the channels to the boundary ($\dot{Q}_{DPFHX,bconv}$), and convection between the gas and the wall as the flow is within the inlet channels, walls, and outlet channels, Figure 72 represents the recovery of (moving down each column) 19895, 18668, 14361, and 13931 W/m for silicon carbide and 16841, 13896, 11021, and 9633 W/m for cordierite, respectively. These results, including the remaining 16 simulations, are presented in Table 15 below (Figure 72 and Table 15 are discussed jointly).

Table 15: Slice Model Heat Recovery Results

Number of Cores	Size of Cores	Filter Material	Heat Recovery (W/m)		
			Engine Operating Point 1	Engine Operating Point 3	Engine Operating Point 5
9	0.75"	Cordierite	7827	16841	28604
5	1"	Cordierite	6460	13896	23599
3	1.3"	Cordierite	5128	11021	18706
2	1.6"	Cordierite	4483	9633	16352
9	0.75"	Silicon Carbide	9235	19895	33813
5	1"	Silicon Carbide	8660	18668	31736
3	1.3"	Silicon Carbide	6678	14361	24384
2	1.6"	Silicon Carbide	6476	13931	23658

The results of Table 15 follow three expected trends for increasing heat recovery: use of smaller cores (0.75"), use of materials of higher thermal conductivity (silicon carbide), and the presence of hotter exhaust inlet conditions (engine operating point 5). Smaller cores and higher thermal conductivities lead to lower temperature differences between the middle of the core and the working fluid, reducing thermal resistance and causing increased heat transfer. By the presence of these trends, the model is shown to react naturally/physically to changing simulation parameters.

Looking deeper into the results, the disparity in heat recovery between the cordierite system with 1.6" cores at engine operating point 1 and the silicon carbide system with 0.75" cores at engine condition 5 appears large. The primary contributing factor to this observation is the impact of the temperature difference between the wall and the exhaust gas. Simply stated, the

temperature difference from 380 K to 492 K is around one-fourth of that from 380 K to 785 K. In fact, the numbers across DPFHX configurations follow this paradigm.

Also, the heat recovery rate of the silicon carbide system with 0.75" cores at engine condition 5 appears high, even while keeping in mind that the results shown account for all the cores. The desirable results are due to the efficient heat recovery arrangement, with flow having a high interaction while passing through porous walls that are on average a short distance from the filter boundary. At axial location z=0, this interaction occurs at the highest temperature differences present anywhere in the device, further creating efficient transfer. In other words, 33813 W would not be recovered in the most efficient device with a length of 1 m. Instead, the heat recovery at individual axial locations (W/m) further downstream would continually exhibit less heat transfer.

When considering the use of larger DPFHX cores (such as 1.6"), the impact of the thermal conductivity of the material is more pronounced. For example, the reduction in heat recovery when compared to the smallest cordierite filters at the first operating point is 3344 W/m; whereas, the 1.6" silicon carbide filters recover 2759 W/m less heat than the smallest of the same. This can be envisioned as a larger drop in performance as the filter size is increased due to larger numbers of cells being able to conduct significant heat to the perimeter of the core. Thus, conduction becomes more important as fewer cells border the perimeter and conduction distances increase.

7.4 Multi-Slice Model

There are major similarities in the geometric calculations of the multi-slice model, and only minor differences in filter energy calculations. However, the procedure of solving the governing equations in the channels (mass, momentum, energy, ideal gas) differs significantly.

The first section of the model description will detail the governing equations and solution mechanism, followed by a presentation of the multi-slice model results.

7.4.1 Multi-Slice Model Description

The similarities in the geometric calculation of the filter begin with the scope, which remains eliminating the simplification of homogenizing the trap and unpairing individual channels. Those similarities, along with the fact that the geometry of each slice is identical, lend themselves to retaining the slice model's 2D geometric calculation strategy, which completely defines the geometry. However, since one wall discretization has been shown to provide adequate accuracy in predicting heat recovery, calculations summing the contributions of multiple wall cells have been removed to streamline the code and shorten simulation times.

Filter geometric parameters are still required to begin the simulation, with additional importance being on the length of the filter. After which all of the measurable items are calculated for each cell, with some of the most important characteristics being: side lengths, centroid location, presence of boundary, cross-sectional area, and cell type (inlet, outlet, flowable wall, non-flowable wall). Those cells classified as boundary cells receive boundary surface area per unit length and boundary arc center calculations.

Another similarity between the slice and multi-slice model is the inlet parameters, which again come from University of Kansas test data. However, the exhaust conditions are stored in matrices that have an additional dimension, to account for a discretization in the axial (z) direction. Thus, matrices for thermodynamic properties, such as the mass flow rate, pressure, temperature, density, and velocity are three-dimensional instead of two-dimensional. Physical properties of the filter and exhaust gas also remain consistent with the slice model.

The final model area of high similarity to the slice model is the initial solution. Mass flow is evenly distributed among the filter wall surface area to create an appropriate profile and other inlet parameters are extended to the filter exit. A filter temperature profile guess is provided for subsequent refinement as the model proceeds toward steady-state.

The model differences occur primarily in the looping structure that pursues steady-state, both in the order of calculations and the equations utilized. Each of the applicable equations will be enumerated, followed by the solution algorithm. To avoid having the reader track an initial derivation in Chapter 4 that was modified for the slice model in Section 7.3 and extended to this section, a number of important details will be repeated from previous sections.

Mass conservation in the inlet channel states that the change in mass corresponds to the flows entering the adjacent walls. Thus, the only differences compared to Eq. (4.7) are the absence of soot (leading to the use of a wall density and velocity) and the summation of exiting flows:

$$\frac{\partial \dot{m}_I}{\partial z} = \sum_{c=1}^{d} -S_{Is}\rho_w u_w \tag{7.28}$$

A similar extension occurs from Eq. (4.8) to Eq. (7.29) below for outlet channels, with the change in mass flow being proportional to the total amount of mass exiting the adjacent walls.

$$\frac{\partial \dot{m}_{II}}{\partial z} = \sum_{c=1}^{d} S_{Is}\rho_w u_w \tag{7.29}$$

Inlet channel pressure profiles result from an expression similar to Eq. (4.17) but using the friction term given by Koltsakis et al. [5]. In the expression, the left term represents the resultant force, while the first right hand side term is the wall friction and the last two terms account for the axial change in flow momentum.

$$\frac{\partial p_I}{\partial z} = -\frac{4F\mu \dot{m}_I}{A_I^2} - \frac{2\dot{m}_I}{\rho_I A_I^2}\frac{\partial \dot{m}_I}{\partial z} + \frac{\dot{m}_I^2}{\rho_I^2 A_I^2}\frac{\partial \rho_I}{\partial z} \tag{7.30}$$

The outlet channel momentum equation follows similarly.

$$\frac{\partial p_{II}}{\partial z} = -\frac{4F\mu \dot{m}_{II}}{A_{II}^2} - \frac{2\dot{m}_{II}}{\rho_{II} A_{II}^2}\frac{\partial \dot{m}_{II}}{\partial z} + \frac{\dot{m}_{II}^2}{\rho_{II}^2 A_{II}^2}\frac{\partial \rho_{II}}{\partial z} \tag{7.31}$$

Energy conservation in the inlet channels follows from Eq. (4.39), repeated below for convenience. The left hand side is the result of the original change in channel energy term, which is balanced by convection heat transfer with the adjacent walls.

$$\frac{\partial T_I}{\partial z} = -\frac{S_I}{c_{p,I}\dot{m}_I}h_{g,I}(T_I - T_d) \tag{4.39}$$

To translate the equation to the form necessary for the multi-slice model, the boundary wall is included and convective interactions with individual filter walls are summed. Similar to Section 7.3, S_O is zero for all cells except next to a boundary wall.

$$\frac{\partial T_I}{\partial z} = \frac{1}{c_{p,I}\dot{m}_I}\left[-S_O h_{g,o}(T_I - T_{wf}) + \sum_{c=1}^{d} -S_I h_{g,I}(T_I - T_w)\right] \tag{7.32}$$

Outlet channel energy follows from Eq. (4.40), repeated below for the reader's convenience. As described in Chapter 4, the additional terms when compared to Eq. (4.39) result from being unable to simplify after substituting the outlet channel mass conservation equation.

$$\frac{\partial T_{II}}{\partial z} = -\frac{S_{II}}{c_{p,II}\dot{m}_{II}}\left[h_{g,II}(T_{II} - T_f) - \rho_w u_w(c_{p,w}T_w - c_{p,II}T_{II})\right] \tag{4.40}$$

The multi-slice outlet channel energy equation utilizes the individual wall flows and accounts for the wall boundary.

$$\frac{\partial T_{II}}{\partial z} = \frac{1}{c_{p,II}\dot{m}_{II}} \left[-S_O h_{g,o}(T_{II}-T_{wf}) + \sum_{c=1}^{d}\left(-S_{II}h_{g,II}(T_{II}-T_f)\right) \right. $$

$$\left. + \sum_{c=1}^{d}(S_{Is}\rho_w u_w c_{p,w} T_w) - c_{p,II}T_{II}\sum_{c=1}^{d}(S_{II}\rho_w u_w) \right] \tag{7.33}$$

Throughout the channels and walls, the exhaust conforms to the ideal gas relationship of Eq. (4.43). Using the one wall velocity model of Chapter 4, the wall equations remain unchanged from the slice model and are repeated below.

$$p_I - p_{II} = \frac{u_{w|avg}\mu_w t_{fw}}{K_{fw}} \tag{4.30}$$

$$p_w = \frac{p_I + p_{II}}{2} \tag{4.29}$$

$$T_w = T_f \tag{4.31}$$

The final calculation determines the filter temperature for each solid cell, whether flowable or non-flowable. Extending Eq. (7.7) of the slice model to include $\dot{Q}_{DPFHX,bcond}$ of Eq. (7.22) and conduction in the z-direction produces:

$$\left(\rho_{f|i,j}c_{f|i,j}A_{i,j}\right)\frac{\partial T_{f|i,j}}{\partial t}$$

$$= \dot{Q}_{cond,x} + \dot{Q}_{cond,y} + \dot{Q}_{cond,z} + \dot{Q}_{conv} + \dot{Q}_{wall} \tag{7.34}$$

$$+ \dot{Q}_{DPFHX,bcond}$$

where any of the terms may be zero and are defined in the same way as for the slice model. Those definitions are repeated here:

$$\dot{Q}_{cond,x} = \frac{2A_{i,j}}{(dx_+ + dx_-)}\left(\frac{dT_{x+}k_{f|x+}}{dx_+} - \frac{dT_{x-}k_{f|x-}}{dx_-}\right) \tag{7.4}$$

$$\dot{Q}_{cond,y} = \frac{2A_{i,j}}{(dy_+ + dy_-)}\left(\frac{dT_{y+}k_{f|y+}}{dy_+} - \frac{dT_{y-}k_{f|y-}}{dy_-}\right) \tag{7.5}$$

$$\dot{Q}_{cond,z} = \frac{2A_{i,j}}{(dz_+ + dz_-)} \left(\frac{dT_{z+}k_{f|z+}}{dz_+} - \frac{dT_{z-}k_{f|z-}}{dz_-} \right) \tag{7.35}$$

$$\dot{Q}_{conv} = h_g \left(S_{x-|i,j+1}(T_{i,j+1} - T_{i,j}) + S_{x+|i,j-1}(T_{i,j-1} - T_{i,j}) \right.$$
$$\left. + S_{y-|i+1,j}(T_{i+1,j} - T_{i,j}) + S_{y+|i-1,j}(T_{i-1,j} - T_{i,j}) \right) \tag{7.8}$$

$$\dot{Q}_{wall} = \rho_{w|i,j} u_{w|i,j} c_p \left(S_{Is|y+|i,j}(T_{i+1,j} - T_{i,j}) + S_{Is|y-|i,j}(T_{i-1,j} - T_{i,j}) \right.$$
$$\left. + S_{Is|x-|i,j-1}(T_{i,j-1} - T_{i,j}) + S_{Is|x+|i,j+1}(T_{i,j+1} - T_{i,j}) \right) \tag{7.9}$$

$$\dot{Q}_{DPFHX,bcond} = - \frac{T_f\big|_{\frac{D_{DPF}}{2}} - T_{wf}}{R_{tz|i,j}} \tag{7.27}$$

Similar to the slice model, the x, y, and z conduction terms require boundary conditions. In fact, the boundary conditions in the x and y direction remain unchanged from Eq.'s (7.18)-(7.21). On the contrary, the boundary conditions in the z-direction neglect any axial conduction occurring beyond $z=0$ and $z=L$, following the approach of Eq. (4.71).

Specification of the inlet channel conditions at $z=0$ remains unchanged from the slice model, where the mass flow rate at the entrance to the inlet channels is governed by the amount of wall surface area. Inlet temperatures and pressures are known from engine test cell data, leading to the calculation of the density.

The procedure for fixing the outlet channel state at $z=0$ is also similar to the slice model in that the initial temperature is determined by the energy of the different flows entering the outlet channel from the adjacent walls according to Eq. (7.26). And in order to retain uniform outlet channel pressure, the pressure drop calculation uses an average wall velocity at a particular z-location, as in Eq. (7.23).

7.4.2 Multi-Slice Model Solution Mechanism

Despite the significant differences between the governing equations of the slice and multi-slice models, as reflected in Section 7.4.1, the solution algorithm differs only slightly. An overview of the strategy employed to resolve the entire filter is shown by Figure 73.
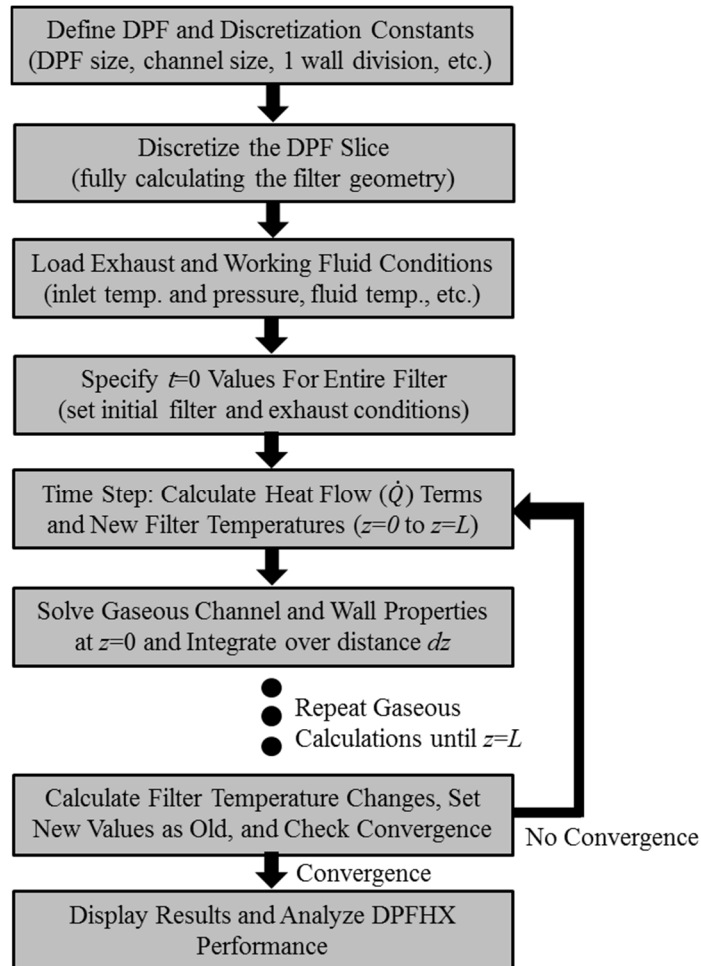
Figure 73: Overview of multi-slice model solution mechanism

Since any single slice of the filter has the same geometry, the first two steps of the multi-slice code are nearly identical to the slice model. The only point of difference is the multi-slice model's requirement of using one wall division, an assumption that was previously shown to have little impact on the overall heat transfer. Future efforts can involve running the code with multiple wall divisions to quantify changes in the overall results.

Continuing the similarity at the beginning of the single slice and multi-slice codes, the first calculation after completing the geometric description of the filter loads the exhaust and working fluid conditions. Since the exhaust conditions loaded only pertain to the first axial position (z=0), the position simulated by the slice model, exactly the same conditions are loaded as in Table 12. On the contrary, working fluid conditions over the entire length of the DPFHX must be entered; however, due to modeling working fluid boiling within the DPFHX, the working fluid condition (i.e., temperature) is assumed the same throughout the shell side of the DPFHX. This was done as an initial scenario to reduce the computational effort and ensure code convergence. Future efforts can involve simulating the heating of working fluid temperature on the shell side of the DPFHX.

Moving to the FTCS filter simulation, the code initializes variables and sets initial conditions over the length of the filter for the solid and gaseous parts of the filter cores. Due to the steady-state focus of the simulations, the values at t=0 are merely arbitrary. With complete profiles at the initial time, a time step occurs and the solid filter temperatures throughout the device are the first calculation.

Resolving the gaseous conditions in the channels and walls requires a more tactful approach, mainly because the inlet channel conditions at z=0 are the only parameters known. Calculation of the gaseous properties begins by determining the wall and outlet channel gaseous properties at z=0. Using these values, derivatives of the channel conditions can be calculated and held constant until the next z-location. With the channel values at z=0+dz, the properties of the slice at that axial location are completely known after calculating the gaseous properties in the wall. The procedure of extending the derivatives to the next axial location and using the channel and solid wall properties there to fix the wall gas state is repeated until z=L. Following a

convergence check, the code either completes another time step using the algorithm above or exits the loop due to reaching the steady-state solution.

7.4.3 Multi-Slice Simulation Results

The full multi-slice filter model allows the prediction of DPFHX waste heat recovery performance across engine operating conditions assuming a uniform working fluid temperature in the ORC evaporator (i.e., boiling). Simulations use a likely final configuration, based on the slice model results of Section 7.3.3. Critical design parameters are: five 1" cores of 15" length to achieve efficient recovery while not incurring excessive manufacturing costs, Silicon Carbide filter walls to promote heat transfer, and a typical grid geometry with 2 mm channels and 0.5 mm thick walls. As with the slice model, a working fluid is boiling at 380 K on the shell side of the device. Critical performance parameters are: an exhaust gas convection coefficient of 40 W/m^2/K, a working fluid convection coefficient of 650 W/m^2/K, a contact resistance between the cores and the tube interior of 0.55E-4 m^{2}K/W, and a thermal conductivity of the tube of 17 W/m/K.

Using these parameters, retaining the one wall division approach supported in Section 7.3.3, simulation of the third engine operating point under different simulation parameters provides evidence of reaching steady-state. In all simulations, discretization points are equally spaced and consist of 100 axial nodes. Using a time step of 0.01s, the applied convergence criteria between iterations is ΔT<0.000005 K. Use of different axial nodes, time steps, and convergence criteria produce results with a high degree of similarity, indicating the sufficiency of the specified model parameters. For example, strengthening the convergence criteria by a factor of ten (ΔT<0.0000005 K) and adding an additional 50 axial nodes (N=150) only alters the heat transfer by 0.023%. Furthermore, a simple validation of the scheme to calculate the outlet

channel pressure at $z=0$ comes from using two different initial guesses, resulting in the same steady-state pressure to beyond one-thousandth of a Pascal.

Despite many of the physical phenomena occurring in the DPFHX being described through the single slice model, this section reinforces those concepts by looking at the multi-slice model's results for a common running condition of the engine. At this, the third operating point, a total of 2674 W of heat is recovered from the five tube DPFHX. This heat recovery total is the primary result of the model and a discussion later in this section will explore the heat recovery from all the engine operating points, after examining the third operating point results and the physical property trends.

Looking at the two sides of the ideal gas law (Eq. (4.43)) also provides support for the model, as ideal gas agreement is shown by (Figure 74) below for the inlet channel nearest the center of the core.
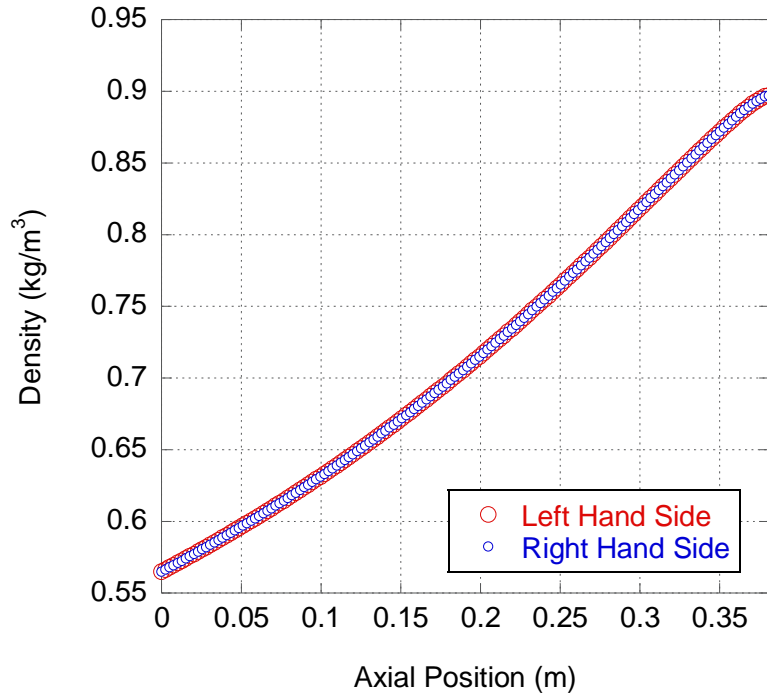
Figure 74: Illustration of the multi-slice model satisfying the ideal gas law.

Further support for the model's accuracy comes from examining other property profiles

for the flowable wall, inlet channel, and outlet channel nearest the center of the core (see Figure

75).
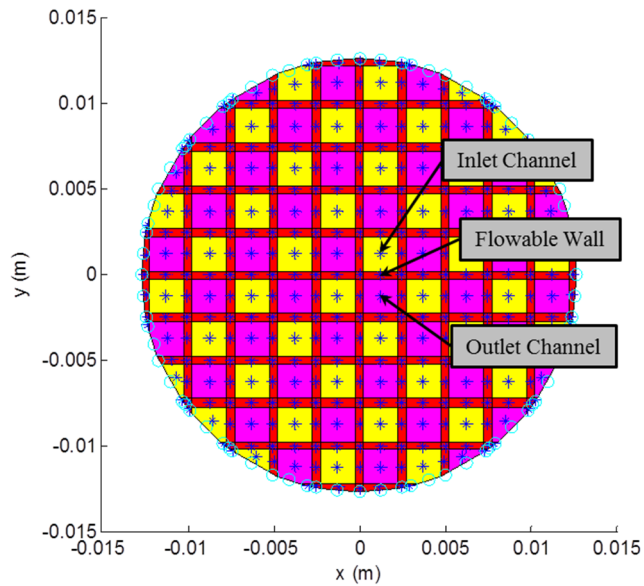
Figure 75: Cells for presentation of axial thermodynamic property profiles.

Temperature profiles for these cells are shown in (Figure 76).
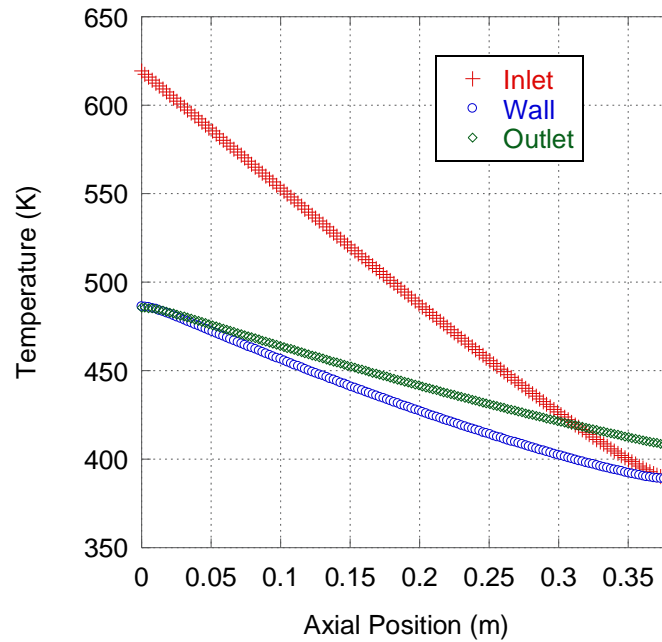
Figure 76: Temperature profiles of neighboring inlet channel, wall, and outlet channel

Here, it must be noted that this model's simulation of unpaired channels impacts the temperature profiles. The inlet channel gases are experiencing convection and flow interactions with four walls, each at different temperatures. Also, the outlet channel is receiving flow from four independent wall segments, each providing flow at the temperature of that wall. However, despite these complexities, these profiles prove the smoothness of the algebraic scheme and display the expected downward trend with larger negative derivatives near $z = 0$.

The easiest trends to understand in Figure 76 are the negative trends of the three cells (inlet, outlet, and wall). Hot exhaust enters the device, which tends to lose heat as the flow proceeds axially towards the exit of the device. Less obvious is the potential for a segment of wall to be at a temperature below the temperatures of the adjacent channels. Posing this question using Figure 75, if the inlet channel above the flowable wall and the outlet channel below the flowable wall are at 455 K and 435 K, respectively, how can the temperature of the wall be 415 K? The answer lies in the ability of the solid cells to conduct heat.

If one end of the wall segment is at a lower temperature than either of the neighboring channels, the heat entering the wall segment has a pathway to escape. This heat transfer mechanism is especially relevant with a silicon carbide filter, as the 15 W/(m·K) thermal conductivity is nearly at the level of stainless steel (17 W/(m·K)). Imagine a tube flowing hot exhaust gas, which then has a rod through the tube running perpendicular to the flow. If one end of the rod extends past the tube and is placed in ice, the rod temperature will be cooler than the hot exhaust gas, as the heat that enters the rod will be lost from the rod as it flows into the ice. An infinitely thermally conductive rod would be entirely the ice temperature, as no thermal resistance would exist between the hot gas and the ice. The same effect occurs in the DPF cores of a DPFHX device, as heat moves towards the cooler working fluid on the outside of the tube.

Since temperature profiles serve a vital role in demonstrating the DPFHX's potential, an area of interest is the temperature profile variation moving away from the center of the DPF cores. Figure 77 provides a detailed look at the temperature profile's dependence on radial position. This figure presents each non-flowable wall in the positive y-direction, holding x=0.
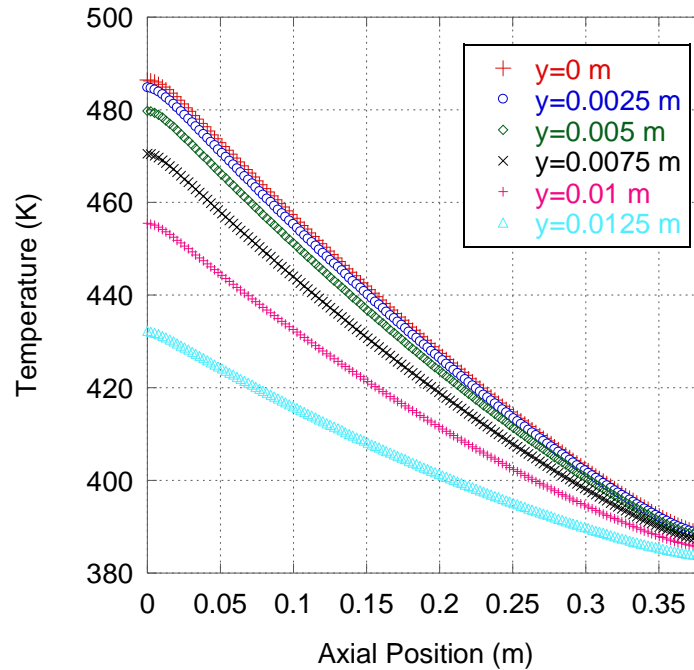
Figure 77: Temperature profiles of non-flowable walls across radial positions

As the cells highlighted in Figure 77 are equally spaced in the *y*-direction, the non-linearity of the profile with radial position is clearly demonstrated. These important profiles apply specifically to DPF heat transfer under the third engine operating point, with the specified heat transfer parameters. Therefore, the profile shown is a unique new result, differing from a radial heat transfer model with uniform heat generation. Both of these differences deserve elucidation.

The grid geometry causes a deviation from purely radial conduction, as conduction toward the working fluid occurs only in the *x* and *y*-directions. Also, since the scale of the DPF channels is approximately one order of magnitude different from the DPF tube diameter, a homogenized model presents a loss of accuracy. Much of the non-linearity results from the non-uniform heat transfer to the cores. Instead of uniform heat generation, heat transfer in the DPFHX cores depends on the temperature difference between the exhaust gas and the solid filter, leading to more heat entering the cores near the perimeter. For example, the exhaust gas enters

all the inlet channels at the same temperature and the walls nearest the perimeter of the DPF are colder, so more heat enters the outer walls than the walls at the center of the DPF core (uniform heat generation would have the same amount of heat entering each wall).

Although temperature is the primary physical property of concern, other property profiles may be examined for comparison with typical DPF results. While mass flow rates are pre-determined based on the available area for flow from each inlet channel, velocities freely vary due to compressible flow. Inlet channel velocities are shown by Figure 78 to exhibit a slightly non-linear concave-up axial decline, while the outlet channels present a similar shape with the opposite trend (concave-down increase) as commonly seen in traditional DPF models [49]. Another result that agrees with the literature is the reduced outlet channel exit velocity when compared to the velocity of flow entering the device; however, this effect is multiplied in a DPFHX due to the considerable heat transfer. This trend is primarily caused by the overall density decrease occurring as the flow cools, resulting in the conservation of mass. Also, the axial velocities shown are moderate for a DPF, which will lead to a slightly lower pressure drop in the channels (and through the walls due to corresponding lower wall velocities).
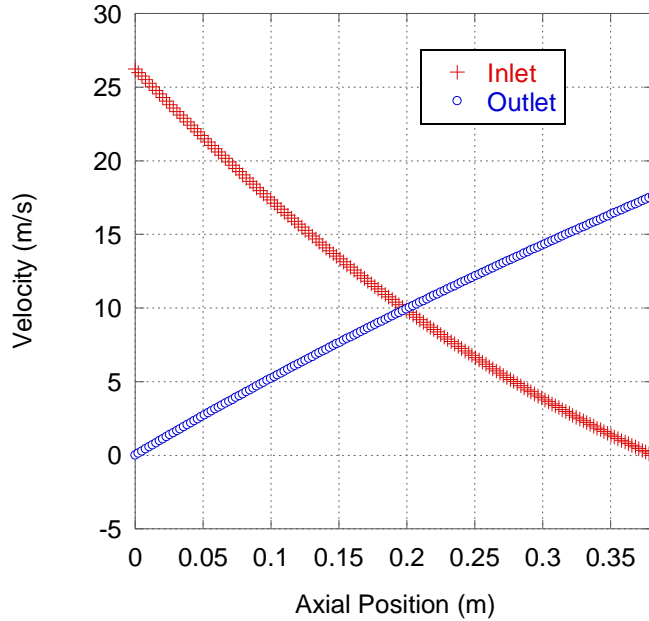
Figure 78: Channel velocity profiles showing slight nonlinearity

To complete the mass flow picture, Figure 79 shows the density profiles, again near the center of the core.
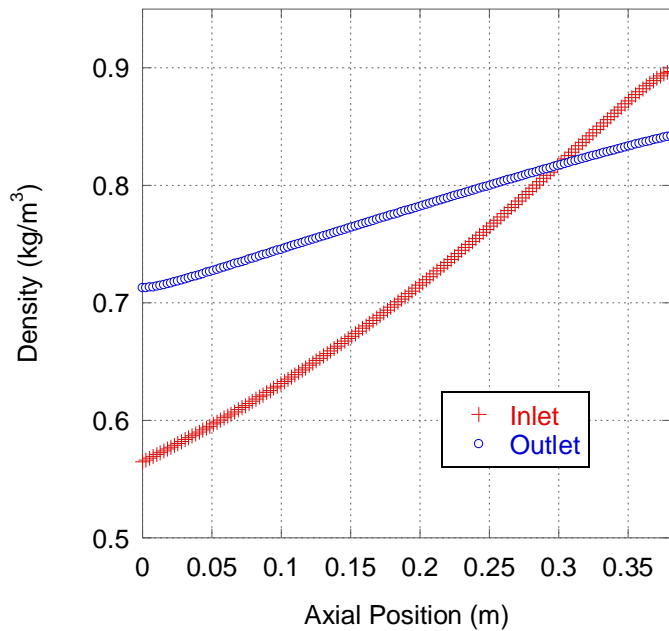
Figure 79: Channel density profiles showing importance of modeling compressibility in DPFHX's

As expected, moving towards the perimeter of the core finds channel gases with higher densities (i.e., cooler temperatures) yet identical profile trends. Also of interest, due to the large variation

in density through the device, Depcik's successful application of a constant density assumption to low heat transfer DPF's [166] is less appropriate in the context of a DPFHX.

Another capability of the multi-slice model is to look at the temperature profile of any axial location, taking an individual slice. Figure 80 below show the temperature profiles at $z = 0,\ z = \frac{L}{2}$, and $z = L$, respectively from top to bottom.
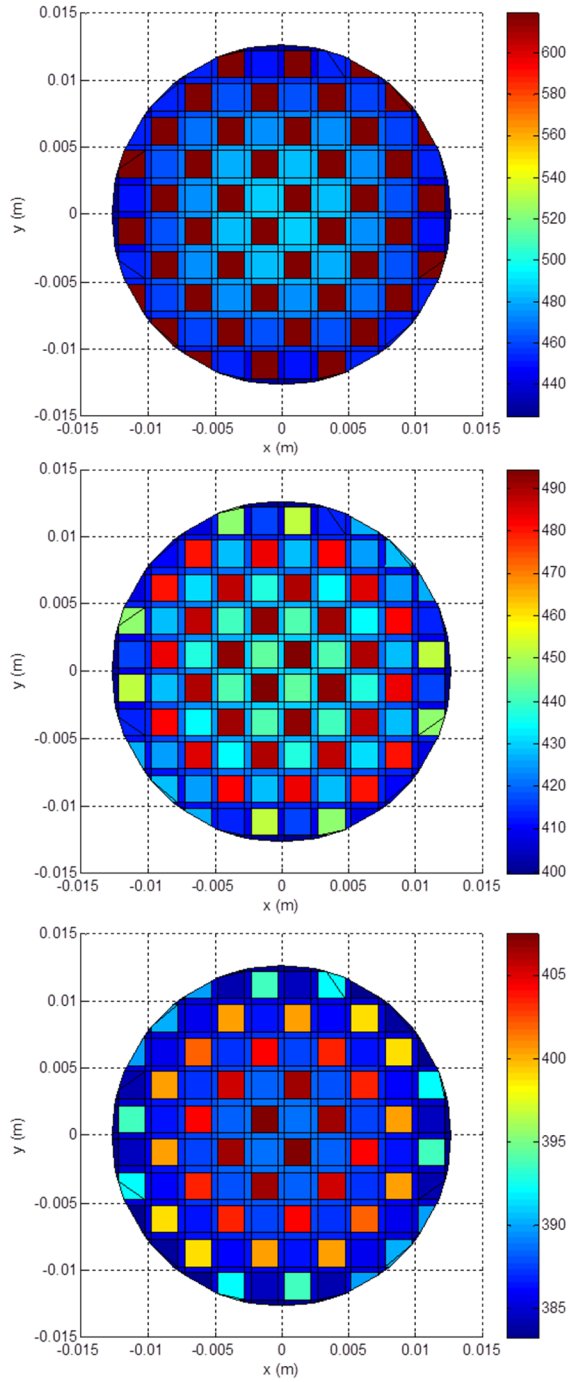
Figure 80: Temperature profiles along axial direction, showing variation in channel and wall profiles

Near the top of Figure 80, the profile at $z = 0$ mirrors Figure 72 in Section 7.3.3, with core

temperatures dropping slightly due to the addition of axial conduction. As heat flows away from

z=0 by solid conduction in the z-direction, the profile at $z = 0$ displays lower temperatures

nearly uniform in temperature as compared to the working fluid.

Figure 80 also offers a visual opportunity to appreciate the similarities and differences

from a purely radial heat transfer model. Similar channel temperatures occur diagonally through

the profile, with sets of yellow, orange, red, and blue channels occurring along diagonal lines.

When looking at these patterns, the diagonal axis of symmetry also becomes apparent. Identical

conditions occur across the axis of symmetry due to the repeating geometric pattern of the DPF.

However, even with the diagonal tendency of the channels, the solid filter exhibits a profile with

temperatures generally decreasing at larger distances from the DPF core's center. This occurs

because, despite the channels altering the heat transfer pathways, heat enters the core throughout

the matrix and proceeds outward following the most direct (least resistance) pathway available.

Simulation of all five engine operating points then provides the performance of the

device across engine loads, as shown in Table 16. Since the working fluid is undergoing phase

change, a behavior with effectively infinite specific heat, the lower heat capacity rate is present

in the exhaust.

Table 16: Multi-slice model heat recovery across engine operating conditions

Engine Operating Point	Waste Heat Recovery (kW)	Engine Power (kW)
1	1.2006	0.2273
2	1.8062	1.7267
3	2.6739	3.4051
4	3.6230	5.0038
5	4.6175	6.2055

These waste heat recovery figures are similar to those from Chapter 3 while operating on around

15% less heat transfer area, demonstrating the potential for efficient DPFHX operation, a pre-

eminent result in the context of evaluating this novel concept. Such large quantities of heat are

only recoverable with efficient heat collectors, such as a DPFHX. By recovering heat at a rate

similar to the engine's power, a heat engine could, for example, boost the engine's efficiency by 10% by operating at 10% efficiency. The quantity of recoverable heat is the main attraction of waste heat recovery technology and the high exergy content of engine exhaust allows more of that heat to be converted to mechanical or electrical power.

At two of the five engine operating points, the rate of heat recovery exceeds the engine's power. The relationship between the two columns of Table 16 depends more on the engine than the waste heat recovery system. In particular, the relationship follows from the relative amounts of exhaust energy available compared to the useful work created by the engine. At the first operating point, the engine produces a small amount of power (0.23 kW) and expels exhaust at a moderate temperature (491 K). Here, the engine is operating inefficiently rather than the DPFHX operating especially well. In fact, the DPFHX performs similarly well across engine operating conditions, with slightly more exhaust energy being expelled at the fifth engine operating point than the first. Knowing the heat transfer rates of the DPFHX across the engine power band, the only further illustration necessary is to translate these heat transfer rates to ORC power generation rates, through the use of another computer model.

7.4.4 ORC Performance using Multi-Slice DPFHX Heat Recovery

Many of this model's parameters are set to match the multi-slice model of Sections 7.4.1-7.4.3, such as the five 1" ID 1.125" OD tubes of 15" length. Also, the heat recovery from the multi-slice DPFHX simulations must be imparted to the working fluid in the ORC evaporator and the evaporating temperature must be 380 K. States of the cycle are similar to those in Chapter 3, with state 1 on the saturated-liquid line ($Q_1=0$) and state 3 on the saturated-vapor line ($Q_3=1$).

Newly selected parameters are based on the high-performing configurations in Chapter 3, where cyclopentane proved to be an attractive working fluid, and operates well at a pressure ratio of 8, leading to reasonable condensing temperatures around 308 K. A pump and expander efficiency of 0.7 and 0.8, respectively, are achievable with current technologies.

Operation of this cycle, using a fixed evaporating temperature and pressure ratio, leads all thermodynamic states to remain identical between engine operating points, with the working fluid flow rate varying significantly. States of the cycle are shown in Table 17.

Table 17: Thermodynamic states of the Organic Rankine Cycle

State	Temperature (K)	Pressure (Pa)	Specific Enthalpy (J/kg)	Specific Entropy (J/kg/K)
1	307.76	60988	-27840	-88.183
2s	307.89	487906	-27256	-88.183
2	308.03	487906	-27006	-87.371
3	380.00	487906	461467	1239.0
4s	314.59	60988	380701	1239.0
4	326.83	60988	396854	1289.3

In operation, the condensing temperature will vary slightly, depending on the amount of heat being rejected from the ORC. At low engine loads, less heat needs to be expelled from the condenser, requiring less of a temperature difference between the ambient air and the condensing working fluid. With this slightly lower condensing temperature at light load engine conditions, the ORC can operate at a higher pressure ratio, enhancing ORC performance as described in Chapter 3. Using the realistic parameters described, Table 18 shows the rate of ORC power generation for each engine operating point using the precise heat recovery indicated by the multi-slice model. The exhaust conditions for the engine operating points referenced in Table 18 can be found in Table 4, and the effectiveness calculation occurs using Eq. (6.2).

Table 18: ORC Power Generation using Heat Recovery of DPFHX.

Engine Operating Point	Pump Work (W)	Expander Work (W)	Evaporator Effectiveness (-)	Cyclopentane Flow Rate (kg/s)	Net ORC Power (W)
1	2.1	158.8	0.515	2.458E-3	156.8
2	3.1	238.9	0.583	3.698E-3	235.8
3	4.6	353.7	0.629	5.474E-3	349.1
4	6.2	479.2	0.660	7.417E-3	473.0
5	7.9	610.8	0.680	9.453E-3	602.9

Consistent with the results of Chapter 3, this ORC offers a thermal efficiency of 13%. As discussed in Chapter 3, since the heat recovery is of similar magnitude to the engine power, this corresponds to roughly a 13% fuel economy improvement. For a more exact measure, the increased efficiency of a Yanmar+DPFHX-ORC system compared to simply a Yanmar engine is shown in Table 19.

Table 19: System Efficiency Improvement by adding DPFHX-ORC

Engine Operating Point	Engine Power (W)	DPFHX-ORC Power (W)	% Efficiency Improvement
1	227.3	156.8	69.0
2	1726.7	235.8	13.7
3	3405.1	349.1	10.5
4	5003.8	473.0	9.5
5	6205.5	602.9	9.7

Table 19 gives the clearest possible indication of the DPFHX-ORC system's potential, with efficiency enhancements from 9.5% to 69.0%. While the 69.0% figure is exceedingly large due to the low load on the engine at that operating point (similar to improving on the 0% efficiency of an engine operating at zero load), it does highlight an additional strength of the system, that power generation can occur without any engine load and can substantially enhance efficiency at low loads. Waste heat is present anytime the engine is running, so power generation will continually occur. With the addition of the DPFHX-ORC system, fuel savings at or above 10% will occur throughout the engine's power band.

Since the translation of recovered heat occurs at the same efficiency across engine operating points, the previous discussion highlighting trends between heat recovery and engine

power applies when comparing ORC power to engine power. The added value of the results in Table 19 comes from measuring the performance impact of the entire DPFHX-ORC system connected to an engine. By adding this system, as described in Chapter 5, hazardous emission conversion remains efficient. At the same time, the use of fuel is significantly reduced. Fuel savings in excess of 10% are simply not achievable by recovering heat from engine coolant, recovering heat from charge air coolers, using turbocompounding, or with advanced in-cylinder techniques. Furthermore, the use of many of the above technologies does not preclude the use of a DPFHX. For example, engine coolant heat could preheat the working fluid before it enters the evaporator, and in-cylinder techniques only have a minor impact on the exhaust conditions entering a DPFHX-ORC system. With the development of the DPFHX-ORC model, the first step towards simulating any of these second generation DPFHX technologies is complete.

Chapter 8

Summary, Conclusions, and Future Work

8.1 Summary and Conclusions

At the outset of this dissertation, a survey of the current internal combustion engine technology motivated the research of a novel aftertreatment device described as a DPFHX. In the recent past, engine manufacturers have employed extensive redesigns to combat the ongoing concerns over fuel prices, oil dependency, and pollution. Thermal efficiency improvements have been achieved using advanced fuel-air mixing, intake air boosting, and changes to valve event timing. However, further gains with these technologies are prohibitively expensive; leading to concerns over whether continually decreasing emission limits and ever-increasing fuel demands can be met. An attractive alternative for reducing fuel consumption and emissions is waste heat recovery, due to the amount of usable energy rejected through the engine exhaust stream and the resurgence of academic and industrial interest in these technologies.

An examination of the energy flows through an ICE reveals that around 1/3 of the fuel's energy is rejected through the engine exhaust at an exergy level sufficient for recovery using a bottoming cycle. Among the available heat engines, organic Rankine cycles are shown to provide efficient WHR using standard components. Furthermore, a historical review of Rankine cycle installations in Chapter 2 suggests the potential for 10% fuel economy improvements [1].

In addition to providing evidence for substantial power generation, the literature guides the construction of an ORC model in Chapter 3 [14].

Historical authors note that proper selection of the cycle's working fluid and expander are crucial in ORC design. Desirable working fluid properties, such as a high critical temperature, low ODP and GWP, low evaporating pressures, and condensing pressures around atmospheric lead to the consideration of eight dry fluids. By using dry fluids, reciprocating expanders with expansion ratios consistent with screw expanders are compatible. Through the creation of a component-based ORC model with reasonable component efficiencies and sizes, cycle efficiencies around 15% and fuel consumption decreases around 10% are shown.

Performance simulations show that butane requires evaporating pressures in excess of 3 MPa, which demands exceedingly robust components for small engines. Air-infiltration concerns with condensing pressures well below atmospheric results in benzene, toluene, and hexane being eliminated from consideration. Of the remaining candidates, pentane and cyclopentane are favored over R245fa and R123 due to higher work outputs across the engine operating points studied. In addition to providing substantial power, pentane and cyclopentane also operate at manageable evaporator and condenser pressures. Using these results, cyclopentane is involved in subsequent DPFHX-ORC simulations, following the creation of a DPF model.

Development of a diesel particulate filter simulation tool is the topic of Chapter 4, where a series of progressively complex efforts individually validate different aspects of the model. Through application of the conservation of mass, momentum, and energy principles to the DPF channels and wall layers, a set of governing equations are established. Solution of these equations occurs in conjunction with the algebraic ideal gas law, leading to the adoption of the DAE solution functionality of MATLAB. The first validation study is the no soot isothermal

212

case [132], where solution of the channels and porous wall layer provide state variable profiles in agreement with [49]. Further advancement of the model takes place by deviating from the isothermal restriction to include a monolith energy equation and soot layer model for the warm up study, leading also to validation with Depcik's 2008 publication. The remaining physical phenomena within the DPF is soot combustion, which is taken into account through comparing a cool down oxidation event featuring fluctuating inlet parameters to published results [49]. This virtual DPF is then available for extension to a DPFHX model, after first describing the DPFHX concept in Chapter 5.

The discussion in Chapter 5 states, "The original DPFHX concept is based on the shell-and-tube heat exchanger geometry, where enlarged tubes contain DPF cores, allowing waste heat recovery from engine exhaust and allowing further energy capture from the exothermic PM regeneration event." A heat transfer mechanism with multiple pathways is described, with a unique pathway for heat to enter the DPFHX tube directly from inlet and outlet channels without requiring the filter substrate as an intermediary. The chapter then concludes with a discussion of the DPFHX in the context of a diesel aftertreatment system with harmful species other than PM requiring conversion. This discussion notes that retaining a DOC before the DPFHX will preserve HC and CO conversion efficiencies, while the SCR catalyst may be moved in front of the DPFHX.

Due to the unique heat transfer mechanism relied upon to heat the working fluid through the DPFHX and future hopes of performing various WHR and ORC experiments in the University of Kansas laboratories, foundational efforts have been made to study waste heat recovery from the Yanmar single cylinder test cell engine. Installment of a custom-built heat exchanger commissioned by another company and later abandoned into the exhaust stream of the

engine, with the proper instrumentation, led to a series of waste heat recovery experiments. Later testing showed an improvement in the energy match between the energy leaving the exhaust and the energy entering the water, suggesting the limitation of water boiling and heat loss to the environment. While the experiments were not meant to evaluate DPFHX performance, the apparatus is available for adoption to waste heat experiments across broader engine operating conditions, and may eventually be used to study a DPFHX prototype. DPFHX performance is instead evaluated through the creation of a novel DPFHX computer model in Chapter 7.

This chapter details the creation of the first DPFHX (and DPFHX-ORC) model through modification of the DPF filter energy equation. Traditional DPF models have a single inlet channel - outlet channel pair, while traditional multi-dimensional DPF models have multiple channel pairs or radial calculation schemes. The model of Chapter 7 began a new type of model with unpaired channels and cells of four types: inlet channels, outlet channels, flowable walls, and non-flowable walls. By calculating the DPF core geometry completely, more detailed calculations covering the entire DPFHX heat transfer mechanism were possible. Using the FTCS numerical scheme, simulations are conducted using input parameters from test cell experiments on a Yanmar L100V engine. These trials iterate until reaching steady-state, at which time the ORC performance can be determined based on the calculated external heat transfer ($\dot{Q}_{DPFHX}$) to the working fluid. Using cyclopentane, the power generation potential of a DPFHX-ORC installation is found at around 11% of the engine output and the convergence criteria are confirmed for pressure, mass flow rate, and temperature. In addition to these gains, the additional benefit of soot combustion suggests that further energy conversion is possible.

Along with the research of the DPFHX's performance, a study of the relevant emissions suggests the device also has the ability to reduce the environmental impact of ICE's. Among the

pollutants under discussion are the EPA governed species of particulate matter, hydrocarbons, carbon monoxide, and nitrogen oxides [2]. Due to the enhanced thermal efficiency of the ICE, around 10% less fuel is being consumed, resulting in 10% less exhaust. This reduces all the emissions to 90% of their former value, before considering the influence of the DPFHX device's impact on converting the harmful species.

After examining the state of low-temperature SCR, the most plausible aftertreatment device sequence is a DOC followed by an SCR catalyst and finally a DPFHX. In this configuration, the conversion of HC and CO in the DOC are unaffected during and after startup. The same rationale is applicable to the removal of NO_x due to placing the SCR before the DPFHX, since WHR occurs downstream of the device. Also, since the catalysts' impact on CO_2 emissions is unaffected, the change in carbon dioxide emissions is proportional to the fuel consumption decrease. The first alteration to the emissions abatement mechanism exists in the DPFHX, where PM filtration must be achieved at reduced temperatures during WHR. Introduction of these conditions is not viewed as a hindrance to PM collection due to the mechanical nature of the filtration mechanisms.

8.2 Future Work

Considering the complexity of the DPFHX-ORC system proposed, and since this dissertation represents the first research of the present concept, numerous opportunities exist for further research. In the immediate future, an expansion of the DPFHX-ORC simulations to define the WHR potential of three ORC working fluids (pentane, cyclopentane, and ammonia) over five engine operating points is warranted. Using these results, further insight into the most appropriate ORC working fluid will be available for use in subsequent efforts.

With respect to experiments, another round of heat transfer trials using the laboratory WHR apparatus can provide further capabilities for future ORC and DPFHX experiments. Adding this functionality will require the accurate measurement of steam production, and thorough insulation to limit heat loss during high temperature operation.

On the modeling side, simulation of regenerative events can substantiate claims of WHR beyond the exhaust's thermal energy due the exothermic oxidation of soot. To complete this study, fixed exhaust conditions entering the DPFHX can be modeled over time with and without the reaction term in the filter energy equation. The difference in WHR over this simulated time period corresponds to the additional energy available to the ORC. Since the ORC model running off of the DPFHX heat recovery is already available, the additional energy flow to the ORC working fluid can also be translated to an increase in power output from the secondary cycle. However, further integration of the DPFHX and ORC models in the future could allow simulation of working fluids in both the liquid and liquid-vapor mixture phases.

A clear example of improving the ORC calculations in the DPFHX-ORC code is using the full ORC code of Chapter 3 to replace the prescribed T_1 of the DPFHX-ORC code with a T_1 calculation as part of the overall solver. Other opportunities in ORC modeling include featuring energy storage in the individual secondary cycle components and developing more detailed models of the components. For instance, the pressure ratio and isentropic efficiency technique for pump and expander modeling can be improved by instead using volumetric ratios and performance maps. Similarly, constant heat transfer coefficients in the condenser can be replaced with published correlations. In the long term, coupling of the DPFHX-ORC model to a virtual engine in the Simulink environment represents a simulation tool not currently discussed in the literature.

References

[1]   C. Sprouse III and C. Depcik, "Review of organic Rankine cycles for internal combustion engine exhaust waste heat recovery," *Applied Thermal Engineering,* vol. 51, pp. 711-722, 2013.

[2]   Environmental Protection Agency. (2012, December 16). *Clean Air Act.* Available: http://www.epa.gov/air/caa/

[3]   H. Teng, G. Regner, and C. Cowland, "Waste Heat Recovery of Heavy-Duty Diesel Engines by Organic Rankine Cycle Part I: Hybrid Energy System of Diesel and Rankine Engines," Society of Automotive Engineers 2007-01-0537, 2007.

[4]   C. Gable and S. Gable. (2013, May 10). *Power Stroke Diesel Engine.* Available: http://alternativefuels.about.com/od/2007dieselvehicles/ig/The-2007-F-Series-Super-Duty-/07_SD-6L-engine.htm

[5]   G. Koltsakis, O. Haralampous, C. Depcik, and J. C. Ragone, "Catalyzed Diesel Particulate Filter Modeling," *Rev Chem Eng,* vol. 29, pp. 1-61, 2013.

[6]   M. Colombo, I. Nova, and E. Tronconi, "A comparative study of the NH3-SCR reactions over a Cu-zeolite and a Fe-zeolite catalyst," *Catalysis Today,* vol. 151, pp. 223-230, 2010.

[7]   G. Qi, Y. Wang, and R. T. Yang, "Selective catalytic reduction of nitric oxide with ammonia over ZSM-5 based catalysts for diesel engine applications," *Catalysis Letters,* vol. 121, pp. 111-117, 2008.

[8]   Transportation Energy Systems. (2012, October 12). *California Energy Outlook 2000.* Available: http://www.hubbertpeak.com/us/ca

[9] T. Endo, S. Kawajiri, Y. Kojima, K. Takahashi, T. Baba, S. Ibaraki*, et al.*, "Study on Maximizing Exergy in Automotive Engines," Society of Automotive Engineers 2007-01-0257, 2007.

[10] Yanmar. (2013, May 10). *L100V Industrial Engine*. Available: http://us.yanmar.com/products/industrial-engines/air-cooled/epa-certified/l-v-series/l100v/

[11] M. Moran and H. Shapiro, *Fundamentals of Engineering Thermodynamics*, 6th ed. Danvers, MA.: John Wiley & Sons, 2008.

[12] C. Wu, *Thermodynamic Cycles: Computer-Aided Design and Optimization*. New York, NY: Marcel Dekker, 2004.

[13] T. Wang, Y. Zhang, Z. Peng, and G. Shu, "A review of researches on thermal exhaust heat recovery with Rankine cycle," *Renewable and Sustainable Energy Reviews,* vol. 15, pp. 2862-2871, 2011.

[14] C. Sprouse III and C. Depcik, "Organic Rankine Cycles with Dry Fluids for Small Engine Exhaust Waste Heat Recovery," *SAE International J Alt Power,* vol. 6, pp. 96-104, 2013.

[15] H. Oomori and S. Ogino, "Waste Heat Recovery of Passenger Car Using a Combination of Rankine Bottoming Cycle and Evaporative Engine Cooling System," Society of Automotive Engineers 930880, 1993.

[16] H. Schmid, "Less Emissions Through Waste Heat Recovery," presented at the Green Ship Technology Conference, London, 2004.

[17] J. Ringler, M. Seifert, V. Guyotot, and W. Hubner, "Rankine Cycle for Waste Heat Recovery of IC Engines," Society of Automotive Engineers 2009-01-0174, 2009.

[18]   N. Espinosa, L. Tilman, V. Lemort, S. Quoilin, and B. Lombard, "Rankine cycle for waste heat recovery on commercial trucks: approach, constraints, and modelling," in *Diesel International Conference and Exhibition*, France, 2010.

[19]   I. Kubo, "Technical and Economic Study of Stirling and Rankine Cycle Bottoming Systems for Heavy Duty Truck Diesel Engines," Cleveland, OH. 1987.

[20]   Y. M. Park and R. E. Sonntag, "A preliminary study of the Kalina power cycle in connection with a combined cycle system," *International Journal of Energy Research,* vol. 14, pp. 153-162, 1990.

[21]   L. Bell, "Cooling, Heating, Generating Power, and Recovering Waste Heat with Thermoelectric Systems," *Science,* vol. 321, pp. 1457-1461, 2008.

[22]   A. I. Kalina, "Combined-Cycle System with Novel Bottoming Cycle," *Journal of Engineering for Gas Turbines and Power,* vol. 106, pp. 737-742, 1984.

[23]   C. Marston, "Parametric Analysis of the Kalina Cycle," *Journal of Engineering for Gas Turbines and Power,* vol. 112, pp. 107-116, 1990.

[24]   U. Desideri, E. Olsson, S. Stecco, and G. Svedberg, "The Ammonia-Water Mixture Rankine Cycle: Considerations on its applicability as Bottoming Cycle," in *IECEC*, Boston, MA, 1991, pp. 449-454.

[25]   C. Marston, "Development of the Adjustable Proportion Fluid Mixture Cycle," *Mechanical Engineering,* vol. 114, pp. 76-81, 1992.

[26]   J. C. Bass, N. Elsner, and F. Leavitt, "Performance of the 1 kW Thermoelectric Generator for Diesel Engines," in *AIP* Kansas City, 1994, pp. 295-298.

[27]   E. Thacher, B. Helenbrook, M. Karri, and C. J. Richter, "Testing of an automobile exhaust thermoelectric generator in a light truck," *Proceedings of the Institution of*

Mechanical Engineers, Part D: Journal of Automobile Engineering, vol. 221, pp. 95-107, 2007.

[28]   E. W. Miller, T. J. Hendricks, and R. B. Peterson, "Modeling energy recovery using thermoelectric conversion integrated with an organic Rankine bottoming cycle," *Journal of Electronic Materials,* vol. 38, pp. 1206-1213, 2009.

[29]   H. Chen, D. Yogi Goswami, M. M. Rahman, and E. K. Stefanakos, "Energetic and exergetic analysis of CO2-and R32-based transcritical Rankine cycles for low-grade heat conversion," *Applied Energy,* vol. 88, pp. 2802-2808, 2011.

[30]   Y. J. Baik, M. Kim, K. C. Chang, and S. J. Kim, "Power-based performance comparison between carbon dioxide and R125 transcritical cycles for a low-grade heat source," *Applied Energy,* vol. 88, pp. 892-898, 2011.

[31]   E. Cayer, N. Galanis, M. Desilets, H. Nesreddine, and P. Roy, "Analysis of a carbon dioxide transcritical power cycle using a low temperature source," *Applied Energy,* vol. 86, pp. 1055-1063, 2009.

[32]   H. E. Khalifa, "Waste Heat Recovery from Adiabatic Diesel Engines by Exhaust-Driven Brayton Cycles," NASA/DOE, 1983.

[33]   M. M. Bailey, "Comparative Evaluation of Three Alternative Power Cycles for Waste Heat Recovery from the Exhaust of Adiabatic Diesel Engines," NASA, 1985.

[34]   M. Bianchi and A. De Pascale, "Bottoming cycles for electric energy generation: Parametric investigation of available and innovative solutions for the exploitation of low and medium temperature heat sources," *Applied Energy,* vol. 88, pp. 1500-1509, 2011.

[35]   F. A. DiBella, L. R. DiNanno, and M. D. Koplow, "Laboratory and on-Highway Testing of Diesel Organic Rankine Compound Long-Haul Vehicle Engine," Society of Automotive Engineers 830122, 1983.

[36]   E. Poulin, R. Demler, I. Krepchin, and D. Walker, "Steam Bottoming Cycle for an Adiabatic Diesel Engine," NASA, 1984.

[37]   S. Stecco and U. Desideri, "Thermodynamic analysis of the kalina cycles: comparisons, problems, perspectives," in *34th ASME International Gas Turbine and Aeroengine Congress and Exposition*, Toronto, Ontario, Canada, 1989.

[38]   M. Jonsson and J. Yan, "Ammonia-Water Bottoming Cycles: A Comparison between Gas Engines and Gas Diesel Engines as Prime Movers," *Energy,* vol. 26, pp. 31-44, 2001.

[39]   M. Jonsson, *Advanced power cycles with mixtures as the working fluid*: Doctoral Thesis, Department of Chemical Engineering and Technology, Energy Processes, Royal Institute of Technology, Stockholm, Sweden, 2003.

[40]   J. Wang, Y. Dai, and L. Gao, "Exergy analyses and parametric optimizations for different cogeneration power plants in cement industry," *Applied Energy,* vol. 86, pp. 941-948, 2009.

[41]   Y. Chen, P. Lundqvist, A. Johansson, and P. Platell, "A comparative study of the carbon dioxide transcritical power cycle compared with an organic rankine cycle with R123 as working fluid in waste heat recovery," *Applied Thermal Engineering,* vol. 26, pp. 2142-2147, 2006.

[42]   S. B. Riffat and X. Ma, "Thermoelectrics: A Review of Present and Potential Applications," *Applied Thermal Engineering,* vol. 23, pp. 913-935, 2003.

[43]   D. M. Rowe, "Thermoelectrics, an Environmentally-Friendly Source of Electrical Power," *Renewable Energy,* vol. 16, pp. 1251-1256, 1999.

[44]   Y. Najjar, "Gas Turbine Cogeneration Systems: A Review of Some Novel Cycles," *Applied Thermal Engineering,* vol. 20, pp. 179-197, 2000.

[45]   S. Quoilin and V. Lemort, "Technological and Economic Survey of Organic Rankine Cycle Systems," presented at the 5th European Conference: Economics and Management of Energy in Industry, Portugal, 2009.

[46]   F. Yang, X. Yuan, and G. Lin, "Waste Heat Recovery using Heat Pipe Heat Exchanger for Heating Automobile using Exhaust Gas," *Applied Thermal Engineering,* vol. 23, pp. 367-372, 2003.

[47]   E. J. Bissett, "Mathematical model of the thermal regeneration of a wall-flow monolith diesel particulate filter," *Chemical Engineering Science,* vol. 39, pp. 1233-1244, 1984.

[48]   E. J. Bissett and F. Shadman, "Thermal regeneration of diesel-particulate monolithic filters," *AIChE Journal,* vol. 31, pp. 753-758, 1985.

[49]   C. Depcik and D. Assanis, "Simulating area conservation and the gas-wall interface for one-dimensional based diesel particulate filter models," *Journal of Engineering for Gas Turbines and Power,* vol. 130, 2008.

[50]   T. C. Hung, "A Review of Organic Rankine Cycles (ORCs) for the Recovery of Low-Grade Waste Heat," *Energy,* vol. 22, pp. 661-667, 1997.

[51]   R. El Chammas, "Combined Cycle for Hybrid Vehicles," Society of Automotive Engineers 2005-01-1171, 2005.

[52]   D. Morgan, "Laboratory Test Results Low Emission Rankine-Cycle Engine with Organic-Based Working Fluid and Reciprocating Expander for Automobiles," in *InterSociety Energy Conversion Engineering Conference*, 1973, pp. 158-164.

[53]   P. Patel, "Compounding the Truck Diesel Engine with an Organic Rankine-Cycle System," Society of Automotive Engineers 760343, 1976.

[54]   E. Doyle, "Installation of a Diesel-Organic Rankine Compound Engine in a Class 8 Truck for a Single-Vehicle Test," Society of Automotive Engineers 790646, 1979.

[55]   M. Hall, "Cogeneration," *Mechanical Engineering,* pp. 22-23, 1981.

[56]   J. Heywood, "Automotive Engines and Fuels: A Review of Future Options," *Progress in Energy and Combustion Science,* vol. 7, pp. 155-184, 1981.

[57]   T. J. Marciniak, "Comparison of Rankine-Cycle Power Systems: Effects of Seven Working Fluids," U.S. Department of Energy, Energy and Environmental Systems Division, , Argonne, 1981.

[58]   G. Angelino, M. Gaia, and E. Macchi, "A review of Italian activity in the field of organic Rankine cycles," *VDI-Berichte,* pp. 465-482, 1984.

[59]   O. Badr, "Thermodynamic and Thermophysical Properties of Organic Working Fluids for Rankine-Cycle Engines," *Applied Energy,* vol. 19, pp. 1-40, 1985.

[60]   J. Martin, "Correlations and Equations used in Calculating the Thermodynamic Properties of Freon Refrigerants," *ASME,* 1959.

[61]   R. Downing, "Refrigerant Equations," *ASHRAE Trans.,* vol. 80, pp. 158-169, 1974.

[62]   O. Badr, "Selecting a Working Fluid for a Rankine-Cycle Engine," *Applied Energy,* vol. 21, pp. 1-42, 1985.

[63]   "Feasibility Test of Compounding the Internal Combustion Engine for Automotive Vehicles - Task II," TECO, Waltham, MA.1975.

[64]   O. Badr, S. Naik, P. W. O'Callighan, and S. D. Probert, "Expansion Machine for a Low Power-Output Steam Rankine-Cycle Engine," *Applied Energy,* vol. 39, pp. 93-116, 1991.

[65]   J. Larjola, "Electricity from industrial waste heat using high-speed organic Rankine cycle (ORC)," *International Journal of Production Economics,* vol. 41, pp. 227-235, 1995.

[66]   T. C. Hung, "Waste Heat Recovery of Organic Rankine Cycle using Dry Fluids," *Energy Conversion and Management,* vol. 42, pp. 539-553, 2001.

[67]   M. Kane, "Small Hybrid Solar Power System," *Energy,* vol. 28, pp. 1427-1443, 2003.

[68]   B.-T. Liu, "Effect of Working Fluids on Organic Rankine Cycle for Waste Heat Recovery," *Energy,* vol. 29, pp. 1207-1217, 2004.

[69]   Wartsila. (2010, December 30th). *High Efficiency Heat Recovery in Service*. Available: http://www.wartsila.com/Wartsila/global/docs/en/about_us/twentyfour7/2_2006/High_efficiency_heat_recovery_in_service.pdf

[70]   R. Stobart, "Heat Recovery and Bottoming Cycles for SI and CI Engines- A Perspective," Society of Automotive Engineers 2006-01-0662, 2006.

[71]   D. Arias, "Theoretical Analysis of Waste Heat Recovery from an Internal Combustion Engine in a Hybrid Vehicle," Society of Automotive Engineers 2006-01-1605, 2006.

[72]   H. Leibowitz, I. Smith, and N. Stosic, "Cost effective small scale ORC systems for power recovery from low grade heat sources," *IMECE2006-14284,* 2006.

[73]   P. Colonna, "Dynamic Modeling of Steam Power Cycles: Part I - Modeling Paradigm and Validation," *Applied Thermal Engineering,* vol. 27, pp. 467-480, 2007.

[74] H. van Putten, "Dynamic Modeling of Steam Power Cycles: Part II - Simulation of a Small Simple Rankine Cycle System," *Applied Thermal Engineering,* vol. 27, pp. 2566-2582, 2007.

[75] D. Wei, "Performance Analysis and Optimization of Organic Rankine Cycle (ORC) for Waste Heat Recovery," *Energy Conversion and Management,* vol. 48, pp. 1113-1119, 2007.

[76] H. Teng, "Waste Heat Recovery of Heavy-Duty Diesel Engines by Organic Rankine Cycle Part II: Working Fluids for WHR-ORC," Society of Automotive Engineers 2007-01-0543, 2007.

[77] P. J. Mago, "Performance Analysis of Different Working Fluids for use in Rankine Cycles," in *Institution of Mechanical Engineers--Part A--Power & Energy*, 2007, pp. 255-264.

[78] R. K. Stobart, S. M. Hounsham, and R. Weerasinghe, "The Controllability of Vapour Based Thermal Recovery Systems in Vehicles," Society of Automotive Engineers 2007-01-0270, 2007.

[79] S. Quoilin, "Experimental Study and Modeling of a Low Temperature Rankine Cycle for Small Scale Cogeneration," Electro-Mechanical Engineer, Aerospace and Mechanical Engineering, University of Leige, 2007.

[80] M. Kadota, "Advanced Transient Simulation on Hybrid Vehicle using Rankine Cycle System," Society of Automotive Engineers 2008-01-0310, 2008.

[81] R. Chacartegui, D. Sánchez, J. Muñoz, and T. Sánchez, "Alternative ORC bottoming cycles for combined cycle power plants," *Applied Energy,* vol. 86, pp. 2162-2170, 2009.

[82]   K. K. Srinivasan, P. J. Mago, and S. R. Krishnan, "Analysis of exhaust waste heat recovery from a dual fuel low temperature combustion engine using an Organic Rankine Cycle," *Energy,* vol. 35, pp. 2387-2399, 2010.

[83]   M. Mohd, "Efficiency of Compact Organic Rankine Cycle System with Rotary-Vane-Type Expander for Low-Temperature Waste Heat Recovery," *Civil and Environmental Engineering,* vol. 2, pp. 11-16, 2010.

[84]   I. Vaja and A. Gambarotta, "Internal combustion engine (ICE) bottoming with organic Rankine cycles (ORCs)," *Energy,* vol. 35, pp. 1084-1093, 2010.

[85]   N. Yamada and M. N. A. Mohamad, "Efficiency of hydrogen internal combustion engine combined with open steam Rankine cycle recovering water and waste heat," *International Journal of Hydrogen Energy,* vol. 35, pp. 1430-1442, 2010.

[86]   S. Quoilin, "Experimental Study and Modeling of an Organic Rankine Cycle using Scroll Expander," *Applied Energy,* vol. 87, pp. 1260-1268, 2010.

[87]   W. Weerasinghe, R. Stobart, and S. Hounsham, "Thermal efficiency improvement in high output diesel engines a comparison of a Rankine cycle with turbo-compounding," *Applied Thermal Engineering,* vol. 30, pp. 2253-2256, 2010.

[88]   J. Roy, M. Mishra, and A. Misra, "Performance analysis of an Organic Rankine Cycle with superheating under different heat source temperature conditions," *Applied Energy,* 2011.

[89]   S. Quoilin, S. Declaye, B. F. Tchanche, and V. Lemort, "Thermo-Economic optimization of waste heat recovery Organic Rankine Cycles," *Applied Thermal Engineering,* 2011.

[90]   W. Gu, Y. Weng, Y. Wang, and B. Zheng, "Theoretical and experimental investigation of an organic Rankine cycle for a waste heat recovery system," *Proceedings of the*

Institution of Mechanical Engineers, Part A: Journal of Power and Energy, vol. 223, pp. 523-533, 2009.

[91]   M. Lee, D. Tien, and C. Shao, "Thermophysical capability of ozone-safe working fluids for an organic Rankine cycle system," *Heat Recovery Systems and CHP,* vol. 13, pp. 409-418, 1993.

[92]   V. Lemort, "Contribution to the Characterization of Scroll Machines in Compressor and Expander Modes," Doctor of Applied Sciences, University of Leige, 2007.

[93]   R. Bowman, A. Mueller, and W. Nagle, "Mean Temperature Difference in Design," *ASME Transactions,* vol. 62, pp. 283-294, 1940.

[94]   F. Kreith, *Principles of Heat Transfer*, 6th ed. Pacific Grove, CA: Brooks/Cole, 2001.

[95]   T. Bergman, A. Lavine, F. Incropera, and D. DeWitt, *Fundamentals of Heat and Mass Transfer*, 7th ed. Hoboken, NJ: Wiley, 2011.

[96]   Air Squared. (2011, March 7th). *Oilless Scroll Compressors and Expanders*. Available: http://airsquared.com/pdf/E15H22N4.25.pdf

[97]   S. H. Oh, J. S. MacDonald, and G. L. Vaneman, "Mathematical modeling of fibrous filters for diesel particulates-Theory and experiment," Society of Automotive Engineers 810113, 1981.

[98]   TSI, "Mechanisms of Filtration for High Efficiency Fibrous Filters- Application Note ITI-041," 2006.

[99]   J. S. MacDonald and G. Vaneman, "Experimental evaluation of fibrous filters for trapping diesel-exhaust particulates," GM, Warren, MI, 1981.

[100]   SAE International. (2013, April 5). *Porous Wall and PM Layer*. Available: www.sae.org

[101]   S. Bensaid, D. Marchisio, D. Fino, G. Saracco, and V. Specchia, "Modelling of diesel particulate filtration in wall-flow traps," *Chemical Engineering Journal,* vol. 154, pp. 211-218, 2009.

[102]   A. Konstandopoulos, L. Gratz, J. Johnson, S. Bagley, and D. Leddy, "Ceramic particulate traps for diesel emissions control: effects of a manganese-copper fuel additive," *SAE Transactions,* vol. 97, pp. 37-53, 1989.

[103]   G. C. Koltsakis and A. M. Stamatelos, "Modes of catalytic regeneration in diesel particulate filters," *Industrial & Engineering Chemistry Research,* vol. 36, pp. 4155-4165, 1997.

[104]   A. G. Konstandopoulos, M. Kostoglou, and P. Housiada, "Spatial non-uniformities in diesel particulate trap regeneration," *SAE Transactions,* vol. 110, pp. 609-620, 2001.

[105]   O. C. Haralampous, G. C. Koltsakis, and Z. C. Samaras, "Partial regenerations in diesel particulate filters," Society of Automotive Engineers 2003-01-1881, 2003.

[106]   C. Depcik and D. Assanis, "One-dimensional automotive catalyst modeling," *Progress in Energy and Combustion Science,* vol. 31, pp. 308-369, 2005.

[107]   C. Depcik, "Simulating the Concentration Equations and the Gas-Wall Interface for One-Dimensional Based Diesel Particulate Filters," *J Eng. Gas Turbines Power,* vol. 132, p. 12, 2010.

[108]   C. Depcik and S. Loya, "Dynamically Incompressible Flow," in *Advanced Methods for Practical Applications in Fluid Mechanics*, ed: INTECH, 2012.

[109]   A. Konstandopoulos and J. Johnson, "Wall-Flow Diesel Particulate Filters; Their Pressure Drop and Collection Efficiency," Society of Automotive Engineers 890405, 1989.

[110] D. Nield and A. Bejan, *Convection in porous media*, 2nd ed. New York, NY: Springer-Verlag, 1999.

[111] F. A. Dullien, *Porous media: fluid transport and pore structure*: Academic Press, 1991.

[112] B. R. Munson, D. F. Young, T. H. Okiishi, and W. W. Huebsch, *Fundamentals of Fluid Mechanics*, 6th ed. Hoboken, NJ: John Wiley & Sons, Inc., 2009.

[113] J. Liu, N. Schorn, C. Schernus, and L. Peng, "Comparison studies on the method of characteristics and finite difference methods for one-dimensional gas flow through IC engine manifold," Society of Automotive Engineers 960078, 1996.

[114] A. Onorati and G. D'Errico, "Fluid dynamic modeling of the gas flow with chemical specie transport through the exhaust manifold of a four-cylinder SI engine," Society of Automotive Engineers 1999-01-0557, 1999.

[115] O. Haralampous and G. Koltsakis, "Oxygen diffusion modeling in diesel particulate filter regeneration," *AIChE Journal,* vol. 50, pp. 2008-2019, 2004.

[116] R. A. Wooding, "Steady State Free Thermal Convection of Liquid in a Saturated Permeable Medium," *J Fluid Mechanics,* vol. 2, pp. 273-285, 1957.

[117] H. C. Brinkman, "A calculation of the viscous force exerted by a flowing fluid on a dense swarm of particles," *Appl Sci Res Sect A,* vol. 1, pp. 27-34, 1947.

[118] H. C. Brinkman, "On the permeability of media consisting of closely packed porous particles," *Appl Sci Res Sect A,* vol. 1, pp. 81-86, 1947.

[119] G. W. Jackson and D. F. James, "The permeability of fibrous porous media," *The Canadian Journal of Chemical Engineering,* vol. 64, pp. 364-374, 1986.

[120] J. L. Beck, "Convection in a box of porous material saturated with fluid," *Physics of Fluids,* vol. 15, p. 1377, 1972.

[121] M. Kostoglou, P. Housiada, and A. G Konstandopoulos, "Multi-channel simulation of regeneration in honeycomb monolithic diesel particulate filters," *Chemical Engineering Science,* vol. 58, pp. 3273-3283, 2003.

[122] A. G. Konstandopoulos, M. Kostoglou, N. Vlachos, and E. Kladopoulou, "Progress in diesel particulate filter simulation," Society of Automotive Engineers 2005-01-0946, 2005.

[123] Y. Cheng and G. Hwang, "Experimental studies of laminar flow and heat transfer in a one-porous-wall square duct with wall injection," *International Journal of Heat and Mass Transfer,* vol. 38, pp. 3475-3484, 1995.

[124] Y. Cheng, G. Hwang, and M. Ng, "Developing laminar flow and heat transfer in a rectangular duct with one-walled injection and suction," *International Journal of Heat and Mass Transfer,* vol. 37, pp. 2601-2613, 1994.

[125] G. Hwang, Y. Cheng, and Y. Chiang, "An experimental study of laminar heat transfer in a one-porous-wall square duct with suction flow," *International Journal of Heat and Mass Transfer,* vol. 40, pp. 481-485, 1997.

[126] G. Hwang, Y. Cheng, and M. Ng, "Developing laminar flow and heat transfer in a square duct with one-walled injection and suction," *International Journal of Heat and Mass Transfer,* vol. 36, pp. 2429-2440, 1993.

[127] R. B. Kinney, "Fully developed frictional and heat-transfer characteristics of laminar flow in porous tubes," *International Journal of Heat and Mass Transfer,* vol. 11, pp. 1393-1401, 1968.

[128] G. Raithby, "G Raithby," *International Journal of Heat and Mass Transfer,* vol. 14, pp. 223-243, 1971.

[129] F. Schmidt and M. Newell, "Heat transfer in fully developed laminar flow through rectangular and isosceles triangular ducts," *International Journal of Heat and Mass Transfer,* vol. 10, pp. 1121-1123, 1967.

[130] J. Yuan, M. Rokni, and B. Sundén, "Simulation of fully developed laminar heat and mass transfer in fuel cell ducts with different cross-sections," *International Journal of Heat and Mass Transfer,* vol. 44, pp. 4047-4058, 2001.

[131] R. Pederson and R. Kinney, "Entrance-region heat transfer for laminar flow in porous tubes," *International Journal of Heat and Mass Transfer,* vol. 14, pp. 159-161, 1971.

[132] C. Sprouse III, M. Mangus, and C. Depcik, "Diesel Particulate Filter Model with Detailed Permeability Analysis," in *2011 Fall Conference of the ASME Energy and Water Scarcity Division*, Denver, CO., 2011.

[133] A. G. Konstandopoulos and M. Kostoglou, "Periodically reversed flow regeneration of diesel particulate traps," *SAE Transactions,* vol. 108, pp. 289-302, 1999.

[134] G. C. Koltsakis and A. M. Stamatelos, "Modeling catalytic regeneration of wall-flow particulate filters," *Industrial & Engineering Chemistry Research,* vol. 35, pp. 2-13, 1996.

[135] A. G. Konstandopoulos and M. Kostoglou, "Reciprocating flow regeneration of soot filters," *Combustion and Flame,* vol. 121, pp. 488-500, 2000.

[136] A. G. Konstandopoulos, M. Kostoglou, E. Skaperdas, E. Papaioannou, D. Zarvalis, and E. Kladopoulou, "Fundamental studies of diesel particulate filters: transient loading, regeneration and aging," Society of Automotive Engineers 2000-01-1016, 2000.

[137] A. G. Konstandopoulos, M. Kostoglou, P. Housiada, N. Vlachos, and D. Zarvalis, "Multichannel simulation of soot oxidation in diesel particulate filters," *SAE Transactions,* vol. 112, pp. 587-604, 2003.

[138] O. Haralampous, C. Dardiotis, G. Koltsakis, and Z. Samaras, "Study of catalytic regeneration mechanisms in diesel particulate filters using coupled reaction-diffusion modeling," *SAE Transactions,* vol. 113, pp. 1145-1161, 2004.

[139] H. Aoki, A. Asano, K. Kurazono, K. Kobashi, and H. Sami, "Numerical simulation model for the regeneration process of a wall-flow monolith diesel particulate filter," Society of Automotive Engineers 930364, 1993.

[140] F. Jacquot, V. Logie, J. Brilhac, and P. Gilot, "Kinetics of the oxidation of carbon black by NO2: Influence of the presence of water and oxygen," *Carbon,* vol. 40, pp. 335-343, 2002.

[141] J. Neeft, T. X. Nijhuis, E. Smakman, M. Makkee, and J. A. Moulijn, "Kinetics of the oxidation of diesel soot," *Fuel,* vol. 76, pp. 1129-1136, 1997.

[142] H. Mohammed, A. P. Triana, and J. H. Johnson, "An Advanced 1 D 2-Layer Catalyzed Diesel Particulate Filter Model to Simulate: Filtration by the Wall and Particulate Cake, Oxidation in the Wall and Particulate Cake by NO2 and O2, and Regeneration by Heat Addition," Society of Automotive Engineers 2006-01-0467, 2006.

[143] G. C. Koltsakis and A. M. Stamatelos, "Modeling thermal regeneration of wall-flow diesel particulate traps," *AIChE Journal,* vol. 42, pp. 1662-1672, 1996.

[144] O. Haralampous, G. Koltsakis, Z. Samaras, C.-D. Vogt, E. Ohara, Y. Watanabe*, et al.*, "Reaction and diffusion phenomena in catalyzed diesel particulate filters," *SAE Transactions,* vol. 113, pp. 435-446, 2004.

[145] O. Haralampous and G. C. Koltsakis, "Intra-layer temperature gradients during regeneration of diesel particulate filters," *Chemical Engineering Science,* vol. 57, pp. 2345-2355, 2002.

[146] Z. Guo, "Multi-dimensional modeling and simulation of wall-flow diesel particulate filter during loading and regeneration," Society of Automotive Engineers 2006-01-0265, 2006.

[147] K. E. Brenan, S. L. Campbell, and L. R. Petzold, *Numerical solution of initial-value problems in differential-algebraic equations*: Society for Industrial and Applied Mathematics, 1987.

[148] A. C. Hindmarsh, "LSODE and LSODI, two new initial value ordinary differnetial equation solvers," *ACM Signum Newsletter,* vol. 15, pp. 10-11, 1980.

[149] J. F. Gardner, *Simulations of machines using MATLAB and SIMULINK*, 1st ed. Pacific Grove, CA: Brooks/Cole, 2001.

[150] L. F. Shampine, M. W. Reichelt, and J. A. Kierzenka, "Solving index-1 DAEs in MATLAB and Simulink," *SIAM review,* vol. 41, pp. 538-552, 1999.

[151] A. Cavallo, R. Setola, and F. Vasca, *Using MATLAB, SIMULINK and Control System Toolbox: a practical approach*: Prentice-Hall, Inc., 1996.

[152] C. Depcik, "Modeling Reacting Gases and Aftertreatment Devices for Internal Combustion Engines," Ph.D, University of Michigan, Ann Arbor, MI, 2003.

[153] P. J. Roache, *Computational Fluid Dynamics*. Albuerque, New Mexico: Hermosa, 1972.

[154] D. M. Young, C. J. Warren, and K. P. Gadkaree, "Silicon carbide for diesel particulate filter applications: material development and thermal design," Society of Automotive Engineers 2002-01-0324, 2002.

[155] I. Kandylas and G. Koltsakis, "Simulation of continuously regenerating diesel particulate filters in transient driving cycles," *Proceedings of the Institution of Mechanical Engineers, Part D: Journal of Automobile Engineering,* vol. 216, pp. 591-606, 2002.

[156] O. Kröcher and M. Elsener, "Combination of V2O5/WO3−TiO2, Fe−ZSM5, and Cu−ZSM5 Catalysts for the Selective Catalytic Reduction of Nitric Oxide with Ammonia," *Industrial & Engineering Chemistry Research,* vol. 47, pp. 8588-8593, 2008.

[157] Z. Zhang, M. Chen, Z. Jiang, and W. Shangguan, "Low-temperature selective catalytic reduction of NO with propylene in excess oxygen over the Pt/ZSM-5 catalyst," *Journal of Hazardous Materials,* vol. 193, pp. 330-334, 2011.

[158] M. Mangus and C. Depcik, "Comparison of ULSD, Used Cooking Oil Biodiesel, and JP-8 Performance and Emissions in a Single-Cylinder Compression-Ignition Engine.," *SAE International Journal of Fuels and Lubricants,* vol. 5, pp. 1382-1394, 2012.

[159] J. Mattson, "Power, Efficiency, and Emissions Optimization of a Single Cylinder Direct-Injected Diesel Engine for Testing of Alternative Fuels through Heat Release Modeling," Master of Science, Mechanical Engineering, University of Kansas, 2013.

[160] C. Depcik, "A Universal Heat Transfer Correlation for Intake and Exhaust Flows in a Spark-Ignition Internal Combustion Engine," *SAE Transactions Journal of Engines,* vol. 111, pp. 734-741, 2002.

[161] V. Arpaci, *Microscales of Turbulence: Heat and Mass Transfer Correlations*. Amsterdam: Overseas Publishers Association, 1997.

[162] M. Kavainy, *Principles of Heat Transfer in Porous Media*. New York: Springer, 1992.

[163]   G. Koltsakis, O. Haralampous, N. Margaritis, Z. Samaras, C.-D. Vogt, E. Ohara, *et al.*, "3-Dimensional Modeling of the Regeneration in SiC Particulate Filters," *SAE International,* vol. 2005-01-0953, 2005.

[164]   O. Haralampous, G. Koltsakis, Z. Samaras, C.-D. Vogt, E. Ohara, Y. Watanabe, *et al.*, "Modeling and experimental study of uncontrolled regenerations in SiC filters with Fuel Borne catalyst," vol. 2004-01-0697, 2004.

[165]   G. Koltsakis, Z. Samaras, H. Echtle, D. Chatterjee, P. Markou, and O. Haralampous, "Flow Maldistribution Effects on DPF Performance," *SAE International,* vol. 2009-01-1280, 2009.

[166]   C. Depcik, C. Langness, and J. Mattson, "Development of a Simplified Diesel Particulate Filter Model Intended for an Engine Control Unit," *SAE International,* vol. 2014-01-1559, 2014.

[167]   Ferro Ceramic. (2013, October 13th). Available: www.ferroceramic.com/Cordierite_table.htm

[168]   Assuratus. (2013, June). *Silicon Carbide Ceramic Properties*.

[169]   C. Sprouse III and C. Depcik, "Combining a Diesel Particulate Filter and Heat Exchanger for Waste Heat Recovery and Particulate Matter Reduction," SAE International 2014-01-0673, 2014.